

UNCLASSIFIED

AD 4 2 3 0 6 4

DEFENSE DOCUMENTATION CENTER

FOR

SCIENTIFIC AND TECHNICAL INFORMATION

CAMERON STATION, ALEXANDRIA, VIRGINIA



UNCLASSIFIED

NOTICE: When government or other drawings, specifications or other data are used for any purpose other than in connection with a definitely related government procurement operation, the U. S. Government thereby incurs no responsibility, nor any obligation whatsoever; and the fact that the Government may have formulated, furnished, or in any way supplied the said drawings, specifications, or other data is not to be regarded by implication or otherwise as in any manner licensing the holder or any other person or corporation, or conveying any rights or permission to manufacture, use or sell any patented invention that may in any way be related thereto.

AS AD No. 423064

423064

**PROCEEDINGS
OF THE
SIXTH SYMPOSIUM ON
HYPERVELOCITY IMPACT**



VOLUME II
PART 2

AUGUST, 1963

**PROCEEDINGS
OF THE
SIXTH SYMPOSIUM ON
HYPERVELOCITY IMPACT**

**CLEVELAND, OHIO
APRIL 30, MAY 1, 2, 1963**

Sponsored by:

U.S. Army

U.S. Air Force

U.S. Navy

Tri-Service Committee:

R. J. Eichelberger, Army, BRL, Chairman

W. H. Dittrich, Air Force, Det. 4, ASD

W. W. Atkins, Navy, NRL

Contract No.

DA-31-124-ARO(D)-16

VOLUME II

PART 2

AUGUST, 1963

The Firestone Tire & Rubber Co. (Conference Host)

VOLUME II - Part 2

HYPERVELOCITY CRATERING DATA AND A CRATER- DEPTH MODEL FOR THE REGIME OF FLUIDITY Olive G. Engel	337
FLUID IMPACT CRATERS AND HYPERVELOCITY - - HIGH-VELOCITY IMPACT EXPERIMENTS IN METALS AND ROCKS H. J. Moore, R. W. MacCormack, and D. E. Gault	367
ENERGY BALANCES IN HYPERVELOCITY PENETRATION R. B. Pond, C. Mobley, and C. M. Glass	401
THE PARTITION OF ENERGY FOR HYPERVELOCITY IMPACT CRATERS FORMED IN ROCK Donald E. Gault and Ezra D. Heitowit	419
TRANSIENT OBSERVATIONS OF CRATER FORMATION IN SEMI-INFINITE TARGETS J. H. Kineke, Jr., and Richard Vitali	457
INFLUENCE OF TARGET STRENGTH ON HYPERVELOCITY CRATER FORMATION IN ALUMINUM J. H. Kineke, Jr., and L. G. Richards	513
SOME PHENOMENA ASSOCIATED WITH IMPACTS INTO ALUMINUM S. M. Halperson	525
PARTICLE-SOLID IMPACT PHENOMENA E. H. Goodman and C. D. Liles	543
INVESTIGATION OF THE IMPACT OF COPPER FILAMENTS INTO ALUMINUM TARGETS AT VELOCITIES TO 16,000 FEET PER SECOND C. Robert Nysmith, James L. Summers, and B. Pat Denardo	577
IONIZATION ASSOCIATED WITH HYPERVELOCITY IMPACT J. F. Friichtenicht and J. C. Slattery	591

INVESTIGATION OF IMPACT FLASH AT LOW AMBIENT PRESSURES Robert W. MacCormack	613
AN INVESTIGATION OF THE PHENOMENA OF IMPACT FLASH AND ITS POTENTIAL USE AS A HIT DETECTION AND TARGET DISCRIMINATION TECHNIQUE J. W. Gehring and R. L. Warnica	627
SUMMARY: THEORETICAL AND EXPERIMENTAL STUDIES OF CRATER FORMATION R. J. Eichelberger	683
AUTHOR INDEX	707

HYPERVELOCITY CRATERING DATA AND A CRATER-DEPTH MODEL
FOR THE REGIME OF PARTIAL FLUIDITY

by

Olive G. Engel

ABSTRACT

A model for hypervelocity cratering in the regime of partial liquefaction is proposed and an equation for maximum crater depth is developed. The equation is found to be in good agreement with hypervelocity crater depth data for the four possible projectile-target combinations of high-purity copper and aluminum. The data cited are both tabulated and presented graphically.

HYPERVELOCITY CRATERING DATA AND A CRATER-DEPTH MODEL
FOR THE REGIME OF PARTIAL FLUIDITY

1. Introduction

The depth of craters produced by normal impact of liquid drops and ductile metal spheres against metal plates is a straight-line function of the impact velocity, V , for impact velocities up to about 1 km/sec. The crater depth, D , is given by the equation [1]^a

$$D = \frac{7.2 d z_p}{c_p (z_p + z_t)} \left[V - V_1 \right] \quad (1)$$

where d is the drop or sphere diameter, c is sound speed, z is acoustic impedance (product of longitudinal wave speed and density), and V_1 is the lowest velocity at which a crater of noticeable depth is formed. The sub-p notation refers the quantity to the projectile drop or sphere and the sub-t notation refers the quantity to the target. The intercept velocity, V_1 , is $19 E_t (z_p + z_t) / (\rho_p c_t z_t^3)^{1/2}$ where ρ is density and E_t is the energy per unit volume that can be absorbed by the target metal without fracture or plastic yield. A similar equation, but with different numerical coefficients, has been found to apply for craters produced by the impact of rigid steel spheres [2].

^a Numbers in brackets refer to literature references at the end of this paper.

CRATERING AND CRATER-DEPTH MODEL

When a metal sphere impinges against a metal plate, shear stresses (τ_A of figure 1) exist around the cylinder of target metal that is set in motion as a result of the impact. Shear stresses (τ_B of figure 1) also exist in the target metal around the point of impingement. The cratering model on which eq (1) is based is that the core of metal that extends through the target plate under the area of impact moves with respect to the remainder of the plate. This mechanism involves plastic deformation under shear stress τ_A of figure 1.

Because it was thought that extensive fluidity might be produced in hypervelocity impacts if the impact velocity was progressively increased, the cratering that occurs when a liquid drop impinges against a liquid was studied. For hemispherical craters, which are produced when the drop liquid and target liquid are the same, it was found [3] that the maximum crater depth, D , is given by

$$D = \left[\left(\frac{d^3 v^2}{6.6667 g} + \frac{311.49 \gamma^2}{g^2 \rho^2} \right)^{1/2} - \frac{17.649 \gamma}{g \rho} \right]^{1/2} \quad (2)$$

where γ is the surface tension of the liquid used for drop and target and g is the acceleration due to gravity. Impacts for which the density of the drop liquid is different from that of the target liquid have not as yet been studied at the National Bureau of Standards. However, from pictures taken by Rupe [4] it appears that if the drop is of a higher-density liquid than the target the crater resembles half a prolate spheroid. For this case a form factor involving the density ratio ρ_t / ρ_p seems to be required; from currently available data it is not possible to determine whether the power to which this ratio must be raised is 1 or 1/2.

CRATERING AND CRATER-DEPTH MODEL

From eq (2), the maximum depth of craters formed in liquids by impact of a liquid drop varies as $V^{1/2}$. Crater depth in hypervelocity impacts has been found to vary as $V^{2/3}$ in the velocity range from about 1 to about 4 km/sec [5]. Depth-versus-velocity data for hypervelocity impacts of the four possible projectile-target combinations of copper and aluminum^b indicate that this power law applies from about 2 to about 7 km/sec. It is noteworthy that $V^{1/2} < V^{2/3} < V^1$ and that on the basis of the variation of crater depth with impact velocity the hypervelocity cratering mechanism that operates in the velocity range from about 2 to about 7 km/sec is intermediate between that for which the target is a solid and that for which the target is a liquid. See figure 2.

A detailed study^{b, c} of the impact of a 0.3-in. right-circular cylinder of polycarbonate resin against a 1.9-in.-thick plate of poly(methyl methacrylate) at 6.635 km/sec, which was photographed at over a million frames per sec, has led to the conclusion that in a hypervelocity impact at this velocity and with this projectile-target combination the amount of matter that liquefies cannot exceed the mass of material that originally occupied the crater volume. In addition, study of high-speed pictures of impacts^b of the four possible projectile-target combinations of copper and aluminum in the velocity range from 2 to 7 km/sec has led to the further conclusion that the ejecta are not wholly fluid but contain distinct solid masses. Consequently, for impacts in this velocity range using these projectile-target combinations, the amount of matter that liquefies must be less than the amount of material that originally occupied the crater volume.

^b The sources of the hypervelocity data discussed in this paper are given in section 4.

^c See WADD Technical Report 60-475, Part III.

CRATERING AND CRATER-DEPTH MODEL

2. Fusion As a Result of Hypervelocity Impact

When a metal sphere impacts a planar metal target at normal incidence, two pressure waves are initiated at the surface of impact. See figure 3. Pressure wave A of figure 3 moves into the target; pressure wave B of figure 3 moves into the sphere. For hypervelocity impacts these pressure waves are shock waves. The particles of metal in both sphere and target that have been traversed by these shock waves have been given energy. The pressure, density, temperature, and entropy of the metal traversed by these shock waves has been increased. For impacts at very high velocity the compressed target metal that has been traversed by shock wave A of figure 3 in the initial phase of the impact has such high energy density that it must flow as a result of the shear stress B of figure 1; the compressed metal in the sphere must also flow.

When shock wave B of figure 3 reaches the bounding surface of the sphere, it reflects as a tension wave that moves back toward the impact surface. As this reflected tension wave traverses the sphere, the heated metal of the sphere is released from compression. Fusion of this metal is to be expected if its temperature after pressure release is in excess of the melting point that is characteristic of the increased entropy state in which it exists. When the reflected tension wave reaches the surface of contact between the impacted sphere and the target, it is partly transmitted into the target and partly reflected back into the sphere. The heated target metal into which the tension wave is partly transmitted will now also undergo fusion if its temperature after pressure release is in excess of the melting point that is characteristic of the increased entropy state in which it exists.

As the impact velocity is progressively increased, the amplitude of the transmitted wave of tension will increase and the amount of target metal that melts will increase. Although cratering according to the low-velocity

CRATERING AND CRATER-DEPTH MODEL

mechanism [1, 2] continues, if the impact velocity is progressively increased a velocity range should be encountered in which fusion of target metal accompanied by the outward flow of the melt may become the dominant process in determining crater size.

3. Crater Depth Equation for the Hypervelocity Regime of Partial Fluidity

If similarity exists in the partition of energy for the limited hypervelocity regime in which crater depth varies as the $2/3$ power of the impact velocity, then the fraction of the impact energy that is used in fusion may be relatively constant within this regime. Although this argument is speculative, it suggests that the equality

$$(\text{constant}) (\text{available energy}) = (\text{volume melted}) \rho_t (\Delta H + E) \quad (3)$$

may be a reasonable assumption to make in deriving a crater-depth equation.

In eq (3), ΔH is the heat required to raise unit mass of target metal to its melting temperature and E is the specific latent heat of fusion. For hemispherical craters of radius D , use of the assumption given by eq (3) would produce the equality

$$\alpha (2\pi D^3 \rho_t / 3) (\Delta H + E) = (\text{constant}) (\pi \rho_p d^3 v^2 / 12) \quad (4)$$

where α is the fraction of the crater contents that melts. From eq (4),

$$D = (\text{constant}) \left[\rho_p d^3 v^2 / \alpha \rho_t (\Delta H + E) \right]^{1/3} \quad (5)$$

Equation (5) applies only to hemispherical craters. Crater depth/diameter data for the four possible projectile-target combinations of copper and aluminum^b are plotted against velocity in figure 4. From figure 4, hypervelocity craters formed in the velocity range from 2 to 7 km/sec by impact of a metal sphere against a thick plate are hemispherical only if the sphere and plate are of the same metal. If the projectile is of higher-density metal than the target, the

CRATERING AND CRATER-DEPTH MODEL

crater resembles half a prolate spheroid just as in impacts of liquid drops against target liquids [4]. For hypervelocity impact of metal spheres against metal plates the acoustic impedance ratio z_t/z_p suggested itself as a form factor rather than the density ratio, and, a posteriori, this proved to be the better choice. On introducing this ratio into eq (4) one obtains

$$\alpha \left[2\pi \rho_t D (z_t D^2 / z_p) / 3 \right] (\Delta H + E) = (\text{constant}) \left[\pi \rho_p d^3 v^2 / 12 \right]. \quad (6)$$

From eq (6), for projectile-target combinations in which $z_p = z_t$, the crater is a hemisphere; for projectile-target combinations in which $z_p < z_t$, the crater should resemble half an oblate spheroid; for projectile-target combinations in which $z_p > z_t$, the crater should resemble half a prolate spheroid. And from eq (6),

$$D = (\text{constant}) (z_p / z_t)^{1/3} \left[d^3 \rho_p v^2 / \alpha \rho_t (\Delta H + E) \right]^{1/3}. \quad (7)$$

To obtain maximum crater depth from eq (7), it is necessary to have an explicit expression for α , the fraction of the crater contents that melts.

It was pointed out in section 1 that crater depth in impacts involving no fluidity ($\alpha = 0$) varies as V^1 , that crater depth in impacts involving partial fluidity ($0 < \alpha < 1$) varies as $V^{2/3}$, and that crater depth in completely fluid impacts ($\alpha = 1$) varies as $V^{1/2}$. The amount of fluidity that is produced increases with the impact velocity. However, the velocity range over which crater depth varies as $V^{2/3}$ is further characterized by the empirical finding that crater volume varies as the impact energy and, therefore, as V^2 .

CRATERING AND CRATER-DEPTH MODEL

Although the absolute amount of fluidity and the crater volume both increase as the impact velocity is increased, it is assumed that in the regime of partial fluidity where crater depth varies as $V^{2/3}$ the ratio of the absolute amount of fluidity to the crater volume, that is, the melt-fraction α , has a very small dependence on V , and, for practical purposes, may be regarded as independent of V . To the extent that α is independent of V , α will be a constant for any given projectile-target combination.

If the tension wave that reflects from the bounding surface of the sphere and returns to the impact surface were an elastic plane wave, the ratio of the stress in the transmitted wave to the stress in the returned wave would be $2 z_t / (z_t + z_p)$. Because the amount of fusion of target metal that can occur depends on the extent to which the reflected tension wave that returns to the surface of contact is transmitted into the target, α may be some function of the acoustic impedance ratio $z_t / (z_t + z_p)$. If α is a function of $z_t / (z_t + z_p)$, it follows that α will have different values for different projectile-target combinations.

Let it be assumed that

$$\alpha = (\text{constant}) z_t / (z_t + z_p). \quad (8)$$

On introducing eq (8) into eq (7) one obtains

$$D = \beta \left[\left\{ 1 / (\Delta H + E) \right\} \left(\rho_p / \rho_t \right) \left\{ (z_t + z_p) / z_t \right\} \left(z_p / z_t \right) \right]^{1/3} d V^{2/3} \quad (9)$$

where the constant of proportionality for α and the constant that limits the amount of the impact energy that is used in fusion are combined in the numerical constant β .

The value of the constant β was found by inserting experimentally observed values of D in eq (9). The value of D at an arbitrary velocity (4 km/sec) was obtained from best-fit curves to data ^b for the four possible projectile-

CRATERING AND CRATER-DEPTH MODEL

target combinations of copper and aluminum for one sphere size (1/8-in. diameter). The four values of β found in this way are given in table 1; they are seen to be in close agreement. From the values of β that were obtained, the value of $\beta = 0.695$ was selected as being the most representative. Introducing this value of β into eq (9),

$$D = 0.695 \left[\left\{ 1/(\Delta H + E) \right\} \left(\frac{\rho_p}{\rho_t} \right) \left\{ (z_t + z_p)/z_t \right\} \left(z_p/z_t \right) \right]^{1/3} d v^{2/3} \quad (10)$$

4. Crater Depth Data and Test of the Crater-Depth Equation

An experiment was designed to collect a variety of crater depth data to test the crater-depth equation. Because there is no light gas gun available at the National Bureau of Standards, the hypervelocity firings were made at Eglin Air Force Base, Florida, and by ARO-Inc., at Arnold Engineering Development Center, Tullahoma, Tennessee. The data to be collected were crater depth, crater diameter, and crater volume for the four possible projectile-target combinations of high purity-aluminum (99.99 per cent aluminum) and oxygen-free high-conductivity copper (99.96 per cent copper).

The spheres were 1/16-in.-diameter, 1/8-in.-diameter, and 3/16-in.-diameter; they were formed from wire made of exactly the same metals as the target plates. The target plates were of different thicknesses up to 2 inches. The criterion used in selecting the plate thickness for a given sphere size and impact velocity was that there should be no noticeable bulge on the reverse side of the plate as a result of the impact. Both the spheres and target plates were annealed to remove work hardening.

All of the firings were made at reduced pressure and with use of sabots to prevent ablation of the projectile spheres as far as feasible. The target plates were at room temperature; they were given edge support only. All of the shots were made at normal incidence and all of the impacts were photographed

CRATERING AND CRATER-DEPTH MODEL

with use of a Beckman and Whitley camera. The impact velocity was determined from the Beckman and Whitley camera pictures of the impinging sphere just before it struck the target. The required information for the velocity determination was the distance travelled by the sphere between consecutive frames just before impact.

The apparent depths of the craters that formed as a result of the firings were measured by the experimenters at the two locations where the firings were made. The apparent crater depth is the distance from the original target surface to the crater floor which in most cases is covered by a residue of the projectile sphere.

After the experimental craters were received at the National Bureau of Standards, the apparent crater depths were measured again. The craters were then cut into two pieces in order to determine the depth of the projectile residue. The cuts were made a little to one side of the center of the crater; the larger section was mounted in plastic. The mounted cross sections were then abraded until the depth of the crater in cross section was close to the previously measured apparent depth. The mounted cross sections were then given a metal-lurgical polish and the depth of the projectile residue in the crater was measured with a machinist's microscope.

The projectile residue was easily discernible in the craters formed by impact of aluminum spheres against copper targets and in those formed by impact of copper spheres against aluminum targets. For impacts in which the sphere and target were of the same metal it was necessary to bring the cross section to a high polish and etch it to bring out the crack between the projectile residue and the target metal. In a small number of cases it proved to be impossible to find the separating crack and in these cases the depth of the projectile residue could not be measured.

CRATERING AND CRATER-DEPTH MODEL

The real depth of the craters is their apparent depth before sectioning plus the depth of the projectile residue found in them. The apparent crater depth that was measured before the craters were sectioned, the depth of the projectile residue found in the craters, and the real depth of the craters is given in table 2. The apparent crater depth tabulated is the average of the value found by the investigators at Eglin Air Force Base or at ARO-Inc. and the value found at the National Bureau of Standards.

The real crater depths are plotted against the impact velocity in figures 5, 6, 7, and 8. In a few cases the two values of apparent crater depth that were averaged were widely different. In these cases a vertical line is drawn through the point on the graph to indicate the limits of real depth that would have been found had they not been averaged. In most cases the variation did not exceed the limits of the symbol (square, circle, triangle) used to indicate the point.

The lines drawn in figures 5, 6, 7, and 8 give the crater depth for various values of impact velocity that were obtained with use of eq (10) for the three sphere sizes and four projectile-target combinations of copper and aluminum that were used. (Properties of copper and aluminum are given in table 3.) From these graphs the agreement between the depths found by eq (10) and the experimentally observed depths is acceptable for the projectile-target combinations and the experimental firing conditions that were used. Because ΔH in eq (10) involves the target temperature, the inclusion of experimental data for targets at temperatures significantly different from room temperature would be desirable to provide a more comprehensive test of the relationship.

Because the model on which eq (10) is based requires some melting of target metal, this equation would not be expected to apply at low impact velocities. The theoretical curves were carried to velocities as low as 2 km/sec. The

CRATERING AND CRATER-DEPTH MODEL

agreement between the theoretical curves and the experimental data at velocities as low as 2 to 3 km/sec, which can be seen in figures 5, 6, 7, and 8, is surprising in view of the finding of Olshaker and Bjork [6] that the threshold velocities for incipient melting in impacts involving three projectile-target combinations of copper and aluminum are: copper-copper, 4.4 km/sec; aluminum-aluminum, 5.0 km/sec; and aluminum-copper, 6.6 km/sec.

It is possible that the threshold velocities for incipient melting reported by Olshaker and Bjork [6] are too high. On the other hand, it is possible that eq (10) is successful in predicting crater depth at velocities below those for which incipient melting occurs because of a real relation between breaking and melting. Furth and Born [7] have advanced the concept that breaking is a form of melting: "melting being nothing else than a breaking due to the action of the heat movement of the atoms; or putting it the other way round, breaking is nothing else than melting enforced by the action of the stress" (see also references [8, 9, 10]).

If eq (10) is successful in predicting crater depth at low velocities because it is able to describe a breaking mechanism by means of the energy needed for melting, then eq (10) is limited in applicability at low velocities to pure metals in the annealed state. It is important to note that the only material strength that eq (10) takes into account is the characteristic strength of a pure metal as represented by the energy per unit mass needed to melt it. Equation (10) does not take into account the strength of metals produced by alloying, heat treatment, and other means. The strength of metals that is produced in these ways is gradually lost as the temperature of the metal is increased. It is possible that eq (10) may be able to predict crater depth for metals of these kinds either at high impact velocities or for heated targets. However, eq (10) should not be used to predict crater depth for these metals

CRATERING AND CRATER-DEPTH MODEL

until this has been shown to be the case by means of experimental data.

5. The Regime of Complete Fluidity

As impact velocity is increased progressively, the fluidity that is produced as a result of the impact will increase; it will finally become extensive. When the amount of fluidity that is produced becomes extensive, crater depth may be found to vary as $v^{1/2}$ as it does for impacts of a liquid drop against a target liquid (see section 1 and eq (2)); but it is not certain that this will be the case. Inspection of figures 5, 6, 7 and 8 shows that in some cases the data points at velocities of 6 to 7 km/sec fall below the theoretical curves. It is possible that this may indicate the onset of transition to the purely liquid regime, but more data are needed to determine whether or not this apparent fall off is real.

6. Acknowledgements

The work described in this paper was conducted under the sponsorship of the Nonmetallic Materials Laboratory, Aeronautical Systems Division, Wright-Patterson Air Force Base, Ohio.

Lt. Thomas E. Shelton was the test officer for the hypervelocity firings made at Eglin Air Force Base. Mr. E.H. Goodman and Mr. C.D. Liles were the project engineers for the hypervelocity firings made by ARO-Inc.

The work of measuring the apparent crater depths at the National Bureau of Standards and the work of mounting and polishing the crater cross sections and measuring the depth of the projectile residues was done by Mr. Raymond L. Hebert and Mr. David P. Dowd.

A helpful conversation with Mr. Henry E. Robinson, Chief NBS Heat Transfer Section, is gratefully acknowledged.

CRATERING AND CRATER-DEPTH MODEL

REFERENCES

1. Olive G. Engel, Pits in metals caused by collision with liquid drops and soft metal spheres, NBS Journal of Research 62, 229 (1959).
2. Olive G. Engel, Pits in metals caused by collision with liquid drops and rigid steel spheres, NBS Journal of Research 64 A, 61 (1960).
3. Olive G. Engel, Crater Depth in Fluid Impacts, to be published in the NBS Journal of Research.
4. Jack H. Rupe, Critical impact velocities of water droplets as a problem in injector-spray sampling, Progress Report No. 4 - 80, Jet Propulsion Laboratory, California Institute of Technology, Pasadena, Calif., September, 1950.
5. Proceedings of the Third Symposium on Hypervelocity Impact, Volume I, Armour Research Foundation, Chicago, Illinois, February 1959.
6. A.E. Olshaker and R.L. Bjork, The role of melting and vaporization in hypervelocity impact, Proceedings of Fifth Symposium on Hypervelocity Impact, Colorado School of Mines, Denver, Col., April 1962.
7. R. Furth and M. Born, Nature 145, 741 (1940).
8. M. Born, J. Chem. Phys 2, 591 (1939).
9. R. Furth, Proc. Roy. Soc. (London) 177 A, 217 (1941).
10. R. Furth, Proc. Cam. Phil. Soc. 37, 34 (1941).

CRATERING AND CRATER-DEPTH MODEL

Table 1

Values of the Constant β from Four Sets of Experimental Data

Sphere Metal	Target Metal	β
copper	copper	0.695
aluminum	aluminum	0.693
copper	aluminum	0.695
aluminum	copper	0.700 ^d

^d In the case of impacts of aluminum spheres against copper targets the impacted sphere vaporizes to a notable extent. The value of β obtained for this projectile-target combination is regarded as less reliable than the other three values.

CRATERING AND CRATER-DEPTH MODEL

Table 2
Summary of Hypervelocity Crater Depth Data

Section (a) Copper Sphere Impinging against Copper Plate at Normal Incidence

Source	Impact Velocity km/sec	Apparent Depth Eglin or ARO cm	Apparent Depth NBS cm	Apparent Depth average cm	Sphere Residue cm	Real Depth cm
Sphere Diameter 1/16 in.						
ARO-Inc.	0.806	0.061	0.066	0.063	0.052	0.115
ARO-Inc.	1.146	0.128	0.124	0.126	0.029	0.155
ARO-Inc.	1.289	0.109	0.125	0.117	0.037	0.154
Eglin AFB	1.468	0.168	0.168	0.168	0.024	0.192
ARO-Inc.	1.798	0.182	0.186	0.184	0.022	0.206
Eglin AFB	2.373	0.264	0.248	0.256	0.011	0.267
Eglin AFB	2.766	0.254	0.305	0.280	0.015	0.295
Eglin AFB	3.156	0.300	0.324	0.312	0.007	0.319
Eglin AFB	4.030	0.363	0.367	0.365	0.012	0.377
Eglin AFB	4.752	0.399	0.463	0.431	0.015	0.446
ARO-Inc.	5.038	0.425	0.412	0.418	0.022	0.440
ARO-Inc.	5.716	0.419	0.412	0.415	--	0.415
ARO-Inc.	6.775	0.484	0.476	0.480	--	0.480
Sphere Diameter 1/8 in.						
Eglin AFB	0.782	0.048	0.049	0.048	0.093	0.141
Eglin AFB	1.408	0.348	0.336	0.342	0.049	0.391
Eglin AFB	1.425	0.343	0.359	0.351	0.051	0.402
Eglin AFB	2.006	0.488	0.487	0.488	0.030	0.518
ARO-Inc.	2.448	0.573	0.565	0.569	0.018	0.587
ARO-Inc.	3.287	0.688	0.651	0.670	0.013	0.683
ARO-Inc.	3.518	0.716	0.669	0.693	0.011	0.704
ARO-Inc.	3.583	0.671	0.667	0.669	0.009	0.678
ARO-Inc.	3.833	0.749	0.745	0.747	0.011	0.758
ARO-Inc.	3.978	0.758	0.748	0.753	0.014	0.767
ARO-Inc.	4.088	0.778	0.785	0.782	0.008	0.790
Eglin AFB	4.718	0.714	0.717	0.716	0.018	0.734
ARO-Inc.	4.908	0.843	0.841	0.842	0.015	0.857
ARO-Inc.	6.304	0.984	0.970	0.977	--	0.977
Sphere Diameter 3/16 in.						
ARO-Inc.	2.926	0.996	1.005	1.001	--	1.001
ARO-Inc.	3.520	1.092	1.101	1.097	0.018	1.115
ARO-Inc.	4.038	1.184	1.184	1.184	--	1.184
ARO-Inc.	4.538	1.256	1.254	1.255	0.010	1.265
ARO-Inc.	4.605	1.292	1.287	1.289	0.011	1.300
ARO-Inc.	4.736	1.260	1.282	1.271	--	1.271
ARO-Inc.	5.270	1.391	1.390	1.390	--	1.390
ARO-Inc.	5.586	1.387	1.420	1.403	--	1.403
ARO-Inc.	5.967	1.394	1.424	1.409	--	1.409

CRATERING AND CRATER-DEPTH MODEL

Table 2
Summary of Hypervelocity Crater Depth Data

Section (b) Copper Sphere Impinging against Aluminum Plate at Normal Incidence

Source	Impact Velocity km/sec	Apparent Depth Eglin or ARO cm	Apparent Depth NBS cm	Apparent Depth average cm	Sphere Residue cm	Real Depth cm
Sphere Diameter 1/16 in.						
ARO-Inc.	0.772	0.229	0.113	0.171	--	0.171
ARO-Inc.	1.312	0.380	0.383	0.381	0.045	0.426
ARO-Inc.	1.912	0.500	0.503	0.502	0.032	0.534
ARO-Inc.	2.276	0.546	0.548	0.547	0.024	0.571
Eglin AFB	2.419	0.493	0.567	0.530	0.024	0.554
Eglin AFB	3.627	0.757	0.749	0.753	0.015	0.768
Eglin AFB	4.284	0.792	0.826	0.809	--	0.809
Eglin AFB	4.770	0.759	0.786	0.772	0.016	0.788
Eglin AFB	5.380	0.744	0.749	0.746	--	0.746
ARO-Inc.	5.687	0.833	0.866	0.850	--	0.850
ARO-Inc.	6.090	0.917	0.876	0.896	--	0.896
ARO-Inc.	6.436	0.917	0.908	0.912	--	0.912
Sphere Diameter 1/8 in.						
Eglin AFB	0.741	0.533	0.539	0.536	0.011	0.547
ARO-Inc.	1.278	0.833	0.828	0.831	0.098	0.929
ARO-Inc.	1.678	0.988	1.019	1.004	0.068	1.072
ARO-Inc.	2.133	1.097	1.172	1.135	0.058	1.193
ARO-Inc.	2.240	1.185	1.173	1.179	0.055	1.234
Eglin AFB	2.707	1.181	1.076	1.128	0.047	1.175
Eglin AFB	3.200	1.377	1.384	1.380	0.044	1.424
Eglin AFB	3.449	1.374	1.401	1.388	0.027	1.415
Eglin AFB	3.580	1.374	1.467	1.420	0.033	1.453
ARO-Inc.	3.604	1.476	1.481	1.478	0.018	1.496
ARO-Inc.	4.206	1.631	1.656	1.643	0.040	1.683
ARO-Inc.	5.340	1.897	1.865	1.881	--	1.881
Sphere Diameter 3/16 in.						
ARO-Inc.	2.690	1.966	1.979	1.972	--	1.972
ARO-Inc.	3.086	2.047	2.077	2.062	0.057	2.119
ARO-Inc.	3.496	2.258	2.273	2.266	--	2.266
ARO-Inc.	3.740	2.276	2.289	2.282	0.079	2.361

CRATERING AND CRATER-DEPTH MODEL

Table 2
Summary of Hypervelocity Crater Depth Data

Section (c) Aluminum Sphere Impinging against Aluminum Plate at Normal Incidence

Source	Impact Velocity km/sec	Apparent Depth Eglin or ARO cm	Apparent Depth NBS cm	Apparent Depth average cm	Sphere Residue cm	Real Depth cm
Sphere Diameter 1/16 in.						
Eglin AFB	0.489	0.046	0.049	0.047	--	0.047
Eglin AFB	1.289	0.104	0.111	0.108	0.038	0.146
Eglin AFB	2.629	0.229	0.232	0.230	0.017	0.247
ARO-Inc.	3.200	0.245	0.255	0.250	--	0.250
Eglin AFB	3.216	0.284	0.269	0.276	0.013	0.289
ARO-Inc.	4.076	0.310	0.307	0.309	0.008	0.317
Eglin AFB	4.128	0.335	0.318	0.326	0.014	0.340
Eglin AFB	4.345	0.323	0.325	0.324	--	0.324
Eglin AFB	4.436	0.352	0.349	0.350	0.008	0.358
Eglin AFB	4.875	0.335	0.360	0.348	--	0.348
Eglin AFB	4.900	0.257	0.378	0.317	0.023	0.340
Eglin AFB	5.128	0.371	0.368	0.370	0.025	0.395
ARO-Inc.	5.322	0.355	0.357	0.356	0.011	0.367
		0.354	0.354	0.354	--	0.354
ARO-Inc.	6.654	0.392	0.402	0.397	0.029	0.426
ARO-Inc.	6.793	0.398	0.392	0.395	--	0.395
ARO-Inc.	6.924	0.373	0.384	0.378	--	0.378
ARO-Inc.	7.292	0.425	0.413	0.419	--	0.419
ARO-Inc.	7.507	0.462	0.414	0.438	--	0.438
Sphere Diameter 1/8 in.						
Eglin AFB	1.498	0.302	0.288	0.295	0.050	0.345
ARO-Inc.	2.048	0.399	0.393	0.396	0.039	0.435
Eglin AFB	2.106	0.419	0.423	0.421	0.030	0.451
ARO-Inc.	2.254	0.445	0.429	0.437	0.032	0.469
ARO-Inc.	2.263	0.445	0.432	0.439	0.033	0.472
ARO-Inc.	2.317	0.408	0.387	0.397	0.037	0.434
ARO-Inc.	2.348	0.469	0.390	0.429	--	0.429
ARO-Inc.	2.548	0.570	0.555	0.562	0.012	0.574
Eglin AFB	3.315	0.630	0.629	0.630	0.014	0.644
Eglin AFB	3.987	0.625	0.638	0.632	0.020	0.652
Eglin AFB	4.026	0.625	0.639	0.632	0.028	0.660
ARO-Inc.	4.549	0.730	0.736	0.733	0.017	0.750
Eglin AFB	4.566	0.696	0.707	0.702	0.021	0.723
ARO-Inc.	4.820	0.678	0.657	0.667	0.016	0.683
Eglin AFB	5.060	0.594	0.736	0.665	--	0.665
ARO-Inc.	5.148	0.758	0.756	0.757	--	0.757
ARO-Inc.	5.289	0.789	0.793	0.791	--	0.791
ARO-Inc.	5.612	0.829	0.825	0.827	--	0.827
ARO-Inc.	5.694	0.790	0.786	0.788	0.026	0.814
ARO-Inc.	5.751	0.737	0.725	0.731	0.024	0.755
ARO-Inc.	5.880	0.828	0.800	0.814	0.019	0.833
ARO-Inc.	6.920	0.936	0.934	0.935	0.019	0.954

Two spheres were fired.

CRATERING AND CRATER-DEPTH MODEL

Table 2
Summary of Hypervelocity Crater Depth Data

Section (c) Aluminum Sphere Impinging against Aluminum Plate at Normal Incidence

Source	Impact Velocity km/sec	Apparent Depth Eglin or ARO cm	Apparent Depth NBS cm	Apparent Depth average cm	Sphere Residue cm	Real Depth cm
Sphere Diameter 3/16 in.						
ARO-Inc.	2.548	0.799	0.808	0.804	0.040	0.844
ARO-Inc.	2.977	0.895	0.917	0.906	0.025	0.931
ARO-Inc.	3.024	0.898	0.899	0.898	0.026	0.924
ARO-Inc.	3.049	0.905	0.914	0.909	0.027	0.936
ARO-Inc.	3.107	0.902	0.908	0.905	0.026	0.931
ARO-Inc.	3.131	0.926	0.934	0.930	0.026	0.956
ARO-Inc.	3.146	0.913	0.909	0.911	0.025	0.936
ARO-Inc.	3.447	0.951	0.947	0.949	0.022	0.971
ARO-Inc.	4.223	1.088	1.085	1.087	--	1.087
ARO-Inc.	4.727	1.194	1.178	1.186	0.020	1.206
ARO-Inc.	5.166	1.298	1.272	1.285	--	1.285
ARO-Inc.	5.404	1.296	1.280	1.288	--	1.288
ARO-Inc.	6.632	1.337	1.325	1.331	--	1.331
ARO-Inc.	6.884	1.363	1.353	1.358	--	1.358
ARO-Inc.	6.876	1.334	1.320	1.327	--	1.327
ARO-Inc.	6.925	1.392	1.377	1.384	--	1.384
ARO-Inc.	7.306	1.429	1.421	1.425	--	1.425

Section (d) Aluminum Sphere Impinging against Copper Plate at Normal Incidence

Sphere Diameter 1/16 in.						
Eglin AFB	1.408	0.033	0.034	0.034	0.045	0.079
Eglin AFB	1.417	0.030	0.031	0.030	0.032	0.062
ARO-Inc.	1.748	0.097	0.065	0.081	0.014	0.095
Eglin AFB	2.373	0.091	0.091	0.091	0.015	0.106
Eglin AFB	2.777	0.094	0.092	0.093	0.027	0.120
Eglin AFB	2.955	0.122	0.122	0.122	0.011	0.133
ARO-Inc.	3.134	0.124	0.109	0.116	0.014	0.130
Eglin AFB	3.318	0.140	0.145	0.142	0.011	0.153
ARO-Inc.	3.513	0.153	0.151	0.152	--	0.152
ARO-Inc.	3.603	0.163	0.166	0.164	--	0.164
Eglin AFB	4.525	0.188	0.162	0.175	0.003	0.178
Eglin AFB	4.566	0.157	0.167	0.162	0.001	0.163
ARO-Inc.	5.106	0.214	0.201	0.207	--	0.207
ARO-Inc.	6.020	0.237	0.240	0.238	0.004	0.242
ARO-Inc.	6.106	0.229	0.216	0.222	--	0.222
ARO-Inc.	6.539	0.240	0.248	0.244	0.005	0.249
ARO-Inc.	7.205	0.254	0.220	0.237	0.003	0.240

CRATERING AND CRATER-DEPTH MODEL

Table 2
Summary of Hypervelocity Crater Depth Data

Section (d) Aluminum Sphere Impinging against Copper Plate at Normal Incidence

Source	Impact Velocity km/sec	Apparent Depth Eglin or ARO cm	Apparent Depth NBS cm	Apparent Depth average cm	Sphere Residue cm	Real Depth cm
Sphere Diameter 1/8 in.						
Eglin AFB	0.562	--	--	--	0.051	0.051
Eglin AFB	1.465	--	0.078	--	0.070	0.148
ARO-Inc.	1.833	0.149	0.149	0.149	0.045	0.194
Eglin AFB	2.160	0.196	0.204	0.200	0.034	0.234
ARO-Inc.	2.324	0.199	0.202	0.200	0.017	0.217
ARO-Inc.	2.990	0.268	0.259	0.264	0.034	0.298
Eglin AFB	3.828	0.325	0.318	0.322	0.008	0.330
Eglin AFB	3.912	0.340	0.337	0.338	0.003	0.341
ARO-Inc.	4.357	0.396	0.392	0.394	--	0.394
Eglin AFB	4.566	0.338	0.345	0.342	0.007	0.349
Eglin AFB	4.616	0.386	0.373	0.380	0.002	0.382
ARO-Inc.	4.710	0.376	0.370	0.373	0.003	0.376
Eglin AFB	5.201	0.335	0.334	0.334	0.002	0.336
ARO-Inc.	5.514	0.425	0.422	0.424	0.004	0.428
ARO-Inc.	6.141	0.461	0.452	0.456	0.003	0.459
ARO-Inc.	6.400	0.478	0.471	0.474	--	0.474
ARO-Inc.	6.944	0.525	0.509	0.517	--	0.517
Sphere Diameter 3/16 in.						
ARO-Inc.	2.697	0.374	0.399	0.386	0.043	0.429
ARO-Inc.	2.973	0.384	0.368	0.376	0.018	0.394
ARO-Inc.	3.729	0.503	0.500	0.502	0.004	0.506
ARO-Inc.	3.914	0.528	0.529	0.528	--	0.528
ARO-Inc.	4.396	0.641	0.644	0.642	0.004	0.646
ARO-Inc.	4.645	0.574	0.582	0.578	0.003	0.581
ARO-Inc.	4.969	0.591	0.586	0.589	0.005	0.594
ARO-Inc.	5.309	0.662	0.657	0.659	--	0.659
ARO-Inc.	5.328	0.634	0.630	0.632	--	0.632
ARO-Inc.	5.377	0.609	0.611	0.610	--	0.610
ARO-Inc.	6.022	0.693	0.693	0.693	0.002	0.695
ARO-Inc.	6.106	0.682	0.688	0.685	--	0.685
ARO-Inc.	6.262	0.613	0.606	0.609	0.002	0.611
ARO-Inc.	6.386	0.734	0.738	0.736	--	0.736
ARO-Inc.	6.563	0.722	0.720	0.721	--	0.721
ARO-Inc.	6.869	0.766	0.761	0.764	0.004	0.768
ARO-Inc.	6.896	0.784	0.787	0.785	0.002	0.787
ARO-Inc.	6.950	0.755	0.757	0.756	--	0.756

✓ Entire deformed sphere remained lodged in crater and protruding above surface of target. The residue reported is the measured distance from the target surface to the bottom of the crater as seen in the cross-sectional cut.

CRATERING AND CRATER-DEPTH MODEL

Table 3

Some Properties of Copper and Aluminum

Property	Dimensions	Aluminum	Copper
Density,	g/cm^3	\checkmark 2.702	\checkmark 8.92
Heat Content, $\Delta H \Big _{298.15}^{T_m}$	ergs/g	\checkmark 7.92×10^9	\checkmark 5.78×10^9
Heat of Fusion, E	ergs/g	\checkmark 3.95×10^9	\checkmark 2.05×10^9
Sound Speed, c	cm/sec	\checkmark 6.318×10^5	\checkmark 4.691×10^5
\checkmark Acoustic Impedance, z	g/sec.cm^2	1.714×10^6	4.184×10^6

\checkmark Values from the Handbook of Chemistry and Physics, 34th Edition, 1952-53.

\checkmark Values from D.R.Stull and G.C.Sinke, Thermodynamic Properties of the Elements, Number 18 of the Advances in Chemistry Series, American Chemical Society, Washington, D.C., 1956.

\checkmark Values of sound speed in infinite medium for 1100-O aluminum and annealed electrolytic tough pitch copper measured in NBS Sound Section by Carroll Tschigg.

\checkmark Product of sound speed and density.

CRATERING AND CRATER-DEPTH MODEL

FIGURE CAPTIONS

- Figure 1. Shear stresses produced in a metal plate by an impinging sphere.
- Figure 2. Schematic relation between various types of projectile-target impacts.
- Figure 3. Schematic representation of a sphere impacting a plate.
- Figure 4. Velocity dependence of crater depth/diameter ratio.
- Figure 5. Crater depth produced by impact of copper spheres against copper plates.
- Figure 6. Crater depth produced by impact of copper spheres against aluminum
plates.
- Figure 7. Crater depth produced by impact of aluminum spheres against
aluminum plates.
- Figure 8. Crater depth produced by impact of aluminum spheres against
copper plates.

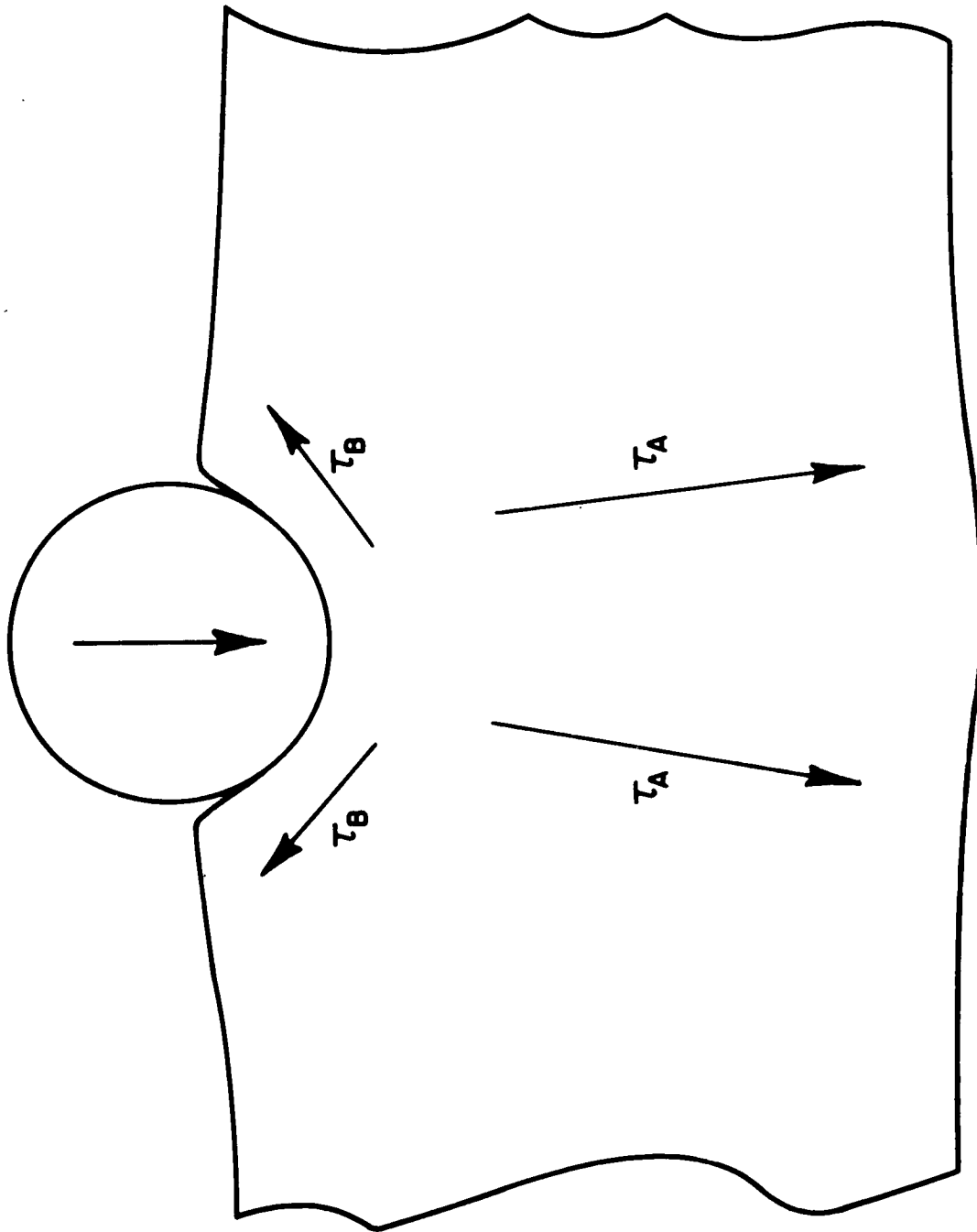


Figure 1. Shear stresses produced in a metal plate by an impinging sphere.

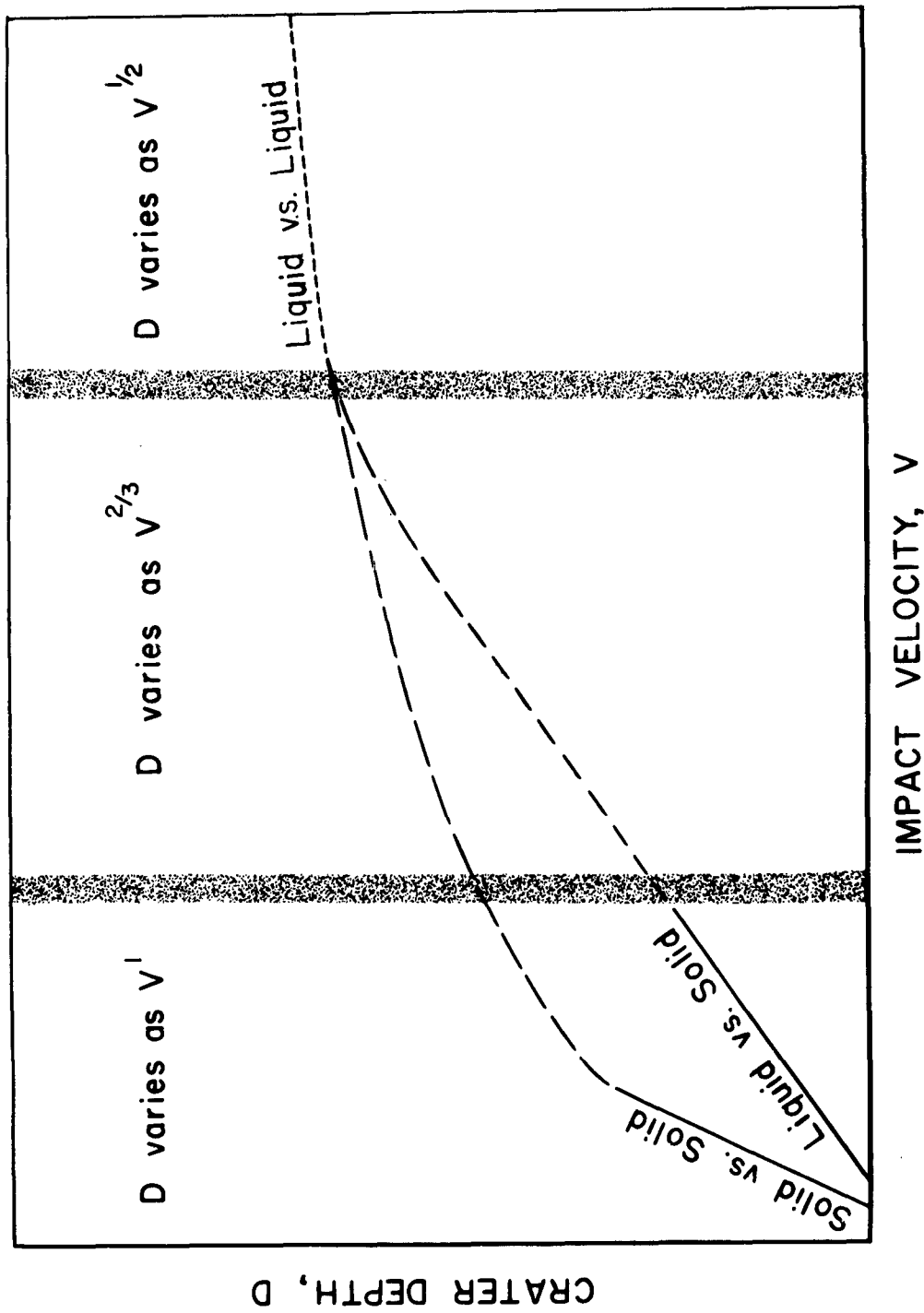


Figure 2. Schematic relation between various types of projectile-target impacts.

CRATERING AND CRATER-DEPTH MODEL

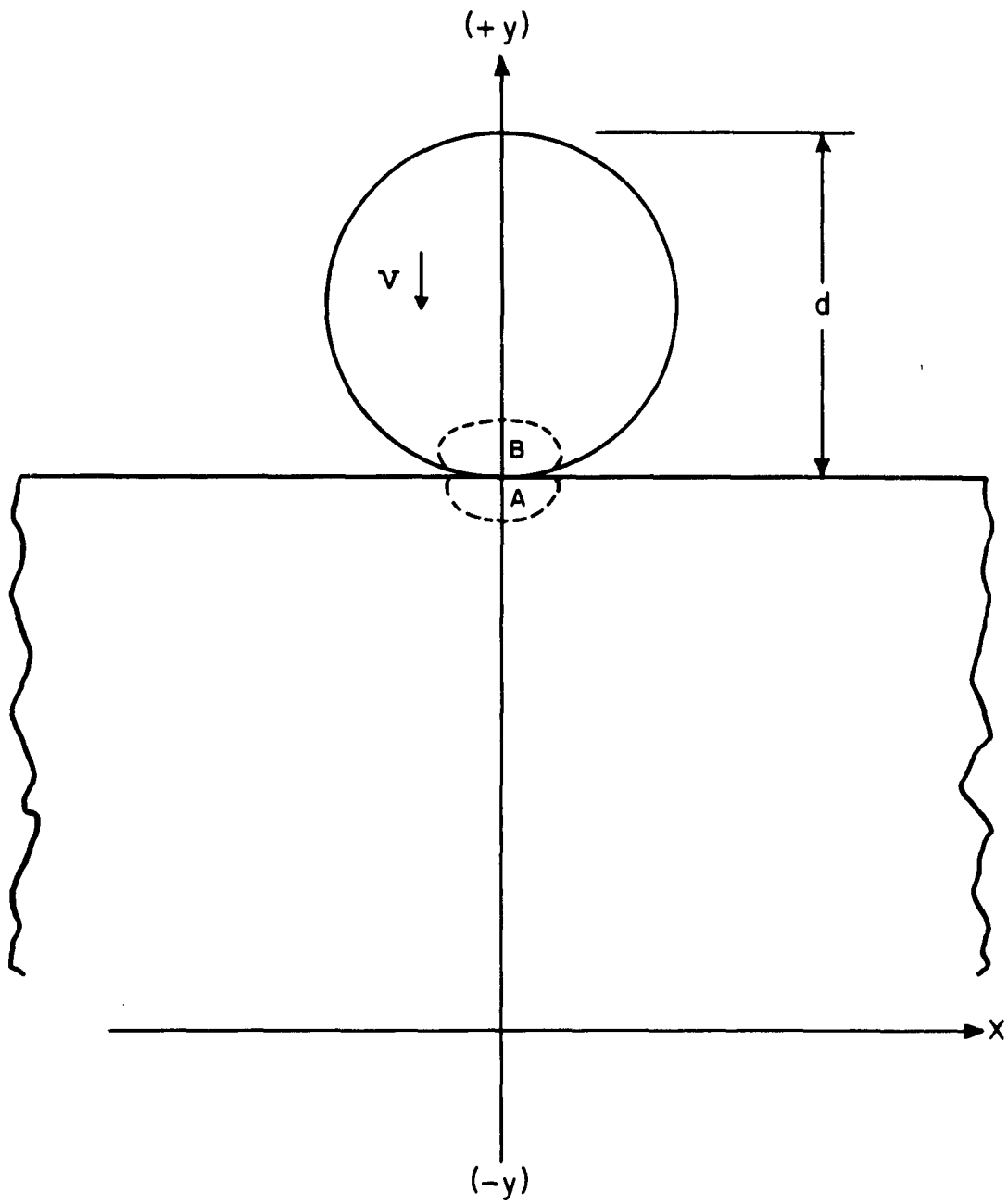
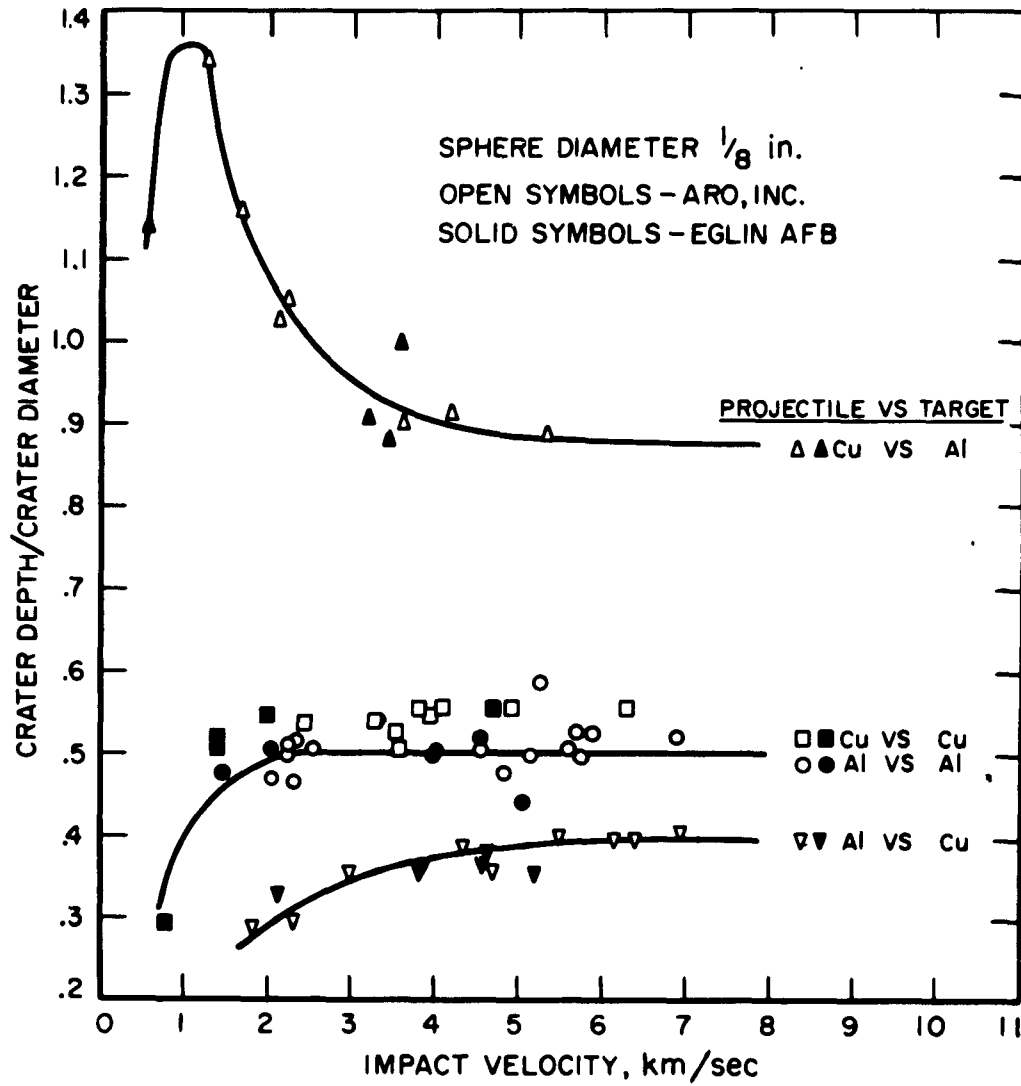


Figure 3. Schematic representation of a sphere impacting a plate.

CRATERING AND CRATER-DEPTH MODEL



VELOCITY DEPENDENCE OF DEPTH/DIAMETER RATIO

Figure 4.

CRATERING AND CRATER-DEPTH MODEL

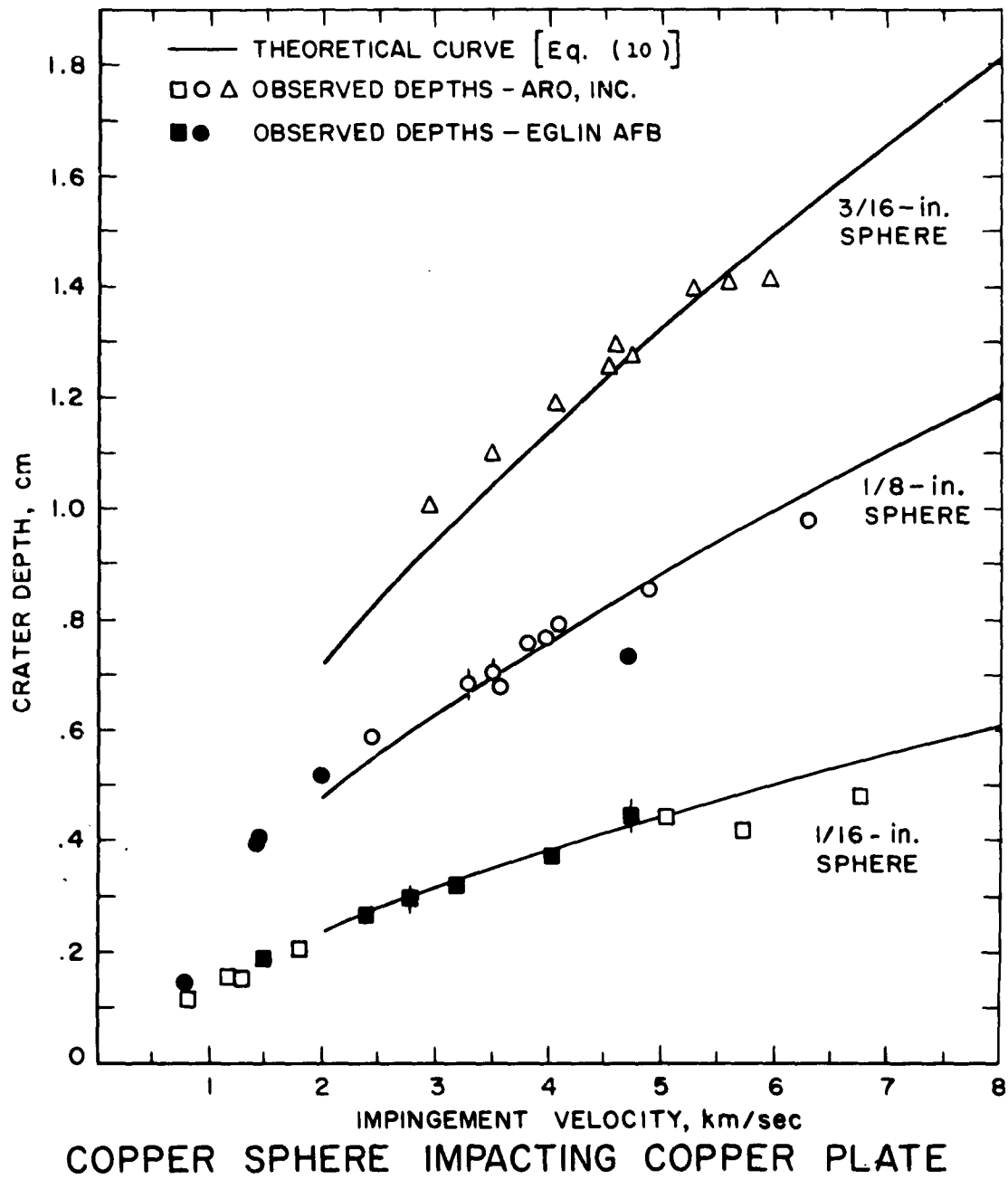
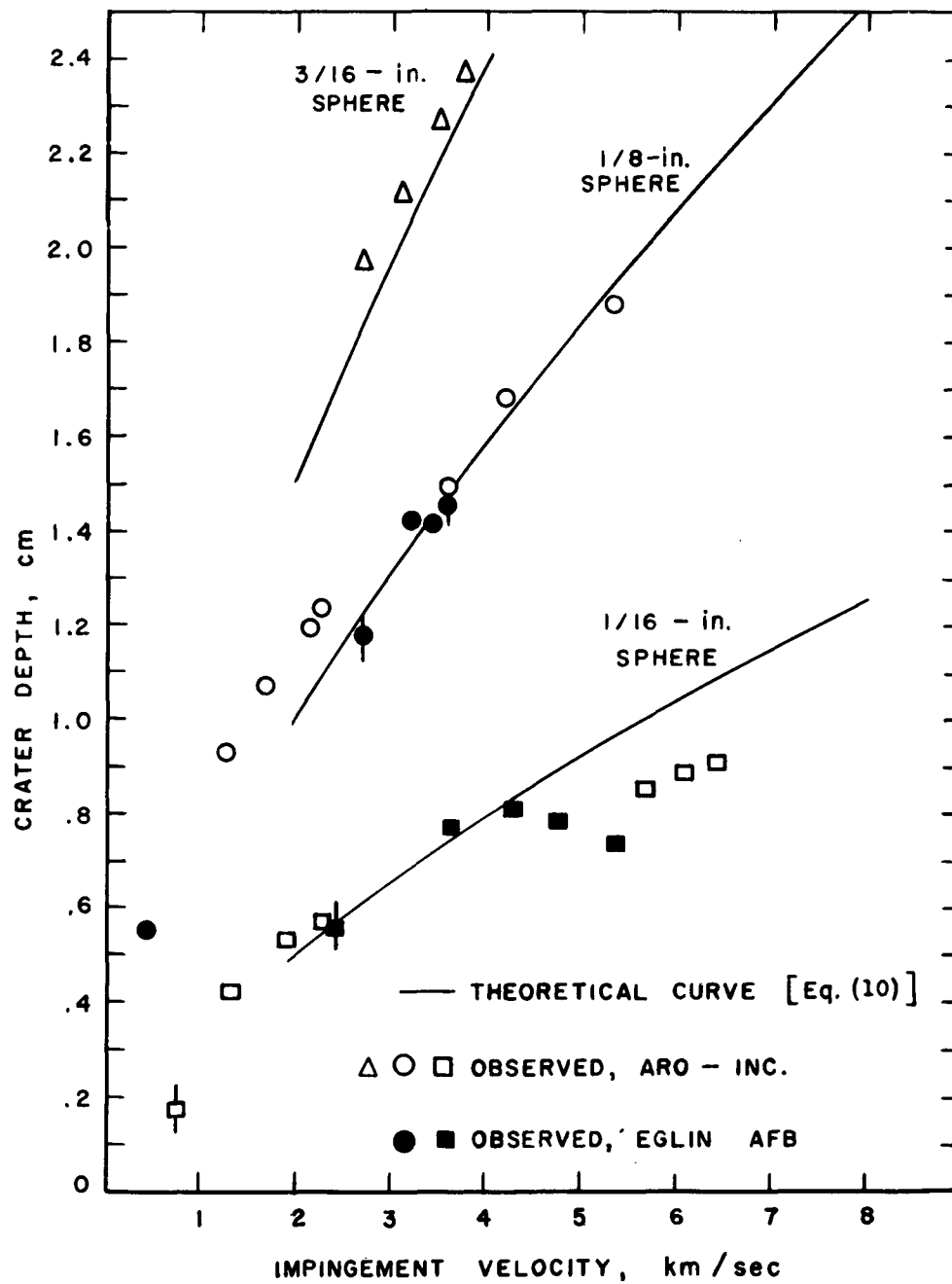


Figure 5.

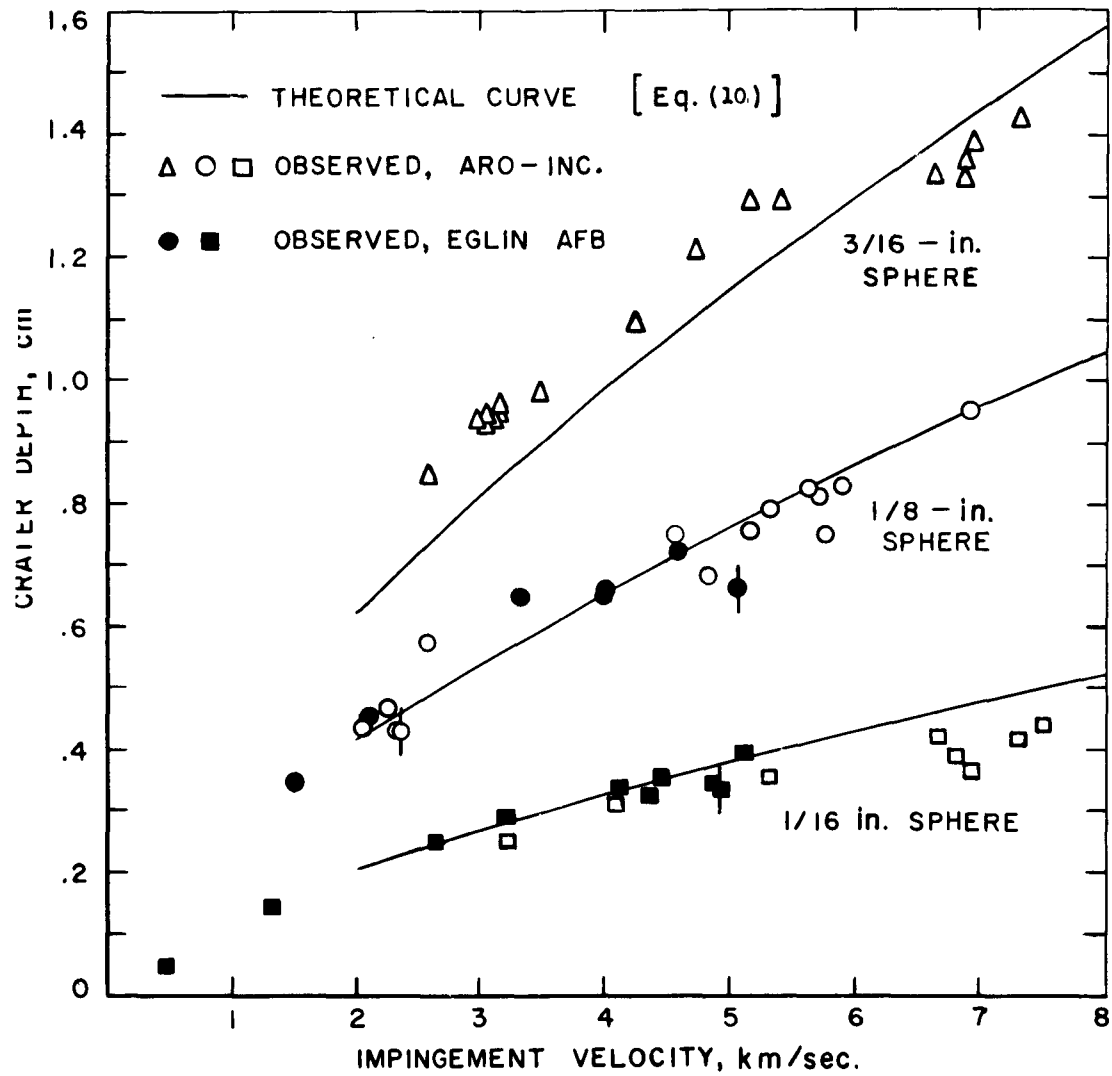
CRATERING AND CRATER-DEPTH MODEL



COPPER SPHERE IMPACTING ALUMINUM PLATE

Figure 6.

CRATERING AND CRATER-DEPTH MODEL



ALUMINUM SPHERE IMPACTING ALUMINUM PLATE

Figure 7.

CRATERING AND CRATER-DEPTH MODEL

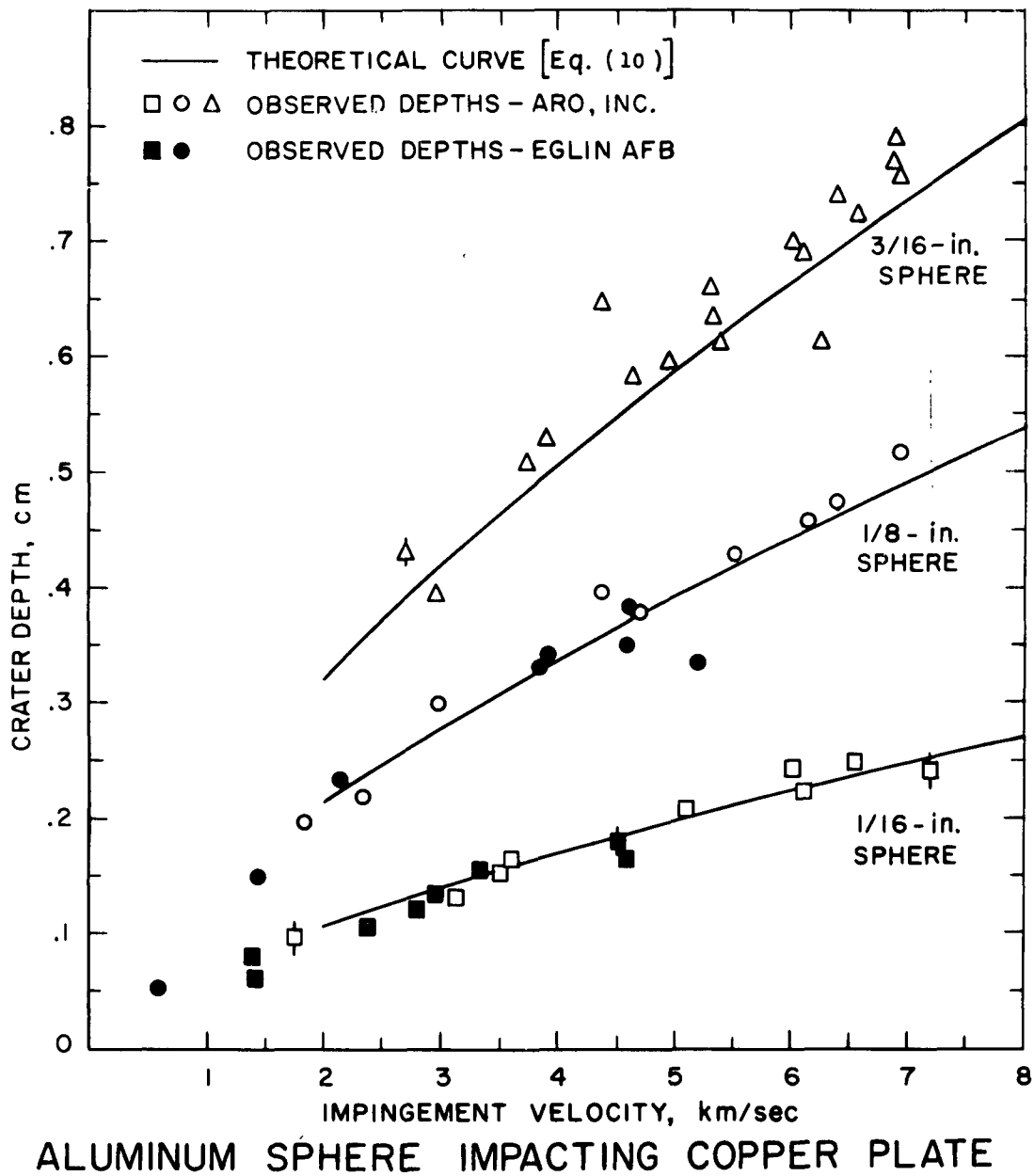


Figure 8.

FLUID IMPACT CRATERS AND HYPERVELOCITY--HIGH-
VELOCITY IMPACT EXPERIMENTS IN METALS AND ROCKS^{1/}

by

H. J. Moore^{2/}, R. W. MacCormack^{3/}, and

D. E. Gault^{3/}

1/ Publication authorized by the Director, U.S. Geological Survey.

2/ U.S. Geological Survey, Menlo Park, California.

3/ Ames Research Center, National Aeronautics and Space Administration,
Moffett Field, California.

IMPACT IN METALS AND ROCKS

Contents

	Page
Introduction-----	371
Cratering theory of Charters and Summers-----	373
Engel's water craters-----	375
Parameters-----	382
Strengths and densities at high confining pressures-----	385
Acoustic velocity as a parameter-----	389
Crater volume-energy relationships-----	390
Conclusions-----	395
References cited-----	397

IMPACT IN METALS AND ROCKS

Illustrations

Page

- Figure 1. Graph comparing deformation strength of water computed by using the mean hydrostatic pressure head, surface tension and estimated strength due to viscosity, and the theory of Charters-Summers----- 381
2. Graph comparing craters produced by impact of water drops into water, metal spheres impacting copper and lead targets, and metal and polyethylene spheres impacting rocks using $\rho_t^{1/2}/S_t^{1/2}$ as measured at normal confining pressures. A plot for copper and lead cratering experiments using the reciprocal of the square root of the target heat of fusion in place of $\rho_t^{1/2}/S_t^{1/2}$ is included----- 383
3. Graph comparing craters produced by impact of water drops into water, metal spheres impacting copper and lead targets, and metal and polyethylene spheres impacting basalt using $\rho_t^{1/2}/S_t^{1/2}$ as estimated for 49 kilobars confining pressure----- 387
4. Comparison of crater volume-energy relationships between various cratering experiments----- 391
5. Normalized volume-energy data for impact cratering experiments using target strength, target density, and projectile density----- 393

IMPACT IN METALS AND ROCKS

Table 1

	Page
Table 1. Computed effective deformation strength of water for craters produced by impact of water drops into water-----	380

FLUID IMPACT CRATERS AND HYPERVELOCITY--HIGH-
VELOCITY IMPACT EXPERIMENTS IN METALS AND ROCKS^{1/}

By H. J. Moore^{2/}, R. W. MacCormack^{3/}, and
D. E. Gault^{3/}

Introduction

The impact phenomena of hypervelocity and high-velocity projectiles with rock and metal targets are being studied in a cooperative research program conducted by the U.S. Geological Survey and the Ames Research Center of the National Aeronautics and Space Administration. This paper deals with the comparison of: (1) fluid-impact craters produced by water drops impacting water, (2) hypervelocity and high-velocity impact craters produced by impact of steel, aluminum, and polyethylene projectiles with basalt, and (3) hypervelocity and high-velocity impact craters in metals.

The theoretical formula of Charters and Summers (1959) has been tested in this investigation and found approximately valid for impact of water drops into water. In addition, the formula indicates that deformation strengths of metals and rocks are placed at some value between a maximum deformation strength of the target material and its compressive strength at low confining pressures. The maximum deformation strength is the

1/ Publication authorized by the Director, U.S. Geological Survey.

2/ U.S. Geological Survey, Menlo Park, California.

3/ National Aeronautics and Space Administration, Ames Research Center, Moffett Field, California.

IMPACT IN METALS AND ROCKS

product of the heat of fusion and the density of the target material. The use of shear strengths and densities of the metal and rock-target materials at 49 kilobars for parameters yields fair agreement between (1) the theory of Charters and Summers, (2) experiments with cratering by water drops impacting water, and (3) hypervelocity impact experiments in and near the fluid-impact regime using rock and metal targets.

The study has concluded that shear strength or compressive strength of the target material is a more realistic parameter than acoustic velocity. When acoustic velocity is used as a parameter, water-drop cratering experiments cannot be correlated with theory or with experimental data on high-velocity to hypervelocity impact cratering in rocks and metals.

IMPACT IN METALS AND ROCKS

Cratering theory of Charters and Summers

A quantitative theory for craters produced by projectile impact in the fluid-impact regime has been proposed by Charters and Summers (1959). In their theory, the momentum or, more precisely, the product of the mass and speed of a uniformly expanding hemispherical shell composed of both the projectile and the target material is assumed to be equal to the projectile momentum

$$m_{fs} \mu_{fs} = m_p V_p, \quad (1)$$

where

m_{fs} = mass of fluid shell,

μ_{fs} = velocity of fluid shell,

m_p = mass of projectile,

V_p = velocity of projectile.

The kinetic energy of the projectile is then compared to the kinetic energy of the fluid shell using the hydraulic analogy of the shaped charge penetration for which

$$\mu_{fs} = \frac{1}{2} V_p, \quad (2)$$

then

$$m_{fs} \mu_{fs}^2 = \frac{1}{2} m_p V_p^2. \quad (3)$$

The kinetic energy of the fluid shell is assumed to be used in the work of deformation in forming the crater:

$$\frac{1}{2} m_{fs} \mu_{fs}^2 = \int_0^p S 2\pi r^2 dr \quad (4)$$

where

S = the deformation strength,

p = the maximum crater depth,

r = the radius of the hemispherical crater cavity.

IMPACT IN METALS AND ROCKS

Integration, when S is constant, gives

$$\frac{1}{2} m_{fs} u_{fs}^2 = \frac{2}{3} \pi p^3 S \quad (5)$$

and since

$$m_{fs} u_{fs}^2 = \frac{1}{2} m_p v_p^2, \quad (6)$$

then

$$m_p v_p^2 = \frac{8}{3} \pi p^3 S \quad (7)$$

or

$$S = \frac{3m_p v_p^2}{8\pi p^3}. \quad (8)$$

Then, taking into account experimental data and rearranging terms, the penetration formula becomes

$$\frac{p}{d} = \frac{1}{2} \left(\frac{\rho_p}{\rho_t} \right)^{1/3} \left(\frac{\rho_p v_p^3}{2S} \right)^{1/3}, \quad (9)$$

which can be rewritten

$$S = \frac{1}{16} \frac{\rho_p^2}{\rho_t} \frac{v_p^2}{\left(\frac{p}{d}\right)^3},$$

where

d = diameter of the projectile,

ρ_p = density of the projectile,

ρ_t = density of the target.

IMPACT IN METALS AND ROCKS

Engel's water craters

Preliminary studies of craters produced by water drops impacting water (Engel, 1961) yield data that permits a quantitative test of the fluid-impact theory of Charters and Summers. The water-drop experiments employed projectiles of 11 mg, 56 mg, and 183 mg which impacted water with velocities of 400 to 700 cm/sec. The experiments of Engel produced temporary craters from 7.25 mm to 21.9 mm in depth. In addition, Engel points out many similarities between the water-drop experiments and some hypervelocity impact experiments.

Deformation strengths of the water for each experiment can be calculated in two ways: (1) by employing a knowledge of the physical properties of water and the experimental measurements and (2) by employing the theory of Charters and Summers.

Three types of resistance oppose the process of crater formation in water: (1) the hydrostatic pressure head, (2) surface tension, and (3) the resistance of the water to flow (or viscosity). The deformation strength then becomes

$$S_w = f(\rho_w g z) + f\left(-\frac{2\gamma}{z}\right) + f\left(-\frac{V_t \mu}{x}\right), \quad (10)$$

where

S_w = deformation strength of water,

ρ_w = density of water,

g = acceleration of gravity,

z = a depth or vertical coordinate,

$\frac{V_t}{x}$ = a velocity gradient,

IMPACT IN METALS AND ROCKS

μ = viscosity of water (10^{-2} dynes-sec/cm²),

γ = surface tension of water (72 dynes/cm).

During the cratering process in water, the deformation strength related to the hydrostatic pressure head increases from zero to some finite value, since z increases from zero to p or the maximum crater depth. The effective deformation strength resulting from the hydrostatic pressure head may be obtained by computing the work required to form a crater against the hydrostatic pressure head and relating this to the final crater volume. The work required to form a hemispherical crater against the hydrostatic pressure head may be expressed

$$W_{hh} = \int_0^F dF \cdot z = \int_0^{Vol} \rho_w g \, d(Vol)z, \quad (11)$$

where

W_{hh} = work expended in overcoming hydrostatic pressure head,

dF = incremental force on an incremental volume of water removed from crater to surface of water,

p = maximum crater depth of hemispherical crater,

ρ_w = density of water,

g = acceleration of gravity,

z = depth or vertical coordinate,

$d(Vol)$ = an incremental volume of water removed from crater to surface of water.

Integration of equation (11) yields

$$W_{hh} = \frac{\pi \rho_w g p^4}{4}. \quad (12)$$

If the mean or effective deformation strength due to the hydrostatic pressure head is defined by S_{hh} , then

IMPACT IN METALS AND ROCKS

$$W_{hh} = S_{hh} \int_0^P 2\pi r^2 dr, \quad (13)$$

and

$$S_{hh} = \frac{3\rho_w g p}{8}. \quad (14)$$

The mean or effective deformation strength due to surface tension may be derived in a similar manner. The work required to overcome surface tension is

$$W_{st} = \int_0^{2\pi p^2} \gamma dA, \quad (15)$$

where

W_{st} = work expended in overcoming surface tension,

γ = surface tension of water,

dA = the change in area,

p = maximum crater depth of hemispherical crater.

Then,

$$W_{st} = 2\pi \gamma p^2, \quad (16)$$

and

$$W_{st} = S_{st} \int_0^P 2\pi r^2 dr, \quad (17)$$

where

S_{st} = effective or mean deformation strength due to surface tension,

or

$$S_{st} = \frac{3\gamma}{p}. \quad (18)$$

Approximate values for the deformation strength of the water due to viscosity during the cratering process may be obtained by assuming that the flow of the projectile and target material occurs near the projectile-target interface. In addition, the flow is assumed to occur within a layer twice as thick as the projectile smeared evenly over a hemispherical crater at maximum depth. Also, it may be assumed that the velocities of

IMPACT IN METALS AND ROCKS

the flow are approximately equal to the radial velocities of the fluid shell. The estimated deformation strength due to viscosity then becomes

$$S_{\mu} = f\left(\frac{v_t}{x}\mu\right) = \mu \frac{1}{t} \int_0^t \frac{\frac{d(z)}{dt}}{\frac{2 \text{ vol}_p}{2\pi p^2}} dt, \quad (19)$$

where

$$\begin{aligned} S_{\mu} &= \text{deformation strength due to viscosity,} \\ \mu &= \text{viscosity of water } \left(\frac{10^{-2} \text{ dynes-sec}}{\text{cm}^2} \right), \\ t &= \text{duration of cratering event,} \\ \frac{d(z)}{dt} &= \text{radial velocity of fluid shell,} \\ \text{vol}_p &= \text{volume of projectile,} \\ p &= \text{maximum crater depth} \\ \frac{v_t}{x} &= \text{velocity gradient.} \end{aligned}$$

Equation 19 can be evaluated using the data of Engel (1961).

The calculated deformation strengths for the individual experiments of water impacting water (Engel, 1961) using the effective deformation strengths due to hydrostatic pressure head, surface tension, and estimated strength due to viscosity, and assuming hemispherical craters are tabulated (table 1).

Deformation strengths for the water craters, assuming spherical projectiles and hemispherical craters, have been calculated using the Charters-Summers theory (equation 9). These deformation strengths are listed in table 1, column 5. In addition, the data are plotted in figure 1, where p is the maximum crater depth.

The assumption of hemispherical water craters which are actually prolate hemi-spheroids leads to minor errors, so that the calculations

IMPACT IN METALS AND ROCKS

represent approximate values for the mean or effective deformation strength of the water craters. The correct values for the mean or effective deformation strength of the water during cratering are very near

$$\frac{1 \times 10^3 \text{ dynes}}{\text{cm}^2} .$$

Table 1. Computed deformation strengths of water for craters produced by impact of water drops into water.

	(1) Hydrostatic pressure head (Equation 14) $\frac{3}{8} \rho_w g p$ (dynes/cm ²)	(2) Surface tension (Equation 18) $\frac{3\gamma}{p}$ (dynes/cm ²)	(3) Estimated strength due to viscosity (Equation 19) $\xi \left(\frac{V_t}{x} \mu \right)$ (dynes/cm ²)	(4) Total de- formation strength (Equation 10) S_w (dynes/cm ²)	(5) Deformation strength cal- culated with Charters- Summers theory (Equation 9) $\frac{1}{16} \frac{\rho^2 p}{\rho_t} \frac{V^2}{(p/d)^3}$ (dynes/cm ²)
Experiment (Engel 1961)					
11-400	0.27x10 ³	0.30x10 ³	0.07x10 ³	0.64x10 ³	0.57x10 ³
11-650	0.36x10 ³	0.22x10 ³	0.13x10 ³	0.71x10 ³	0.61x10 ³
56-400	0.44x10 ³	0.18x10 ³	0.03x10 ³	0.65x10 ³	0.62x10 ³
56-700	0.53x10 ³	0.15x10 ³	0.08x10 ³	0.76x10 ³	1.07x10 ³
182-400	0.62x10 ³	0.13x10 ³	0.03x10 ³	0.78x10 ³	0.73x10 ³
182-700	0.80x10 ³	0.10x10 ³	0.07x10 ³	0.97x10 ³	0.98x10 ³

IMPACT IN METALS AND ROCKS

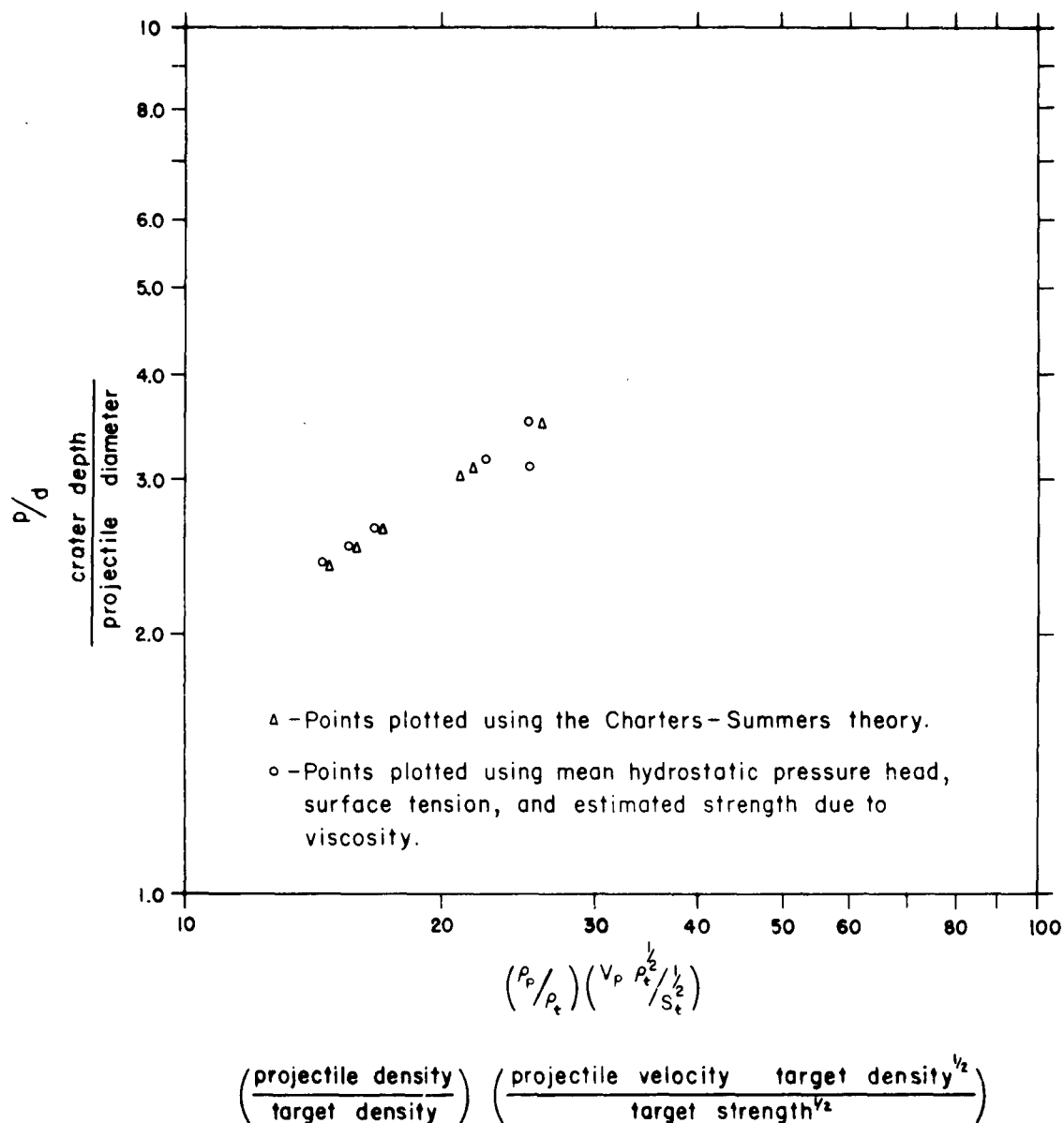


Figure 1. Graph comparing deformation strength of water computed by using the mean hydrostatic pressure head, surface tension and estimated strength due to viscosity, and the theory of Charters-Summers.

Parameters

Various parameters have been used to correlate hypervelocity fluid-impact experiments. The familiar empirical formula of Charters and Summers (1959) relates the experimental data on penetration to the projectile diameter, projectile density, target density, projectile velocity, and the acoustic velocity of the target material:

$$\frac{p}{d} = 2.28 \left(\frac{\rho_p}{\rho_t} \right)^{2/3} \left(\frac{V_p}{C} \right)^{2/3}. \quad (20)$$

The acoustic velocity is then correlated with Young's modulus (E_t) of the target material:

$$C^2 = \frac{E_t}{\rho_t}. \quad (21)$$

In addition to the above parameters, the following may be used:

$$\frac{p}{d} = K \left(\frac{\rho_p}{\rho_t} \right)^{2/3} \left(\frac{V_p \rho_t^{1/2}}{S_t^{1/2}} \right)^{2/3} \quad (22)$$

where

K = a constant,

S_t = deformation strength.

These parameters were selected primarily on the basis of equation 9.

The term $\rho_t^{1/2}/S_t^{1/2}$ has the dimensions of time/distance.

Experimental data using equation 22 and values for densities and shear strengths at normal confining pressure for impact of metal projectile into metal, metal projectile into rock, and water projectile into water are shown in figure 2. In addition, a plot using the reciprocal of the square root of the heat of fusion in place of $\rho_t^{1/2}/S_t^{1/2}$ has been included in figure 2. This parameter, which has been suggested by Whipple (1958) and Bromberg (in Palmer and others, 1960, p. 8), also has the dimensions of time/distance.

IMPACT IN METALS AND ROCKS

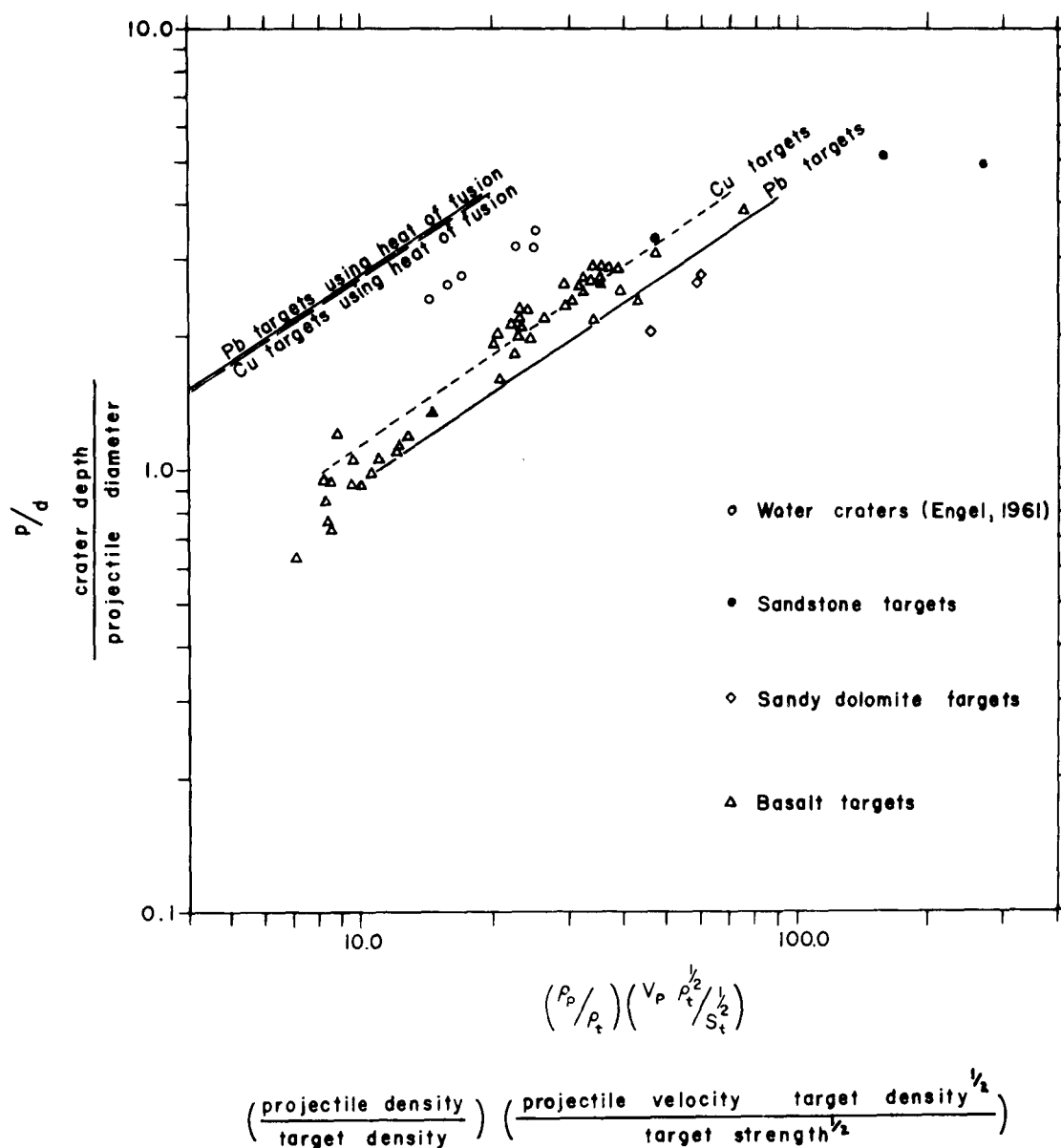


Figure 2. Graph comparing craters produced by impact of water drops into water, metal spheres impacting copper and lead targets, and metal and polyethylene spheres impacting rocks using $\rho_t^{1/2}/S_t^{1/2}$ as measured at normal confining pressures. A plot for copper and lead cratering experiments using the reciprocal of the square root of the target heat of fusion in place of $\rho_t^{1/2}/S_t^{1/2}$ is included.

IMPACT IN METALS AND ROCKS

Figure 2 is based on experimental data for impacts using rock targets; information from Moore and Gault (1963), Summers (1959), the Metals Handbook (Lyman, 1958, p. 905-909, 961-962); and actual determination of shear strengths of the rocks. The shear strengths used were as follows:

copper - 1.53×10^9 dynes/cm²

lead - 1.26×10^8 dynes/cm²

basalt - 8.6×10^8 dynes/cm²

sandy dolomite - 2.8×10^8 dynes/cm²

sandstone - 1.9×10^8 dynes/cm².

A value for the heat of fusion of 2.12×10^9 ergs/gram was used for copper targets and 2.62×10^8 ergs/gram was used for lead targets.

If the sum of the mean hydrostatic pressure head, the mean surface tension factor, and the viscous head loss is considered to be analogous to compressive strength which is twice the shear strength for ideal plastic failure, the plot of the experimental data for metals and rocks is moved toward the left by a factor of $\sqrt{2}$ when compressive strengths are used instead of shear strengths. Such a shift reduces the difference between the experimental data for metals and rocks and the data for water.

The strength of rocks and metals with increasing confining pressure is not constant. More precise plotting of data would require a knowledge of the strength of the target material at the high confining pressures which are produced during crater formation by impact of hypervelocity projectiles. The maximum strength of the target may be taken as the product of the heat of fusion and density of the target material, and the minimum strength taken as the compressive strength at low confining pressures. The deformation strength during cratering by hypervelocity and high-velocity impacts would lie between these two values.

IMPACT IN METALS AND ROCKS

Strengths and densities at high confining pressures

A good deal is known about the density of some materials up to 700 kilobars confining pressure, and in some cases up to several megabars (Rice and others, 1958, Al'tshuler and others, 1960). Little is known about the strength of materials above 49 kilobars. However, the existing data on the strengths and densities of metals and rocks may be used to illustrate how correlation of impact-cratering experiments could be improved by the parameter $\rho_t^{1/2}/S_t^{1/2}$ and the plot of cratering experiments in and near the fluid-impact regime.

The plots of hypervelocity-impact data for copper and lead in and near the fluid-impact regime indicate that $\rho_t^{1/2}/S_t^{1/2}$ is constant because of the constant slope of \mathcal{V}_s (Summers, 1959). If it is further assumed that $\rho_t^{1/2}/S_t^{1/2}$ for metals becomes constant at and above 49 kilobars and that ρ_p/ρ_t is essentially constant, the shear strength and density at 49 kilobars (Bridgman, 1935; Rice and others, 1958) may be used to evaluate $\rho_t^{1/2}/S_t^{1/2}$ at high pressures.

The assumption that ρ_p/ρ_t is constant may be justified from compressibility data obtained with shock techniques. Compressibility ratios for copper, lead, aluminum, iron, and magnesium projectiles impacting copper and lead targets range between 0.850 and 1.065 at 100 kilobars and 0.850 and 1.174 at 500 kilobars. Thus the assumption of a constant ratio for ρ_p/ρ_t is valid within ± 10 percent at 100 kilobars and ± 16 percent at 500 kilobars. This range is within the scatter of experimental data for metals and rocks (see, for example, Charters and Summers, 1959; Summers, 1959, p. 13). The shear strengths for lead and copper at 49 kilobars are 710 kg/cm^2 ($6.96 \times 10^8 \text{ dynes/cm}^2$) and 4700 kg/cm^2 ($4.6 \times 10^9 \text{ dynes/cm}^2$)

IMPACT IN METALS AND ROCKS

(Bridgman, 1935). The densities of lead and copper which were obtained by extrapolation of densities obtained with shock-wave techniques (Rice and others, 1958) and static compression techniques (Bridgman, 1935) are 12.4 grams/cm³ and 9.35 grams/cm³ at 49 kilobars.

The use of the shear strengths and densities at 49 kilobars confining pressure yields good results (compare fig. 3). Impact data for lead and copper are practically coincident at this pressure, whereas at low confining pressures they vary. In addition, craters produced by water drops impacting water agree more closely with craters produced by metal projectiles impacting metal targets near the fluid-impact regime.

Similar data are available for some rocks. There are no data on basalt for shear strengths at 49 kilobars. However, 15.5×10^9 dynes/cm² for the strength of basalt at high confining pressures can be estimated by comparing the shear strength of basalt glass, which is 17.0×10^9 dynes/cm², and pyroxenite, which is 14.0×10^9 dynes/cm² (Bridgman, in Robertson, 1955). This estimate is justified by generalizations of shear strengths of rocks which tend to be approximately the same at high confining pressures (Robertson, 1955). The density of basalt at 49 kilobars may be estimated with data from shock-wave techniques (Lombard, 1961). Such an estimate yields 2.9 to 3.0 grams/cm³.

The data plotted in figure 3 for basalt fall to the left of those for the metals and water, confirming that the cratering process in rocks differs from that in metals and water. This difference is due to the low tensile strength of rocks at low confining pressures. For craters of the size produced in the laboratory experiments, a projectile that has impacted rock is ejected completely from the crater along with rock debris, whereas one that has impacted metal smears out and plates the crater floor and

IMPACT IN METALS AND ROCKS

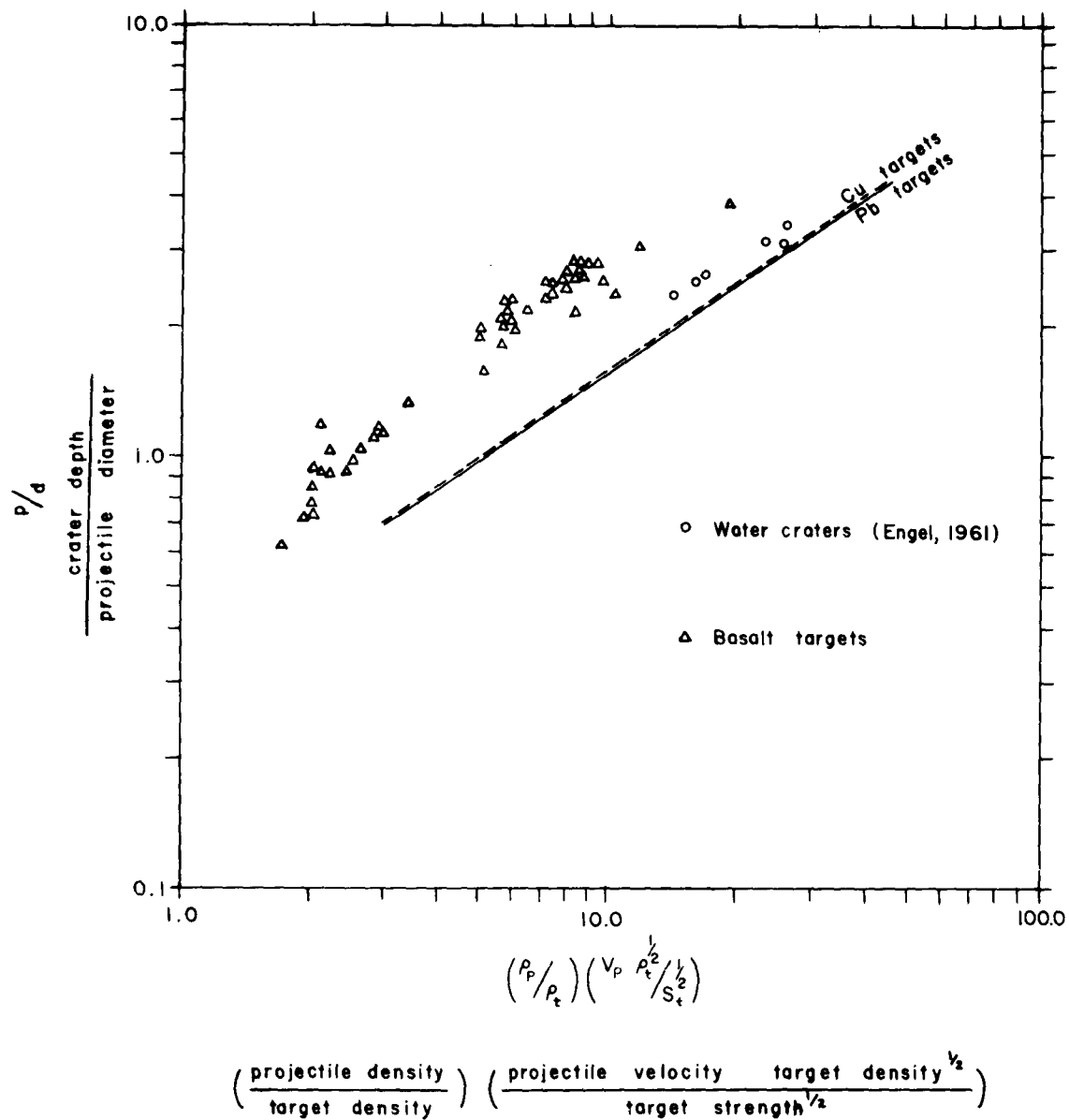


Figure 3. Graph comparing craters produced by impact of water drops into water, metal spheres impacting copper and lead targets, and metal and polyethylene sphere impacting basalt using $\rho_t^{1/2}/S_t^{1/2}$ as estimated for 49 kilobars confining pressure.

IMPACT IN METALS AND ROCKS

walls (Summers, 1959). Plating also occurs in craters produced by water-drop impacts with water (Engel, 1961; Charters, 1960).

Proper appraisal and use of the parameters in equation 22 requires knowledge of the average deformation strength of the target, the average density of the projectile, and the average density of the target during the cratering process.

IMPACT IN METALS AND ROCKS

Acoustic velocity as a parameter

The primary problem with acoustic velocity as a parameter is shown clearly in the case of fluid impacts of water into water. The use of the acoustic velocity of water (which is 1.5 km/sec) in Engel's experiments did not permit plotting of the fluid-impact water-drop experiments and the fluid-impact metal and rock experiments in the same decade on log-log paper. The use of either shear or compressive strength at either low or high confining pressure, divided by either the target density or the target heat of fusion, does permit such a plot.

IMPACT IN METALS AND ROCKS

Crater volume-energy relationships

The relationships between crater volume and the energy of the devices producing the craters further illustrates the effects of the properties of the target material (see fig. 4). For example, in figure 4 the volumes of hypervelocity impact craters in copper are almost one order of magnitude smaller than hypervelocity impact craters in lead although the projectile energies are about the same (Summers and Nysmith, 1962, oral and written communications). The volumes of hypervelocity impact craters produced in aluminum by hypervelocity aluminum projectiles with energies comparable to the projectiles used for the lead and copper experiments would be smaller than the volumes of the craters in lead but larger than the volumes of the craters in copper (Halperson and Atkins, 1962). The yields for the copper, lead, and aluminum hypervelocity impact craters range between about $5 \times 10^{-11} \text{ cm}^3/\text{erg}$ and $5 \times 10^{-10} \text{ cm}^3/\text{erg}$. Temporary water craters with volumes comparable to the craters in metals are produced by water impacting water with energies seven to eight orders of magnitude less than the energies of the metal projectiles used in producing the craters in metals. Yield for the temporary water craters are about $10^{-3} \text{ cm}^3/\text{erg}$. In addition craters in paraffin wax produced by paraffin wax projectiles yield about $2.4 \times 10^{-9} \text{ cm}^3/\text{erg}$ (Palmer and others, 1960). Hypervelocity impact craters in rocks show similar discrepancies. For example, the volumes of hypervelocity impact craters in basalt are almost two orders of magnitude smaller than the volume of a hypervelocity impact crater in diatomaceous earth, although the projectile energies are about the same.

In addition to the problems associated with the properties of the materials used in an experiment, there is a problem of the effects of the size of the cratering event or experiment. Because it has been suggested

IMPACT IN METALS AND ROCKS

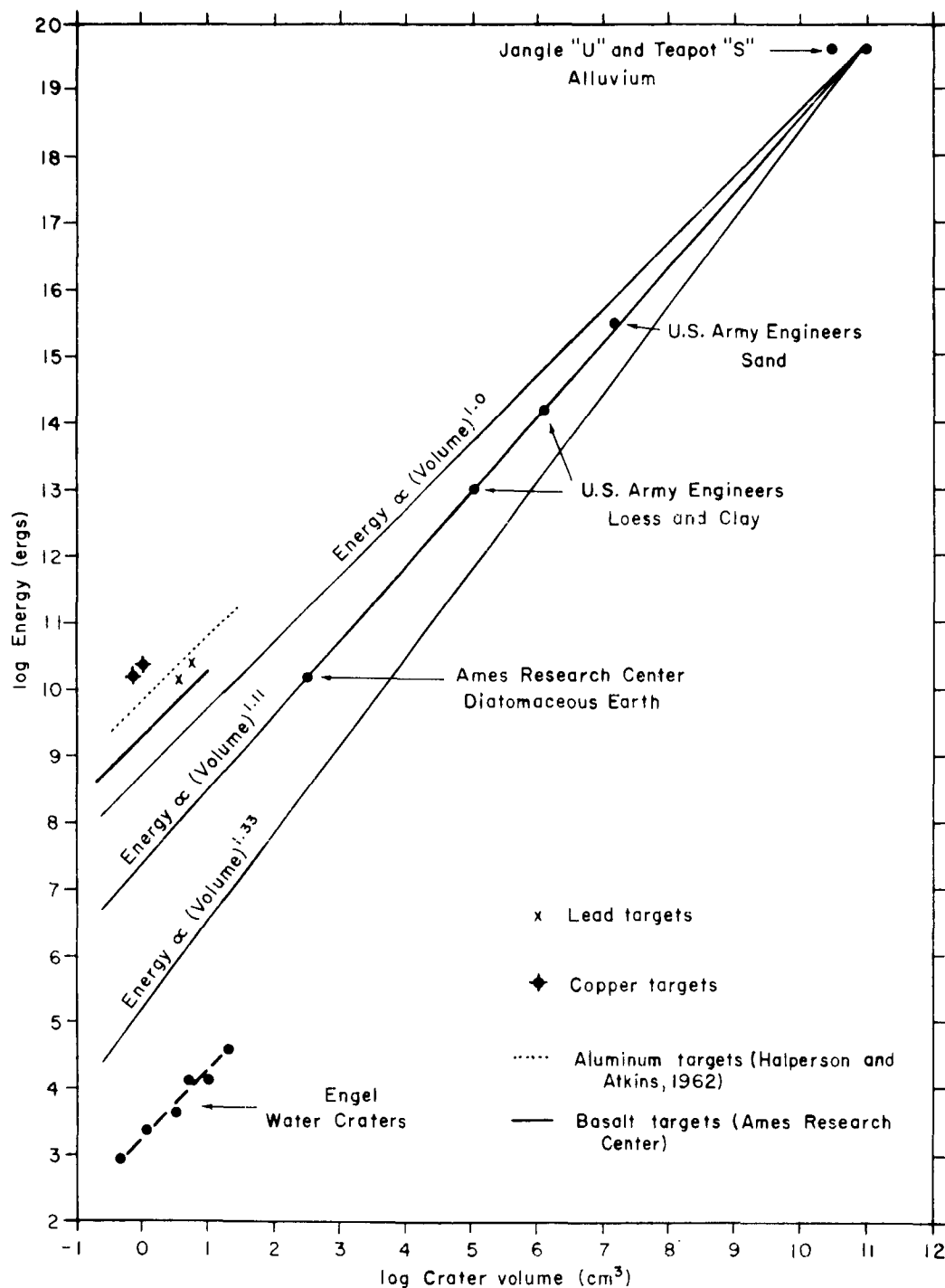


Figure 4. Comparison of crater volume-energy relationships between various cratering experiments.

IMPACT IN METALS AND ROCKS

that chemical and nuclear explosive craters might correlate with hyper-velocity impact craters (Shoemaker, 1960), some cratering experiments using chemical (U.S. Army Engineers, sand, loess, and clay) and nuclear explosives (Jangle "U" and Teapot "S", alluvium) at shallow depths of burial are included in figure 4. The three lines, labelled energy \propto (volume)^{1.0}, energy \propto (volume)^{1.11}, and energy \propto (volume)^{1.33}, represent Lampson's scaling (see for example, Shoemaker, 1960, p. 431), empirical scaling developed at the Nevada Test Site (Nordyke, 1962), and gravity scaling (Chabai and Hankins, 1960).

The separation of the volume-energy data for impact cratering experiments (fig. 4) may be substantially reduced by normalization of the projectile energy using the requirements imposed by equation 9 and assuming the ratio $\frac{\rho_p}{\rho_t}$ to be constant (fig. 5):

$$\left(\frac{1}{2} m_p v_p^2\right) \left(\frac{\rho_t}{S_t}\right) \left(\frac{\rho_p}{\rho_t}\right) \propto Vol_t \rho_t. \quad (23)$$

In equation 23, ρ_p and ρ_t are constant and equal to their respective values at normal confining pressures; whereas in the ratio $\frac{\rho_t}{S_t}$, both ρ_t and S_t at elevated confining pressures dictated by the experimental conditions should be used. A semiquantitative appraisal of the ratio $\frac{\rho_t}{S_t}$ has been used in figure 5 where $\frac{\rho_t}{S_t}$ at 49 kilobars has been used for copper, lead, aluminum, and basalt targets. In the case of the ratio $\frac{\rho_t}{S_t}$ for water craters, ρ_t was taken as 1.0 g/cm³ and S_t was taken from table 1. In figure 4, the volumes of the appropriate prolate hemispheroids have been used for the temporary water craters instead of the hemispherical shape assumed in the calculations of effective deformation strength. The value of $\frac{\rho_t}{S_t}$ for the wax target was taken from data at 20 kilobars because the highest velocities used for wax experiments, which were 2×10^5 cm/sec, require a Bernoulli stagnation pressure near 20 kilobars (Palmer and others, 1960,

IMPACT IN METALS AND ROCKS

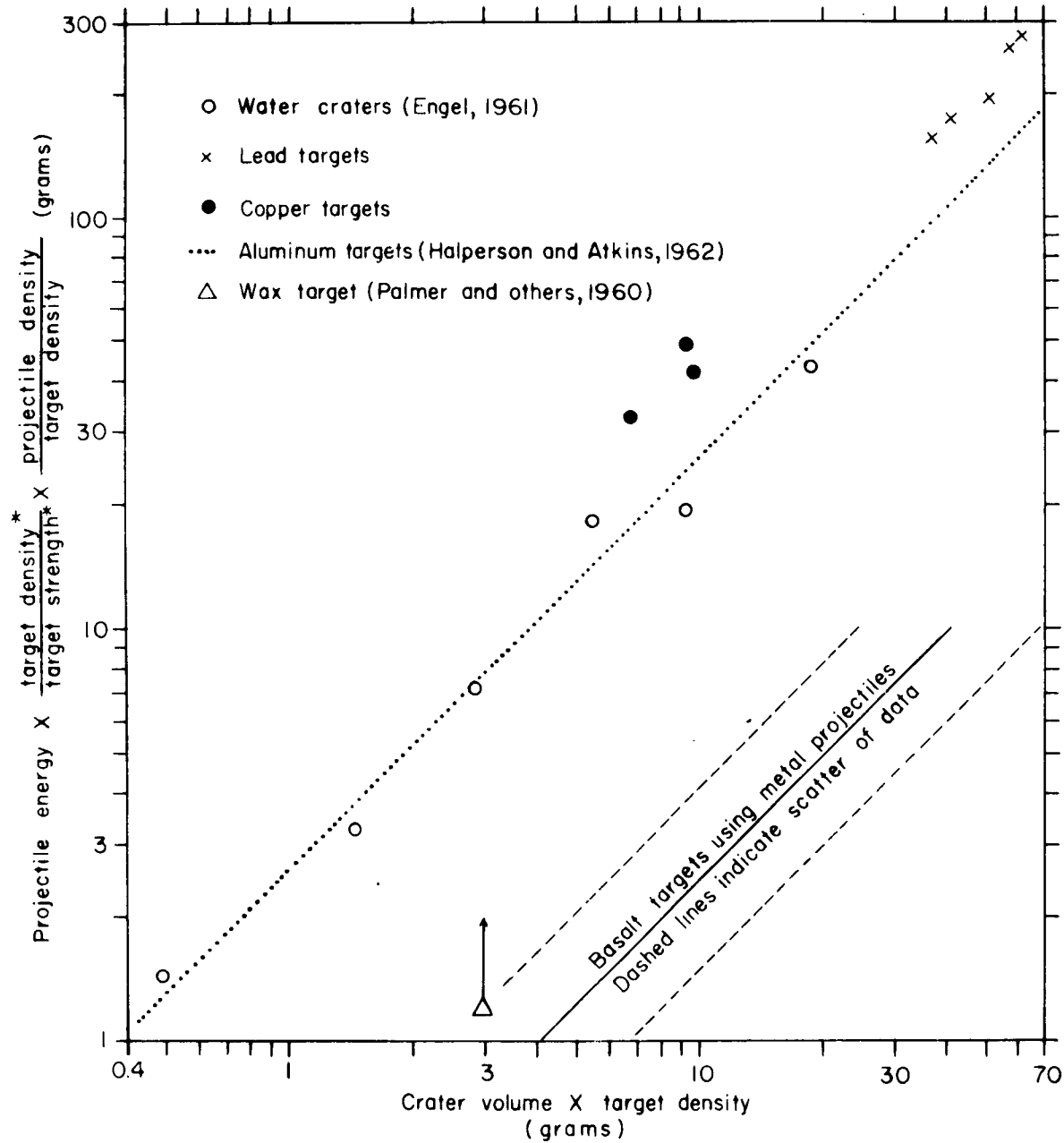


Figure 5. Normalized volume-energy data for impact cratering experiments using target strength, target density, and projectile density. Terms marked with asterisk from data measured at 49 kilobars confining pressure for lead, copper, aluminum and basalt, from data measured at 20 kilobars confining pressure for wax, and from table 1 for water craters.

IMPACT IN METALS AND ROCKS

p. 14). For the ratio $\frac{\rho_t}{S_t}$ for wax at 20 kilobars, ρ_t was estimated from the Hugoniot of plastic wax (Frasier, 1962, p. 384) which is comparable to the Hugoniot of paraffin (Frasier, 1962, p. 386). A value for S_t at 20 kilobars was obtained from static measurements of the shear strength of paraffin at elevated confining pressures (Bridgman, 1935, p. 833). The ratio for $\frac{\rho_t}{S_t}$ for paraffin wax at 20 kilobars is too small (see fig. 5). This should be expected because most of the failure and flow of the paraffin should occur at lower confining pressures with the decay of confining pressures in the stress waves from 20 kilobars to one bar with a concomitant decrease in shear strength of the paraffin (see Bridgman, 1935, p. 833). The yield, or crater volume per unit energy, for paraffin should decrease with increasing projectile velocity when projectile masses are constant because the shear strength of paraffin increases with increased confining pressure. Although Palmer and others (1960) do not report a decrease in yield for their paraffin data, a decrease in yield for hypervelocity impact craters in Petroflex Plastic Wax (a petrolatum-paraffin mixture) with increased projectile velocities using constant projectile masses has been reported (Frasier, 1962, p. 374).

Normalized data for craters produced by hypervelocity impacts with basalt are about one order of magnitude larger than the corresponding normalized craters in copper, lead, aluminum, and water. This difference is caused by the spalling which is produced by tensile failure during reflection of stress waves from the free surface around the point of impact of rock targets (see for example, Moore, Gault, and Lagn, 1962).

IMPACT IN METALS AND ROCKS

Conclusions

1. Target strength is a more realistic parameter than target acoustic velocity for correlation of data on hypervelocity impact craters in the fluid-impact regime with those on low-velocity hydrodynamic or fluid-impact craters. The partial success obtained when using target acoustic velocity is probably the result of a close correlation between strength and acoustic velocity for certain materials (see for example, Maurer and Rinehart, 1960), but the correlation does not hold for water.
2. The theory of Charters and Summers is approximately valid for craters produced by water drops impacting water and other craters in the fluid-impact regime.
3. The dynamic strength of a material which yields under impact in the fluid-impact regime is greater than the strength at low confining pressure, and probably less than the product of the target density and heat of fusion, when significant amounts of vaporization of the target do not occur.
4. The effects of target strength and target density at elevated confining pressures for craters in rocks and metals produced in the fluid-impact regime can be semiquantitatively estimated using the existing data at 49 kilobars. Strengths measured at this pressure not only give fair agreement between theory and experimental results with water-water impact, but also reduce the discrepancy between lead and copper experimental data when shear strengths at low confining pressures are used.
5. Hypervelocity impact craters in rocks should be deeper than corresponding craters in metals and water in the fluid-impact regime, because a projectile that has impacted rock is ejected along with debris, whereas one that has impacted metal smears out and plates the crater floors and walls.

IMPACT IN METALS AND ROCKS

6. The volumes of hypervelocity impact craters in rocks should be larger than the corresponding volumes of craters in metals and water because of the spalling of the rock produced by tensile failure related to the reflections of stress waves from the free surfaces around the point of impact.

7. More data on strengths at elevated confining pressures are needed in order to select proper parameters for correlation of hypervelocity impact data.

IMPACT IN METALS AND ROCKS

References cited

- Al'tshuler, L. V., Kormer, S. B., Brazhnik, M. I., Vladimirov, L. A., Speranskaya, M. P., and Funtikov, A. I., 1960, The isentropic compressibility of aluminum, copper, lead, and iron at high pressures: Soviet Physics JETP, v. 11, p. 766-775.
- Bridgman, P. W., 1935, Effects of high shearing stress combined with high hydrostatic pressure: Phys. Rev., v. 48, p. 825-847.
- Chabai, A. J., and Hankins, D. M., 1960, Gravity scaling laws for explosion craters: U.S. Atomic Energy Comm., SC-4541 (RR), 18 p.
- Charters, A. C., 1960, High speed impact: Sci. Am., v. 203, no. 4, p. 128-140.
- Charters, A. C., and Summers, J. L., 1959, Some comments on the phenomena of high-speed impact, in Decennial symposium, May 26, 1959, White Oak U.S. Naval Ordnance Laboratory, Silver Spring, p. 1-21.
- Engel, O. G., May 1961, Collisions of liquid drops with liquids: U.S. Nat. Bur. Standards Tech. Note 89, 30 p.
- Frasier, J. T., 1962, Hypervelocity impact studies in wax: Symposium on hypervelocity impact, 5th, Denver 1961, Proc., v. 1, pt. 2, p. 371-388.
- Halperson, S. M., and Atkins, W. W., 1962, Observations of hypervelocity impact: Symposium on hypervelocity impact, 5th, Denver 1961, Proc., v. 1, pt. 2, p. 497-509.
- Lombard, D. B., 1961, The hugoniot equation of state of rocks, in Symposium on rock mechanics, 4th, March 30, 31, and April 1, 1961, Proc.: Pennsylvania Min. Indust. Expt. Sta. Bull. no. 76, p. 143-152.
- Lyman, Taylor, ed., 1959, Metals handbook: Cleveland, Ohio, American Society for Metals, 1332 p.

IMPACT IN METALS AND ROCKS

References cited--Continued

- Maurer, W. C., and Rinehart, J. S., 1960, Impact crater formation in rock: Jour. Appl. Physics, v. 31, p. 1247-1252.
- Moore, H. J., and Gault, D. E., 1963, Relations between dimensions of impact craters and properties of rock targets and projectiles: U.S. Geol. Survey, Astrogeologic studies Annual progress report to NASA, August 25, 1961--August 24, 1962, pt. 8, p. 38-79.
- Moore, H. J., Gault, D. E., and Lugn, R. V., 1962, Experimental hypervelocity impact craters in rock: Symposium on hypervelocity impact, 5th, Denver 1961, Proc., v. 1, pt. 2, p. 625-643.
- Nordyke, M. D., 1962, An analysis of cratering data from desert alluvium: Jour. Geophys. Research, v. 67, p. 1965-1974.
- Palmer, E. P., Grow, R. W., Johnson, D. K., and Turner, G. H., 1960, Cratering, experiment and theory: Symposium on hypervelocity impact, 4th Eglin Air Force Base, Florida, 1960: U.S. Air Proving ground center APGC-TR-60-39, 17 p.
- Rice, M. H., McQueen, R. G., and Walsh, J. M., 1958, Compression of solids by strong shock waves: Solid State Physics, v. 6, p. 1-63.
- Robertson, E. C., 1955, Experimental study of the strength of rocks: Geol. Soc. America Bull., v. 66, p. 1275-1314.
- Shoemaker, E. M., 1960, Penetration mechanics of high velocity meteorites, illustrated by Meteor Crater, Arizona: International Geol. Cong., 21st, Copenhagen 1960, pt. 18, p. 418-434.
- Summers, J. L., 1959, Investigation of high speed impact--regions of impact and impact at oblique angles: U.S. Natl. Aeronautics and Space Admin. Tech. Note D-94, 18 p.

IMPACT IN METALS AND ROCKS

References cited--Continued

Whipple, F. L., 1958, The meteoritic risk to space vehicles, in Alperin, Morton, Stern, Marvin, and Wooster, Harold, eds., *Vistas in Astronautics*, v. 1: New York, Pergamon Press, p. 115-124.

ENERGY BALANCES IN HYPERVELOCITY PENETRATION

R. B. Pond, C. Mobley
The Johns Hopkins University
Baltimore, Maryland

and

C. M. Glass
Ballistic Research Laboratories
Aberdeen Proving Ground, Maryland

ENERGY BALANCES IN PENETRATION

ABSTRACT

A technique for developing a balance between the kinetic energy of the pellet and the dynamic energy absorbed by the target is demonstrated. A proposed dynamic stress-strain diagram is used to develop the mechanical energy equivalent as a function of strain.

The strain gradient under the crater is developed by a delineation of grain size after annealing the target as well as an extended tapered tensile specimen. The technique shows the kinetic energy to be absorbed by five processes; i.e., pellet disintegration, crater lip formation, crater disintegration, development of a high shear strain volume, and development of a low shear strain in the rest of the target. After a determination of the geometry of the fields in the last four processes and the strain gradients therein imposed, the mechanical energy equivalent is applied to disclose the energy balance.

ENERGY BALANCES IN PENETRATION

Introduction

Previous work^(1,2) has indicated that hyper-velocity penetration not only results in crater formation but also produces a strain affected region in the target material closely associated with the crater. Earlier papers by the authors^(2,3) have been concerned with the use of mechanical energy equivalents in an attempt to effect balances between dynamic and static energies. The purpose of this effort is to suggest an approach for partitioning the kinetic energy input into the variously deformed volumes such as the crater or the strain affected region by using the mechanical energy equivalent concept.

Generation of the mechanical energy equivalent is accomplished by developing a static true-stress, true-strain tensile curve for the target material as well as the pellet material. The target material is tested in the dead annealed state since the target itself is provided in this state for penetration. A characteristic tensile curve is illustrated in Fig. 1. The rupture stress σ_r is taken as the maximum stress in the proposed dynamic stress-strain diagram. The material is proposed to not strain harden during the high velocity deformation and

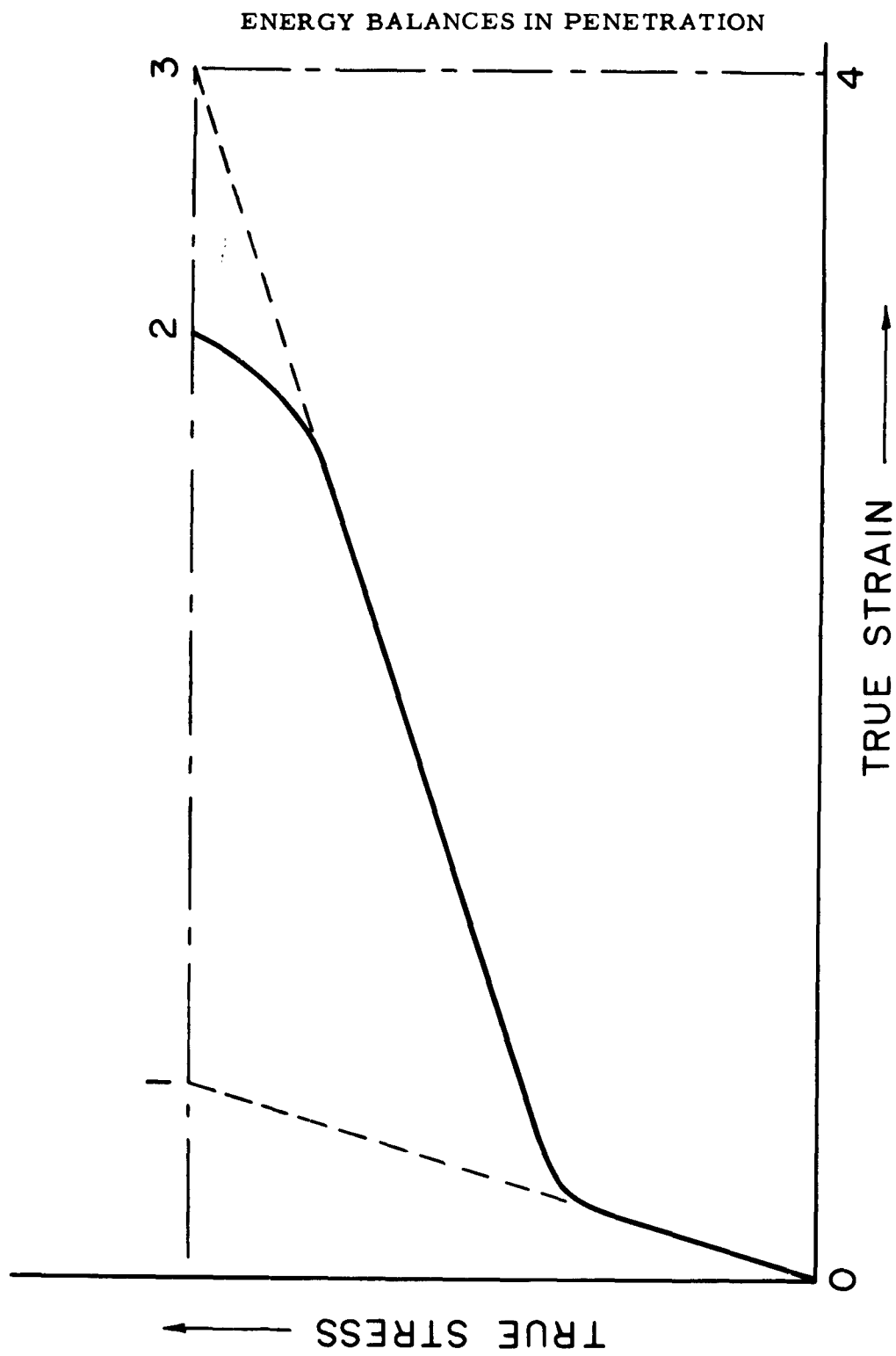


FIGURE 1

ENERGY BALANCES IN PENETRATION

therefore the elastic portion of the curve is followed by a plastic portion wherein the strain hardening index (or the slope of the curve) is zero. However the rupture strain at high velocity is taken as point $\bar{2}$ rather than point $\underline{2}$.

This rupture strain is used for the following reasons: At the beginning of necking during the tensile test all of the deformation occurs in the necked volume and this continues to be so during the rest of the test. Therefore in the true-stress, true-strain plot the instantaneous gauge length during necking should be taken as the length of the necked region. If this is carried out and this observed strain added to the previously documented strain, the slope of the plastic portion of the static curve is found to remain constant until rupture. This observation was made possible by taking motion pictures of tensile test specimens during the entire tensile test and determining the geometry of the specimen from the picture record at all desired stages of the test. This observation was found to be consistent for an array of aluminum alloys, copper, lo-carbon steel and an array of stainless steels.

The mechanical energy equivalent per unit volume

ENERGY BALANCES IN PENETRATION

is taken as the area under the dynamic curve (012340 in Fig. 1) for portions of the metal which are deformed to the rupture strain limit. The energy equivalent for all other strains is taken as the area of the curve up to the strain limit being considered.

Procedure and Results

The targets to be used were all annealed in the identical manner and were then penetrated with a drill rod pellet. The crater volume was determined by titration. Because it was desired to study the effects of the minor craters on the target surface the volumes of all the craters were taken. After the volume determination the specimen was again annealed and then sectioned through the center of the crater. The sectioned surface was ground flat, metallographically prepared and etched. Fig. 2 illustrates the characteristic appearance of the crater, the lip, and the strain affected region after this procedure.

The strain affected region is delineated because the residual strain energy in a metal determines the grain size for a particular recrystallization schedule. In order that the varying grain size field of the strain affected region could be documented in terms of strain,

ENERGY BALANCES IN PENETRATION

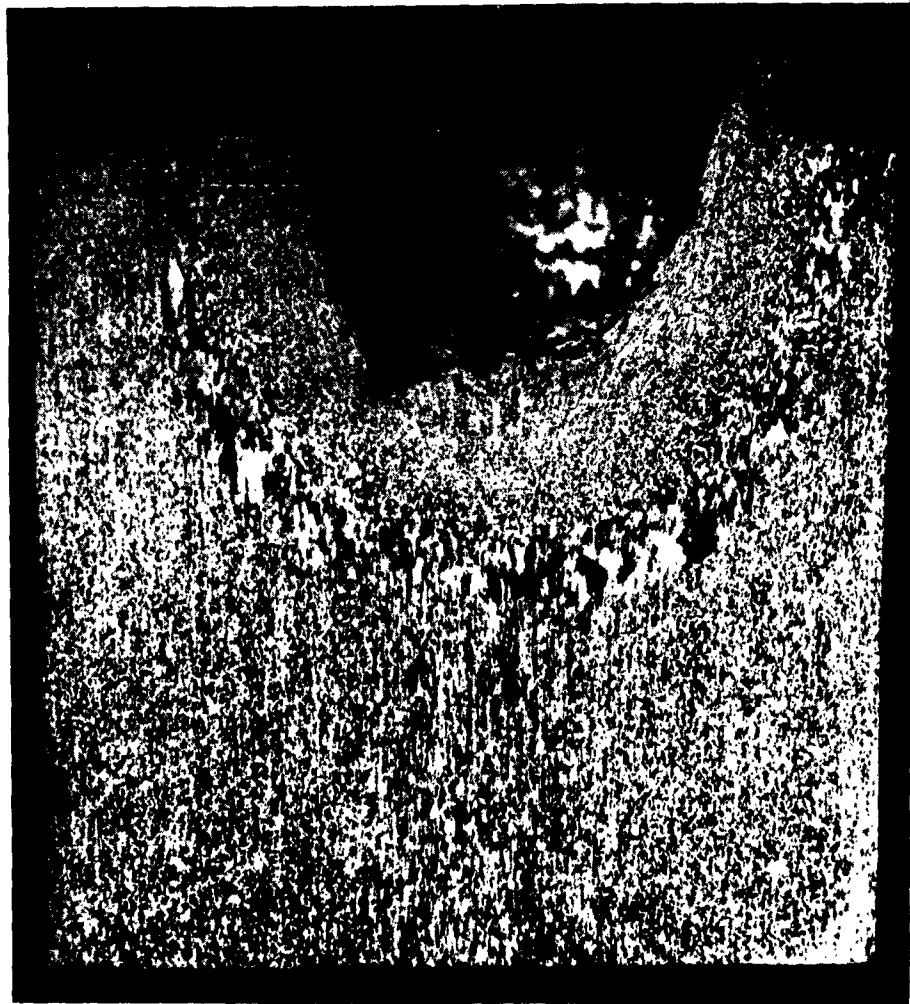


FIGURE 2

ENERGY BALANCES IN PENETRATION

tapered tensile specimens were extended to rupture, the strain measured along the length and (after annealing) the recrystallized grain size correlated with the strain. Using this correlation the strain gradient in the strain affected volume can be determined.

An energy balance for copper targets was completed using the following equation:

$$\begin{aligned} \text{Impact Energy} = & \text{Crater Formation Energy} + \\ & \text{Affected Volume Energy} + \\ & \text{Low Strain Energy} + \\ & \text{Lip Energy} + \text{Projectile Breakup Energy} \end{aligned}$$

The impact energy for each target was computed from data given by Aberdeen Proving Ground ($\frac{1}{2} MV^2$). Crater formation energy is the crater volume times the energy per unit volume under the dynamic stress-strain curve up to dynamic rupture strain (55.6% for Cu). Thus

$$\begin{aligned} \text{Crater Formation Energy} &= V_{\text{crater}} \left(\frac{E}{V} \right)_{\text{crater}} \\ \text{For copper targets } \left(\frac{E}{V} \right)_{\text{crater}} &= 199.5 \frac{\text{Joules}}{\text{cc.}} \end{aligned}$$

The affected volume energy is the sum of two terms. The first term is the integral of the dynamic stress and the volume as a function of strain with limits from $0.045 \frac{\text{in.}}{\text{in.}}$ to the dynamic rupture strain, $0.556 \frac{\text{in.}}{\text{in.}}$. The lower limit of the integral is obtained from the data on the copper tapered specimens. It was found that at this strain the largest grains were observed. The second term is the volume of the affected region times the energy per unit volume under the dynamic stress-strain curve from strain $0.045 \frac{\text{in.}}{\text{in.}}$

ENERGY BALANCES IN PENETRATION

to zero strain. This energy per unit volume below

$0.045 \frac{\text{in.}}{\text{in.}}$ was calculated to be 15.58 Joules/cc.

Thus:

Affected Volume Energy -

$$\int_{0.045}^{0.556} 6 \frac{2\pi}{3} [r^3 - r_0^3] d\epsilon + V_{RR} \left(\frac{E}{V} \right)_{\text{Below } 0.045 \frac{\text{in.}}{\text{in.}}}$$

After plotting the curve of "Strain vs. Length from Crater" for three different copper targets (Nos. 3, 4, & 6) it was decided that a decaying exponential curve would fit the experimental data. An equation of the type

$$\epsilon = e^{-\alpha(r-C)}$$

was tried and found to fit. The constants α and C are determined from the radius of the crater (r_0) and the maximum radius of the affected region ($r_{\text{max.}}$). Since the strain values are known for these two radii, two equations may be solved simultaneously to determine α and C . Knowing strain as a function of radius, the volume can be found as a function of strain. The Low Strain Energy term is due to the plastic deformation of the entire specimen minus the affected volume and crater. This term is the total volume of the specimen

ENERGY BALANCES IN PENETRATION

minus crater volume and affected volume times the energy per unit volume under the static true stress - true strain curve for copper from approximately 0.01 in./in. strain to zero strain. This energy per unit volume term below 0.01 in./in. was found to be 0.294 Joules/cc. Thus

Low Strain Energy =

$$V_{\text{total}} - (V_{\text{crater}} + V_{\text{AR}}) \left(\frac{E}{V} \right)_{\text{low strain value}}$$

The particular strain to be used for this term is very difficult to measure and should be considered a best estimate value.

The Lip Energy is the volume of the lip times the energy per unit volume under the dynamic stress-strain curve up to rupture strain. Thus

$$\text{Lip Energy} = V_{\text{Lip}} \left(\frac{E}{V} \right)_{\text{crater}}$$

The Projectile Breakup Energy is the volume of the projectile times the energy per unit volume under the dynamic stress-strain curve up to rupture strain for the projectile material. For the drill rod used this energy per unit volume is 243.17 Joules/cc. Then

$$\text{Projectile Breakup Energy} = V_{\text{Projectile}} \times \left(\frac{E}{V} \right)_{\text{Projectile}}$$

ENERGY BALANCES IN PENETRATION

Copper Targets

<u>Specimen #</u>	<u>Impact Energy</u>	<u>Crater Energy</u>	<u>Affected Volume Energy</u>	<u>Low Strain Energy</u>	<u>Total</u>
1	1967	190.5	1155.9	95.0	1441.4
2	1970	214.6	1581.1	92.3	1888.0
3	2097	349.0	1706.9	90.2	2146.1
4	1836	278.8	1576.1	92.3	1947.2
5	1923	269.7	1564.7	92.3	1926.7
6	1983	167.5	1628.2	91.2	1886.9
7	1955	172.5			

All energies are in Joules

ENERGY BALANCES IN PENETRATION

Since the lip volume and projectile volume are not measured for each target, and the value of the sum of lip energy and projectile breakup energy is much less than 50 Joules, 50 Joules has been added to cover these two terms plus other small effects (light energy, etc.,).

Typical values for a copper specimen (No. 6) are

Impact Energy = 1983 Joules

Crater Formation Energy = 167.5 Joules

Affected Volume Energy = 1048.0 Joules +
580.2 Joules

Low Strain Energy = 91.2 Joules

Lip Energy = 17.3 Joules

Projectile Breakup Energy = 5.6 Joules.

The balance is then

$$\begin{aligned} 1983 \text{ Joules} &= 167.5 \text{ Joules} + 1628.2 \text{ Joules} + \\ &91.2 \text{ Joules} + 17.3 \text{ Joules} + 5.6 \text{ Joules} \\ &= 1909.8 \text{ Joules} \end{aligned}$$

which is within 3.7% of being correct.

Using the above approach a number of copper targets have been evaluated at one level of kinetic energy input and an array of 2-S aluminum targets have been evaluated at three levels of kinetic energy input. The following tabulations indicate the spread of data.

ENERGY BALANCES IN PENETRATION

Aluminum Specimen No.	E _{crater}	E _{affected Region}	E _c + E _{AR}	E _{Impact}	C	α	E _I - E _o
1	490.7	[699.2(1025.70)]	[1189.9(1516.4)]	2028	0.99	2.85(2.28)	1537.3
2	708.2	1510.6	2218.8	1954	0.83	1.82	1245.9
3	649.6	-	-	1827	-	-	1177.4
4	547.2	-	-	-	-	-	-
5	669.8	1323.2	1993.0	1906	0.94	1.90	1236.2
6	717.2	1331.8	2049.0	1885	0.94	1.98	1167.8
7	584.1	[1084.5(1287.5)]	[1668.6(1871.6)]	2046	0.95	2.07(1.90)	1461.9
8	593.8	-	-	1963	-	-	1369.2
9	586.2	781.6	1367.8	1898	1.09	2.85	1311.8
10	515.1	1024.7	1539.8	1908	0.85	2.07	1392.9
11	875.4	-	-	-	-	-	-
12	1032.3	2117.9	3150.2	3047	0.82	1.54	2014.7
13	1012.7	-	-	3114	-	-	2101.3
14	929.8	2174.0	3103.8	3056	0.89	1.66	2126.2
15	622.4	-	-	3119	-	-	2496.6
16	1053.9	2144.5	3198.4	3157	0.95	1.76	2103.1
17	733.2	1475.7	2208.9	3032	1.06	2.07	2298.8
18	961.2	2550.0	3511.2	3087	0.77	1.54	2125.8
19	671.9	1516.4	2188.3	3155	0.74	1.68	2483.1
20	1083.8	2117.9	3201.7	3080	0.82	1.54	1996.2
21	1512.5	-	-	7234	-	-	5721.5
22	2033.9	-	-	-	-	-	-
23	2315.2	4041.96	6357.2	9003	1.60	1.33	6687.8
24	3798.7	-	-	-	-	-	-

All energies are in Joules. α is in (cm.)⁻¹. C is in centimeters.
 For specimens #4, 11, 22 and 24 the velocity of the projectile is not known.
 Specimens #13 and 15 were melted while annealing.
 Specimen #21 has not been sectioned yet.

ENERGY BALANCES IN PENETRATION

Measurements were made of strain affected volumes as well as crater volumes for the primary craters and the smaller craters in a number of targets. Fig. 3 shows the relationship of the two volumes involved as the crater volume increases. It is apparent from these curves that as the crater takes on any appreciable size, the ratio of crater volume to strain affected volume rapidly approaches a constant value of approximately .15. The energy distribution on these volumes is not the same ratio due to the strain gradient in the affected region. It should be noted in the tabulation of energy distribution that the bulk of the kinetic energy (approximately 60% in Al and 80% in Cu) is consumed by developing the strain affected volume. The peak values in Fig 3 may be inaccurate due to difficulty in accurately determining the strain affected volume when the crater volume is less than $.1 \times 10^{-3}$ cc. However, the peak values insinuate that the kinetic energy input per unit area probably has a pronounced effect on the amount of energy going into crater formation or on crater size. This postulation suggests the examination of crater volume- affected volume ratios as a function of increased kinetic energy input where the target material and condition and the projectile profile are maintained constant. In the Al series herein reported on, the ratio has remained at approximately .15 for crater volumes of 17 cc.

During the determination of the energy balances for the Al series, it was noted that α and c vary with

VOLUME CRATER
VS. VOLUME CRATER
VOLUME AFFECTED REGION

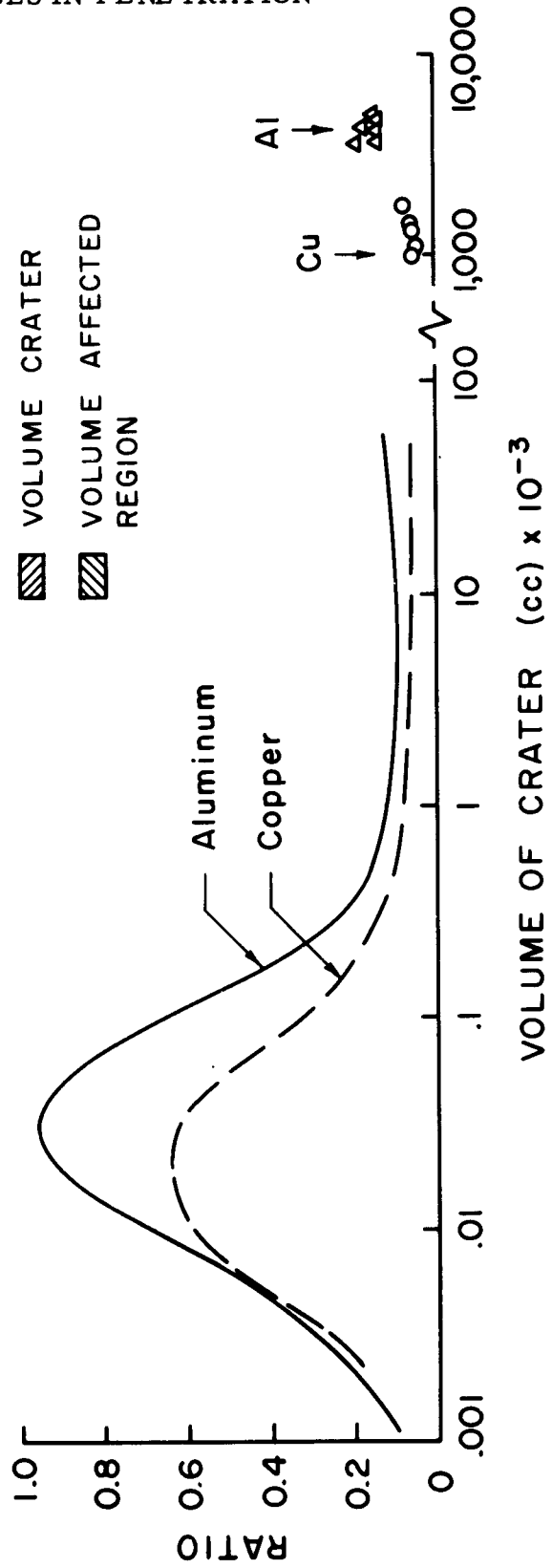


FIGURE 3

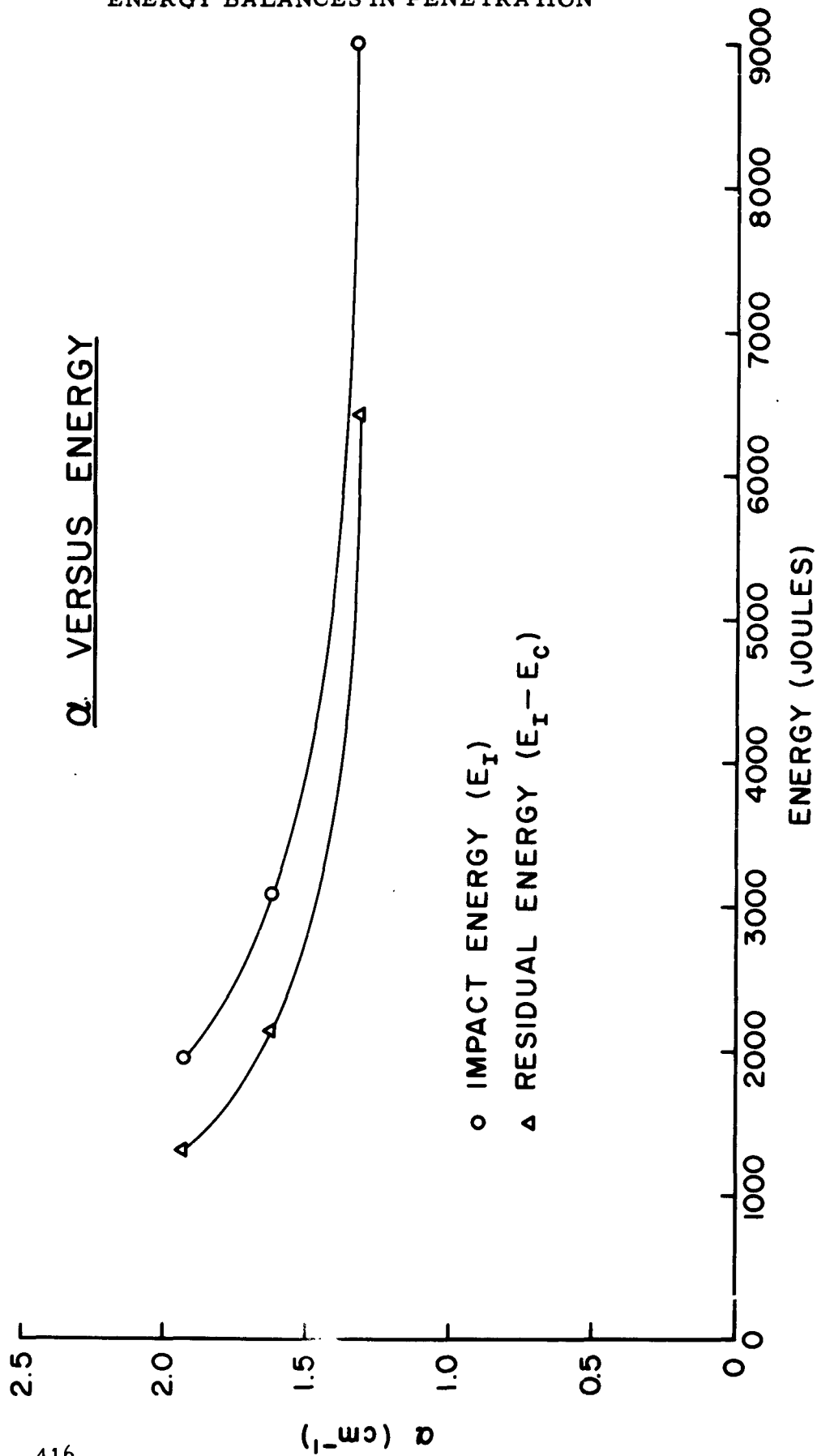


FIGURE 4

ENERGY BALANCES IN PENETRATION

impact energy or residual energy. The variation in \underline{c} is small relative to the variation in $\underline{\alpha}$. $\underline{\alpha}$ is probably a function of three variables, i.e., impact energy, target material properties, and target geometry. Since the target material and geometry were maintained constant, it is possible to plot $\underline{\alpha}$ Vs. impact energy and residual energy as in Fig. 4. The first two points on the graph are averages of values from five and six specimens respectively. The last point on the graph is the value from only one specimen (#23) which is the only high energy input target to be completely analyzed so far.

It is suggested that for 1100 Al and with this graph and the average value for \underline{c} , an energy balance can be determined without sectioning the specimen.

Acknowledgements

The sincerest appreciation is extended to Mrs. E. Harrison for her assistance in every aspect of this investigation and to Mr. John Kineke for his cooperation in performing penetration of the targets.

References

1. E.P. Palmer, R.W. Grow, D.K. Johnson, and G.H. Turner, Proceedings of Fourth Symposium on Hypervelocity Impact Vol I (1960) 15.
2. C.M. Glass and R.B. Pond, Proceedings of Fourth Symposium on Hypervelocity Impact, Vol III (1960) 16.
3. R.B. Pond and C.M. Glass, Response of Metals to High Velocity Deformation, Interscience Publisher, New York, (1960) 145-161.

THE PARTITION OF ENERGY FOR HYPERVELOCITY
IMPACT CRATERS FORMED IN ROCK

By Donald E. Gault and Ezra D. Heitowit

National Aeronautics and Space Administration
Ames Research Center
Moffett Field, Calif.

ABSTRACT

An analysis is presented of the manner in which energy was expended from the original reservoir of projectile kinetic energy during the formation of impact craters in rock. The study is based on an extensive series of cratering experiments employing aluminum projectiles launched with a nominal velocity of 6.25 km/sec against blocks of macroscopically homogeneous basalt. It is shown that a major fraction of the projectile kinetic energy reappears in kinetic form in the ejecta spewed out of the craters. Significant, but smaller, fractions of energy are trapped irreversibly as heat in the rock and projectile material and expended in the creation of free surfaces by fragmentation.

THE PARTITION OF ENERGY FOR HYPERVELOCITY IMPACT CRATERS FORMED IN ROCK

By Donald E. Gault and Ezra D. Heitowit

National Aeronautics and Space Administration
Ames Research Center
Moffett Field, Calif.

INTRODUCTION

The collision of a large meteoroid with the lunar or terrestrial surface is one of the ultimate examples of hypervelocity impact in the solar system. On a time scale measured in minutes, large geological structures can be produced, even for what corresponds to a relatively modest event. A terrestrial example of a planetary impact is the 1.2 km diameter crater at Meteor Crater, Arizona, but many others including the Holleford (2.3 km), Brent (3.5 km), Deep Bay (12 km) Craters, the Ries Basin (27 km), Germany, and the Vredefort Ring (60 km), South Africa, have been interpreted as impact features (refs. 1 - 4). From dimensional considerations alone, these and countless similar lunar structures illustrate the violence of a cosmic impact and attest that the energy expenditures for formation of the craters may dwarf by orders of magnitude the energy released by the largest nuclear explosions.

Because of the obvious manifestations of the violence of such events, including evidence for fusion of the meteorite and country rock, as well as structural similarities to chemical and nuclear explosion craters, a remarkably persistent concept has been perpetuated that meteorite craters are produced by explosion of the meteorite body and rock heated by the collision. This concept has been so widely disseminated that any craters formed by hypervelocity impact are commonly referred to as explosion craters. The logic for this belief stems from a simple computation in which the specific kinetic energy of the projectile is equated to the specific internal energy of the projectile at the moment of impact. For impact velocities in excess of approximately 4.5 km/sec, a velocity well below the usual geocentric velocity of large meteoroids, it is easily found that the specific internal energies thus calculated exceed the enthalpy of vaporization for any solid at atmospheric pressures. The obvious, although incorrect, conclusion is that the heated mass of projectile explodes.

The principal fallacy in such a calculation (first pointed out, to the authors' knowledge, by Shoemaker (ref. 1)) is in the neglect of the manner in which energy is partitioned in the projectile and target by shock processes. Moreover, the simple computation totally ignores the equation of state of the materials under shocked conditions. Hypervelocity impact can, in fact, produce very high specific internal energies. These energies are, however, the consequences of the mechanical compression by the projectile as it penetrates the target, rather than the cause of the compression. Moreover, when one considers the equation of state of the materials involved,

ENERGY PARTITION IN BASALT

only a fraction of the increase in specific internal energy is found to be irreversibly trapped as heat for fusion and/or vaporization. The remaining fraction of the internal energy is used in furthering the propagation of the shock waves through the media. In effect, any energy expended in fusing or vaporizing target or projectile material is lost to the cratering process and detracts from any physical enlargement of an impact crater. An impact, accompanied by vaporization, is an explosion only to the extent that debris is thrown upward and out of a transient cavity.

The energy partition described by Shoemaker is valid only during the earliest stages of energy transfer from projectile to target and provides no information on the ultimate deposition of the kinetic energy from the projectile at the conclusion of the cratering process. Notwithstanding this limitation, the significance of the analysis as related to "explosive" cratering is evident and it emphasizes that energy partition during a cratering event is one of the most interesting and fundamental problems which confront experimentalists and theorists in the field of hypervelocity impact.

Of the three quantities - mass, momentum, and energy - which are necessary to describe the motion of one body relative to another body, energy is by far the most difficult to trace through any complicated physical process. For this reason, there is very little hope for either formulating a theoretical model for impact cratering or interpreting experimental results with any insight into the physical processes of the phenomena, until a thorough understanding is obtained of the various paths into which the projectile kinetic energy is channeled during the formation of a crater.

As part of a general study at the Ames Research Center of the mechanics of hypervelocity impact and role of collision processes as an evolutionary factor in the solar system, it is the purpose of this paper to present results of an analysis which has been made to explore the manner in which energy is partitioned during the formation of impact craters in rock. The analysis is an outgrowth of earlier work reported by Moore, et al. (ref. 5) at the 5th Hypervelocity Impact Symposium, and by Gault, et al. (ref. 6) in relation to environmental factors of lunar impacts. The analysis is based on an extensive series of cratering experiments employing aluminum projectiles launched with a nominal velocity of 6.25 km/sec against blocks of macroscopically homogeneous basalt. The study makes use of high-speed framing records (5×10^3 , 1.5×10^5 and 10^6 frames/sec) of impact events, mass size distributions of the fragmented rock ejecta, spallation of the back of the target blocks, ballistic pendulum measurements, and Hugoniot equations of state for aluminum and basalt.

ENERGY PARTITION IN BASALT

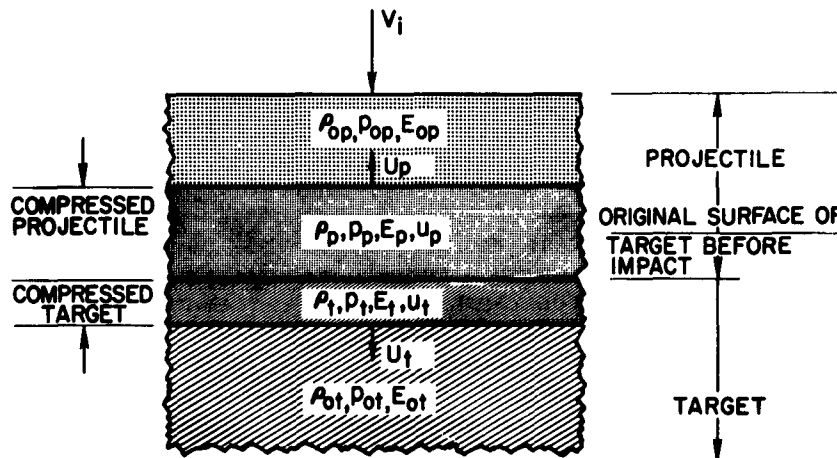
ANALYSIS

Preliminary Consideration

A review of the initial energy transfer from projectile to target will be helpful to the subsequent discussion of the manner in which energy is partitioned during crater formation in rock. An exact treatment of the early stages of impacts is, of course, not possible at the present time, but an acceptable approximate solution can be obtained based on the hypothetical case of two semi-infinite bodies colliding along a plane surface. That is, the initial stage of the impact is considered as a problem in one-dimensional flow, a problem which is tractable mathematically and, at the same time, amenable to gaining some insight into early stages of the energy partition.

Initial Partition of Energy

With reference to the accompanying sketch, upon contact of the projectile against the target, shock waves will be propagated from the interface into both of the colliding bodies. Both shock waves will engulf a continuously increasing mass of material as the undisturbed



Sketch (a)

$$P_p = P_t$$

(1)

ENERGY PARTITION IN BASALT

projectile continues to advance toward the target with the impact velocity V_1 . In a coordinate system referenced to the undisturbed media, application of the laws of conservation of mass, momentum, and energy across the shocks leads to the well-known Rankine-Hugoniot equations

$$\rho_o U = \rho(U - u) \quad (2)$$

$$p - p_o = \rho_o U u \quad (3)$$

$$E - E_o = \frac{1}{2} (p + p_o) \left(\frac{1}{\rho_o} - \frac{1}{\rho} \right) = \frac{1}{2} u^2 \quad (4)$$

where U is the propagation velocity of the shock wave into the undisturbed medium, u is the mass velocity of the compressed material behind the shock wave, again relative to the undisturbed material, and p , ρ , and E are the pressure, density, and specific internal energy, respectively, with the subscript o denoting conditions in the undisturbed medium.

For conditions during a hypervelocity impact, $p \gg p_o$ and the last two expressions are frequently approximated as

$$p = \rho_o U u \quad (3a)$$

$$E - E_o = \frac{1}{2} p \left(\frac{1}{\rho_o} - \frac{1}{\rho} \right) = \frac{1}{2} u^2 \quad (4a)$$

It is to be noted that to the same degree of approximation, the total work done on the medium by the shock compression is $p(1/\rho_o - 1/\rho)$. Thus equation (4a) indicates that the energy added by the shock process is equally partitioned in the compressed material between the specific kinetic energy ($1/2 u^2$) and an increase in the specific internal energy ($E - E_o$).

Since the density ρ_o may be considered a known quantity, the Rankine-Hugoniot equations provide three equations with four unknowns, ρ , p , U , and u . In order to fully describe the conditions behind the shock front, a fourth equation is required. Any algebraic equation involving two of the four unknowns would be satisfactory, but what is required in principle is a relationship which describes the thermodynamic properties of the material, that is, an equation of state.

The equation of state of solids has received increasing attention in recent years by workers in the field of solid-state physics. A discussion of this important subject is beyond the scope of this study and it is

ENERGY PARTITION IN BASALT

sufficient to note here only that a wealth of information on the subject has accumulated in the open literature. Most of the available data is concerned with metals, a wide selection up to pressures of a few megabars¹ (refs. 7 - 9) and a few metals for pressures approaching 10 megabars (ref. 10). Data for rocks and minerals are relatively scarce and confined to pressures less than 700 kilobars (ref. 11). For the present analysis for the impact of aluminum into basalt, the data of Walsh, et al. (ref. 8) and Al'tshuler, et al. (ref. 9) will be used for the aluminum and the data of Lombard (ref. 11) for a basalt from the Nevada Test Site will be employed for the target medium.

The usual manner of presenting the equation of state under shock conditions is the so-called Hugoniot curve describing the locus of points for the specific volume ($v = 1/\rho$) to which a material is compressed by any given pressure jump across the shock front. The appropriate Hugoniot curves for Al and basalt are shown in figure 1. The two materials have similar Hugoniots with the Al being stiffer in the sense that the percentage change in the volume for a given pressure is less than that for the basalt. It must be emphasized that the Hugoniot curves themselves do not indicate a continuous compression cycle to a pressure p ; the curves are only the locus of points for the states attained by discontinuous pressure jumps.

The experimental Hugoniot curves (fig. 1), together with equations (2), (3a), and (4a), permit the evaluation of U , u , p , $E - E_0$, and ρ in terms of each other for any given conditions. The application of these data, however, would be cumbersome if it were not for the fortuitous result that an "equation of state" expression can be given algebraically in terms of the shock wave and mass velocities U and u . It has been found that an excellent approximation for the experimental results over a wide range of pressure can be made by an expression in the form

$$U = a + bu \quad (5)$$

where a and b are constants. Departures from this linear relationship are usually associated with phase changes and/or high dynamic yield strengths, both of which may lead to conditions for which a single shock system is unstable and breaks down into a system of two or more compression waves (ref. 12). The graphical representation of the equations for aluminum and basalt is shown in figure 2, with the numerical forms used herein being

$$U_p = 5.30 + 1.37 u_p \quad (6)$$

¹One bar = 10^6 dynes/cm² (i.e., approximately 1 atmosphere).

ENERGY PARTITION IN BASALT

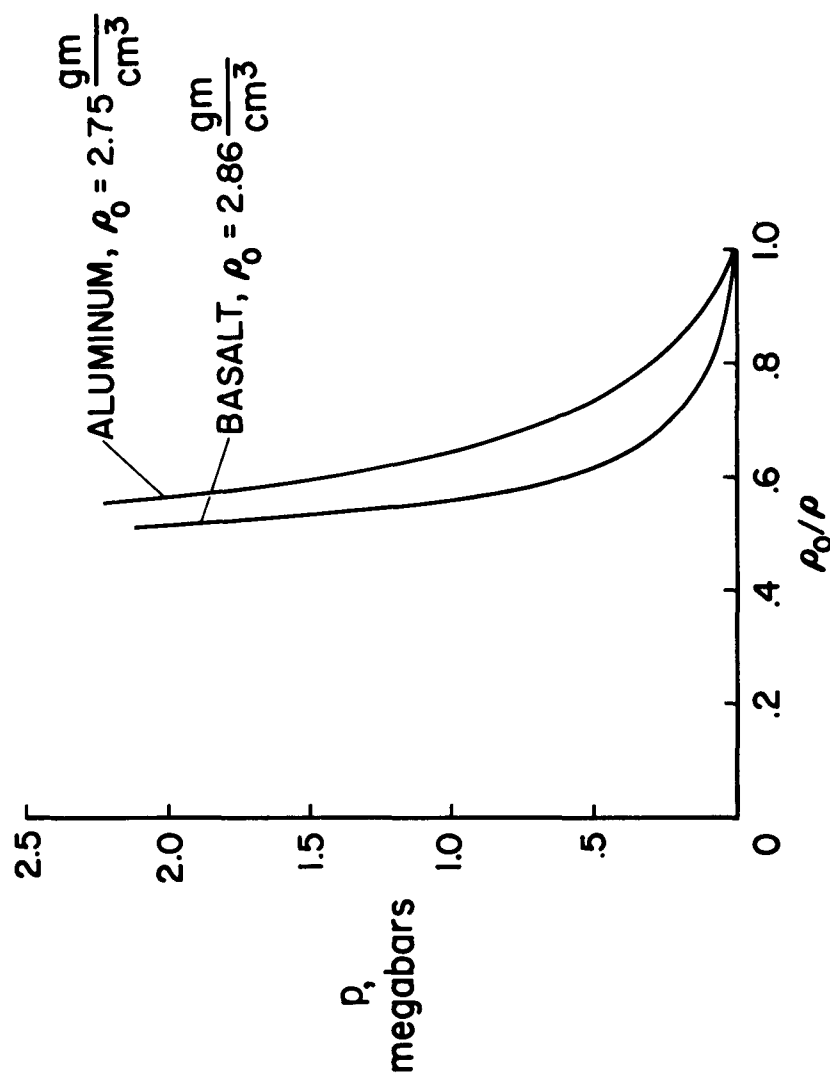


Figure 1.- Hugoniot curves for aluminum and basalt.

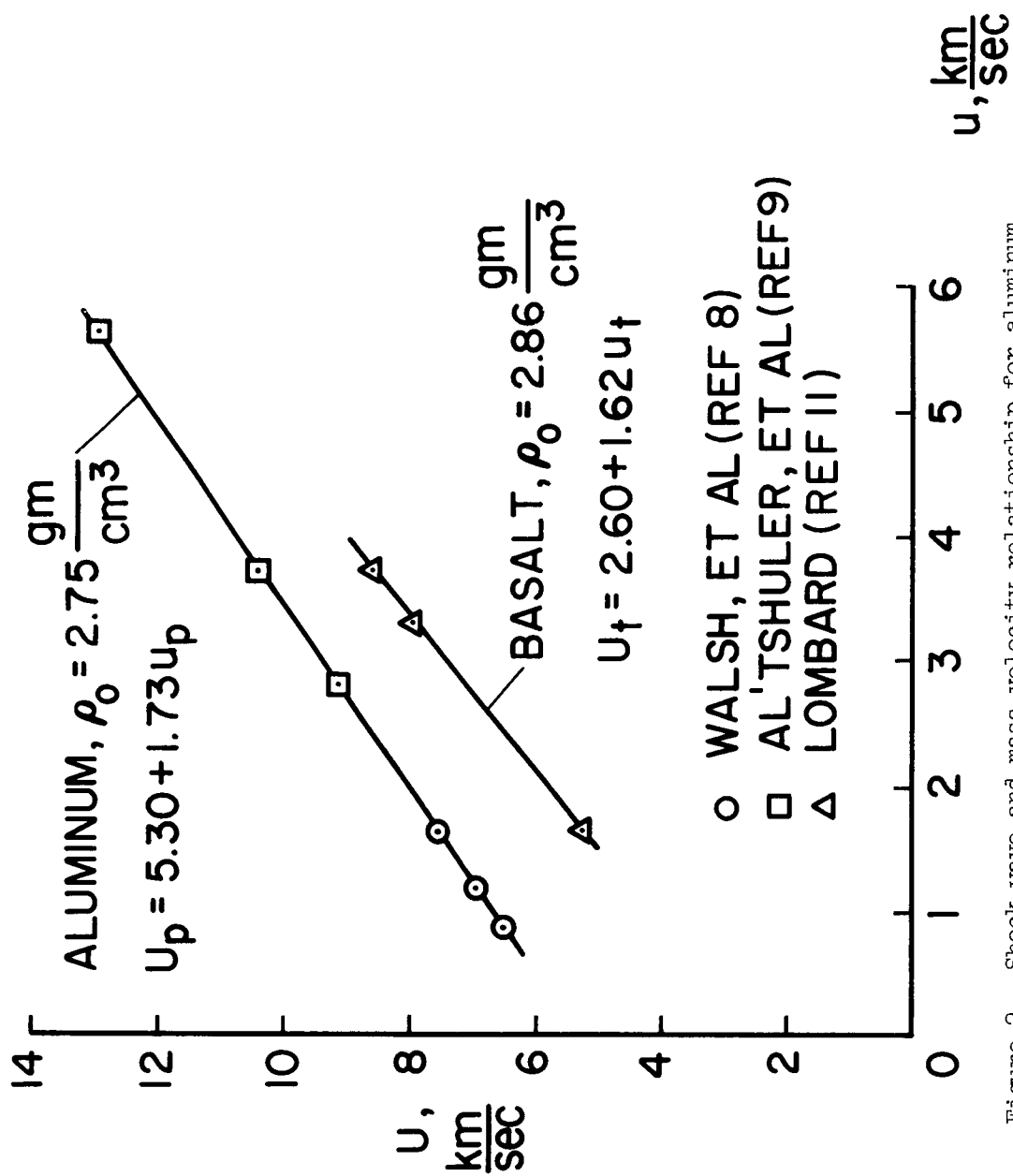


Figure 2.- Shock-wave and mass velocity relationship for aluminum and basalt.

ENERGY PARTITION IN BASALT

for the aluminum projectile and

$$U_t = 2.60 + 1.62 u_t \quad (7)$$

for the basalt target.

Although equations (6) and (7), when combined with equations (2), (3a), and (4a), provide a simple algebraic solution for U , u , p , ρ , and $E - E_0$ in terms of each other for any given conditions, it remains to relate the conditions behind the wave fronts to the impact velocity V_i . Toward this end, with the aid of sketch (a), it is readily verified that since the compressed projectile must have the same relative velocity to the undisturbed target ($V_i - u_p$) as the velocity of the compressed target medium (U_t) to maintain physical contact at the projectile-target interface, there results

$$V_i = u_p + u_t \quad (8)$$

When the shock velocity U is eliminated between equations (3a) and (5), so that

$$p = \rho_o(a + bu)u \quad (9)$$

and equation (8) is employed to eliminate u_p (or u_t), one may write

$$p_p = \rho_{op}[a_p + b_p(V_i - u_t)](V_i - u_t) \quad (10)$$

$$p_t = \rho_{ot}(a_t + b_t u_t)u_t \quad (11)$$

Then, because the pressure in the shocked target and projectile media must be equal, a simple quadratic in V_i and u_t (or u_p) results

$$[a_p + b_p(V_i - u_t)](V_i - u_t) = \rho_{ot}(a_t + b_t u_t)u_t \quad (12)$$

which, in principle, permits an exact algebraic solution for all the required parameters as a function of the impact velocity V_i . In practice, however, a simple graphical solution can be obtained which is more in keeping with the spirit of the approximate analysis of the initial energy partition for the impact based on one-dimensional flow. When one notes that the pressure p can be calculated as a function of the mass velocity u from equation (9),

ENERGY PARTITION IN BASALT

equation (8) suggests the question, "At what pressure p will the sum of the mass velocities u_t and u_p (measured with respect to the undisturbed materials) equal a given value of the impact velocity V_1 ?" The graphical solution to this question is indicated in figure 3, together with the variation of p with V_1 for the particular case under consideration of aluminum into basalt.² For the nominal impact velocity of 6.25 km/sec in this analysis, the pressure at impact is found to be 750 kilobars with $u_t = 3.30$ km/sec and $u_p = 2.35$ km/sec. The remaining parameters are easily determined from equations (6), (7), (2), (3a), and (4a).

$$U_t = 7.95 \text{ km/sec}$$

$$U_p = 9.34 \text{ km/sec}$$

$$E_t - E_{t0} = 1/2 U_t^2 = 5.45 \times 10^{10} \text{ erg/g}$$

$$E_p - E_{p0} = 1/2 U_p^2 = 4.35 \times 10^{10} \text{ erg/g}$$

$$\rho_t/\rho_{ot} = 1.71$$

$$\rho_p/\rho_{op} = 1.46$$

It is now possible to ascertain the initial partition of energy between projectile and target within, of course, the limitations of the one-dimensional analysis. At the instant the entire projectile becomes engulfed by the shock compression over the length (diameter) d , the interface between target and projectile will have advanced a distance $(u_t/U_p)d = 0.353d$ into the target and the shock front in the target will have advanced a distance $(U_t/U_p)d = 0.851d$ from the face of the target. The total mass of the engulfed projectile will be $\rho_{op}d = 2.75d \text{ g/cm}^2$, while $\rho_{ot}(U_t/U_p)d = 2.44d \text{ g/cm}^2$ of target material will be consumed by the shock compression. The increase in internal energy for the projectile is $1/2\rho_{op}u_p^2d = 1.2d \times 10^{11} \text{ erg/cm}^2$ and for the target $1/2\rho_{ot}(U_t/U_p)u_t^2d = 1.33d \times 10^{11} \text{ erg/cm}^2$. The kinetic energy in the compressed target medium will also be $1.33d \times 10^{11} \text{ erg/cm}^2$, while the residual kinetic energy in the projectile, traveling at a velocity u_t relative to the undisturbed target will be $1/2\rho_{op}u_t^2 = 1.5d \times 10^{11} \text{ erg/cm}^2$. A summation of these energies gives $1/2\rho_{op}V_1^2d = 5.36d \times 10^{11} \text{ erg/cm}^2$, the kinetic energy of the original undisturbed projectile material.

²The NTS basalt has a density of $\rho_o = 2.68 \text{ g/cm}^3$. The basalt employed in the experiments has a density of 2.86 g/cm^3 ; the latter value has been used in the calculations.

ENERGY PARTITION IN BASALT

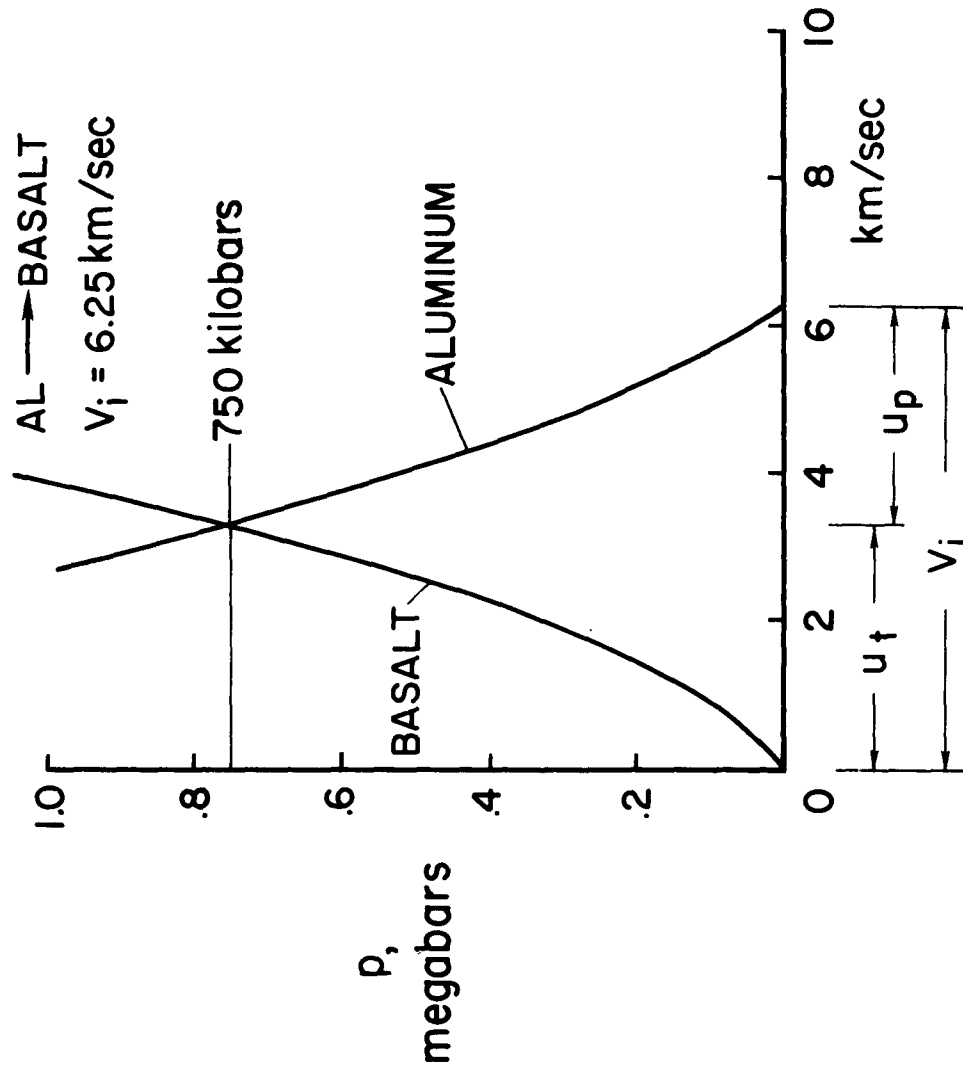


Figure 3.- Graphical solution for determining pressure and mass velocities for one-dimensional impact of dissimilar materials.

ENERGY PARTITION IN BASALT

A summary of the initial partition of energy for the Al into basalt at 6.25 km/sec is given in the following table:

	<u>Energy</u>	<u>Percent of original projectile kinetic energy</u>	
Projectile	Internal, $E_p - E_{po}$	22.3	50.2
	Kinetic, $1/2\rho_p u_t^2$	27.9	
Target	Internal, $E_t - E_{to}$	24.9	49.8
	Kinetic, $1/2\rho_t u_t^2$	24.9	

It should be noted that general algebraic expressions for the initial energy partition can be given if the energy retained by the projectile is considered to be (in normalized form)

$$\frac{\text{Energy retained by projectile}}{1/2\rho_{op}V_i^2} = \frac{u_p^2 + u_t^2}{(u_p + u_t)^2} = \frac{1 + (u_p/u_t)^2}{(1 + u_p/u_t)^2} \quad (13)$$

so that the fraction of the original projectile kinetic energy delivered to the target becomes

$$\frac{\text{Energy delivered to target}}{1/2\rho_{op}V_i^2} = \frac{2u_p/u_t}{(1 + u_p/u_t)^2} \quad (14)$$

Although the energy delivered to the target is equally split between the increase in internal energy and the kinetic energy of the compressed mass behind the shock front, the energy retained by the projectile is composed of residual kinetic energy,

$$\frac{\text{Residual projectile kinetic energy}}{1/2\rho_{op}V_i^2} = \frac{1}{(1 + u_p/u_t)^2} \quad (15)$$

and the increase in internal energy

$$\frac{\text{Projectile internal energy}}{1/2\rho_{op}V_i^2} = \left(\frac{u_p/u_t}{1 + u_p/u_t} \right)^2 \quad (16)$$

ENERGY PARTITION IN BASALT

Equations (13) and (14) clearly indicate that, except for the special case involving impacts of similar materials for which $u_p = u_t = 1/2V_i$ (see eq. (12)), the energy retained by the projectile will never be equal to that transferred to the target. For the particular case in which the projectile density is much greater than the target density, say Fe into the basalt, u_t becomes large compared to u_p and the fraction of energy transferred to the target becomes relatively smaller (eq. (14)). Moreover, within the projectile, the increase in internal energy becomes less and most of the original kinetic energy is retained in kinetic form by the compressed projectile material. Results similar to the previous tabulation for Fe into basalt at 6.25 km/sec are tabulated below:

	<u>Energy</u>	<u>Percent of original projectile kinetic energy</u>	
Projectile	Internal, $E_p - E_{op}$	10.5	56.2
	Kinetic, $1/2\rho_p u_t^2$	45.7	
Target	Internal, $E_t - E_{ot}$	21.9	43.8
	Kinetic, $1/2\rho_t u_t^2$	21.9	

For these calculations $U_p = 3.75 + 1.66u_p$ (ref. 9) and $\rho_o = 7.85 \text{ g/cm}^3$.

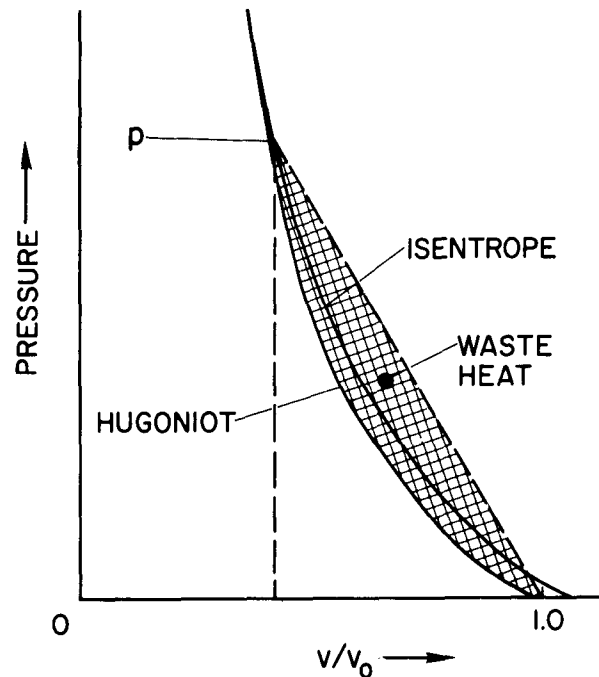
The summary tabulations and equations (13) through (16) demonstrate just one of the errors in equating projectile kinetic energy to specific internal energy in the projectile material for an "explosive" impact.

Irreversible Heating

The conditions following the initial partition of energy for an impact are roughly analogous to those occurring after an abrupt removal of a steady force which has bodily accelerated and compressed a simple coil spring along its longitudinal axis. Once the external accelerating force has been removed from the spring, the internal forces produced by the stresses set up in the compressed coils are unopposed and will cause the spring to expand back to its original length. In the somewhat analogous situation, once the projectile is totally engulfed by the shock wave racing out from the projectile-target interface, the internal forces arising from the compressive stresses in the shocked material are unopposed at the free surface of the back of the projectile and will cause the compressed mass to expand. The expansion is accomplished by pressure release (i.e., rarefaction) waves which propagate back into the shocked material and relieve the stresses to zero.

ENERGY PARTITION IN BASALT

The expansions for both the spring and impact, of course, are capable of doing useful work. It is to be noted that for the particular case of an impact, any internal energy expended as useful work during the expansion of the compressed mass reduces the energy which can be ultimately deposited thermally at the zero pressure state. This point can be illustrated with the aid of the accompanying sketch. The sketch shows schematically a Hugoniot curve and a pressure release curve for an isentropic ($dS = 0$)



Sketch (b)

rarefaction wave relieving the pressure from p_1 to zero. In contrast to the Hugoniot, the isentrope describes a continuous process. The useful work done by the expansion, therefore, is represented by the cross-hatched area below the isentrope. Since the shock compression increases the internal energy by an amount equivalent to the triangular area indicated by the dashed lines, there is effectively a "hysteresis loop" in the compression-release cycle for the target and projectile materials which contribute energy for irreversible heating of the shocked media. Thus, not only is the increase in internal energy in, say, the projectile, a fraction of the original projectile kinetic energy (as previously discussed), but only a fraction of the fractional increase is ever made available for fusing and/or vaporizing target and projectile material. The concept of "explosive" impact totally ignores both the initial partition of energy and the energy returned as useful work during the expansion of the shock compressed mass.

ENERGY PARTITION IN BASALT

For the present analysis of the impact of Al into basalt, the one-dimensional model from the previous section provides a convenient basis for estimating the energy deposited irreversibly as heat in the projectile. Under the assumption of one-dimensional flow and having a complete p, v, E, s equation of state, it has been shown by Rice, et al. (ref. 12) that the pressure p_a along any adiabatic release curve can be obtained from the integration of the linear first-order differential equation

$$\frac{dp_a}{d\bar{v}} + \frac{\gamma}{\bar{v}} \left[1 + \frac{d}{d\bar{v}} \left(\frac{\bar{v}}{\gamma} \right) \right] p_a = \frac{dp_h}{d\bar{v}} + p_h \left(\frac{\gamma}{\bar{v}} \right) \frac{d}{d\bar{v}} \left(\frac{\bar{v}}{\gamma} \right) - \frac{\gamma}{\bar{v}} \frac{dE_h}{d\bar{v}} \rho_0$$

Here, the subscripts a and h denote conditions on, respectively, the pressure release and Hugoniot curves with $\gamma = \gamma(\bar{v})$ the Grüneisen ratio and $\bar{v} = \rho_0/\rho$ the ratio of specific volumes. Rice, et al. (ref. 12) and Walsh and Christian (ref. 8) have presented results for 24ST aluminum for expansion from 513 kbars and 350 kbars, respectively. Additional calculations have been carried out by the authors for other pressures. Once $p_a = p_a(\bar{v})$ is known, the $p v$ work done by the expansion to zero pressure is easily calculated, and the residual internal energy irreversibly trapped in the projectile, ΔE_p , is found from

$$\Delta E_p = \frac{1}{2} u_p^2 - (p v \text{ work})$$

The results for ΔE_p normalized with respect to the original increase in internal energy, $E_p - E_{p0} = 1/2 u_p^2$, are shown in figure 4 as a function of the impact velocity, V_i . For the impact velocity of 6.25 km/sec, 8.2×10^9 erg/g, or only 19 percent of the increase in the projectile specific internal energy, is expended for irreversible heating. This corresponds to only 4 percent of the original projectile kinetic energy.

With a mean value for the specific heat of 10^7 erg/g/°C, sufficient energy, however, is deposited as heat to partially melt the projectile. Incipient melting in Al occurs at a temperature of approximately 660° C, a temperature that requires 6.4×10^9 erg/g starting from a nominal room temperature of 20° C. Approximately 1.8×10^9 erg/g is, therefore, available for fusion. Since the heat of fusion for Al is 3.9×10^9 erg/g, the impact should fuse approximately one-half (0.46) of the projectile mass.

Although this analysis illustrates the error in equating projectile kinetic energy to an increase in the specific internal energy of the projectile, the numerical results must be considered only an approximation based on the one-dimensional flow model. Two additional important factors must be considered. For a projectile with finite dimensions, rarefaction waves will eat in from the surfaces at the lateral boundaries of the projectile. These waves will act to attenuate the intensity of the shock

ENERGY PARTITION IN BASALT

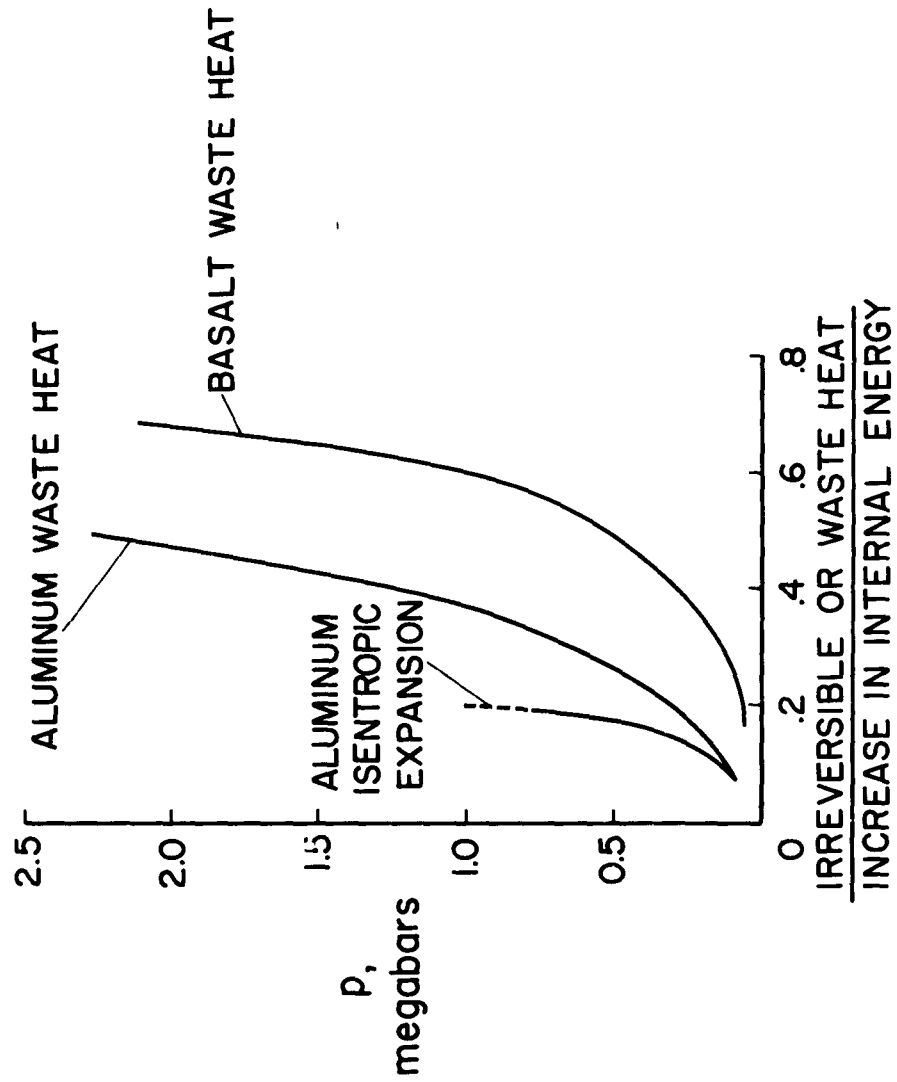


Figure 4.- The variation of irreversible and waste heat with pressure.

ENERGY PARTITION IN BASALT

compression and, at the same time, strong pressure gradients within the projectile will cause material to flow laterally away from the point of impact. It is this lateral flow which effectively turns the projectile "inside out" and plates the projectile material on the interior of the embryonic crater (ref. 13). The reduction in the intensity of the shock pressures, of course, will tend to reduce the energy ultimately converted to heat. On the other hand, considerable energy will be expended in doing work against the viscous forces arising within the semiplastic or fluid mass flowing laterally toward the free surfaces of the projectile.

Evidence for the significance of shear stresses as a means of expending energy has been presented by Moore, et al. (ref. 14) for the case of a steel projectile impacting (4.25 km/sec) Coconino sandstone obtained from the site of the Arizona meteor crater. Less than 5 percent of the energy required to fuse the projectile could have been supplied by the shock compression, yet approximately 10 percent of the projectile mass (most of which was recovered in the ejecta) was obviously melted as a result of the impact. The total energy expended as heat in the steel projectile, therefore, must have been at least two to three times greater than the energy calculated from one-dimensional shock theory.

Similar effects unquestionably would occur as the result of the Al impact in basalt at 6.25 km/sec, but there is, unfortunately, no simple basis upon which to estimate the over-all results. In the absence of a more rigorous means for taking into account the counterbalancing effects of the rarefaction waves and the viscous dissipation of energy, the factor of 3 indicated by the experimental results for the steel into Coconino sandstone will be arbitrarily invoked for establishing an upper limit for the energy trapped as heat in the aluminum. By this means, it is suggested that perhaps as much as 60 percent of the increase in the specific internal energy in the aluminum was trapped as heat. This increase in energy would be adequate to fuse the entire projectile and vaporize approximately 14 percent of the projectile mass. Such a result is consistent with both optical and electron microscopic examination of the ejecta recovered from the impacts. No fragments of the projectile could be identified in the ejecta recovered from the impacts at 6.25 km/sec. Ample evidence for melting was present, however, in the form of submicron spherules, the shape only a true liquid would assume under the action of surface tension.

Turning now to the target, the calculation of the irreversible heating is beset with two problems. The first and most serious problem is the lack of a thermodynamic equation of state for the basalt, or, in fact, for any rock. Specifically, without some knowledge of the decompression isentropes which depend on a complete thermodynamic description of the material, it is impossible to calculate either the internal energy which can be recovered as useful work, or the energy which would be spent as irreversible heat.

To circumvent this lack of a thermodynamic description of the basalt equation of state, the concept of "waste heat" will be employed as a means for estimating the irreversible heating of the target medium (ref. 15). In so doing, the Hugoniot curve is taken as an approximation for the expansion isentrope (see sketch (b)).

ENERGY PARTITION IN BASALT

With the Hugoniot curve approximation for the expansion isentrope after a material is shocked to a pressure p , it can be shown that the energy for irreversible heating (waste heat) can be expressed

$$\Delta E_t = \frac{1}{2} u^2 \left\{ 1 - 2 \left[\frac{a}{bu} + \left(\frac{a}{bu} \right)^2 \log \left(\frac{a}{a + bu} \right) \right] \right\} \quad (17)$$

where the relationship given as equation (11) can be used to express $u = u(p)$. An alternative form which will be useful later in the discussion is

$$\Delta E_t = \frac{1}{\rho_0} \frac{1}{2} p \eta - \left(\frac{a}{b} \right)^2 \left[\frac{b \eta}{1 - b \eta} + \log(1 - b \eta) \right] \quad (18)$$

with

$$\eta = 1 - \frac{v}{v_0} = 1 - \frac{\rho_0}{\rho}$$

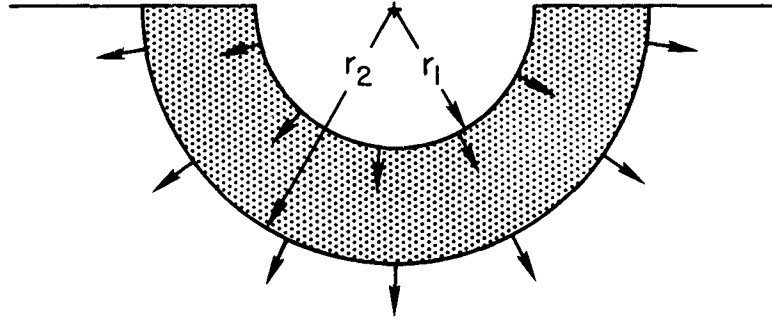
Results for the basalt are shown in figure 4. Although this procedure will overestimate the energy trapped irreversibly in a metal (as shown in fig. 4 for the aluminum) the overestimation is only a factor of 2 and, in effect, will probably account for the additional energy spent against viscous forces as previously discussed. The "waste heat" approximation is probably most valid for rocks, however, and particularly for porous media such as pumice, tuff, sand, and sandstone. These latter materials, because of the intergranular pore spaces, return after the compression-release cycle to a higher density than their original unshocked values.

In contrast to the projectile for which a given mass is shocked to a nominal pressure and then decompressed, only a small fraction of the target mass which is engulfed by shock attains the nominal pressure calculated from the one-dimensional model. The radial propagation of the shock away from the point of impact into the target will tend to smear the energy of the impact through a progressively increasing mass of target material. Since the total energy within the shock system must remain constant (or decrease as the result of ejecta thrown out of the transient cavity), the specific energy behind the shock must decrease as the wave engulfs more and more mass. The shock pressures, therefore, must decrease with increasing distance from the point of impact and the heat deposited irreversibly at any point in the target becomes a function of the distance from the point of impact. An estimate for the irreversible heating of the target, therefore, depends on the pressure decay and, interdependently, the pressure decay depends on the consumption of the available energy by the irreversible heating.

It will be instructive at this point to neglect the irreversible heating at first and consider two simplified cases for the pressure decay.

ENERGY PARTITION IN BASALT

Toward this end, reference is made to an adaptation of the Charters and Summers (ref. 16) ballistic model of cratering, as illustrated in the sketch. Here the shock front, assumed hemispherical in form, has propagated outward from the point of impact a distance r_2 into the target



Sketch (c)

medium. The radius of the transient cavity is r_1 and the mass in the hemispherical shell of thickness $(r_2 - r_1)$ is

$$\frac{2}{3} \pi \rho_0 r_2^3$$

For simplicity and following Charters and Summers, the pressure or stress is assumed constant within the shell of compressed material. Then, if the energy delivered to the target is E_t and this energy is uniformly distributed throughout the compressed mass behind the shock front, one can write

$$E_t = \rho_0 \frac{2}{3} \pi r_2^3 p (v_0 - v) = \frac{2}{3} \pi r_2^3 p \eta \quad (19)$$

where $p(v_0 - v)$ is the specific energy added to the mass $\rho_0 (2/3) \pi r^3$ by the shock compression to a pressure p . For the special case in which the Hugoniot is linear

$$p = c\eta$$

with c equal to a constant, the total energy becomes

$$E_t = \frac{2}{3} \pi r_2^3 \frac{p^2}{c} \quad (20)$$

so that

$$p \sim r^{-3/2} \quad (21)$$

ENERGY PARTITION IN BASALT

When an experimental Hugoniot is inserted in equation (19)

$$E_t = \rho_0 \frac{\pi}{3} r_2^3 \left[\frac{2p}{\rho_0 b} + \left(\frac{a}{b} \right)^2 - \frac{a}{b} \sqrt{\frac{a^2}{b} + \frac{4p}{\rho_0 b}} \right] \quad (22)$$

and one finds that for high pressures, say $p > 1$ mbar, the pressure variation tends to

$$p \sim r^{-3} \quad (23)$$

while in the lower range, $p > 100$ kbar, the pressure variation with r tends toward the inverse $3/2$ relationship. In both cases (eqs. (21) and (23)) the length of the wave, that is, the distance $(r_2 - r_1)$, would increase as the pressure decreases in accordance with physical reality, but the model is obviously an oversimplification of the actual cratering process, since rarefaction waves would preclude maintaining the entire shell at a pressure p . Nevertheless, the model is useful in showing how the spherical divergence of the shock front produces a rapid decay in the pressure with distance from the point of impact. Ultimately, of course, the front decays into simple elastic waves and it is to be noted that Rinehart (ref. 17) has shown that for an elastic wave of constant length, velocity, and shape, the pressure decays inversely with the first power of the radial distance.

It should be expected that incorporating the effects of irreversible heating in the model should accelerate the decay of the pressures relative to the preceding examples, particularly at the higher pressures for which the irreversible heating becomes a major fraction of the increase in internal energy. This can be shown rather easily if one considers that as the shock front engulfs a differential mass

$$\rho_0 \pi r^2 dr$$

energy is deposited in the differential mass irreversibly, making use of equation (18), in the amount of

$$\rho_0^2 \pi r^2 \Delta E_t dr$$

The total energy expended by this process would be

$$E_w = 2\pi\rho_0 \int_0^r \Delta E_t r^2 dr$$

ENERGY PARTITION IN BASALT

Since the pressure will remain approximately constant while the projectile is being consumed by shock, this irreversible energy expenditure (waste heat) can be recast into a more convenient form

$$E_w = \frac{2}{3} \pi \rho_0 r_0^3 \Delta E_{t1} + 2\pi \rho_0 \int_{r_0}^r \Delta E_t r^2 dr$$

where it is to be understood that r_0 is the effective radius of the plug of compressed target material which has been subjected to an increase in the specific internal energy ΔE_{t1} during the initial partition of energy. An energy balance similar to those in equations (19) and (22) can be written, therefore, as

$$E_a = E_t - E_w \quad (24)$$

with

$$E_a = \frac{2}{3} \pi r^3 \left\{ \frac{1}{2} p\eta + \rho_0 \left(\frac{a}{b} \right)^2 \left[\frac{b\eta}{1 - b\eta} + \log(1 - b\eta) \right] \right\}$$

$$E_t = \frac{2}{3} \pi r_0^3 p\eta$$

$$\eta = \frac{1}{2} \frac{\rho_0}{p} \left[\frac{2p}{b\rho_0} + \left(\frac{a}{b} \right)^2 - \left(\frac{a}{b} \right) \sqrt{\left(\frac{a}{b} \right)^2 + \frac{4p}{b\rho_0}} \right]$$

Here the energy available for doing useful work in furthering the propagation of the shock through the target has been equated to the difference between the total energy input and the energy lost by irreversible heating.

An explicit solution of equation (24), an integral equation, cannot be obtained for the variation of pressure with radial distance. A numerical solution has been obtained,³ however, and the results are shown in figure 5, together with the previously discussed $p = p(r)$ variations. With an eye to what follows, the pressure p is presented in all three cases in terms of the dimensionless parameter r/r_0 where r_0 is, as previously indicated, the effective radius of the compressed target mass at the end of the initial partition of energy.

As expected, the pressure decays more rapidly when consideration is given to the energy deposited irreversibly in the target. At the initial shock pressure of 750 kbars, the pressure varies approximately with $r^{-3.6}$

³The authors are indebted to Paul F. Byrd of the NASA Ames Research Center for this solution.

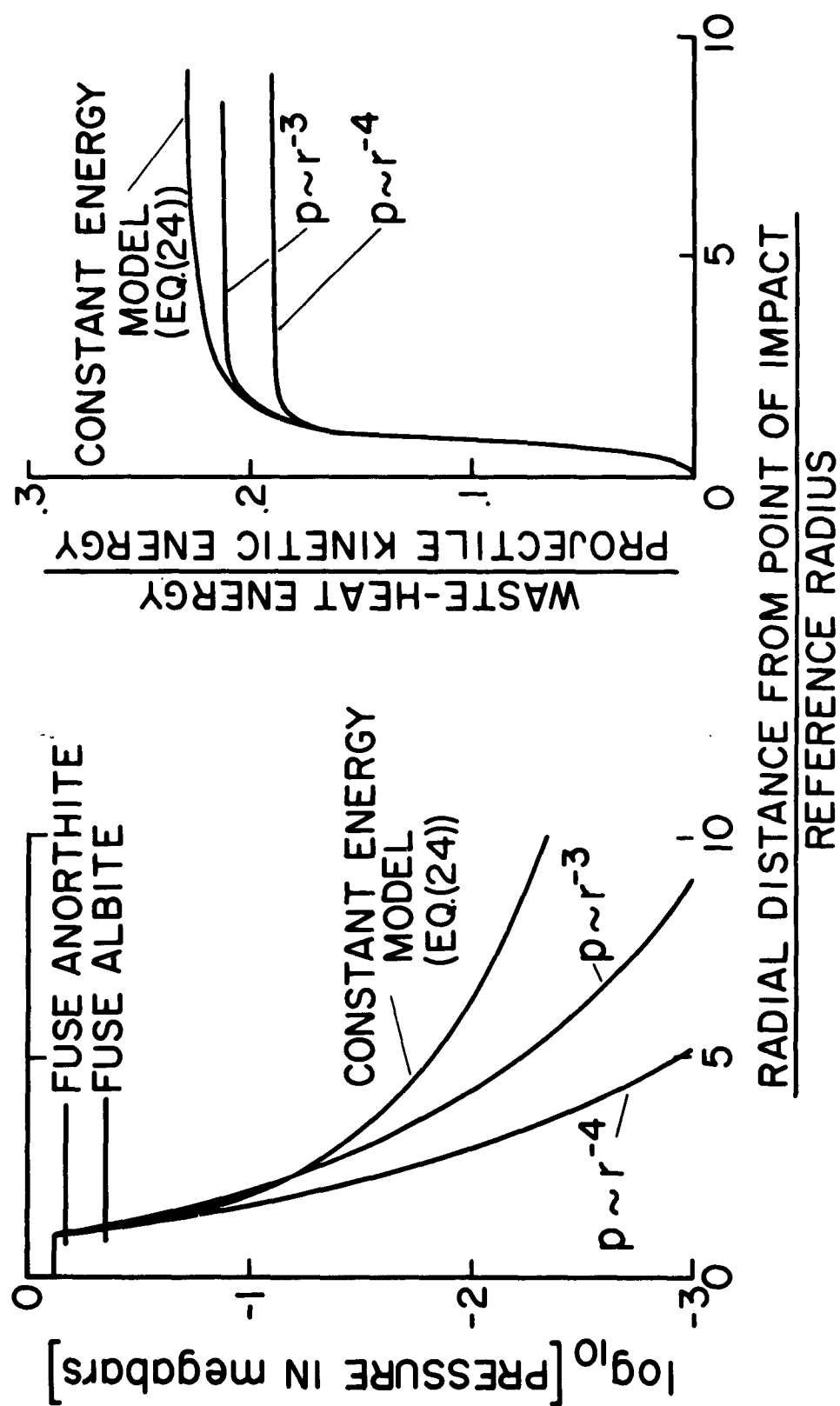


Figure 5.- The radial pressure decay and waste heat in basalt target.

ENERGY PARTITION IN BASALT

with waste heat removed from the system (eq. (14)) while the neglect of the waste heat (eq. (12)) yields an $r^{-2.6}$ variation. By the time the pressure has decayed to 100 kbars, these variations have become, respectively, $r^{-2.6}$ and $r^{-2.0}$. At still lower pressures, both calculated results tend toward the $r^{-1.5}$ variation.

It should be pointed out that at pressures lower than about 100 kbars, a multiple wave structure probably occurs in the basalt as a result of material rigidity and the possibility of phase changes in the constituent minerals. In the spirit of the present analysis, however, the presence of multiple waves can be neglected; the computed pressures should be approximately equal to the total pressure jump across one or more waves and the existence of multiple waves would not alter the significant result that waste heat deposited in the target acts to accelerate the decay of pressure with distance from the point of impact.

To estimate the irreversible heating in the basalt target, it should be remembered that, subsequent to the initial penetration of the projectile into the target, rarefaction waves will eat in from the free surface of the interior of the embryonic crater. These waves will attenuate the strength of the shock front even more rapidly than that indicated by equation (24), which is based on a model of cratering which assumes a shell of compressed material with no radial pressure gradients. Since the waste heat decreases with decreasing shock-wave strength, the attenuation of the shock front brought about by the rarefaction waves will reduce the total amount of waste heat which can be deposited in the target as compared to that calculated from equation (24). Thus, although based on a simplified cratering model, equation (24) nevertheless provides a means for estimating the maximum amount of energy deposited irreversibly in the target.

The numerical results calculated for the waste heat from equation (24) are shown in figure 5 normalized with respect to the projectile kinetic energy. For purposes of illustrating the potential attenuating influence of rarefaction waves, results are also presented for two special cases for which $p \sim r^{-3}$ and $p \sim r^{-4}$. It is to be noted that whereas equation (24) corresponds to a conservative system, the two exponential pressure variations represent systems in which the total energy content decreases as the shock front propagates radially outward.

The comparison shown in figure 5 is significant to the present analysis from three considerations. First, it is apparent that the steeper the radial pressure gradient, the less energy is lost irreversibly, as pointed out in a previous paragraph. Second, the major fraction of the irreversible heating occurs during the initial partition of energy (16 percent of the projectile kinetic energy for $r/r_0 < 1.0$) and most of the remaining fraction occurs within a short distance of the original point of impact ($1.0 < r/r_0 < 2$). Finally, the total amount of energy lost to waste heat is relatively insensitive to the choice of radial pressure gradients, varying from a maximum of 23 percent of the projectile kinetic energy for

ENERGY PARTITION IN BASALT

equation (24) to a minimum of 19 percent of the projectile kinetic energy for $p \sim r^{-4}$. For the present analysis, a range of 19 to 23 percent will be adopted, therefore, for the energy lost to irreversible heating in the target.

The peak specific irreversible heating, amounting to 56 percent of the increase in specific internal energy, is 3×10^{10} ergs/g. This is more than adequate to fuse the mineral constituents of the basalt. Two of these minerals, for example, anorthite and albite, require approximately 1.7×10^{10} and 1.2×10^{10} ergs/g for fusion, respectively. The energy in excess of that required for fusion is insufficient, however, to vaporize these target materials.

Because the specific irreversible heating decreases rapidly with decreasing shock pressures, the radial limits for fusion in the target are attained very quickly as the shock strength decays with radial distance. Figure 6 suggests that the limit of fusion is reached when r/r_0 has a value of about 1.10. From the cube of this value (the ratio of the mass of fused target material to the mass of target material engulfed by shock at the termination of the initial partition of energy) multiplied by the ratio of 2.44d/2.75d (see eq. (1)), it is estimated that approximately one projectile mass of target material was fused by the impact. Evidence for this melting in the form of submicron spherules, as mentioned previously, was found in the ejecta recovered from the impacts.

Comminution Energy

Although the strength of the shock wave propagating from the point of impact decays rapidly below the level commensurate with the deposition of a significant amount of irreversible heat energy, the pressure behind the shock front nevertheless persists at a high level relative to the strength of the basalt for a considerable distance into the target. Ultimately, of course, the shock wave decays into elastic waves traveling at the appropriate acoustic velocities for the material, but not before an appreciable mass is subjected to stresses of sufficient magnitude to completely fragment and crush the basalt into fine debris. The energy expended for the comminution of the target medium consumes an important fraction of the projectile kinetic energy.

Before undertaking the calculation of the energy requirements for crushing the basalt, however, it is interesting to note that it is possible to make a reasonable estimate of the mass of material which is crushed as the result of the impact. The compressive strength (unconfined) of the basalt has been determined by conventional static tests to be between 2 and 3 kbars. Grine and Fowles (ref. 18) have indicated that the dynamic strengths of rocks are usually several times greater than static strengths and may be as much as an order of magnitude greater than the static strength. On this basis, therefore, adopting a mean value of 2.5 kbars for the static compressive strength, the dynamic compression strength for the macroscopically

ENERGY PARTITION IN BASALT

homogeneous basalt employed for these studies would be expected to be between 8 and 25 kbars. For the calculated pressure variation with radial distance shown in figure 5, these pressures are attained for values of r/r_0 between 3.7 and 7. Since r_0 is approximately equal to the radius of the projectile and the projectile and target densities are also approximately equal, it would be expected that a mass of basalt between 50 (the cube of 3.7) and 350 times the mass of the projectile would be crushed by the impact.

Now it has been found, from the experiments, that a total of approximately 370 projectile masses of debris are ejected from the craters for impacts at 6.25 km/sec. Most of this ejected mass consists of large spall plates which occur as the result of shear and tensile failures by the action of rarefaction waves eating in from the free surface of the target face. Between 1/3 to 1/4 of the ejected mass, however, is composed of particles finer than 1 mm, and an approximately equal mass of crushed material forms a lens of fragments at the bottom of the crater. Experimentally, therefore, a mass of crushed fragments of the order of 200 times the projectile mass was produced by the impacts in satisfactory agreement with the estimates based on consideration of the dynamic strength and the pressure decay shown in figure 5. It is to be noted that the use of a target strength of 2.5 kbars, the static value, leads to an unrealistic estimate of 3,000 projectile masses crushed by the impact.

The energy expended for fracturing and crushing the basalt target material will be calculated by two methods. The first and probably the most satisfactory method is based on calculations of the new surface area of the fragmented material. Experimentally determined cumulative mass-size distributions of the fragmented material reported by Gault, et al. (ref. 6) have shown that a simple comminution law

$$\frac{m}{M_e} = \left(\frac{l}{L} \right)^\alpha \quad (25)$$

can be used to describe the size distribution of the basalt fragments. Here m is the cumulative (integrated) mass of fragments with a size equal to or smaller than l , M_e is the total mass ejected from the crater, L is the size of the largest fragment, and α is a constant. This expression has been shown to be valid (ref. 6) over a size range 40 microns $< l < L$ with values of $0.3 < \alpha < 0.6$. For fragments smaller than 40 μ , the exponent α gradually increases as l approaches what seems to be a cutoff at a minimum size l_m . The cutoff for the present experiments appears to be about 0.1 micron.

To calculate the new surface area, A , created by the fragmentation of the target basalt, a modified form of equation (25) is introduced.

$$\frac{m}{M_e} = \left(\frac{l - l_m}{L} \right)^\alpha \quad (26)$$

ENERGY PARTITION IN BASALT

where it is to be understood that $l_m \ll L$, so that when $l = L$

$$\frac{m}{M_e} = \left(\frac{L - l_m}{L} \right)^\alpha \approx 1$$

Taking the derivative of equation (26) one obtains the differential mass of fragments dm with fragment sizes between l and $l + dl$

$$dm = \alpha M_e L^{-\alpha} (l - l_m)^{\alpha-1} dl \quad (27)$$

Then, when dN is defined as the number of fragments with sizes between l and $l + dl$ there results

$$dm = (K_m \rho l^3) dN \quad (28)$$

with K_m a constant that depends on the geometry of the fragments. Similarly, when dA is defined as the surface area of the dN number of fragments,

$$dA = (K_a l^2) dN \quad (29)$$

with K_a another geometrical constant. Combining these last three equations, the new surface area A can be expressed

$$A = \left(\frac{K_a}{K_m} \frac{\alpha M_e}{\rho L^\alpha} \right) \int_{l_m}^L \frac{(l - l_m)^{\alpha-1}}{l} dl \quad (30)$$

A solution for A in explicit form can be obtained only for certain values of α . For the present analysis, a conservative value of $\alpha = 1/2$ is appropriate and leads to

$$A = \frac{\pi}{2} \frac{K_a}{K_m} \frac{M_e}{\rho L} \left(\frac{L}{l_m} \right)^{1/2} \quad (31)$$

To evaluate equation (31) numerically, it will be noted that K_a/K_m has a value of 6 for spherical and cubic particles. For rectangular or approximately equidimensional blocks or plates representative of the finer fragments which contribute most of the area, values of 5 to 7 for K_a/K_m are appropriate. A value of 6, therefore, will be adopted herein.

The mass M_e for the present case of Al into basalt at 6.25 km/sec is approximately 17 g; L can be taken (ref. 6) as 1.7 cm, and $\rho_o = 2.86 \text{ g/cm}^3$. With a cutoff size $l_m = 10^{-5}$ cm, the surface area of the ejecta produced by the impacts becomes

ENERGY PARTITION IN BASALT

$$A = 1.4 \times 10^4 \text{ cm}^2$$

More than 90 percent of this area is contributed by particles finer than 2×10^{-3} cm. Since the grain size⁴ of the minerals in the basalt is almost exclusively between 2×10^{-2} cm and 2×10^{-3} cm, the area is produced by the fragmentation of individual mineral grains, chiefly plagioclase feldspar and augite.

Morrison and Allen (ref. 19) have found that 5.9×10^4 ergs/cm² were required to crush a limestone sand by impact at velocities from 0.81 to 0.95 km/sec. Remarkably similar results have been reported by Zeleny and Piret (ref. 20) for drop weight crushing of multiple quartz grains, 7.3×10^4 ergs/cm². Although there are differences in loading rates and specific energies between the two sets of data, the lower value for the limestone might be expected, since calcite, the principal constituent of a limestone, has well-defined cleavage planes which should tend to reduce its work input per unit area requirements relative to quartz. Plagioclase feldspar and augite are similar to calcite in this respect. Since they comprise⁵ approximately 85 percent by both mass and volume of the basalt, it would seem that the data of Morrison and Allen are probably the most applicable to the present analysis. In view of the uncertainties, however, a mean value of 6.6×10^4 ergs/cm² will be adopted for estimating the energy required for fracturing and crushing.

With a new surface area of 1.4×10^4 cm², the energy expenditure becomes 9.2×10^8 ergs for the ejected mass of 17 grams. The projectile kinetic energy is 9×10^9 ergs, so that approximately 10 percent of the kinetic energy reservoir was extracted for the comminution of the ejecta.

The impacts break up considerably more mass than the fragments thrown out of the crater. The bottom of the crater, as previously mentioned, consists of a lens of finely crushed and packed debris. In addition, there is an extensive series of radial concentric fractures within and beyond the geometric limits of the cavity, as described by Moore, et al. (ref. 5) at the 5th Hypervelocity Impact Symposium. The surface area and mass of material involved cannot be estimated with any great accuracy but certainly these quantities do not exceed those for the ejected material. On this basis it is believed that the total energy for fracturing and crushing the basalt is greater than 10 percent but could not exceed 20 percent of the projectile kinetic energy.

The percentage values for the comminution energy for the basalt are smaller than the 33 to 40 percent quoted by Morrison and Allen (ref. 19) for the impacts in the limestone sand. The difference is probably attributable to the difference in the impact velocities. In marked contrast to Morrison and Allen's low-speed impact results, 19 to 23 percent of the projectile kinetic energy is lost via irreversible heating of the basalt.

⁴Based on petrographic examination by Henry J. Moore, U. S. Geol. Survey, Menlo Park, Calif.

⁵Ibid.

ENERGY PARTITION IN BASALT

Most of this fraction of energy trapped as heat in the basalt would, at lower impact velocities, become available for fracturing and crushing. For this reason, the sum of comminution energy and irreversible heat energy in the target basalt, 29 to 43 percent, is a more valid basis for comparison with Morrison and Allen's results for low-speed impact.

As an alternative method for estimating the comminution energy, it is interesting to note that Innes (ref. 2), on the basis of results from nuclear explosion experiments, adopts a value of 6.4×10^7 ergs/g to calculate the energy requirements for the formation of large terrestrial meteorite craters. Innes also indicates that (in a personal communication) MacPhail has estimated 6.5×10^7 ergs/g from a study of the debris at the Arizona meteor crater. For purposes of comparison, the present analysis yields a value of 5.4×10^7 ergs/g for the material ejected from the craters in basalt. The three values, obtained by three different methods of analysis, are in surprisingly close agreement and lend support for the belief that a value of 6×10^6 ergs/g suggested by Opik (ref. 21) is unrealistically low.

Application of the values quoted by Innes gives a crushing energy from 12 to 24 percent of the original projectile energy. The 20-percent increase over the values obtained from the work input-free surface area calculations is hardly significant in view of the approximations and generalizations incorporated in the analysis. In the spirit of the analysis, however, a summarizing estimate for the comminution energy will be taken as 10 to 24 percent of the original projectile kinetic energy.

Ejecta Kinetic Energy

The analysis to this point has considered only the energy expended in altering the physical properties and state of target and projectile materials. The formation of the actual crater implies an additional energy expenditure for transporting material away from the point of impact. This energy expenditure associated with the excavation of the crater appears in kinetic form in the fragmented material set in motion by the combined effects of the shock compression and subsequent expansion. As will be shown, a major fraction of the projectile kinetic energy is consumed by this process.

In a previous report Gault, et al. (ref. 6) have presented estimates for the mass-velocity distribution and ejection angle-velocity distribution of the ejecta produced by the impacts in basalt. These data, reproduced herein as figures 6 and 7, respectively, were derived from a series of high-speed framing camera records (nominal 10^4 , 10^5 , and 10^6 frames/sec) of the impact events. The material ejected with the highest velocity, approximately three times the impact velocity, is believed to be the result of a jetting phenomenon (refs. 22-24) which ejects material from between the projectile-target interface during the earliest stages of the initial shock compression of the two media. The jetted material is ejected at

BASALT TARGETS
ALUMINUM PROJECTILES (SPHERES)
IMPACT VELOCITY, $V_i = 6.1$
TO 6.4 km/sec

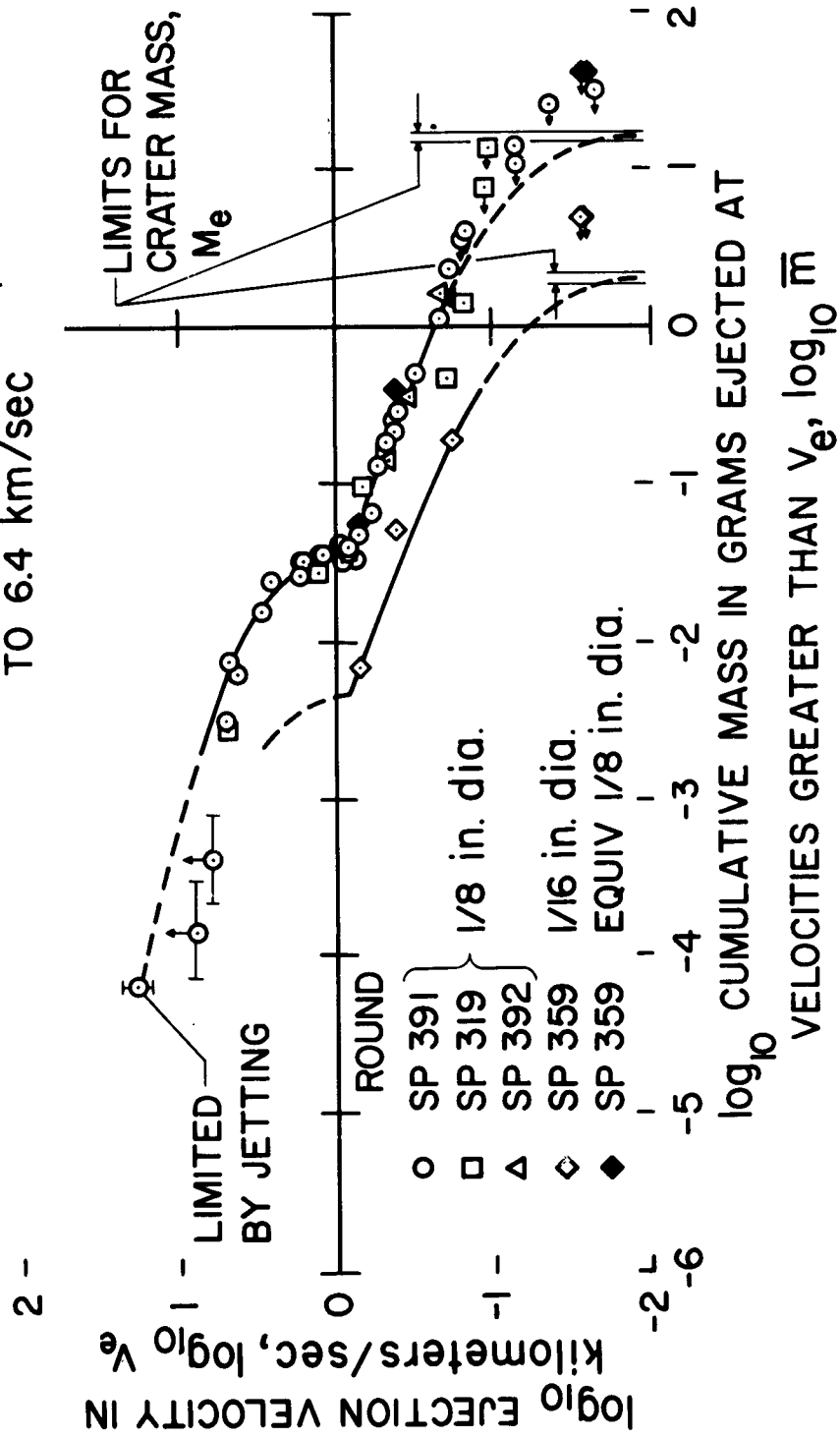


Figure 6.- Cumulative mass-velocity distributions for the ejecta from the craters formed in basalt.

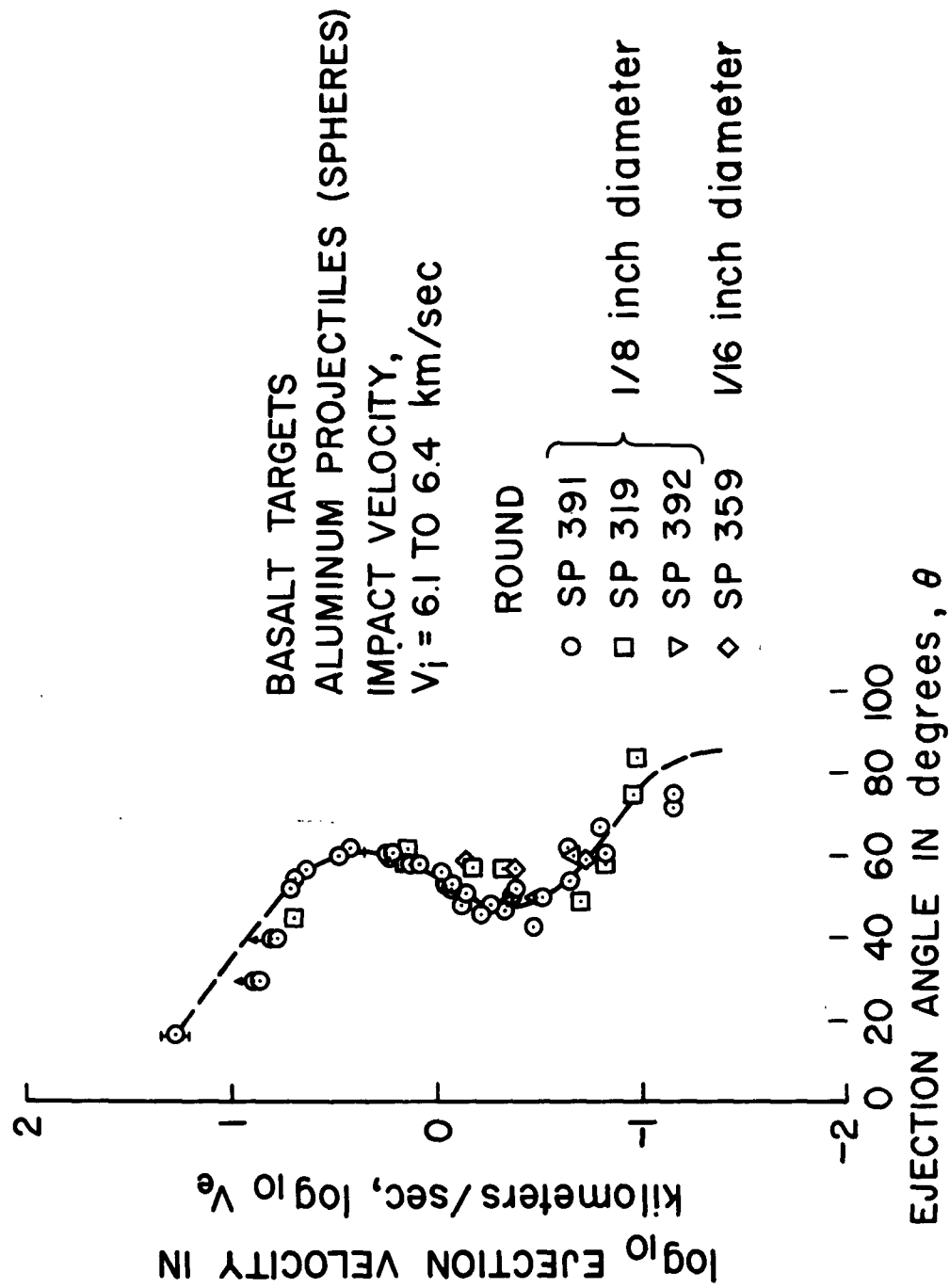


Figure 7.- Ejection angle-velocity distribution for the ejecta from craters formed in basalt.

ENERGY PARTITION IN BASALT

relatively low angles ($\theta < 30^\circ$) relative to the target face and probably consists of fused matter produced by the impact. During the subsequent stages of ejection, the velocity decays rapidly and the ejection angle increases to $\theta = 60^\circ$, decreases to about 50° , and finally tends toward 90° as the major fraction of the ejected mass leaves the crater in progressively increasing fragment sizes. The discontinuous variation in the mass-velocity distribution appears to correlate with shock pressures which are consistent with the probable dynamic compressive strength of the basalt. For this reason, the discontinuity is believed to be associated with a transition from plastic to elastic flow behind the shock front as it propagates radially outward from the point of impact.

It is to be noted that figure 6 presents the cumulative mass \bar{m} of material ejected with velocities in excess of a given value of velocity V_e . In functional form one can write

$$\bar{m} = f(V_e) \quad (32)$$

so that

$$d\bar{m} = \frac{d}{dV_e} [f(V_e)] dV_e$$

where $d\bar{m}$ is the differential mass of material ejected with velocities between V_e and $V_e + dV_e$. In this manner, the kinetic energy of the differential mass $d\bar{m}$ can be written

$$\frac{1}{2} \frac{d}{dV_e} [f(V_e)] V_e^2 dV_e$$

and the total kinetic energy contained in the mass ejected from the crater becomes

$$\frac{1}{2} \int_{V_{e\max}}^0 V_e^2 \frac{d}{dV_e} [f(V_e)] dV_e \quad (33)$$

Similarly if the ejection angle θ is expressed as

$$\theta = g(V_e)$$

the component of ejection momentum, acting normal to the target face would be

$$\int_{V_{e\max}}^0 V_e \frac{d}{dV_e} [f(V_e)] \sin [g(V_e)] dV_e \quad (34)$$

ENERGY PARTITION IN BASALT

The results obtained from a numerical integration of equations (33) and (34) using the data presented as figures 6 and 7 are shown as figure 8 in normalized form with respect to projectile values. Both the kinetic energy and the momentum are shown in terms of cumulative or integrated quantities measured from the initial mass of material jetted outward by the impact.

The numerical results indicate that 48 percent of the projectile kinetic energy is retained in kinetic form by the ejecta. Most of this energy, approximately 35 percent, is contributed by material spewed out at velocities greater than 1 km/sec. Since the fairing of the experimental data is somewhat arbitrary over the upper range of ejection velocities, several different fairings were evaluated and found to yield values for the kinetic energy content in the ejecta differing by approximately ± 5 percent of the projectile kinetic energy. On this basis, therefore, the kinetic energy for the ejected mass from the craters in basalt is taken to be from 43 to 53 percent of the projectile kinetic energy.

It is interesting to note that although not specifically concerned with the energy partition for the impacts in basalt, the calculated total momentum of the ejecta is in satisfactory agreement with results from ballistic pendulum measurements of the momentum imparted to the target blocks. In contrast to the kinetic energy, most of the momentum in the ejecta is provided by material traveling at velocities less than 1 km/sec. The scatter in the ballistic pendulum data is attributable to erratic spalling of the largest fragments thrown out of the craters. The mass of the largest fragments is between one to two orders of magnitude greater than the projectile mass while the ejection velocity is from one to two orders of magnitude less than the impact velocity. The combined effect of erratic mass and ejection velocity for large fragments, therefore, can readily produce large fluctuations in the momentum sensed by the pendulum.

Elastic Wave and Radiant Energy

Although the strong shock wave produced in the target by the impact ultimately decays into elastic waves which cause no permanent damage to the target material, the energy contained in the waves has not been considered in the preceding analysis. Evidence of such waves is demonstrated by the spallation fractures observed in the back of all the target blocks, as illustrated by figure 9. As for most rocks, the tensile strength (100 to 200 bars) of the basalt is much lower than the compressive strength (2 to 3 kbars). For this reason, any elastic compressive disturbance when reflected from the free surface of the basalt as a tension wave would produce tensile failures even though the peak compressive stresses are inadequate to produce compressive failures.

A thorough discussion of wave reflection from a free surface has been given by Rinehart (ref.17) and will be omitted here. It is sufficient to note that the spallation at the back of the target, shown in figure 9,

ENERGY PARTITION IN BASALT

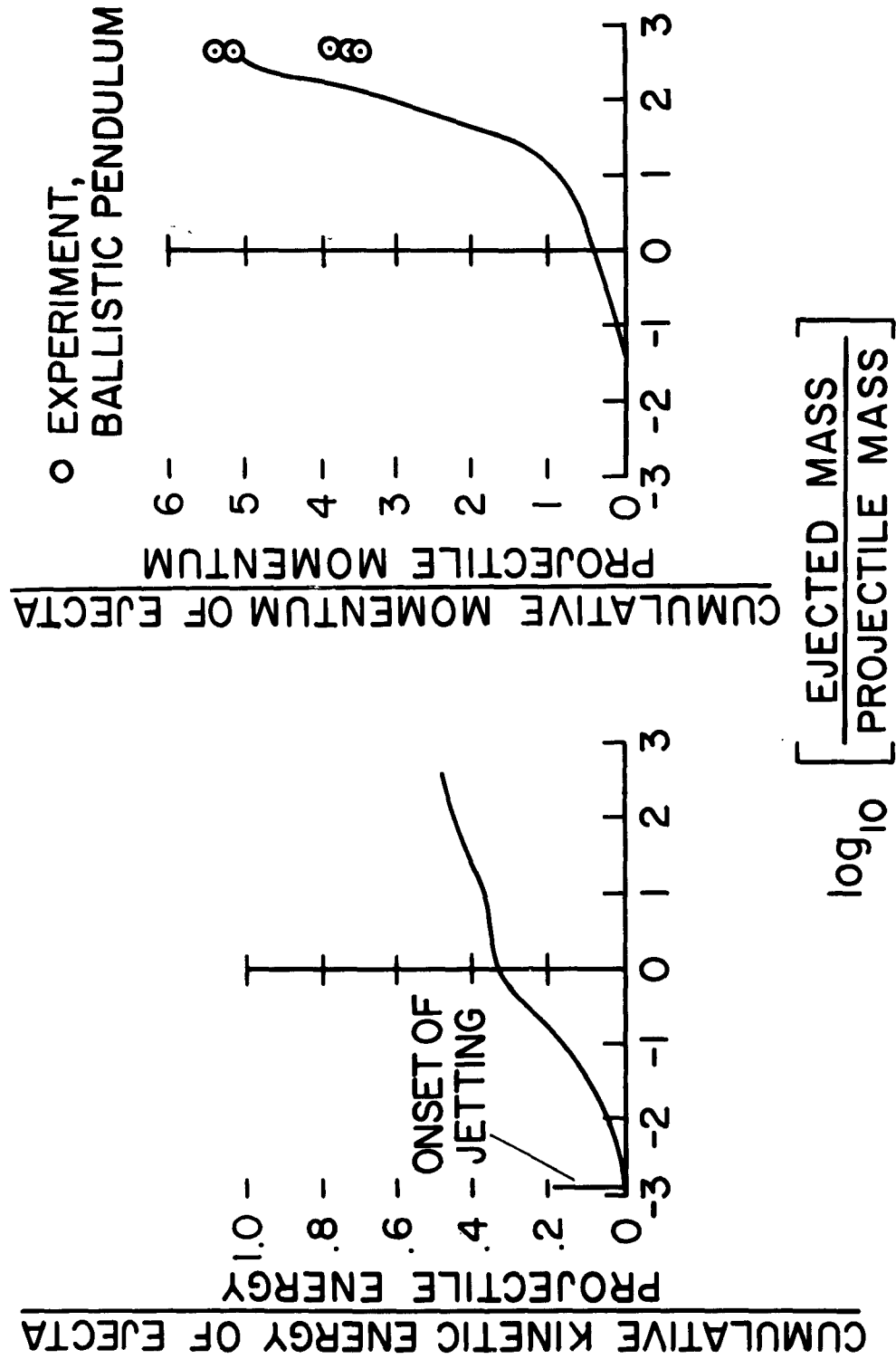


Figure 8.- Cumulative kinetic energy and cumulative momentum of the ejecta from the craters formed in basalt.



Figure 9.- Photograph of sectioned crater in basalt showing spall fractures at the back of the target block.

ENERGY PARTITION IN BASALT

indicates three spalls were produced by the impact. With a tensile strength of 200 bars, the peak stress in an incident elastic compressive wave must have been at least 600 bars and perhaps approached 800 bars. Since the distance from the free surface to the last spallation surface is 1.2 cm, the length of the compressive wave was probably between 1.2 and 1.6 cm. If the stress distribution along the wave is assumed to decrease linearly from the peak value (triangular wave shape) and the particle velocity for the peak stress is estimated by means of equation (3a) (using a density of 2.86 g/cm^3 , and the acoustic velocity of 5.5 km/sec), the total energy content of the elastic wave (taken to have a hemispherical geometry) could not exceed 1 percent of the original projectile kinetic energy.

One final method for expending energy deserves mention, the production of radiant energy associated with impact flash commonly observed in the laboratory. Results described by MacCormack (ref. 24) for the impact of Al into Al at a nominal 2.5 km/sec give a value for the total radiant energy of the order of 10^{-4} percent of the projectile kinetic energy. Although this result is based on conditions which differ in materials and impact velocity from those of the present study, the result suggests that the contribution of radiant energy for present purposes can be safely ignored. This is particularly true if the radiant energy represents a conversion of ejecta kinetic energy to light as concluded by MacCormack; consideration has been given to the ejecta kinetic energy, and the subsequent conversion or expenditure of the ejecta energy to radiant energy would be redundant for the present analysis.

CONCLUDING REMARKS

The results from the analysis of the partition of energy for the impact of aluminum into basalt are summarized in the following tabulation:

<u>Energy expended for:</u>	<u>Percentage of projectile kinetic energy</u>
(1) Irreversible and waste heat	
Projectile	4 to 12
Target	19 to 23
(2) Comminution	10 to 24
(3) Ejecta throwout	43 to 53
(4) Miscellaneous	
Residual elastic wave	less than 1
Radiant	negligible
<hr/>	
Total:	77 to 113

ENERGY PARTITION IN BASALT

The final results in terms of an energy balance indicate that the analysis has accounted for the expenditure of 95 ± 18 percent of the original projectile kinetic energy. This balance is, perhaps, entirely satisfactory in view of the uncertainties and approximations introduced during the analysis. It is believed, however, the results are somewhat better than one might judge from just a superficial examination of the tabulation. The minimum values in the table for both the comminution energy and projectile irreversible heat are unrealistically low. Better minimum value estimates would be 14 to 16 and 8 to 10 percent, respectively. With these new values, the final balance would become 100 ± 12 or 13 percent. This latter balance is believed to provide a more representative quantitative interpretation of the results.

It is interesting to note that the maximum energy expenditure required for removing material from the crater is less than 10^{-5} percent of the original projectile kinetic energy. Approximately one-half of the original reservoir of projectile energy, therefore, was wasted by ejection of debris with velocities far in excess of those required to move material beyond the geometric limits of the final crater. In addition, approximately 30 percent of the projectile kinetic energy was wasted as heat in the target and projectile. Of the remaining 20 percent of the available projectile energy, only about 10 percent can be considered to have been spent usefully in crushing the target material actually removed from the crater. Excavation of a crater by hypervelocity impact would appear to be an extremely inefficient process.

Although an estimated 30 percent of the projectile kinetic energy was expended as heat in target and projectile material, most of this heat energy was utilized for fusion and, perhaps, on the basis of a tenuous assumption, some vaporization of the projectile. The analysis and calculated results, however, clearly provide no supporting evidence for perpetrating the concept of "explosive" cratering. The craters formed in basalt occurred as the result of fracturing and crushing the target material by a mechanical shock compression followed by an ejection of the fragmented debris by the action of rarefaction waves.

Finally, attention is drawn to the fact that for higher impact velocities, the percentage of the projectile kinetic energy lost by irreversible heating will increase at the expense of the energy available for fragmentation and ejection of target material. Since higher impact velocities imply higher ejection velocities, the relative increase in irreversible heat would be at the expense of fragmentation. With constant energy input, therefore, total ejected mass and crater dimensions should decrease as the impact velocity increases. This interpretation suggests that one cannot expect a direct mass (or volume) proportionality with projectile energy throughout a wide range of impact velocities.

ENERGY PARTITION IN BASALT

REFERENCES

1. Shoemaker, Eugene M.: Impact Mechanics at Meteor Crater, Arizona. Open File Report, U. S. Geological Survey, Menlo Park, Calif., 1959.
2. Innes, M. J. S.: Gravity of Meteorite Craters. Jour. Geo. Res., vol. 66, no. 7, 1961, pp. 2225-2239.
3. Shoemaker, E. M., and Chow, E. C. T.: Impact Origin of the Ries Basin, Bavaria, Germany. Jour. Geo. Res., vol. 66, 1961, pp. 3371-3378.
4. Dietz, Robert S.: Vredefort Ring Structure: Meteorite Impact Scar? Jour. of Geol., vol. 69, Sept. 1961, pp. 499-516.
5. Moore, H. J., Gault, D. E., and Lugn, R. V.: Experimental Hypervelocity Impact Craters. Proc. 5th Symposium on Hypervelocity Impact, vol. I, pt. 2, April 1962, pp. 625-643.
6. Gault, Donald E., Shoemaker, Eugene M., and Moore, Henry J.: Spray Ejected From the Lunar Surface by Meteoroid Impact. NASA TN D-1767, 1963.
7. McQueen, R. G., and Marsh, S. P.: Equation of State for Nineteen Metallic Elements from Shock-Wave Measurements to Two Megabars. Jour. of Appl. Phys., vol. 31, no. 7, July 1960, pp. 1253-1269.
8. Walsh, John M., Rice, Melvin H., McQueen, Robert G., and Yarger, Frederick L.: Shock Wave Compressions of Twenty-Seven Metals. Equations of State Metals. Phys. Rev., vol. 108, no. 2, Oct. 1957, pp. 196-216.
9. Al'tshuler, L. V., Kormer, S. B., Bakanova, A. A., and Trunin, R. F.: Equation of State for Aluminum, Copper and Lead in the High Pressure Region. Soviet Physics JETP, vol. 11, no. 3, Sept. 1960, pp. 573-579.
10. Al'tshuler, L. V., Bakanova, A. A., and Trunin, R. F.: Shock Adiabats and Zero Isotherms of Seven Metals at High Pressures. Soviet Physics JETP, vol. 15, no. 1, July 1961, pp. 65-74.
11. Lombard, David B.: The Hugoniot Equation of State of Rocks. UCRL-6311, University of California, Lawrence Radiation Laboratory, Feb. 1961.
12. Rice, M. H., McQueen, R. G., and Walsh, J. M.: Compression of Solids by Strong Shock Waves. Solid State Physics, vol. 6, Academic Press, 1958, pp. 1-63.

ENERGY PARTITION IN BASALT

13. Charters, A. C.: High Speed Impact. Scientific American, vol. 203, 1960, pp. 128-140.
14. Moore, H. J., Gault, D. E., Lugn, R. B., and Shoemaker, E. M.: Hypervelocity Impact of Steel into Coconino Sandstone. Proc. Geophysical Laboratory - Lawrence Radiation Laboratory Cratering Symposium. UCRL-6438, Paper N, pt. II, Oct. 1961.
15. Porzel, F. B.: Close-in Shock Time-of-Arrival Measurements and Hydrodynamical Yield. Proc. Second Flowshare Symposium, UCRL-5674, pt. I, 1959, pp. 28-49.
16. Charters, A. C., and Summers, James L.: Comments on the Phenomena of High-Speed Impact. NOLR 1238, U. S. Naval Ordnance Laboratory, White Oak, Silver Springs, Md., May 25-26, 1959, pp. 200-221.
17. Rinehart, John S.: On Fractures Caused by Explosions and Impacts. Quarterly of the Colorado School of Mines, vol. 55, no. 4, Oct. 1960.
18. Grine, D. R., and Fowles, G. R.: The Attenuation of Shock Waves in Solid Materials with Seismic Applications. Third Symposium on Rock Mechanics, Colorado School of Mines Quarterly, vol. 54, 1959, pp. 251-269.
19. Morrison, H. L., and Allen, W. A.: New Surface Area Formed by a Projectile Striking Limestone Particles. Meteoritics, vol. I, no. 3, 1955, pp. 328-335.
20. Zeleny, Richard A., and Piret, Edgar L.: Studies of the Energy Requirements for Crushing. Third Symposium on Rock Mechanics, Colorado School of Mines Quarterly, vol. 54, 1959, pp. 35-42.
21. Öpik, E. J.: Meteor Impact on Solid Surface. Irish Astronomical Journal, vol. 5, no. 1, March 1958, pp. 14-36.
22. Walsh, J. M., Shreffler, R. B., and Willig, F. J.: Limiting Conditions for Jet Formation in High Velocity Collisions. Jour. Appl. Phys., vol. 24, no. 3, March 1953, pp. 349-359.
23. Birkhoff, Garret, MacDougall, Duncan P., Pugh, Emerson M., and Taylor, Geoffery: Explosives With Lined Cavities. Jour. Appl. Physics, vol. 19, June 1948, pp. 563-582.
24. Allen, William A., Morrison, Harvey L., Ray, Daniel B., and Rogers, James W.: Fluid Mechanics of Copper. The Physics of Fluids, vol. 2 no. 3, May 1959, pp. 324-333.
25. MacCormack, Robert W.: Investigation of Impact Flash at Low Ambient Pressures. Paper presented at the 6th Symposium on Hypervelocity Impact, Cleveland, Ohio, April 30-May 1,2, 1963.

TRANSIENT OBSERVATIONS OF CRATER FORMATION
IN SEMI-INFINITE TARGETS

John H. Kineke, Jr.

Richard Vitali

Ballistic Research Laboratories
Aberdeen Proving Ground, Maryland

CRATER FORMATION — SEMI-INFINITE TARGETS

ABSTRACT

Crater growth in lead targets has been observed at impact velocities up to 5 km/sec. Results indicate that the minimum outside crater diameter varies linearly with the logarithm of the time after impact. A technique is described for measuring the decay of stress velocity under impact conditions.

CRATER FORMATION — SEMI-INFINITE TARGETS

INTRODUCTION

The crater formation process is presently being studied theoretically by a number of investigators. Purely hydrodynamic models (1a, 2a) and visco-plastic models^(1b, 1c) are currently being employed in attempts to describe hypervelocity impact phenomena. The theoretical treatments generally consist in solving a system of non-linear partial differential equations by numerical techniques. Because a purely hydrodynamic model cannot be used to describe the entire crater formation process^(2b), it is desirable to compare instantaneous values of crater dimensions at different times with results of the theoretical analyses. The purpose of this paper, then, is to report experimental results obtained at the Ballistic Research Laboratories on transient observations of crater dimensions in metallic targets, and to describe a technique which is being used to measure the decay of stress velocity under impact conditions.

CRATER GROWTH IN LEAD

At the Fifth Hypervelocity Impact Symposium, observations of crater growth in lead targets were reported for one impact velocity^(1d). These observations have been expanded to include fourteen sets of impact conditions, with projectiles of various masses, and velocities up to 5 km/sec. The projectiles used in these experiments were steel discs fired from air-cavity charges^(3a, 4). Projectile masses were obtained by recovery in low density material, and velocities were measured from multiple flash radiographs.

CRATER FORMATION—SEMI-INFINITE TARGETS

Time-dependent crater measurements were made from flash radiographs (Figure 1). Since lead is opaque to x-rays, only a shadowgraph could be taken of the crater lip extending above the surface of the semi-infinite target. The minimum outside diameter of the crater was measured on the x-ray negative, with a correction being applied for magnification. Since only a single observation could be made of a given crater, it was necessary to make a series of observations at various times after impact, using the same charge design. The time at which the x-ray tube flashed was monitored on an oscilloscope, and compared with the projectile arrival time at the surface of the target. The projectile arrival time was determined by extrapolation of x-ray observations of pellet position relative to the target surface.

Raw data, in the form of minimum outside crater radius r , as a function of time after impact, is plotted in Figures 2 - 15. Most of the observations were made at times between 30 and 150 μsec after impact, when r was between forty and ninety percent of its final value. The scatter in the data can be attributed to two sources: 1. Uncertainty in determination of the arrival time of the projectile at the target, of the order of five μsec ; and 2. Randomness of projectile orientation on striking the target, which leads to a five percent scatter in the crater diameter. Because a range of masses and velocities have been used, resulting in a range of final crater sizes, it has been necessary to normalize

CRATER FORMATION—SEMI-INFINITE TARGETS

the radius data. Since it has been shown^(3a) that the crater inside diameter is proportional to the product of the one-third power of the projectile mass and the two-thirds power of the projectile velocity, it is reasonable to expect that the outside diameter varies in the same manner. The second degree polynomials in Figures 2 - 15 are all plotted in Figure 16, with the ordinate normalized by dividing by $m_p^{1/3} v_p^{2/3}$. While the resultant group of lines all tend toward the same value of the final crater radius, it is still necessary to normalize the time. There is a tendency for these lines to be arranged in order of increasing energy, suggesting use of the same normalizing factor employed with r . When this is done a composite regression for all fourteen sets of data is obtained, as shown in Figure 17. Also plotted are the individual datum points, which show no systematic trends about the regression, despite considerable scatter. If one were to differentiate this regression, an admittedly inexact operation with experimental data of this sort, expansion rates of 100 to 200 meters per second are obtained, which qualitatively indicate that for the range of time considered the craters are expanding at rates which are very small fractions of the impact velocity.

The raw data considered above have been subjected to a second reduction technique which tends to eliminate bias resulting from the direct fitting of a second degree polynomial. For each of eight impact conditions the data were smoothed by finding a series of centroids, taking three points at a time. This operation was repeated

CRATER FORMATION—SEMI-INFINITE TARGETS

two or three times, depending on the scatter within a given set of data. The original data and the points resulting from the smoothing are shown in Figures 18 - 25. Semi-log and log-log plots with the smoothed points were used to examine the functional relationship between diameter and time, with the result that in each case an exponential relation was indicated.

$$t = a e^{bD}$$

Both t and D were then normalized by dividing each by D_0 , the average value of the final crater outside diameter for each set of impact conditions. Considering only those normalized points where the crater was between 50 and 90 percent of its final value, a second centroid smoothing operation was performed. A least square exponential fit then yielded the relation shown in Figure 26. This exponential is compared with the eight individual sets of data in Figures 27 - 34. Subsequently the smoothing operation was performed on three additional sets of data, which are shown in Figures 35 - 37. These are compared with the exponential in Figures 38 - 40.

STRESS VELOCITY

Theoretical considerations of the crater formation process warrant observation of the propagation of the stress front from the point of impact on the target. Measurements of the stress front position as a function of time have been reported^(1d) in materials which are transparent to visible light. Dense metallic targets

CRATER FORMATION—SEMI-INFINITE TARGETS

present an additional problem, however, being opaque to both visible light and x-rays. A new technique has been devised which eliminates the problem by the use of holes through the target, through which light beams can be passed.

Essentially, the technique uses a streak camera to record the passage of the stress front past small holes parallel to the plane of the impact surface. The target is split, to facilitate the machining of grooves on one half, and held in place with C-clamps (Figure 41). Impact occurs on the plane where the two parts of the target meet, a plane of symmetry (Figure 42). Argon bomb backlighting is used to indicate the position of each hole, the image of which is swept across the film at a constant rate. Passage of the stress front closes each hole in succession so that a position-time record is obtained of the location of the stress front. After impact, the lines in the region near the crater exhibit large displacements, indicating large deformations (Figure 43).

Actually, a Fastax camera with the framing system removed, and a six inch objective lens, were used to obtain film records, one of which is shown in Figure 44. The effective writing speed was about 0.05 mm/ μ sec, with an image demagnification of 13 to 1. Two sets of data, obtained in recording the impact of 0.7 gram titanium pellets at 3.05 km/sec on lead targets, are plotted in Figure 45. The ordinate, r , is the distance from the point of impact, while the abscissa, t , is the time after the pellet struck the target. While the relationship

CRATER FORMATION—SEMI-INFINITE TARGETS

among the time values is accurate, the time origin is somewhat arbitrary, having been determined from extrapolation to the impact surface. Minimal scatter is apparent between the two sets of data, despite the fact that one impact occurred 0.2 cm from the plane of symmetry, and the second 0.5 cm from the plane of symmetry. The slope of the plotted data is a constant with a value of 0.207 cm/ μ sec, which compares with Bridgman's measurement of 0.202 cm/ μ sec for the adiabatic "sound" speed. Thus, it can be concluded that under these impact conditions, at a distance greater than 0.4 cm from the point of impact, a supersonic shock front does not exist.

This result, of course, could have been predicted without any experimental effort. The value of this technique will accrue when higher impact velocities are used, and decaying shocks can be observed. At present, an investigation of the response time of the pinholes is underway, in order to determine experimental accuracy.

CRATER FORMATION—SEMI-INFINITE TARGETS

ACKNOWLEDGMENTS

The authors wish to acknowledge the efforts of Mr. Lee S. Holloway in making the observations of both crater formation and stress velocity, and to thank Mr. Boyd C. Taylor for suggesting the technique for measuring stress velocities.

CRATER FORMATION—SEMI-INFINITE TARGETS

REFERENCES

1. Fifth Hypervelocity Impact Symposium, Denver, October 1961.
 - a. A. E. Olshaker and R. L. Bjork -- Hydrodynamics Applied to Hypervelocity Impact.
 - b. T. D. Riney and P. R. Chernoff -- Inertial, Viscous and Plastic Effects in High Speed Impact.
 - c. Pei Chi Chou--Visco-Plastic Flow Theory in Hypervelocity Perforation of Plates.
 - d. J. H. Kineke, Jr. -- Observations of Crater Formation in Ductile Materials.
2. Sixth Hypervelocity Impact Symposium, Cleveland, April, 1963.
 - a. J. M. Walsh and J. H. Tillotson -- Hydrodynamics of Hypervelocity Impact.
 - b. J. H. Kineke, Jr., and L. G. Richards -- Influence of Target Strength on Hypervelocity Crater Formation in Aluminum.
3. Fourth Hypervelocity Impact Symposium, Elgin AFB, April, 1960.
 - a. John H. Kineke, Jr. -- An Experimental Study of Crater Formation in Metallic Targets.
4. John H. Kineke, Jr. and Lee S. Holloway -- "Macro-Pellet Projection with an Air Cavity High Explosive Charge for Impact Studies". Ballistic Research Laboratories Memorandum Report No. 1264, April 1960.

CRATER FORMATION—SEMI-INFINITE TARGETS

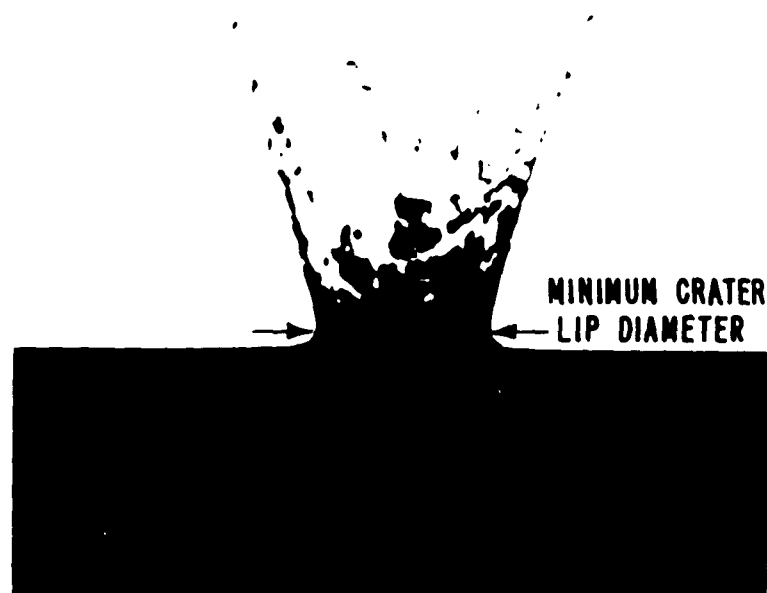


Figure 1

CRATER FORMATION—SEMI-INFINITE TARGETS

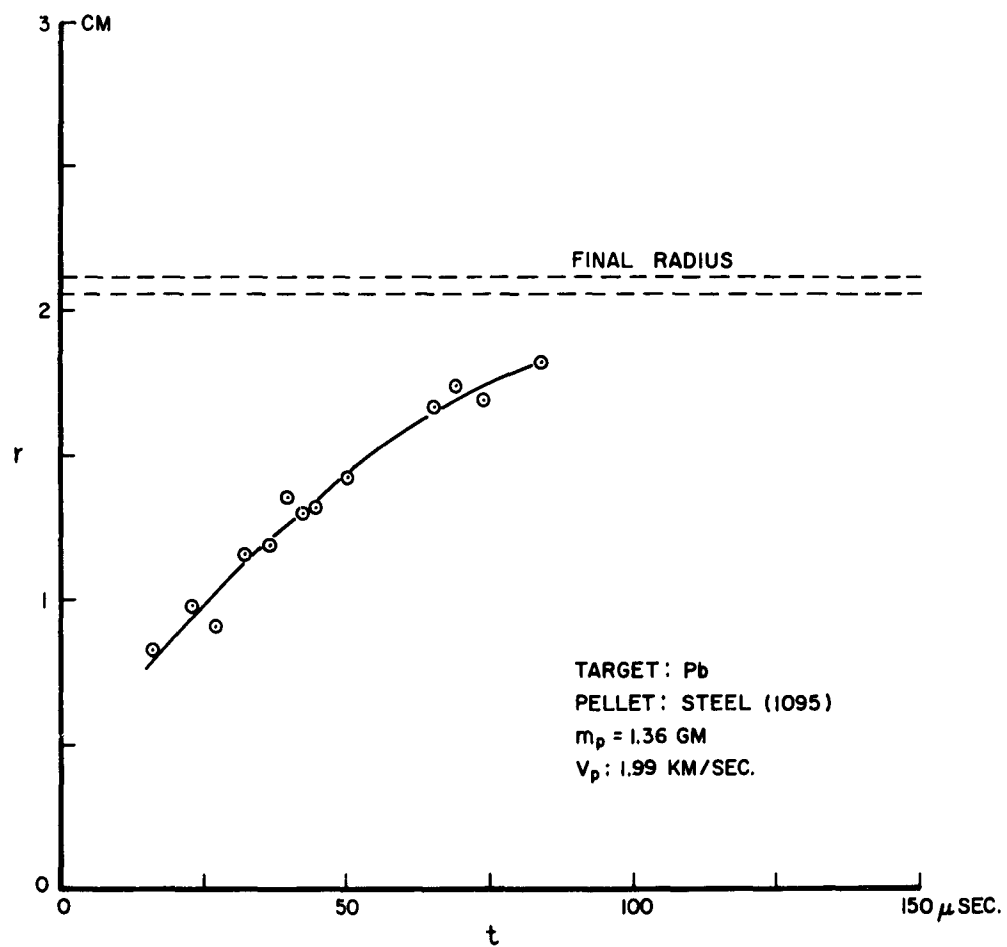


Figure 2

CRATER FORMATION—SEMI-INFINITE TARGETS

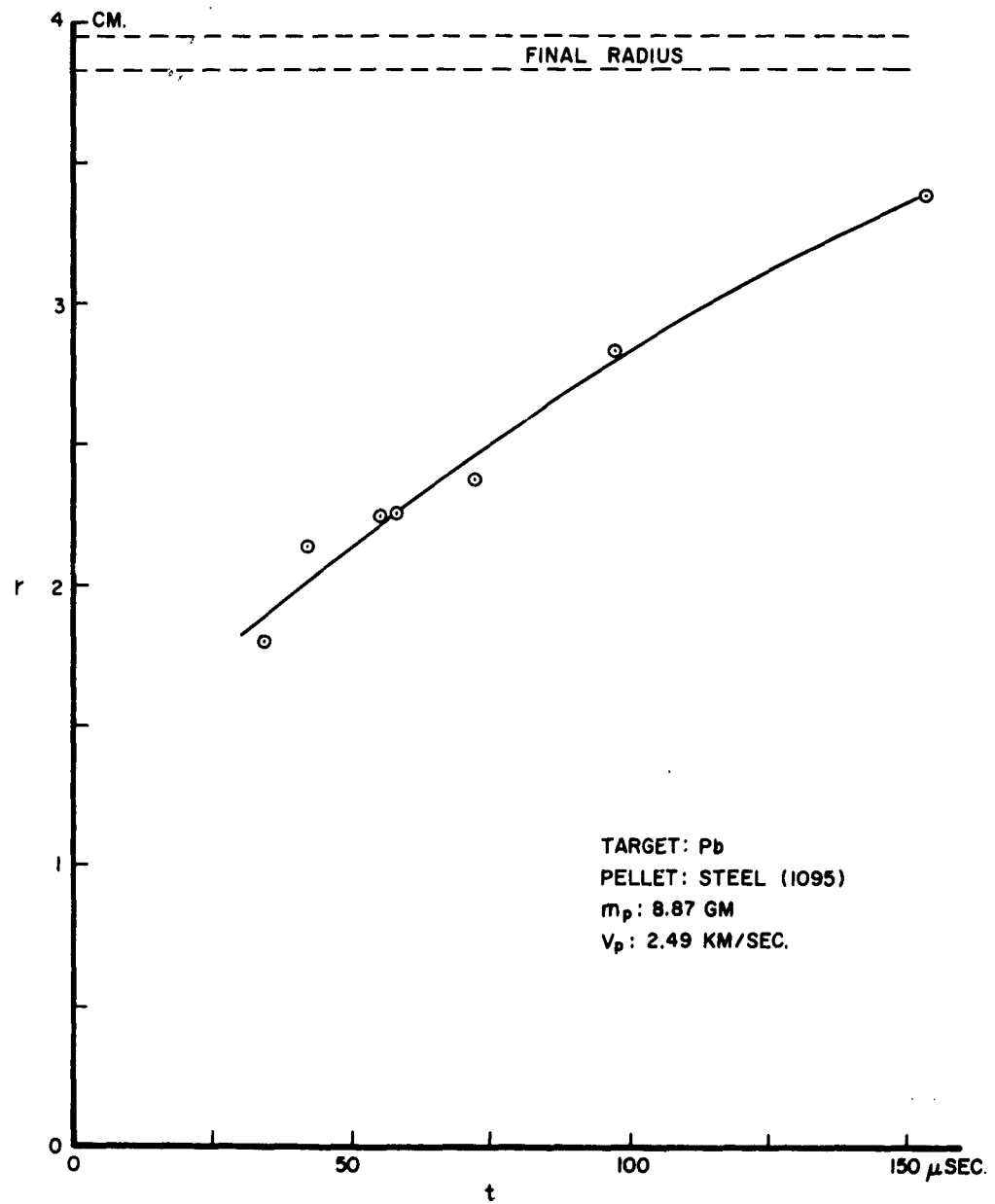


Figure 3

CRATER FORMATION—SEMI-INFINITE TARGETS

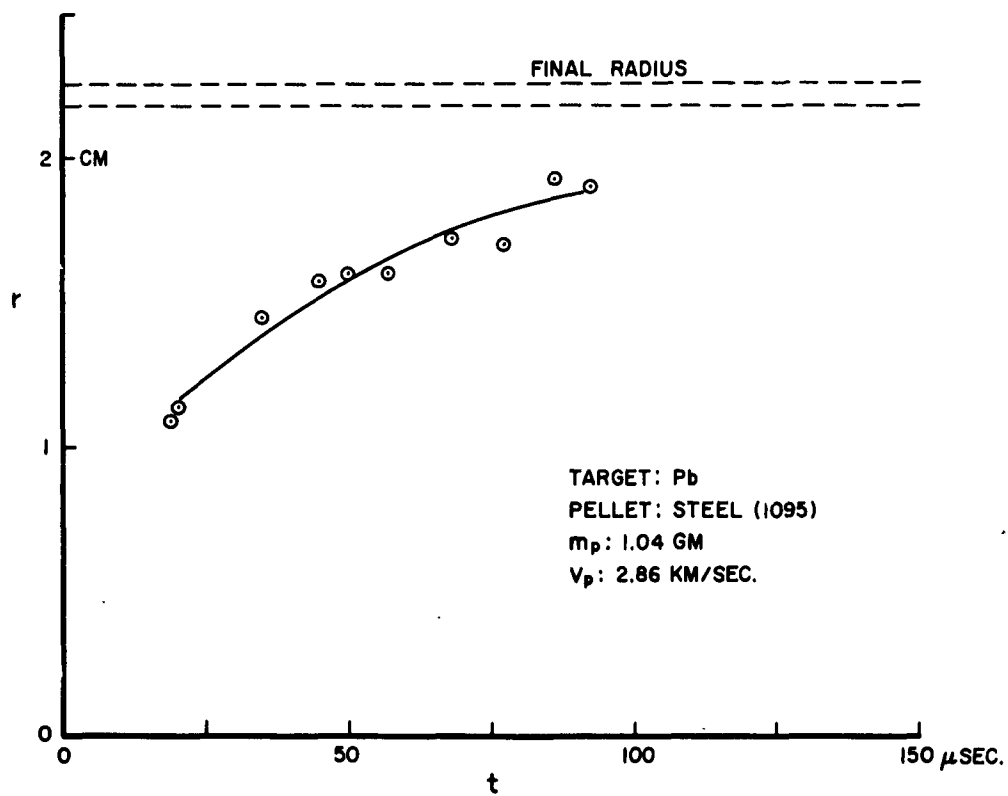
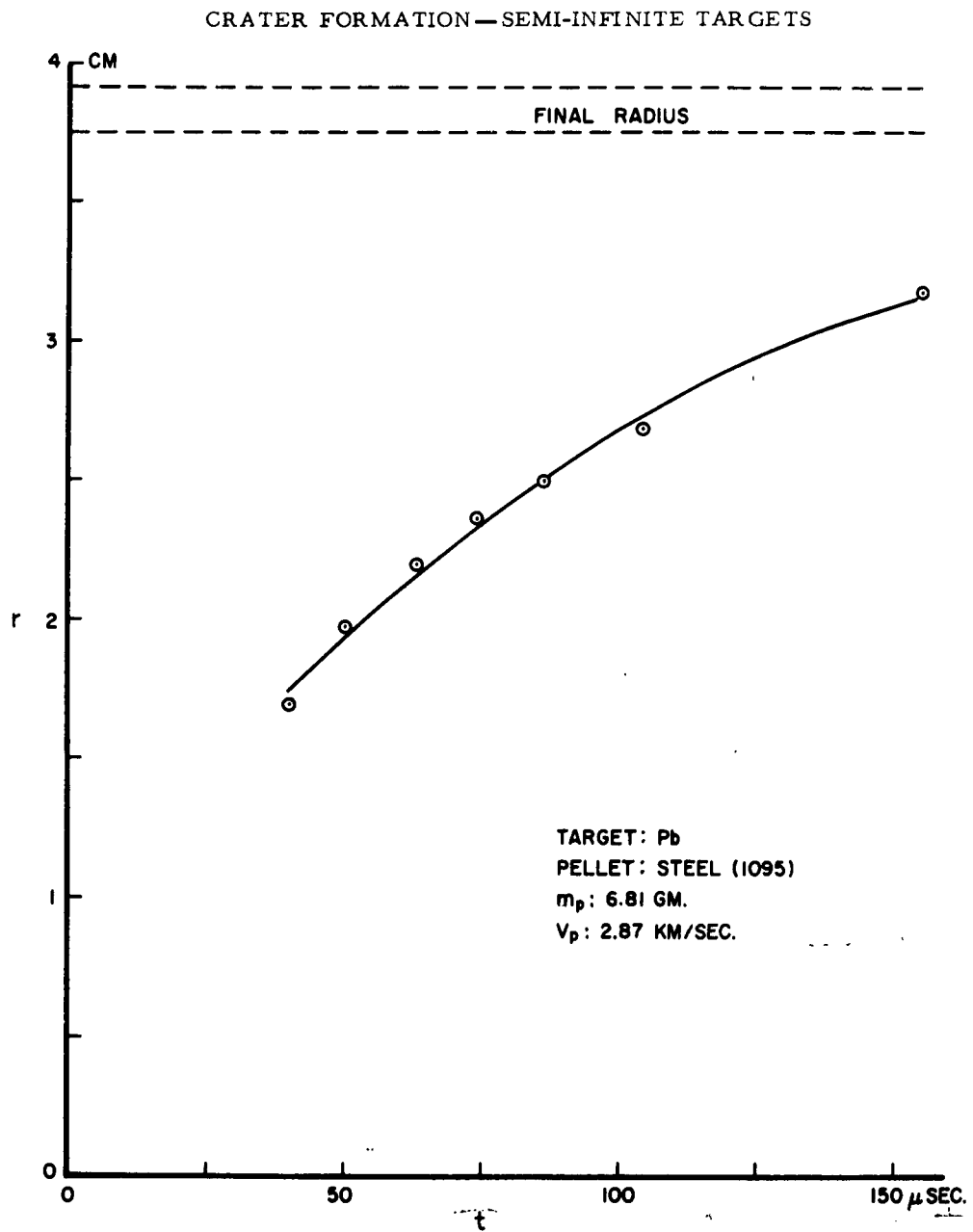


Figure 4

CRATER FORMATION—SEMI-INFINITE TARGETS



CRATER FORMATION—SEMI-INFINITE TARGETS

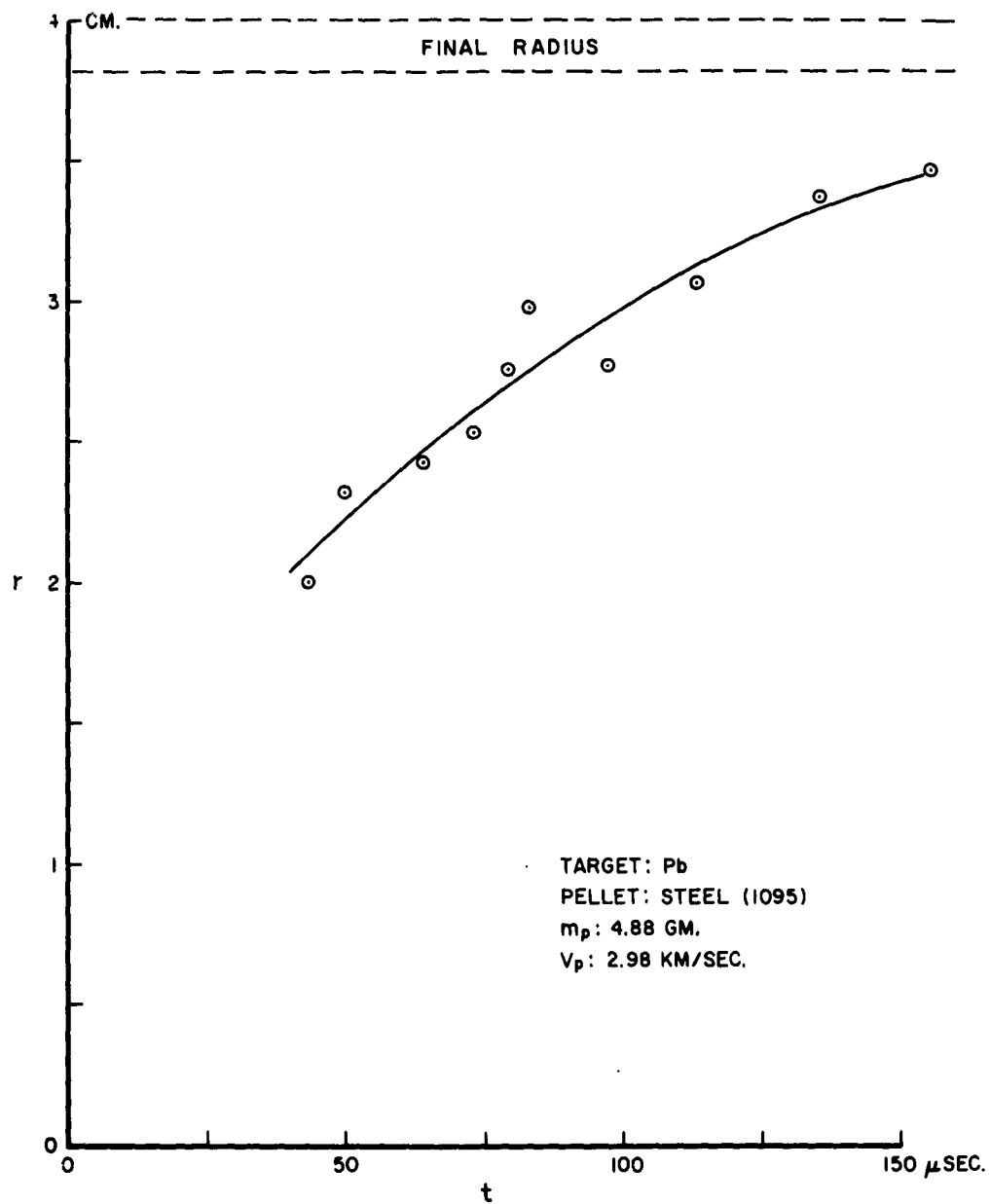


Figure 6

CRATER FORMATION—SEMI-INFINITE TARGETS

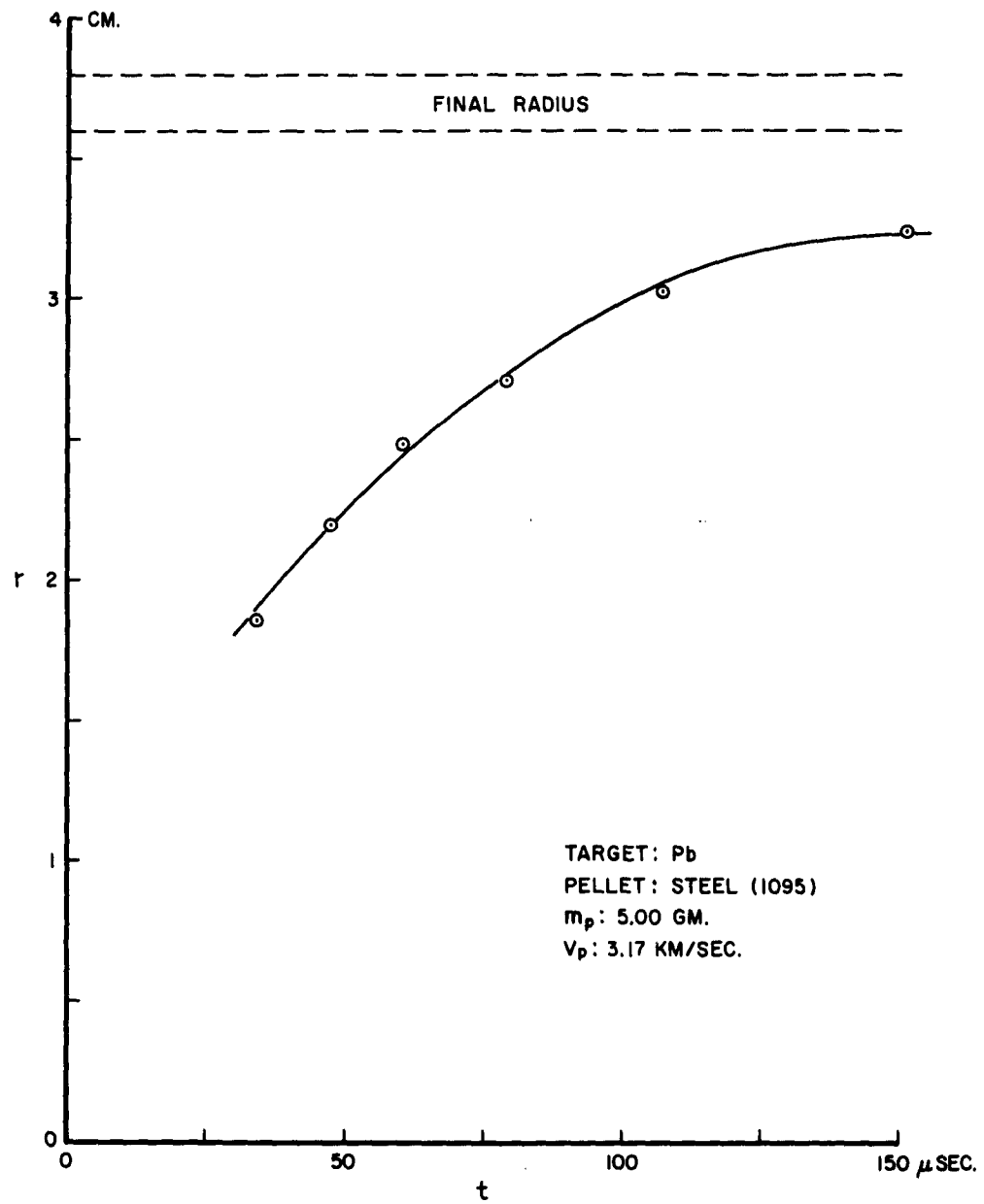


Figure 7

CRATER FORMATION—SEMI-INFINITE TARGETS

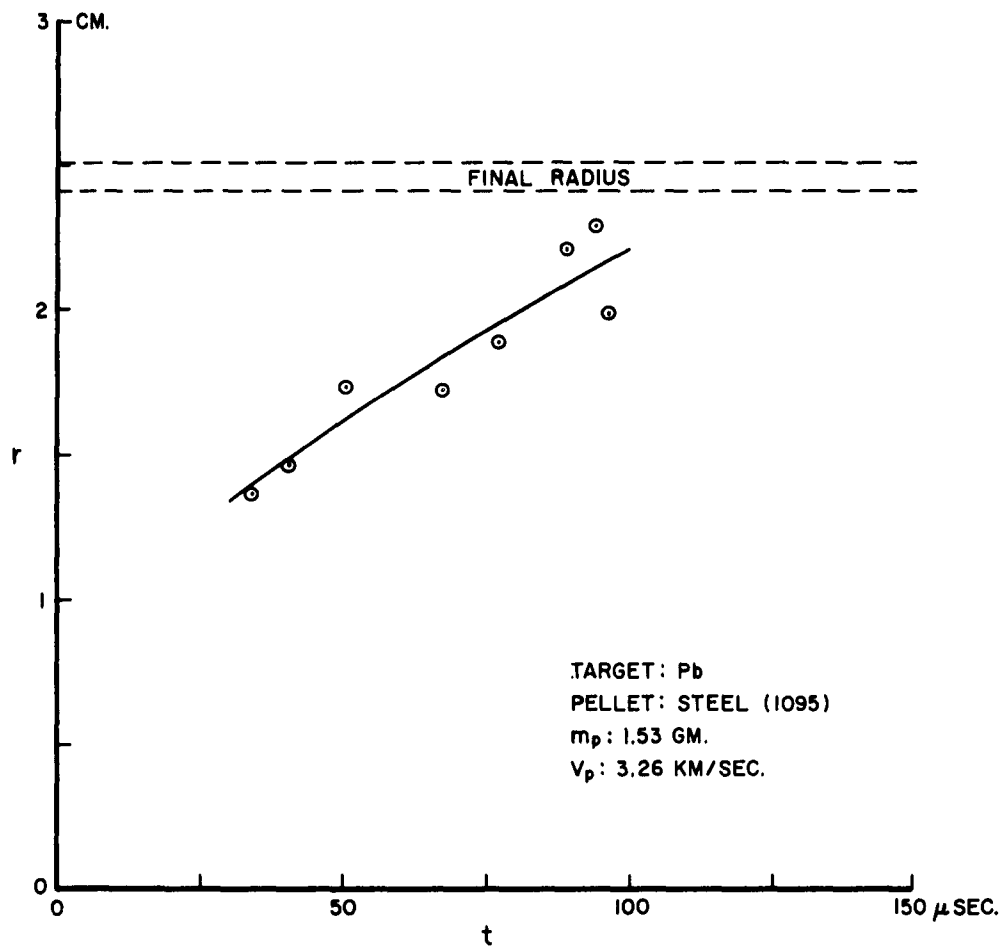


Figure 8

CRATER FORMATION — SEMI-INFINITE TARGETS

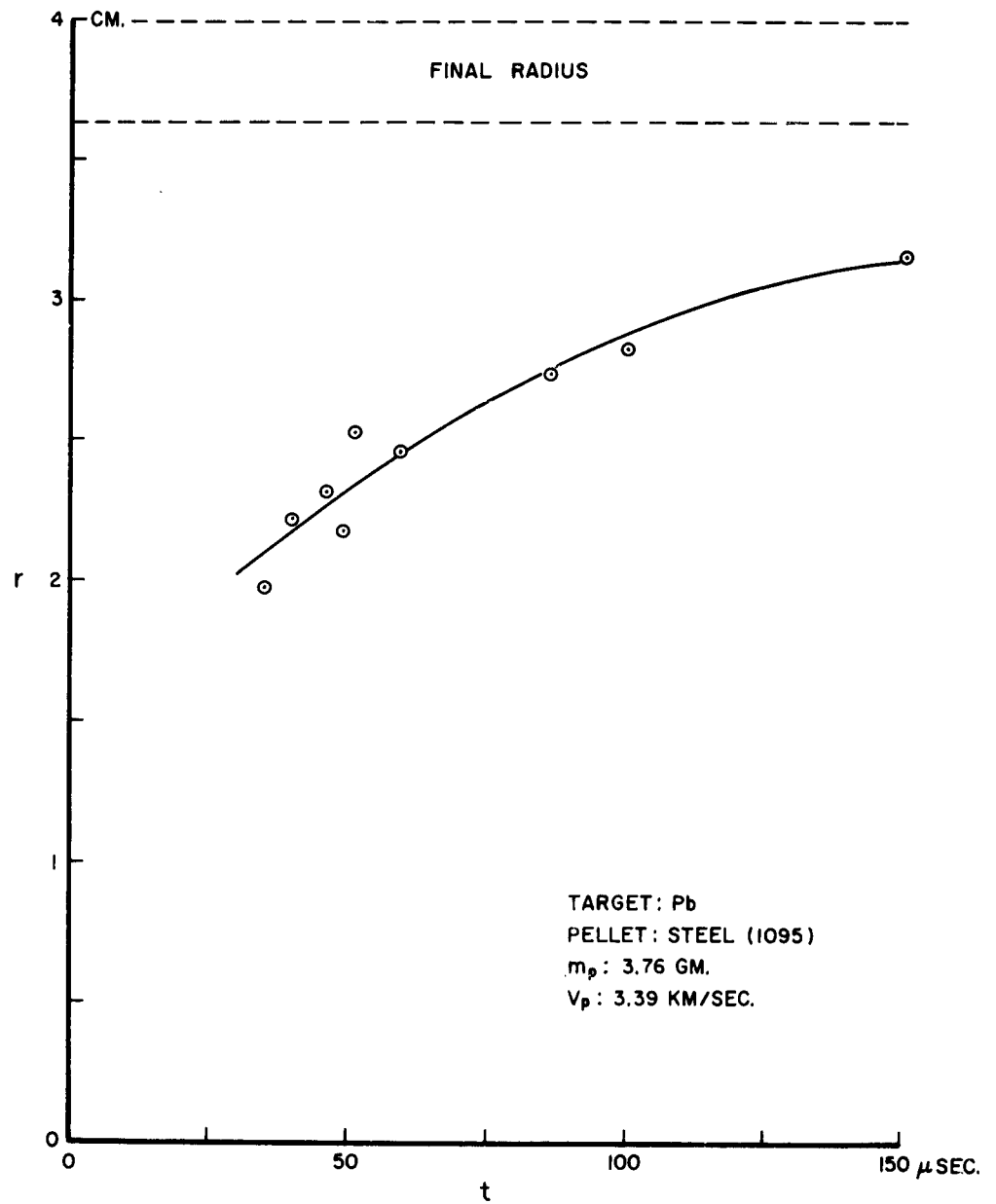


Figure 9

CRATER FORMATION—SEMI-INFINITE TARGETS

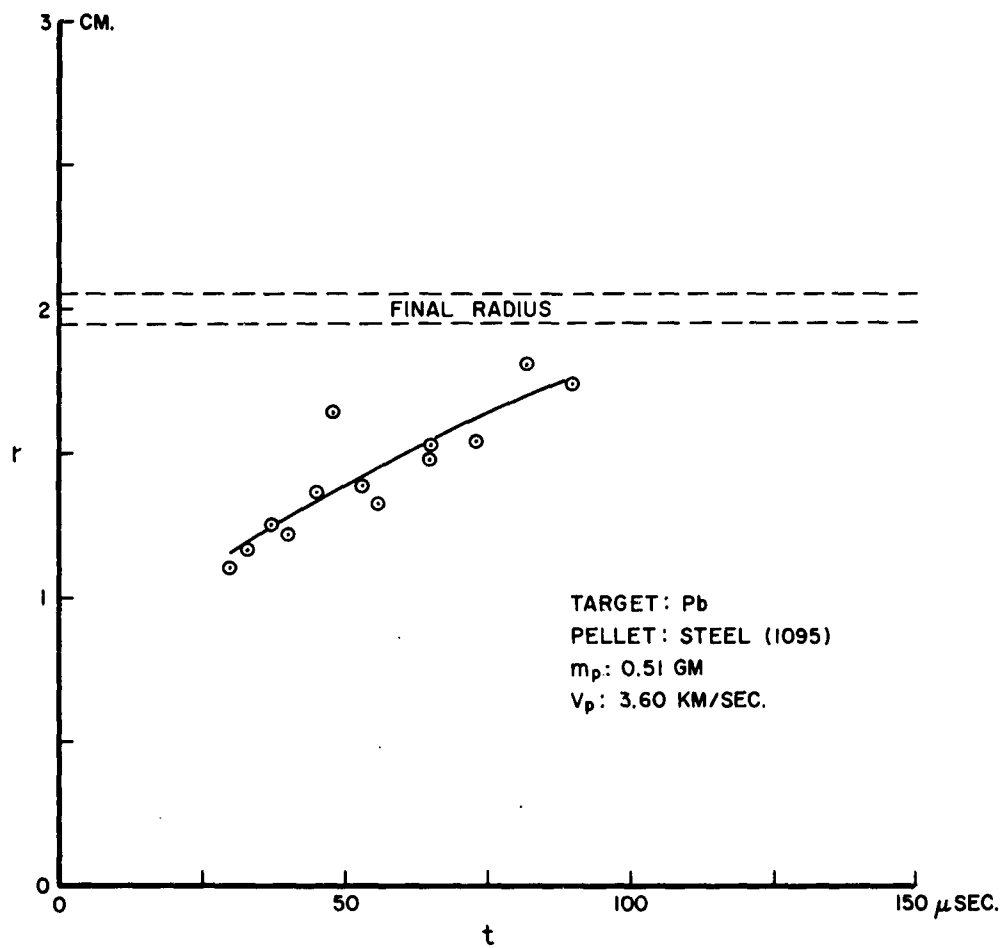


Figure 10

CRATER FORMATION—SEMI-INFINITE TARGETS

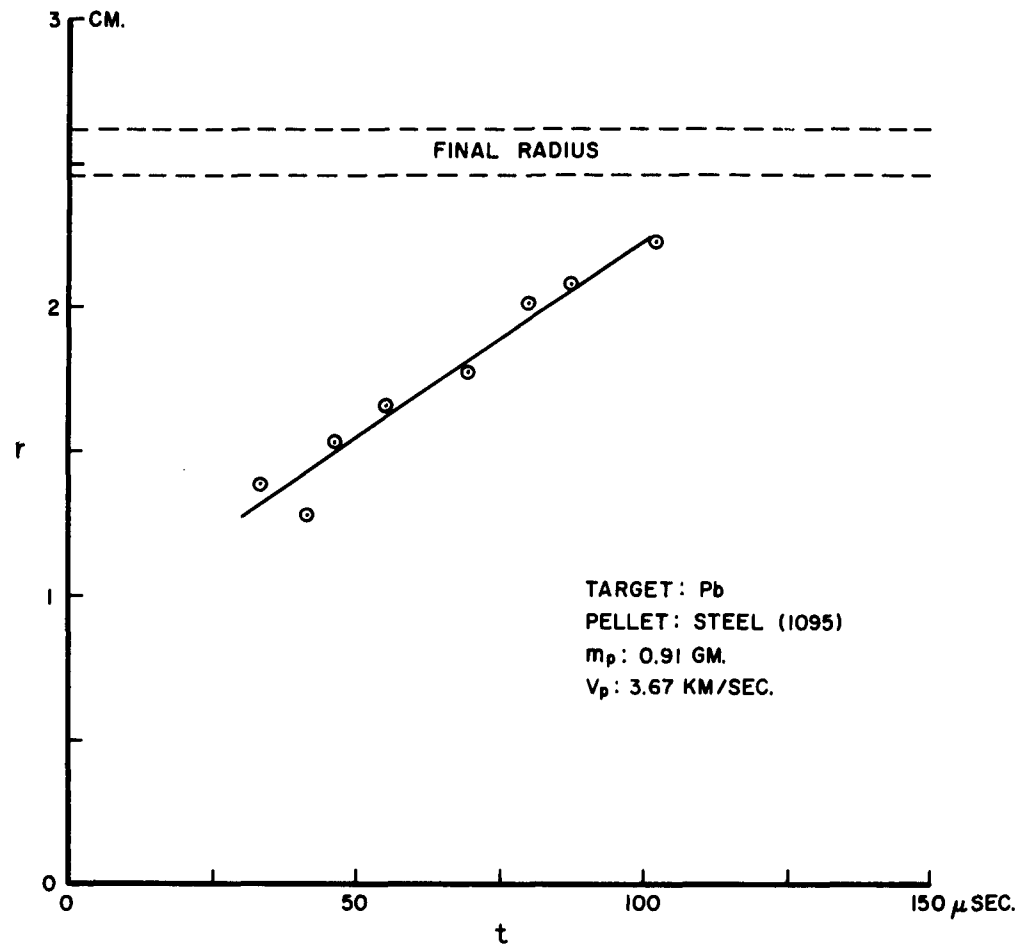


Figure 11

CRATER FORMATION—SEMI-INFINITE TARGETS

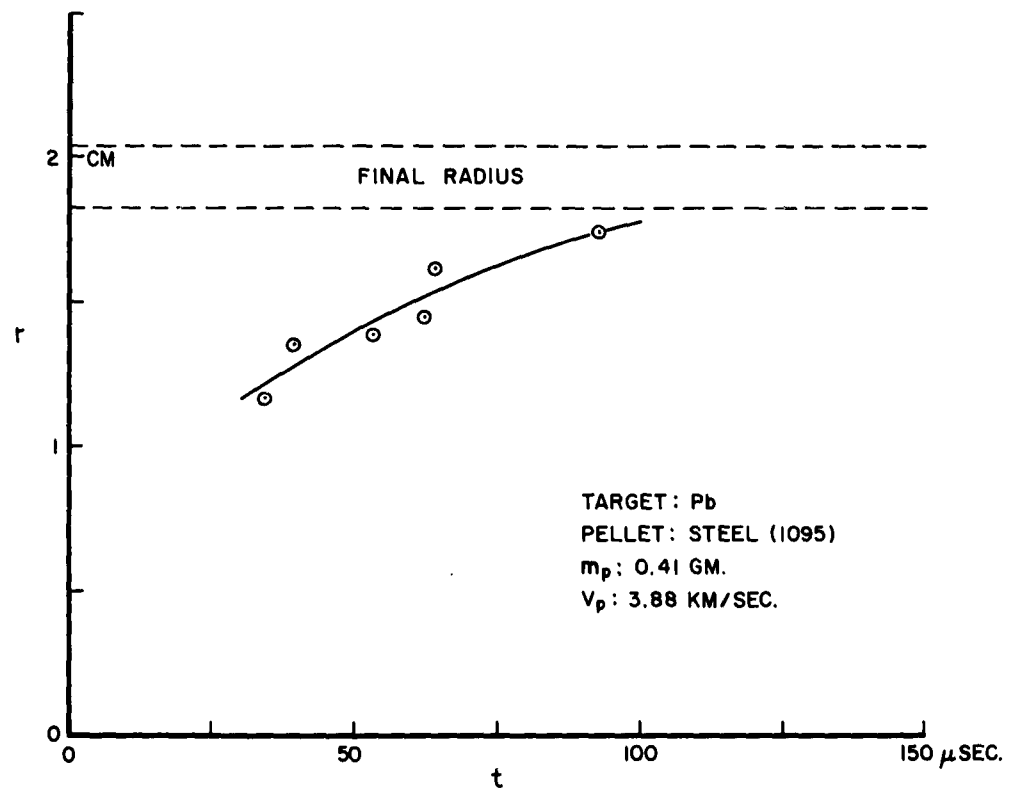


Figure 12

CRATER FORMATION — SEMI-INFINITE TARGETS

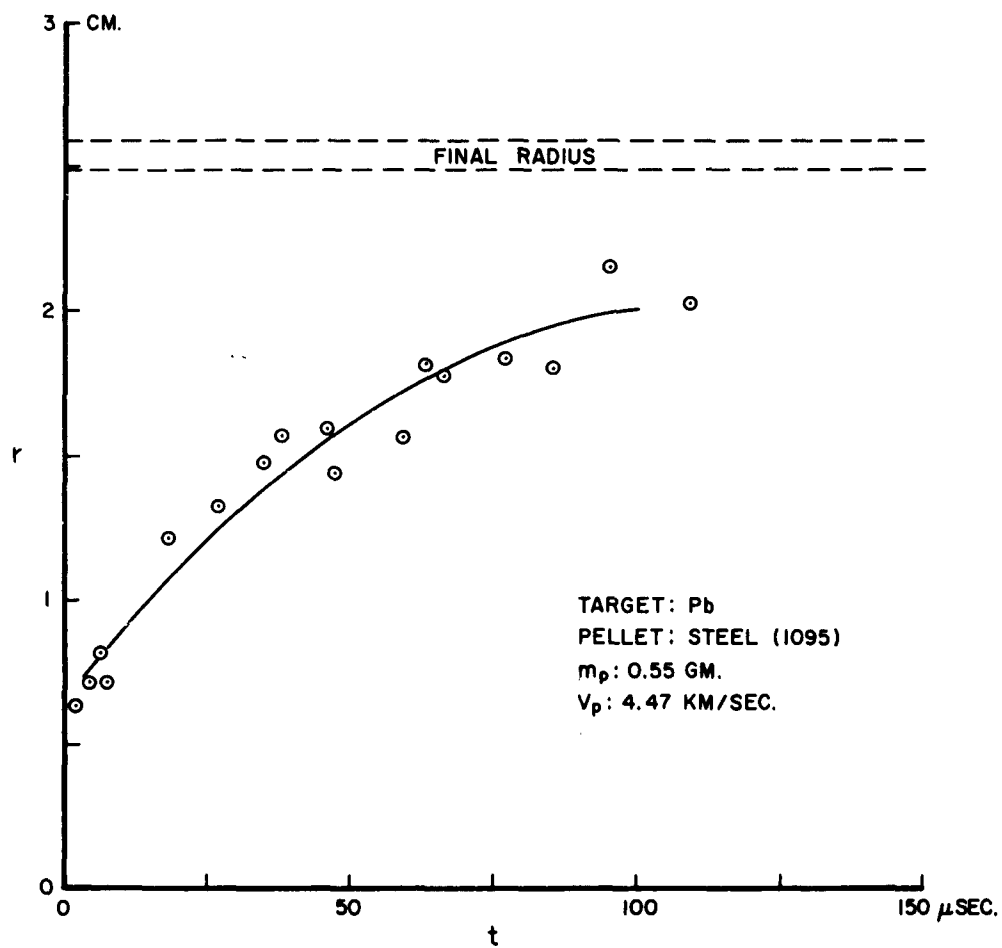


Figure 13

CRATER FORMATION — SEMI-INFINITE TARGETS

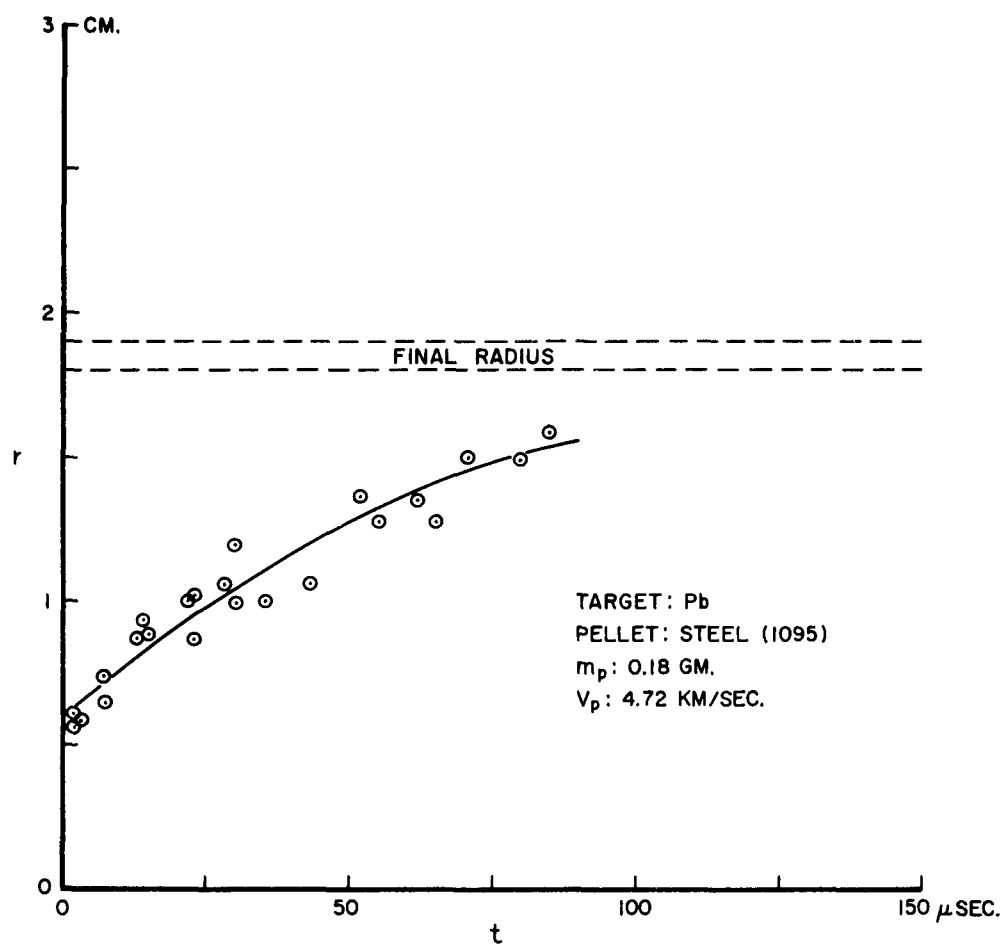


Figure 14

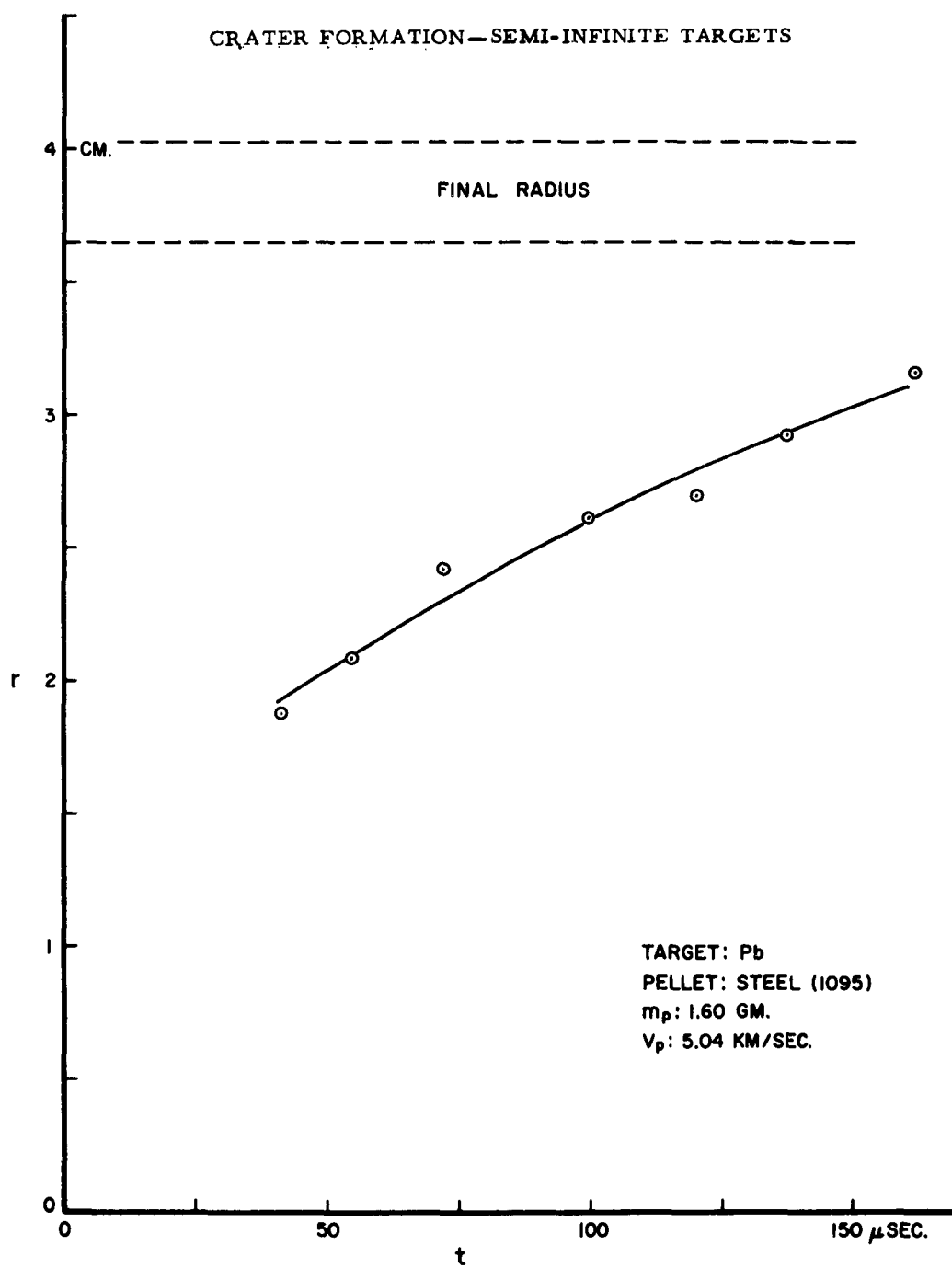


Figure 15

CRATER FORMATION — SEMI-INFINITE TARGETS

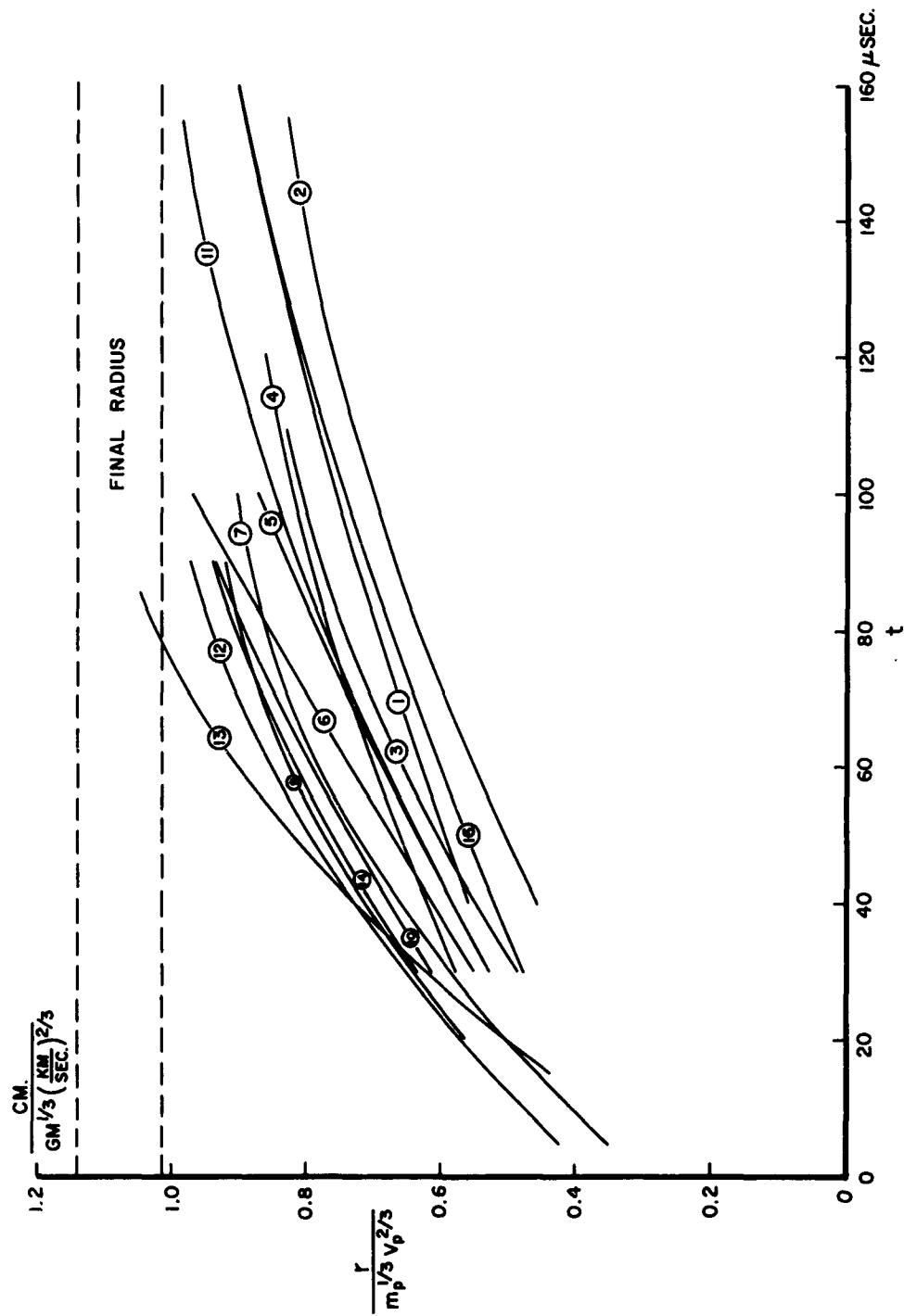


Figure 16

CRATER FORMATION — SEMI-INFINITE TARGETS

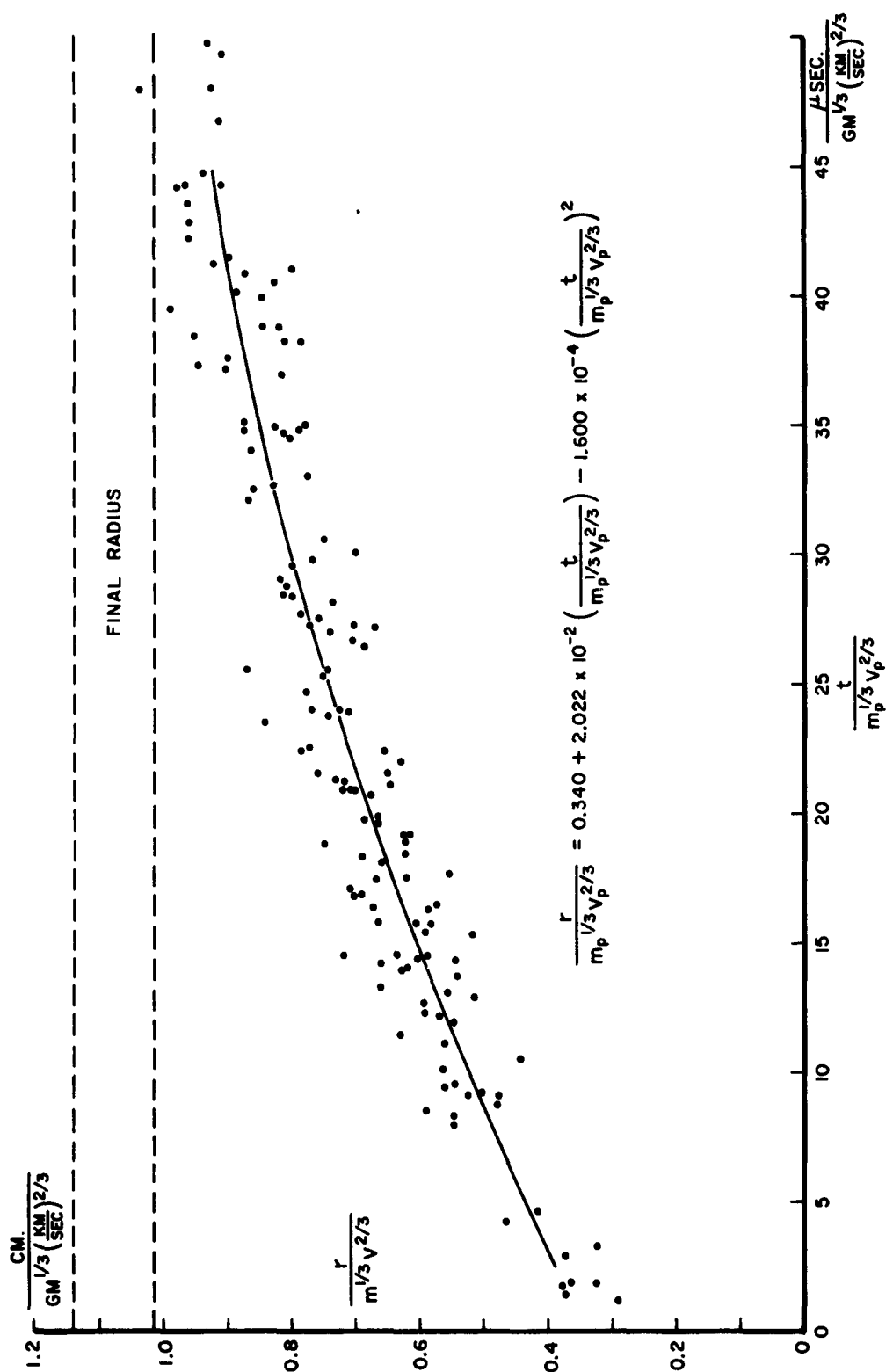


Figure 17

CRATER FORMATION — SEMI-INFINITE TARGETS

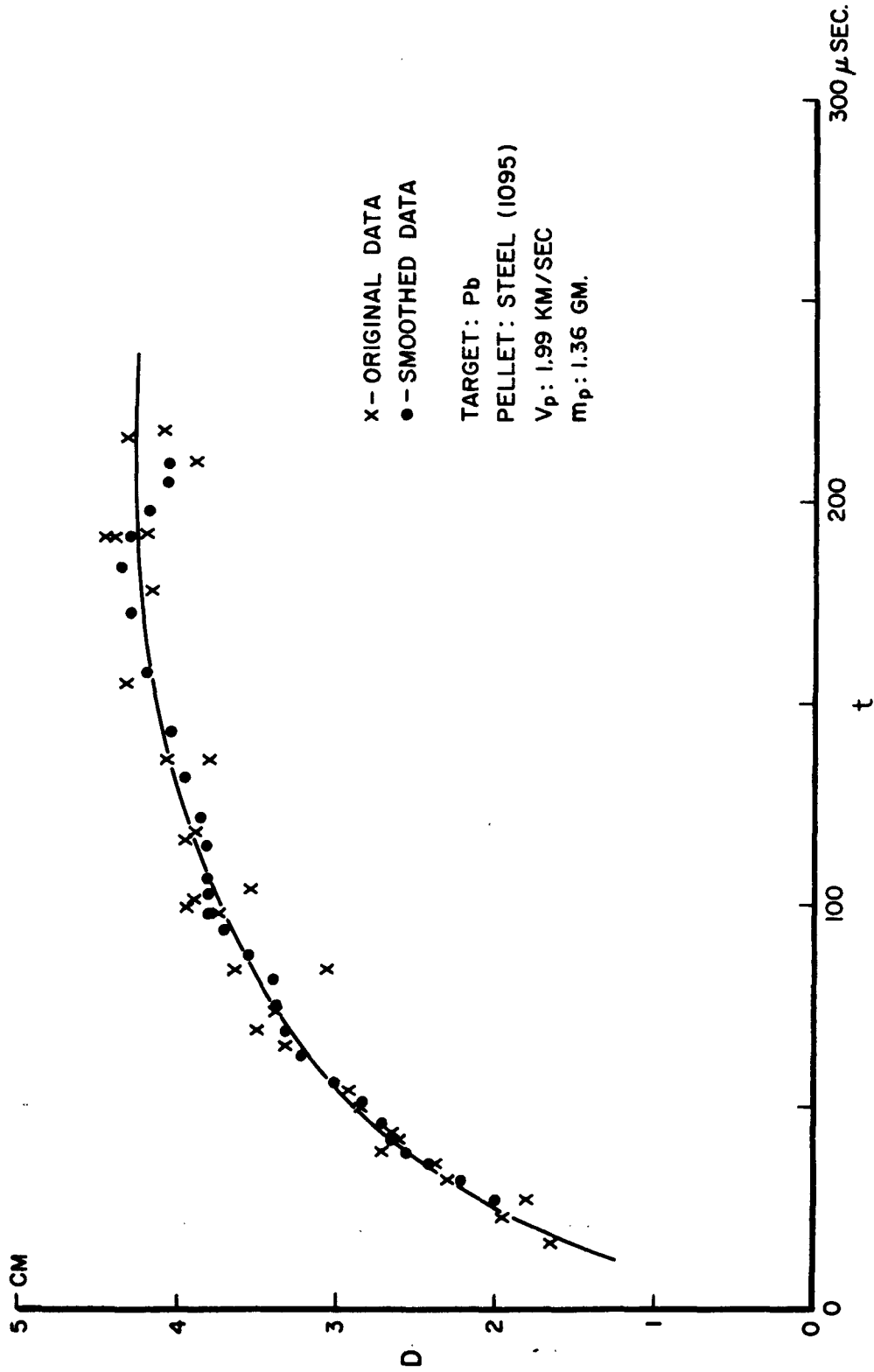


Figure 18

CRATER FORMATION—SEMI-INFINITE TARGETS

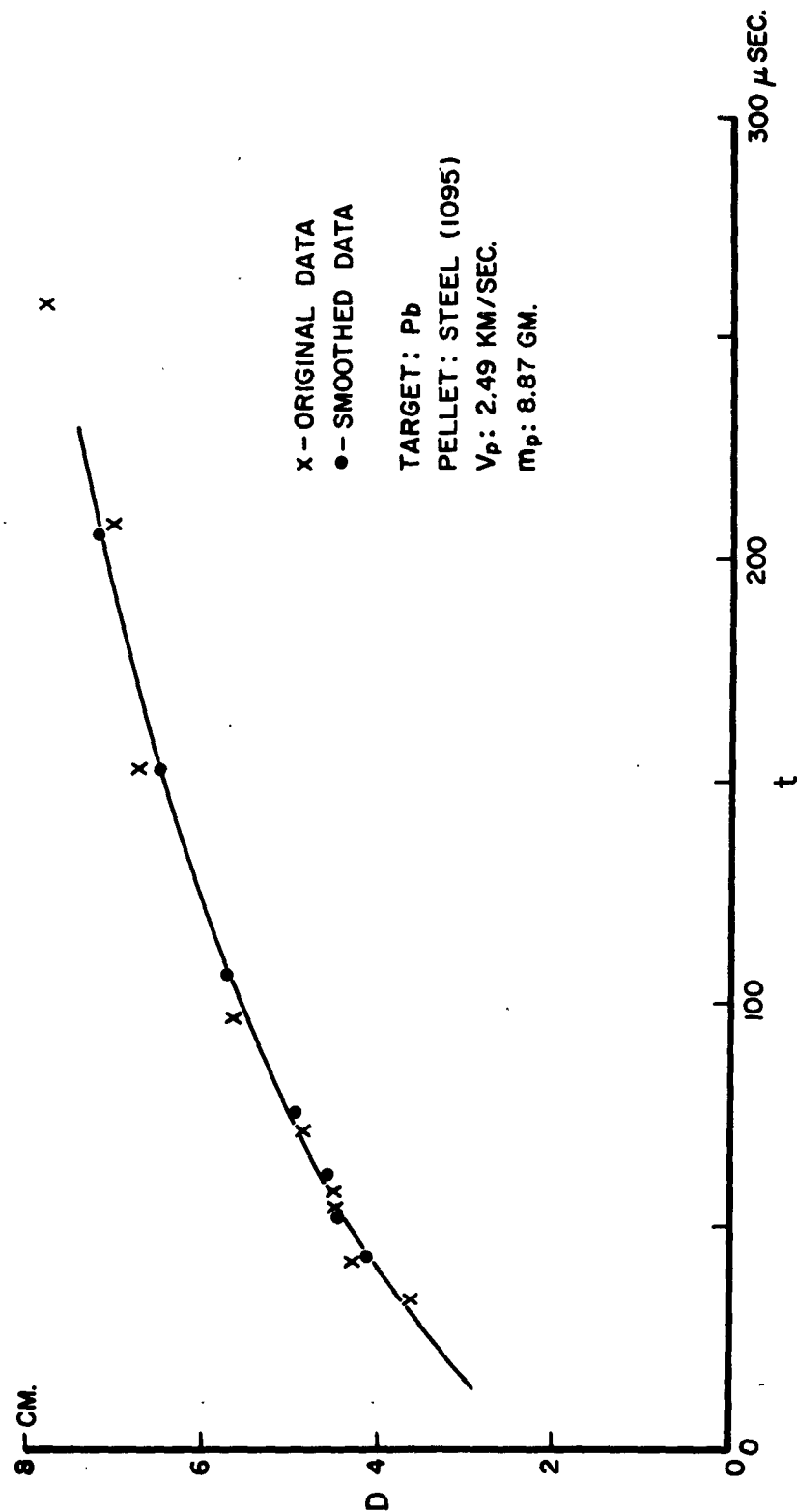


Figure 19

CRATER FORMATION—SEMI-INFINITE TARGETS

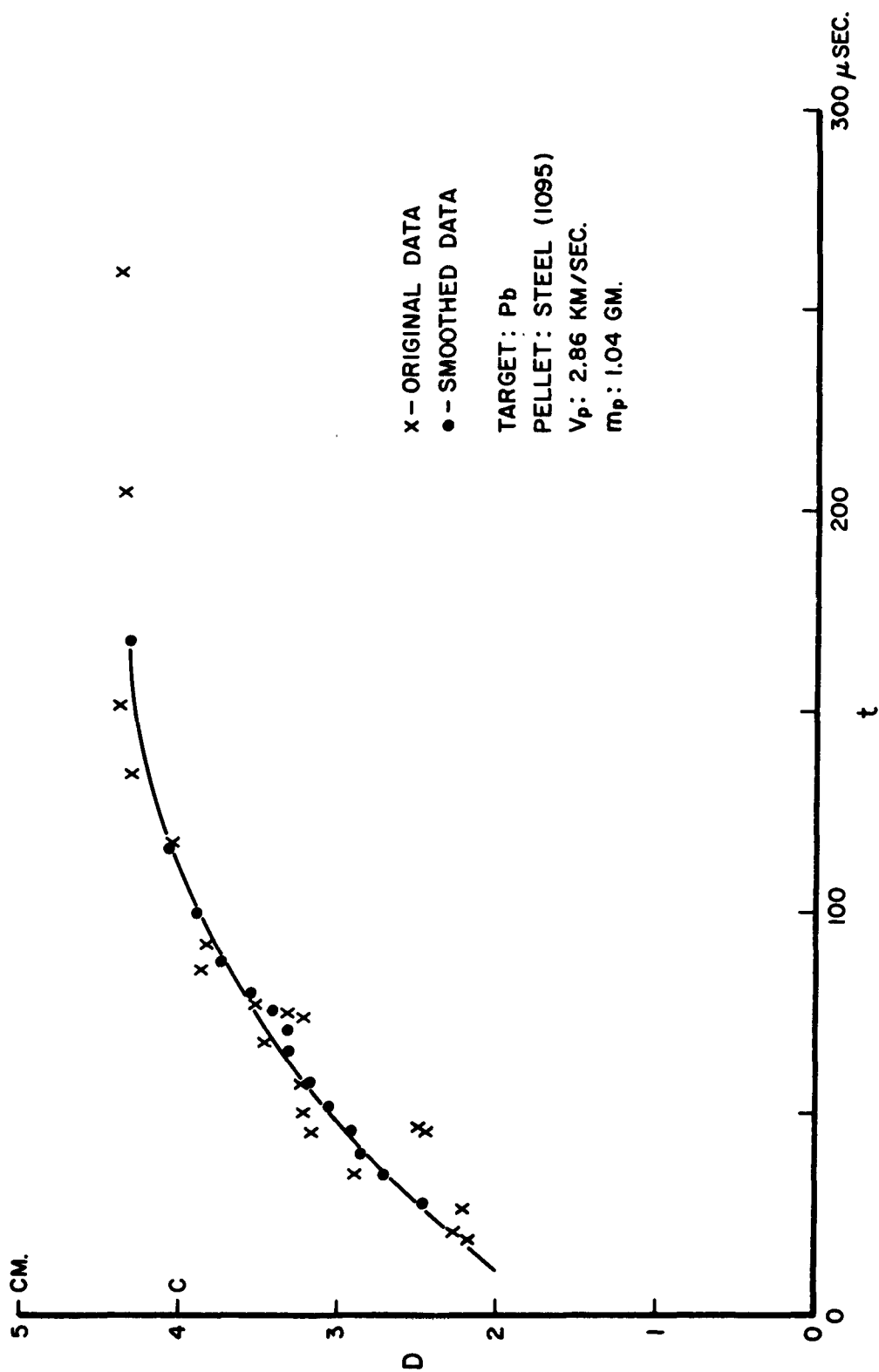


Figure 20

CRATER FORMATION—SEMI-INFINITE TARGETS

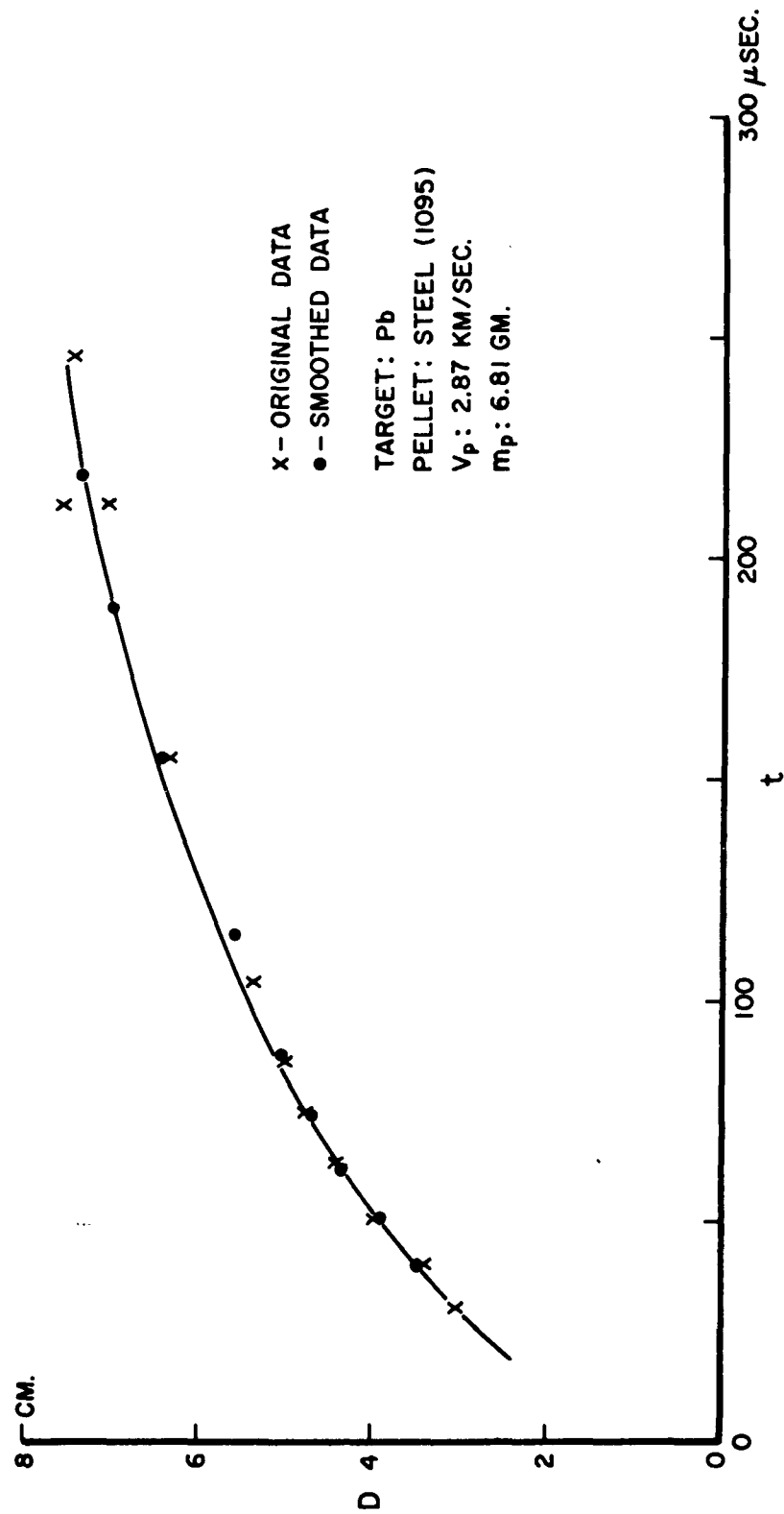


Figure 21

CRATER FORMATION—SEMI-INFINITE TARGETS

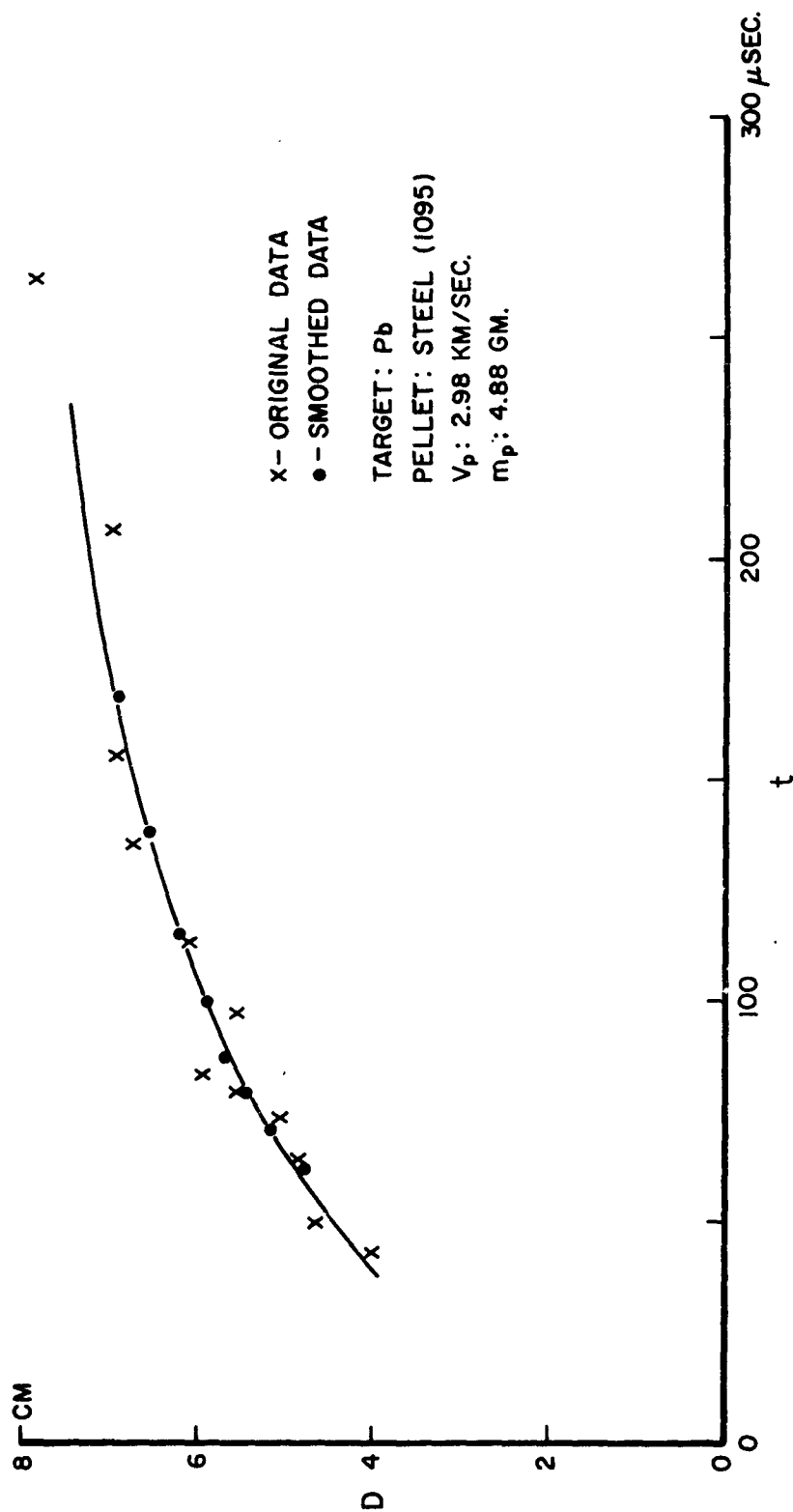
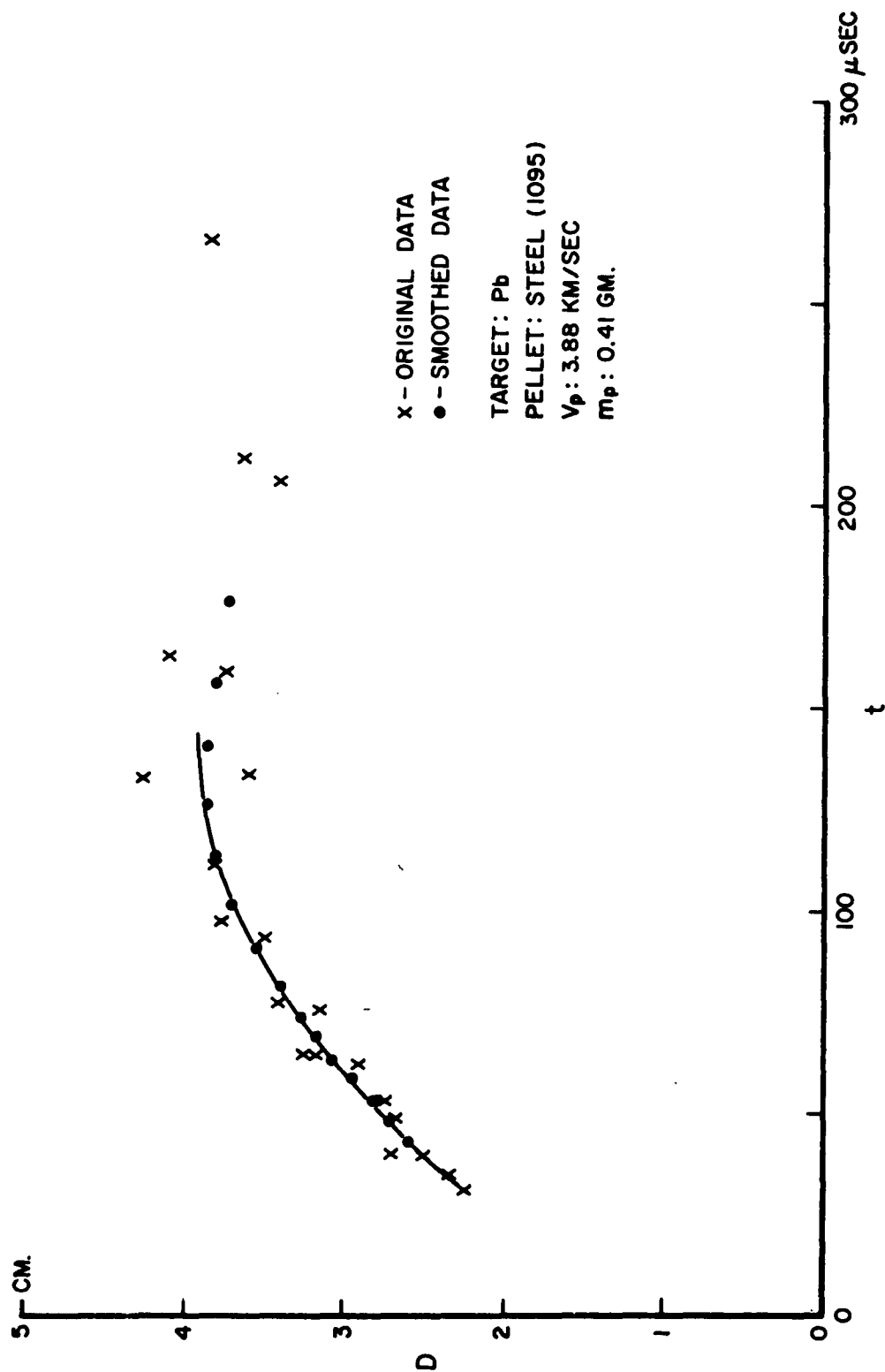


Figure 22

CRATER FORMATION — SEMI-INFINITE TARGETS



CRATER FORMATION - SEMI-INFINITE TARGETS

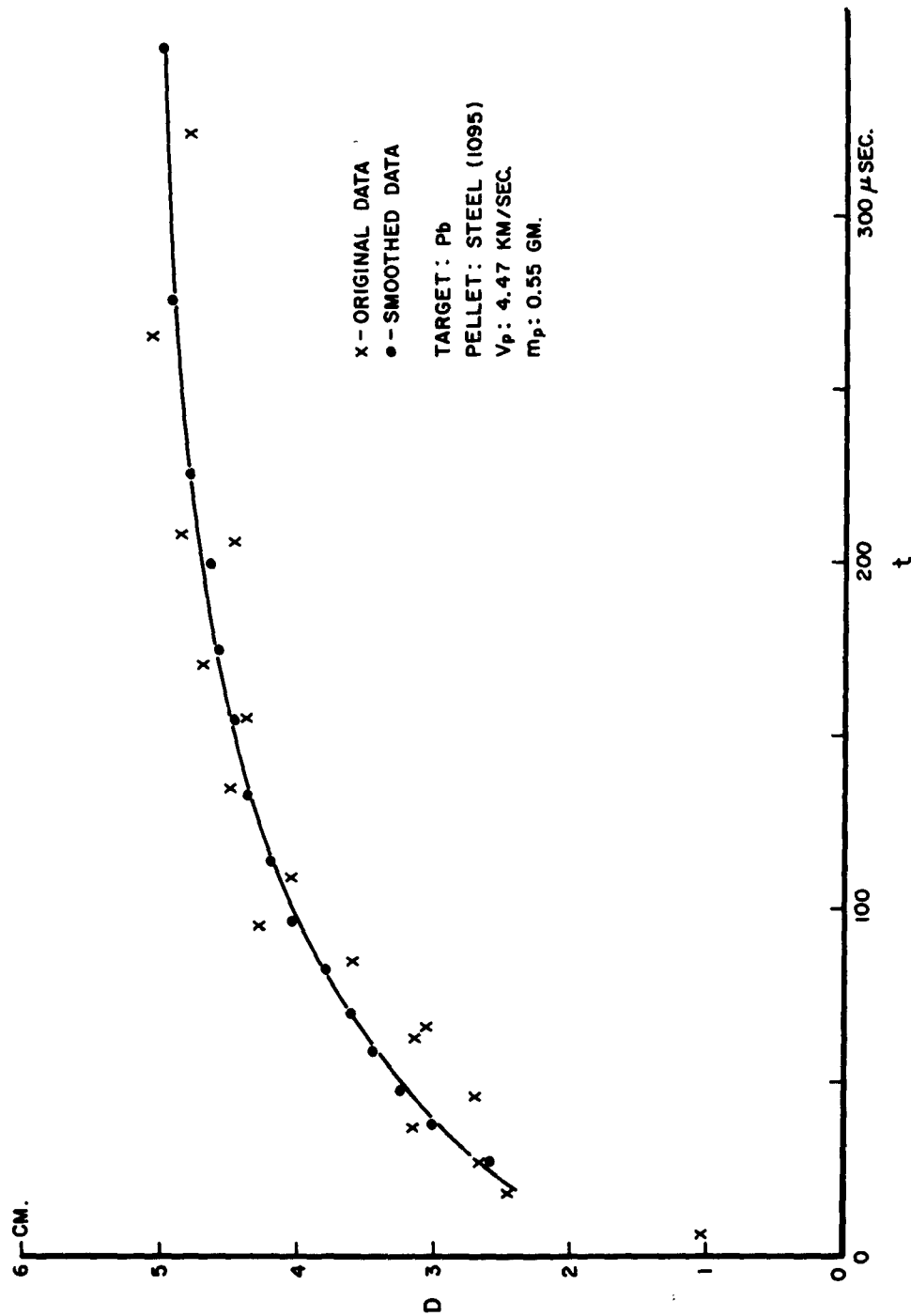


Figure 24

CRATER FORMATION — SEMI-INFINITE TARGETS

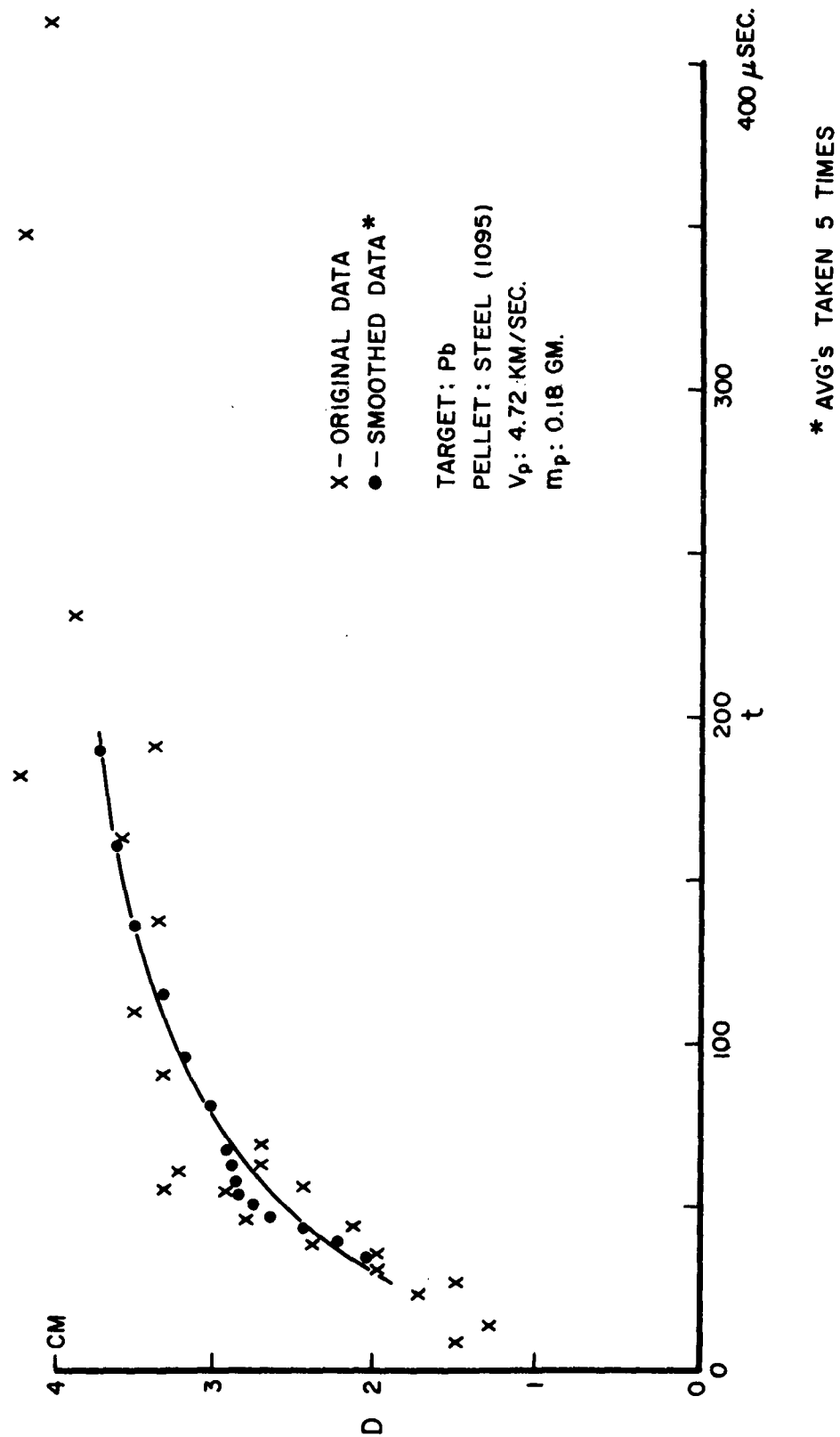


Figure 25

CRATER FORMATION—SEMI-INFINITE TARGETS

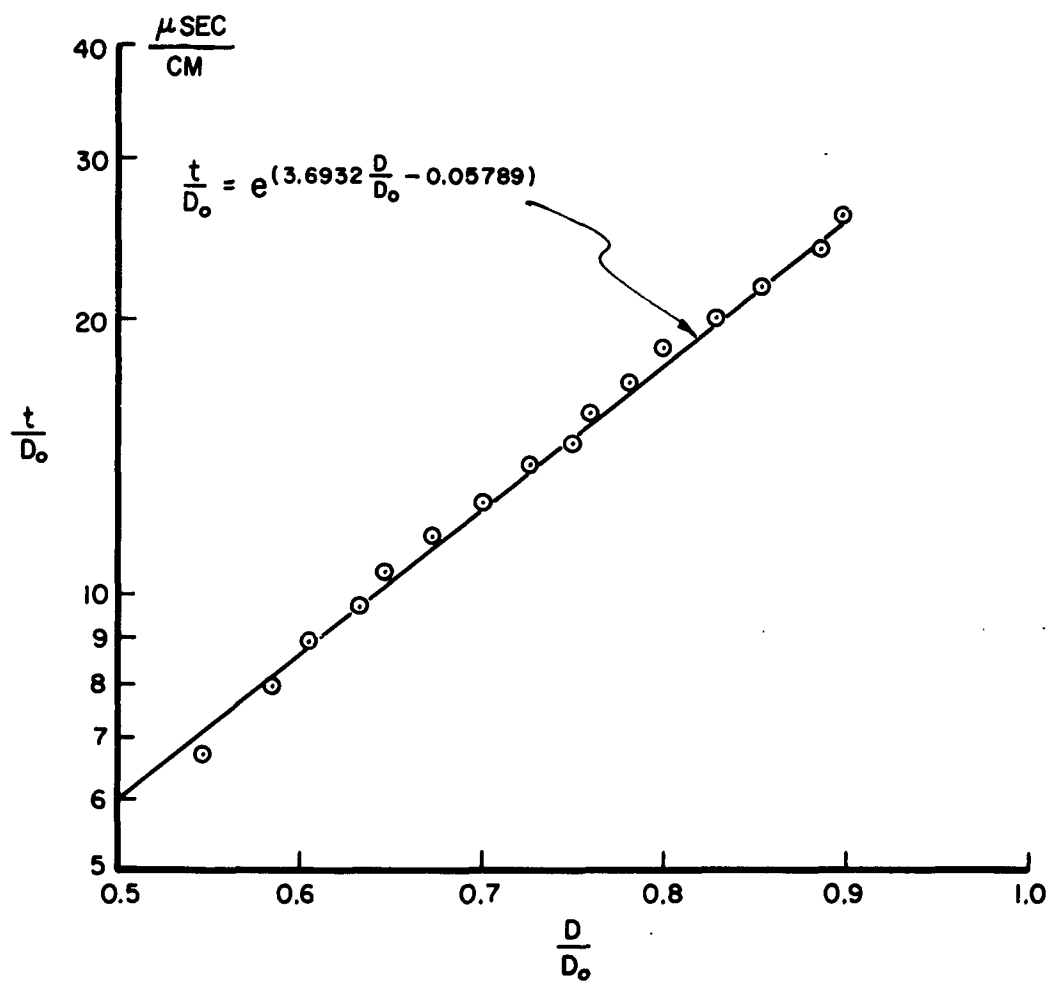


Figure 26

CRATER FORMATION—SEMI-INFINITE TARGETS

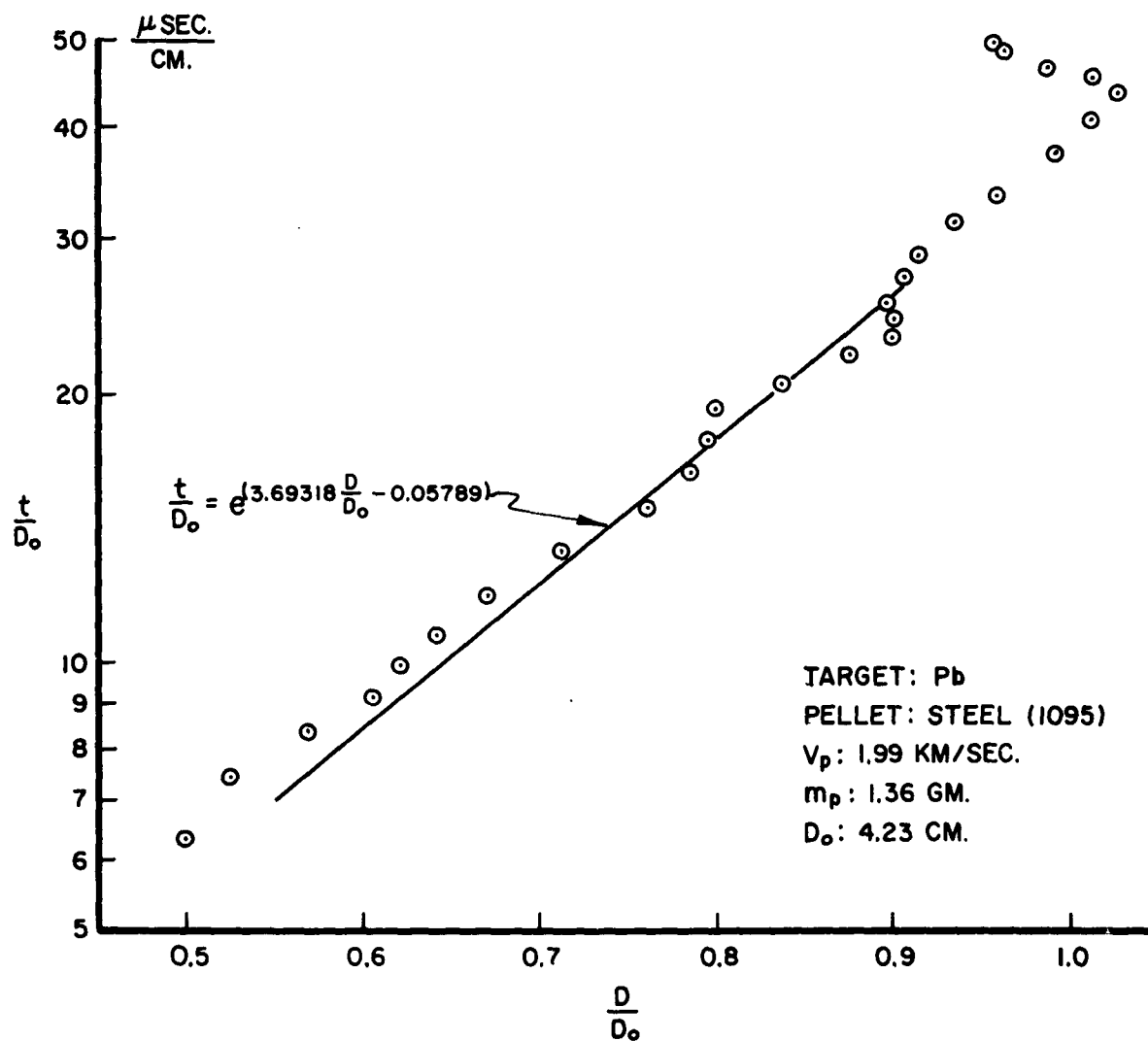


Figure 27

CRATER FORMATION— SEMI-INFINITE TARGETS

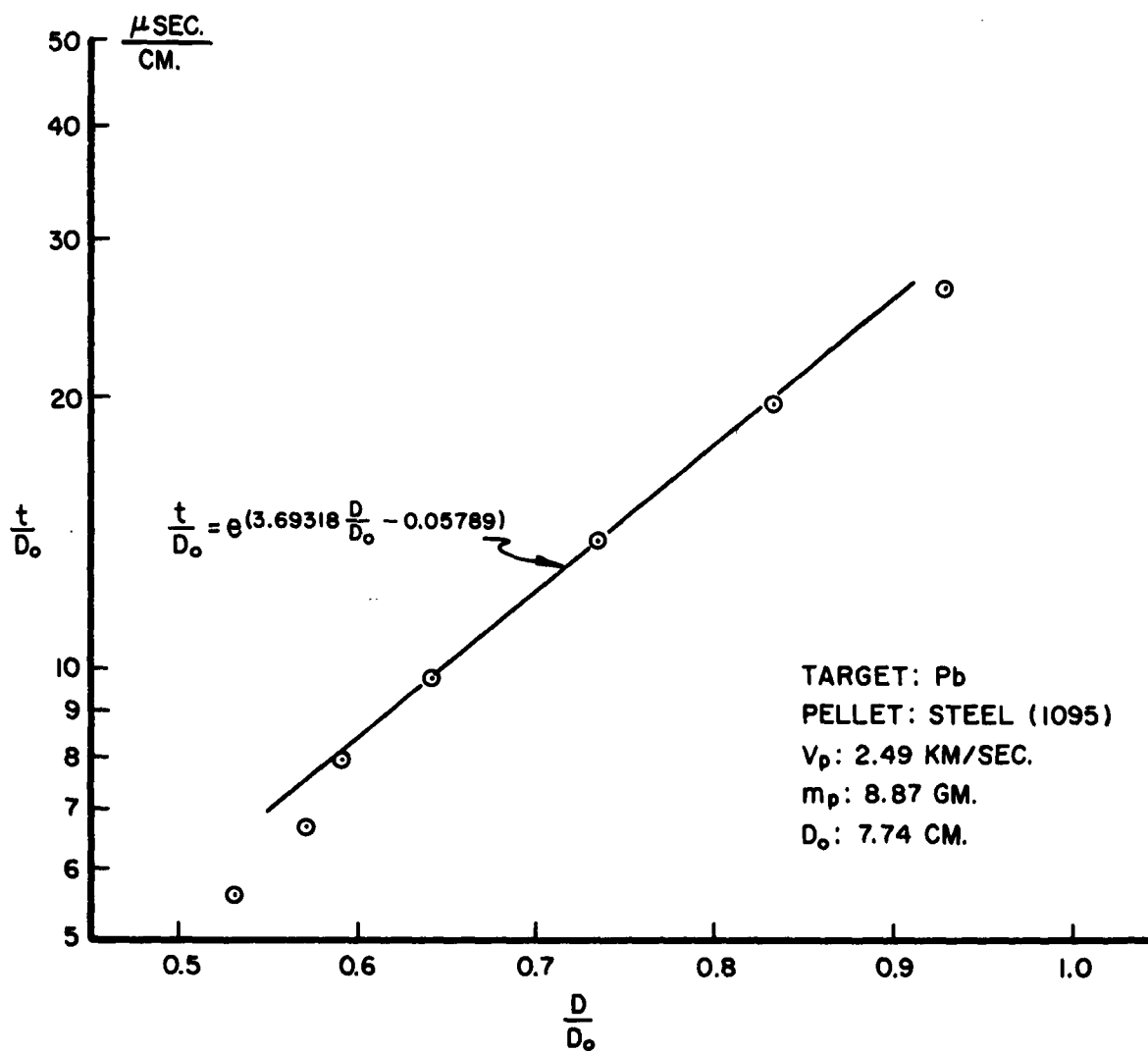


Figure 28

CRATER FORMATION—SEMI-INFINITE TARGETS

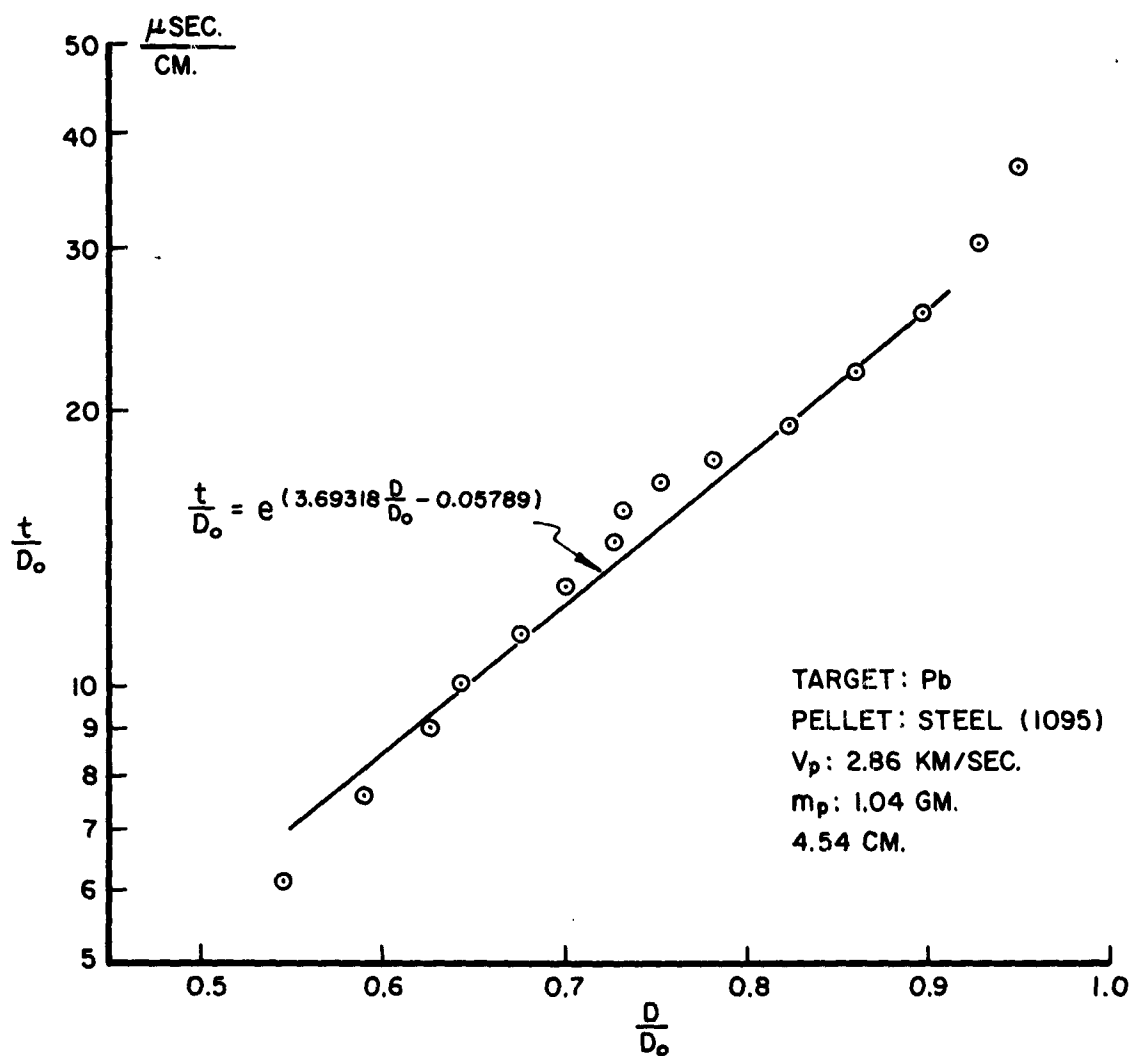


Figure 29

CRATER FORMATION—SEMI-INFINITE TARGETS

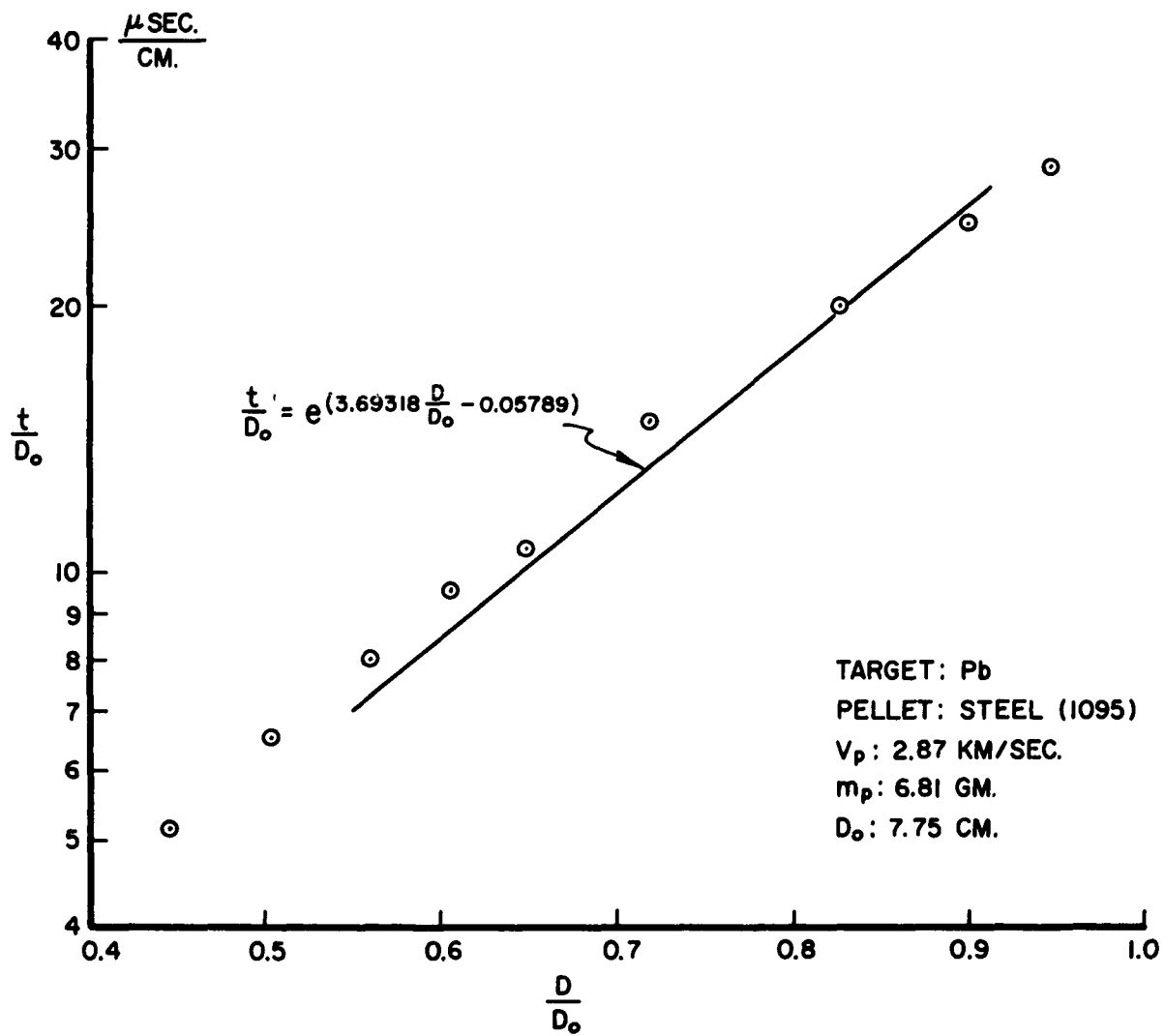


Figure 30

CRATER FORMATION—SEMI-INFINITE TARGETS

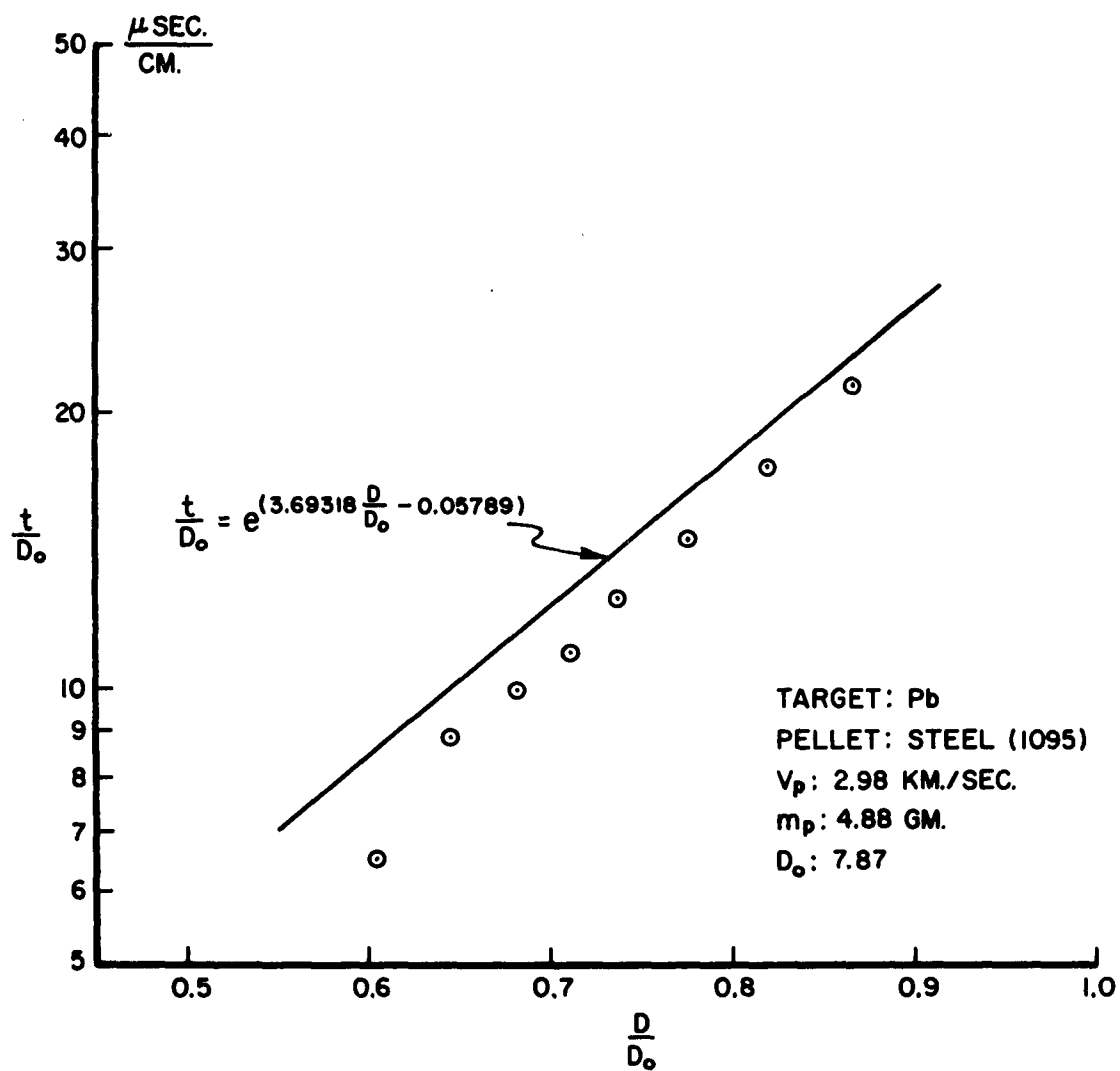


Figure 31

CRATER FORMATION—SEMI-INFINITE TARGETS

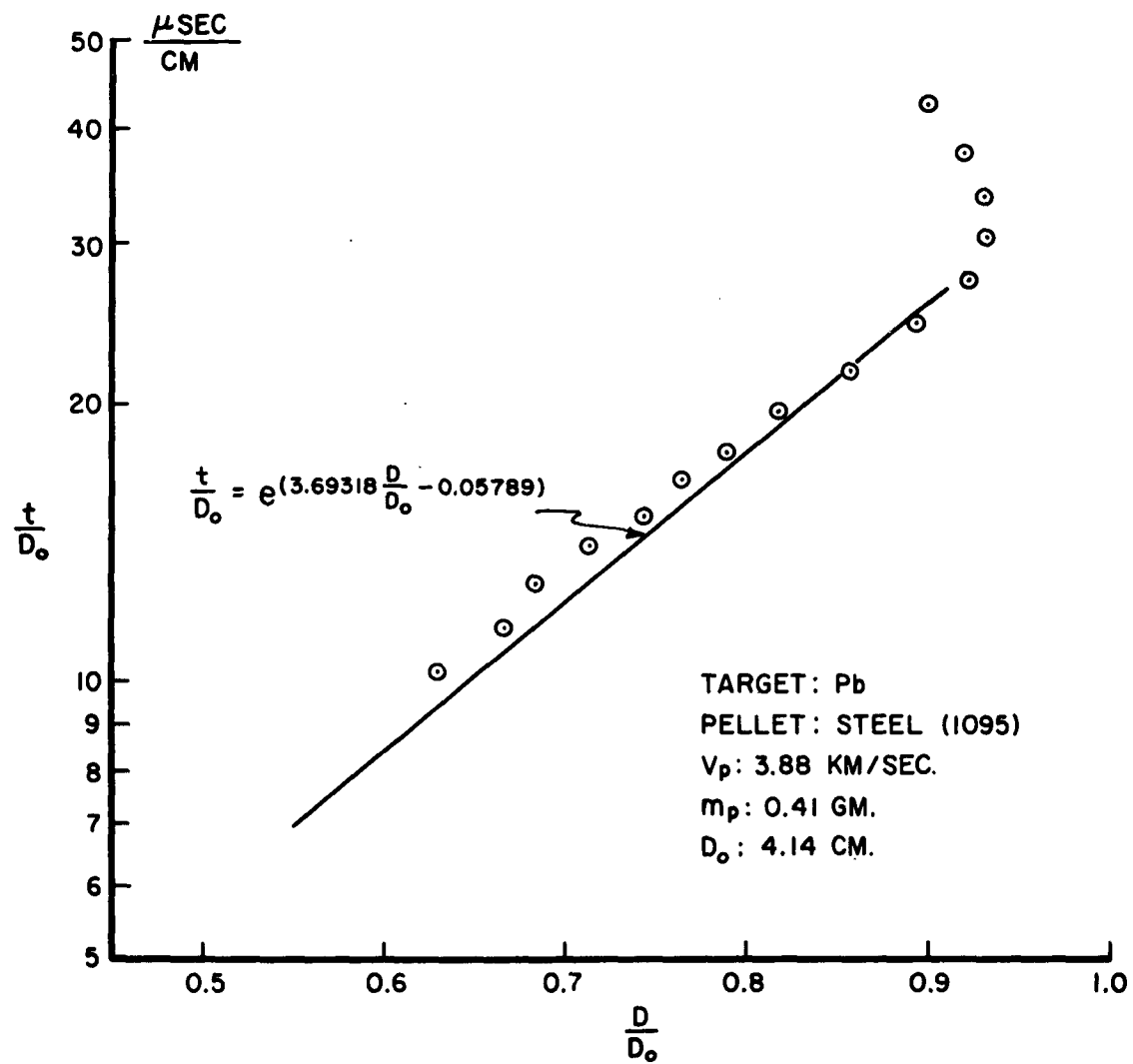


Figure 32

CRATER FORMATION — SEMI-INFINITE TARGETS

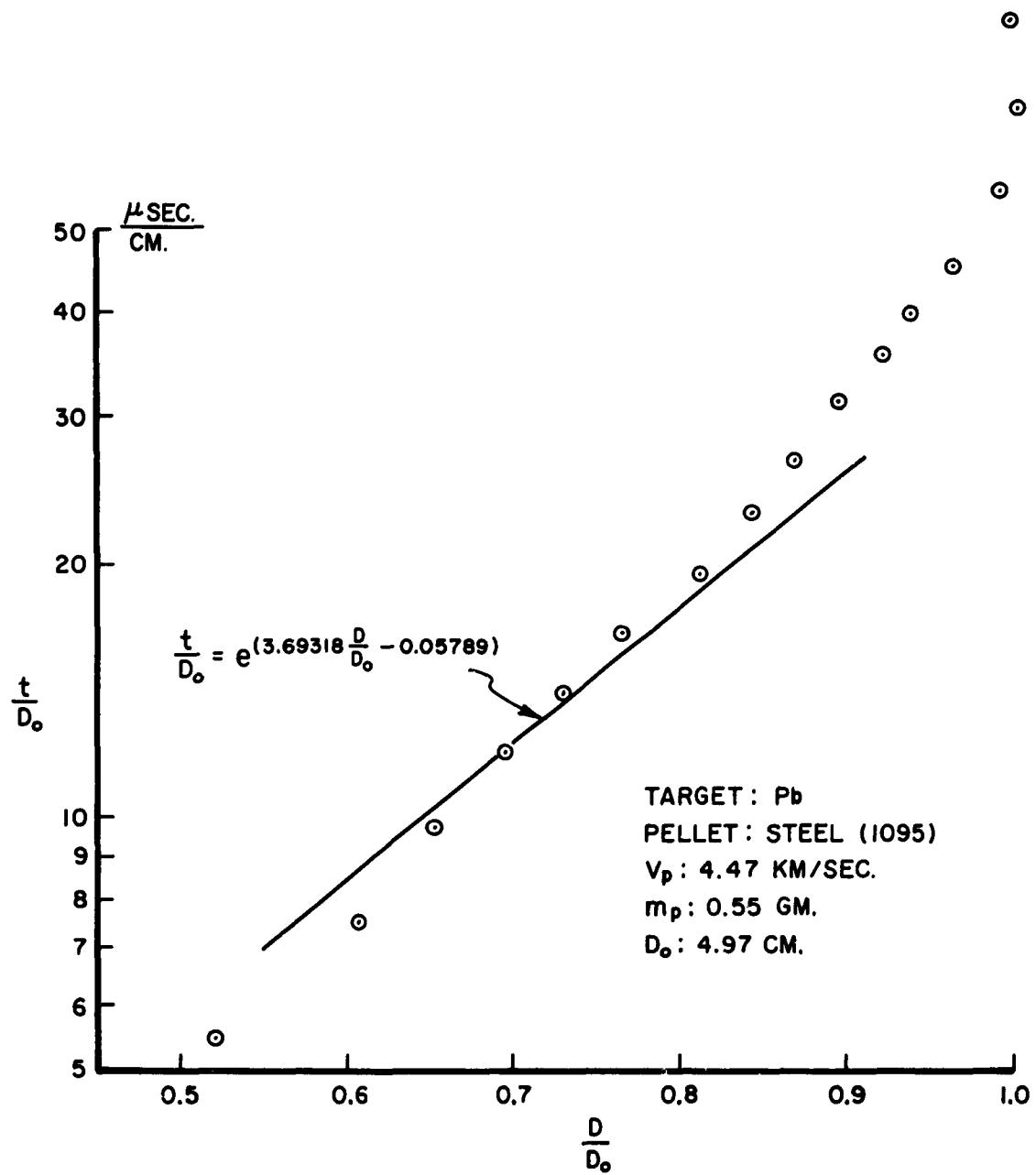


Figure 33

CRATER FORMATION — SEMI-INFINITE TARGETS

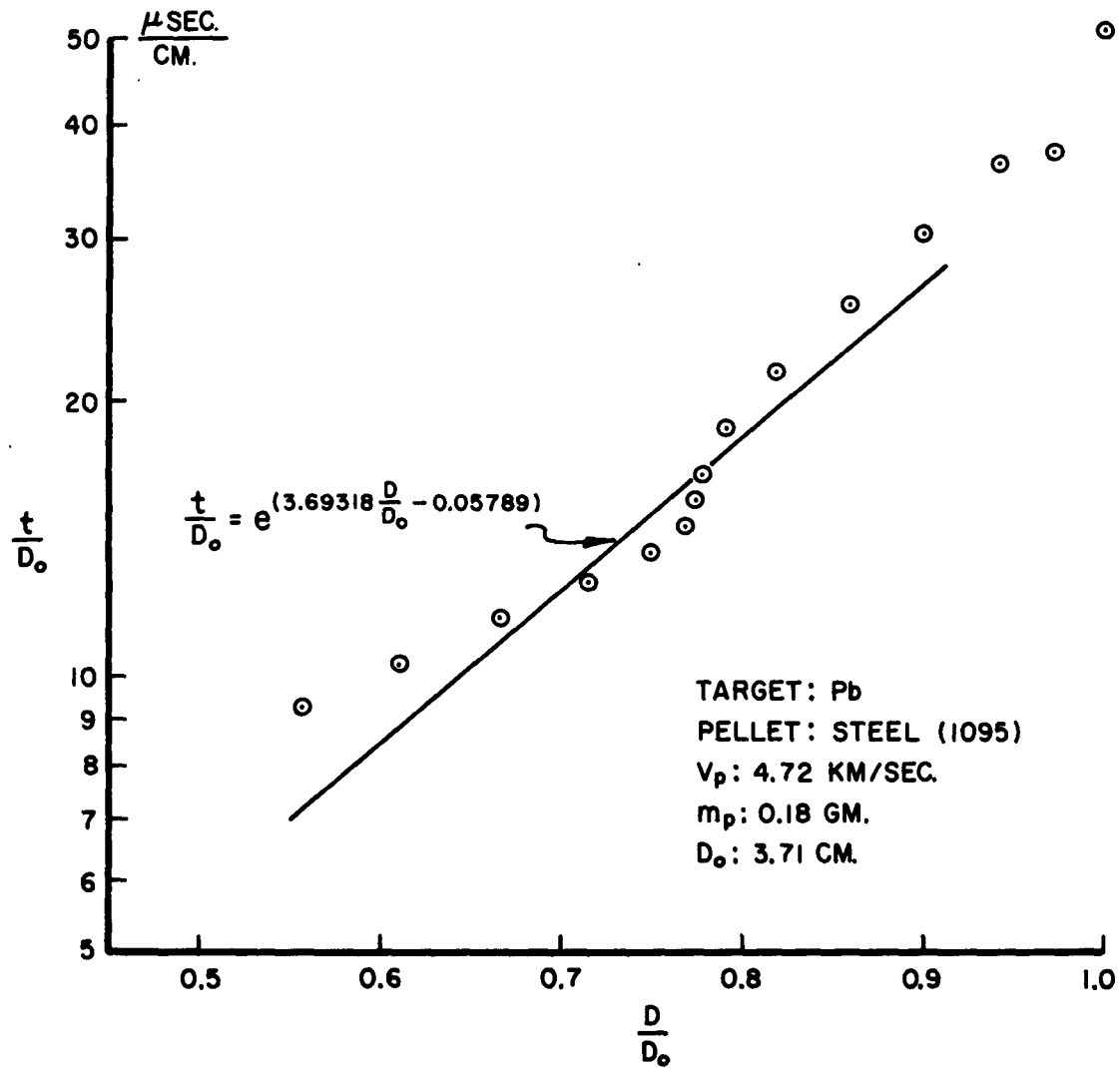
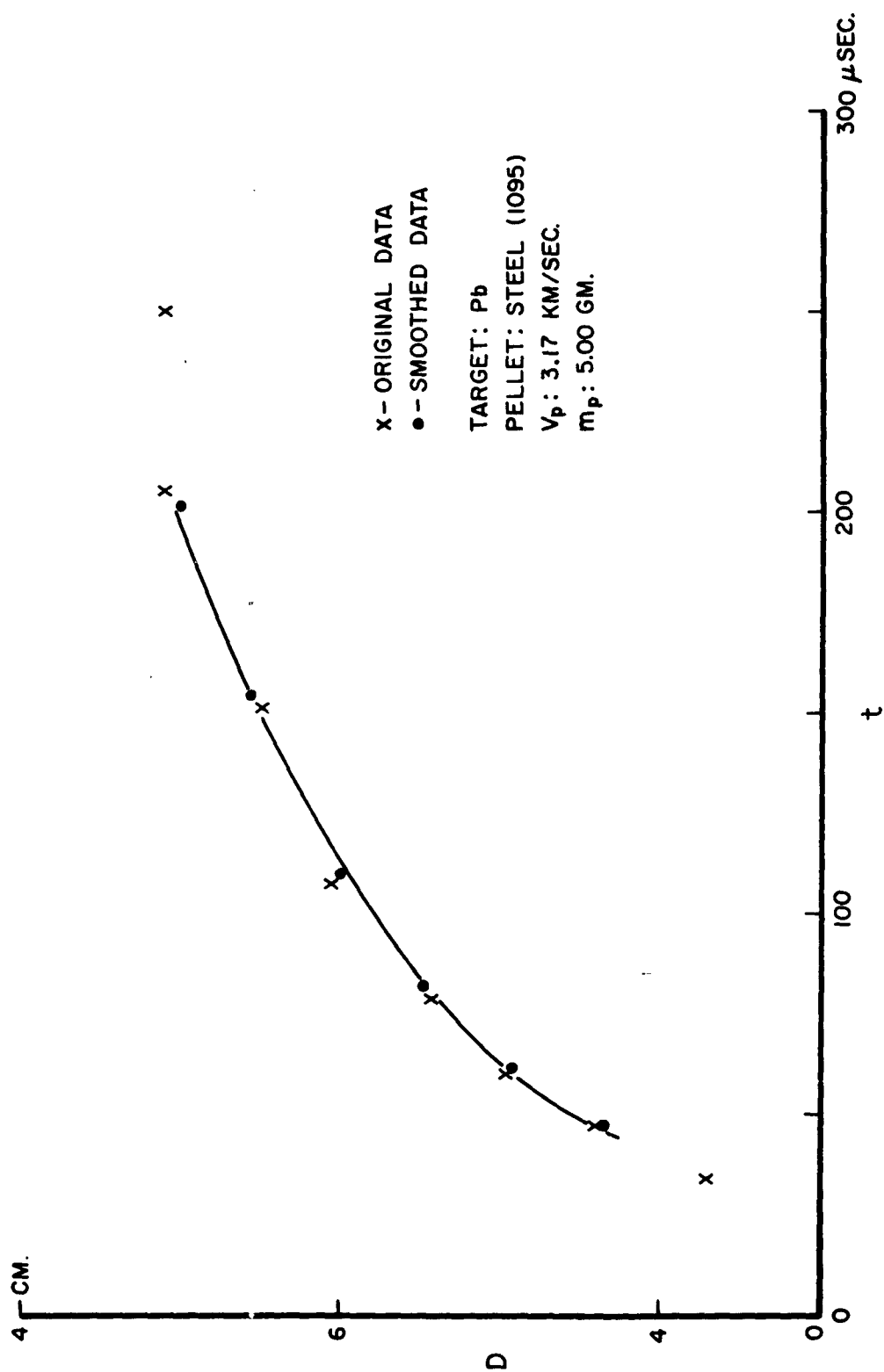


Figure 34

CRATER FORMATION — SEMI-INFINITE TARGETS



CRATER FORMATION — SEMI-INFINITE TARGETS

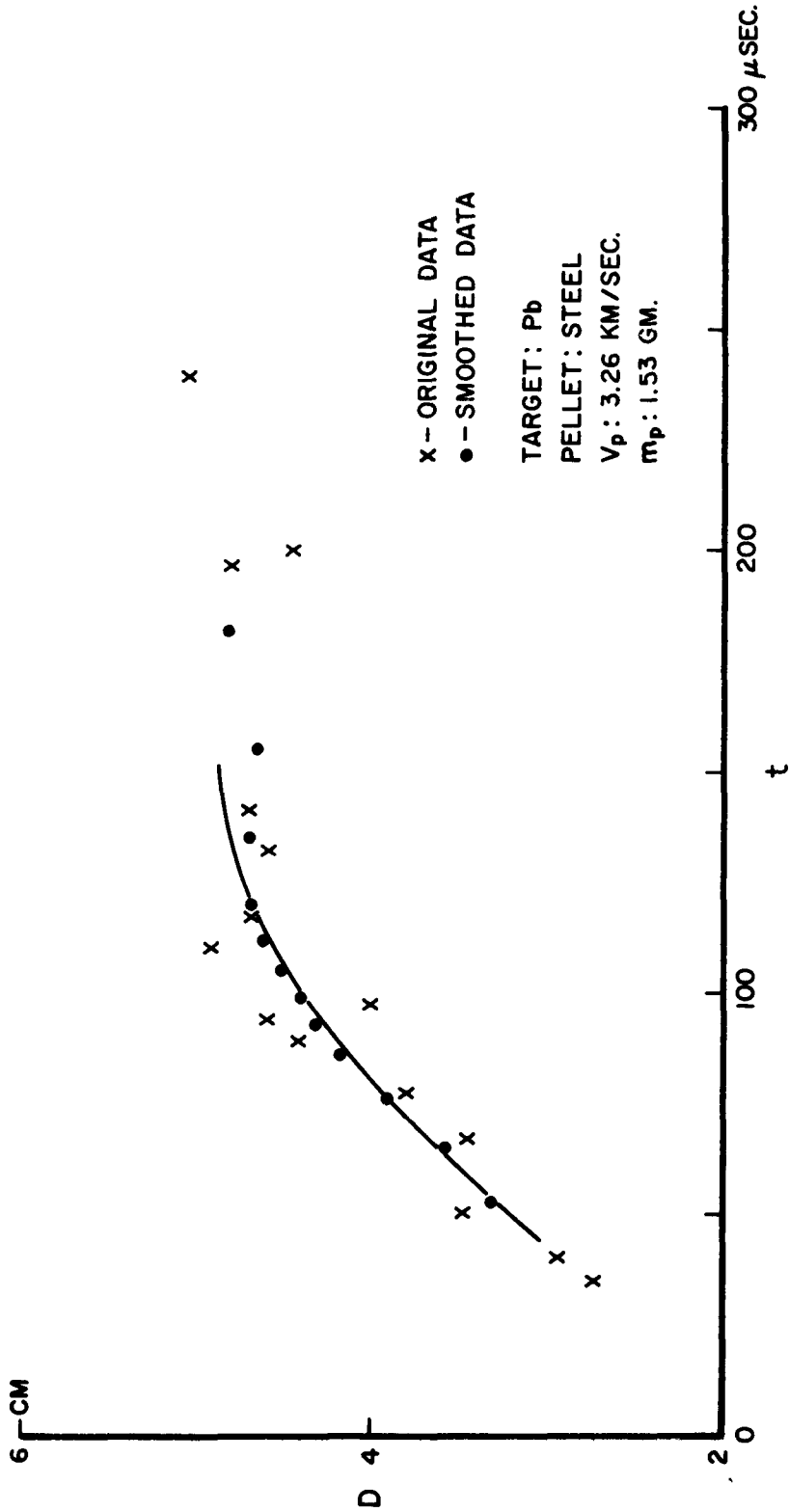
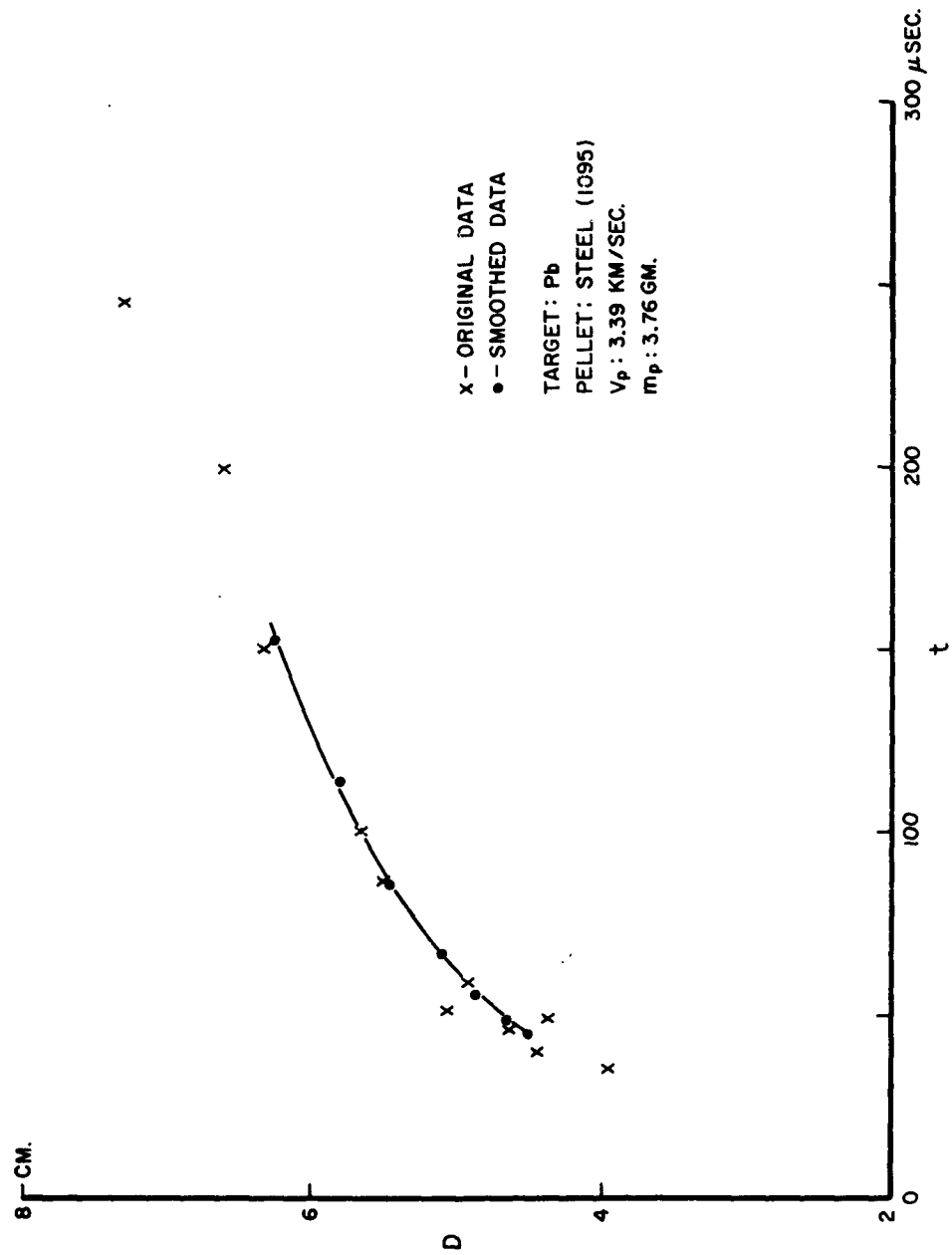


Figure 36

CRATER FORMATION — SEMI-INFINITE TARGETS



CRATER FORMATION — SEMI-INFINITE TARGETS

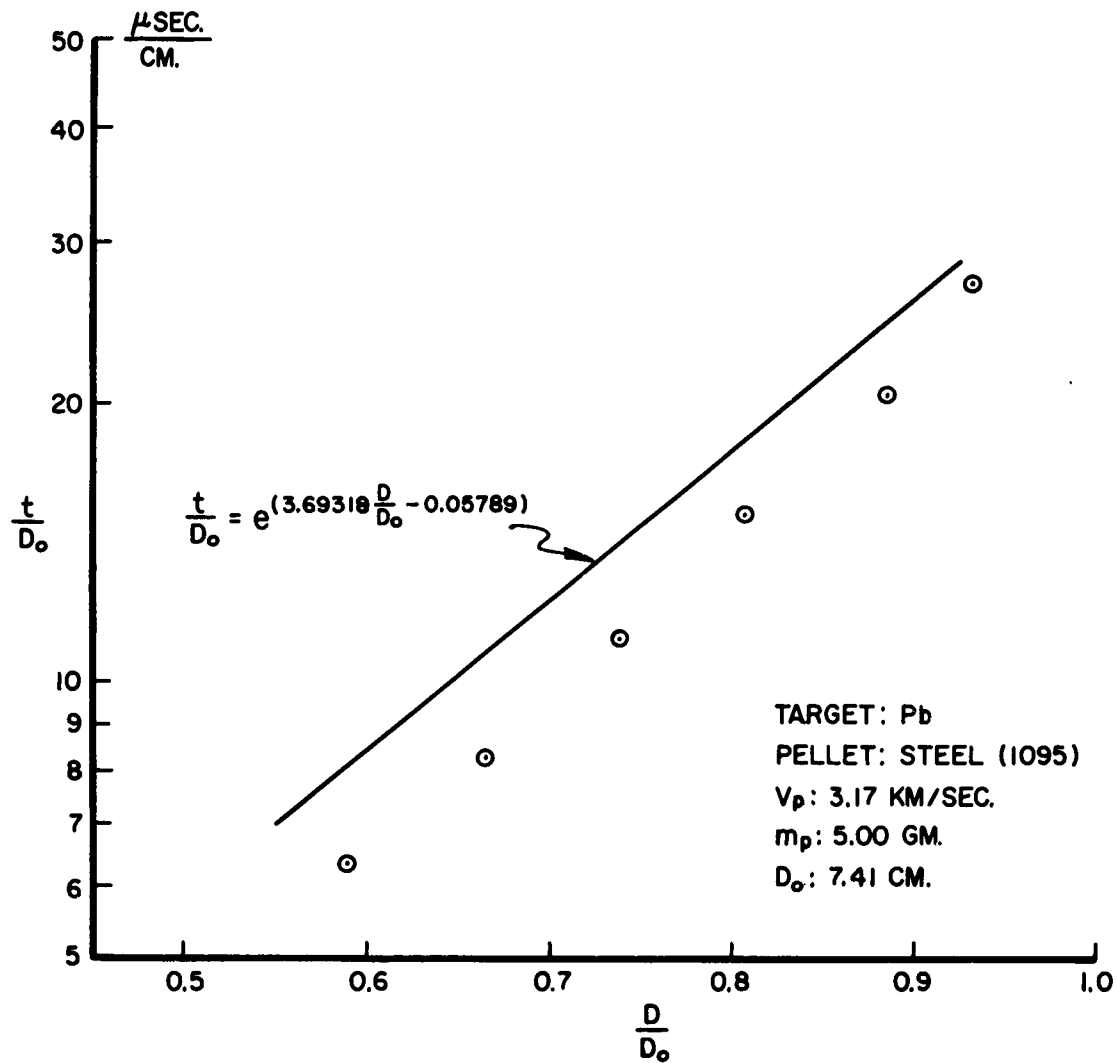


Figure 38

CRATER FORMATION — SEMI-INFINITE TARGETS

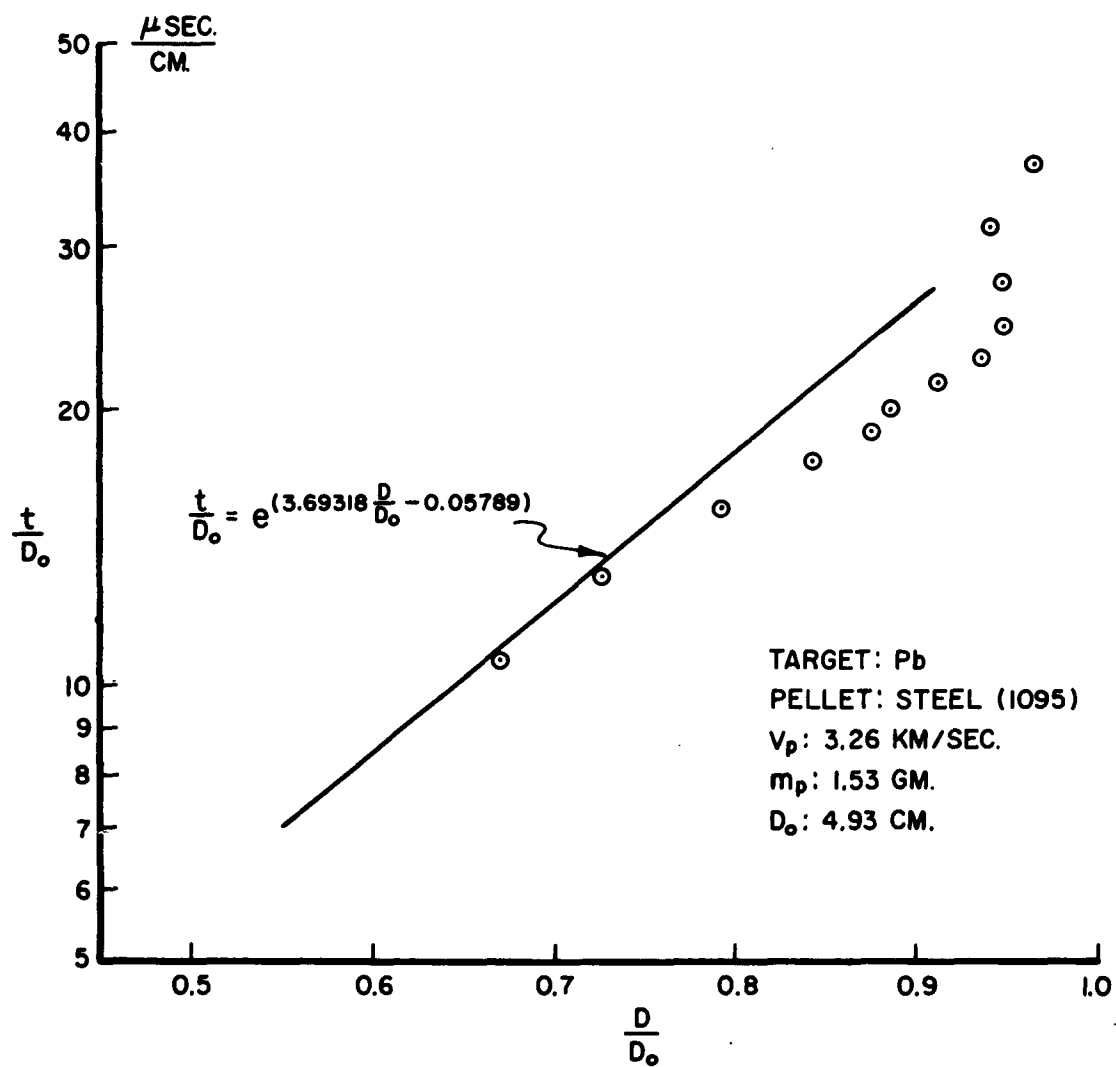


Figure 39

CRATER FORMATION — SEMI-INFINITE TARGETS

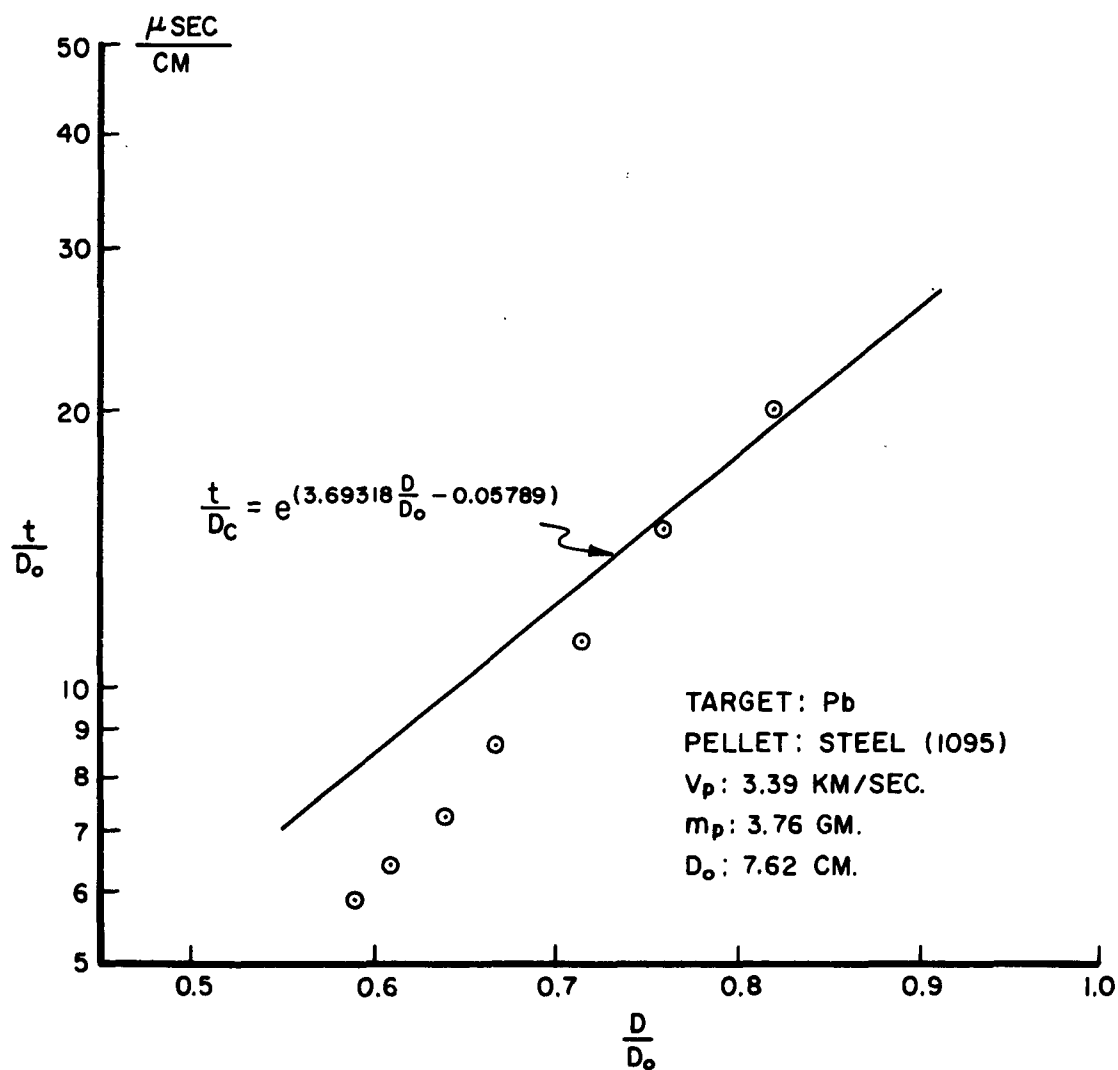
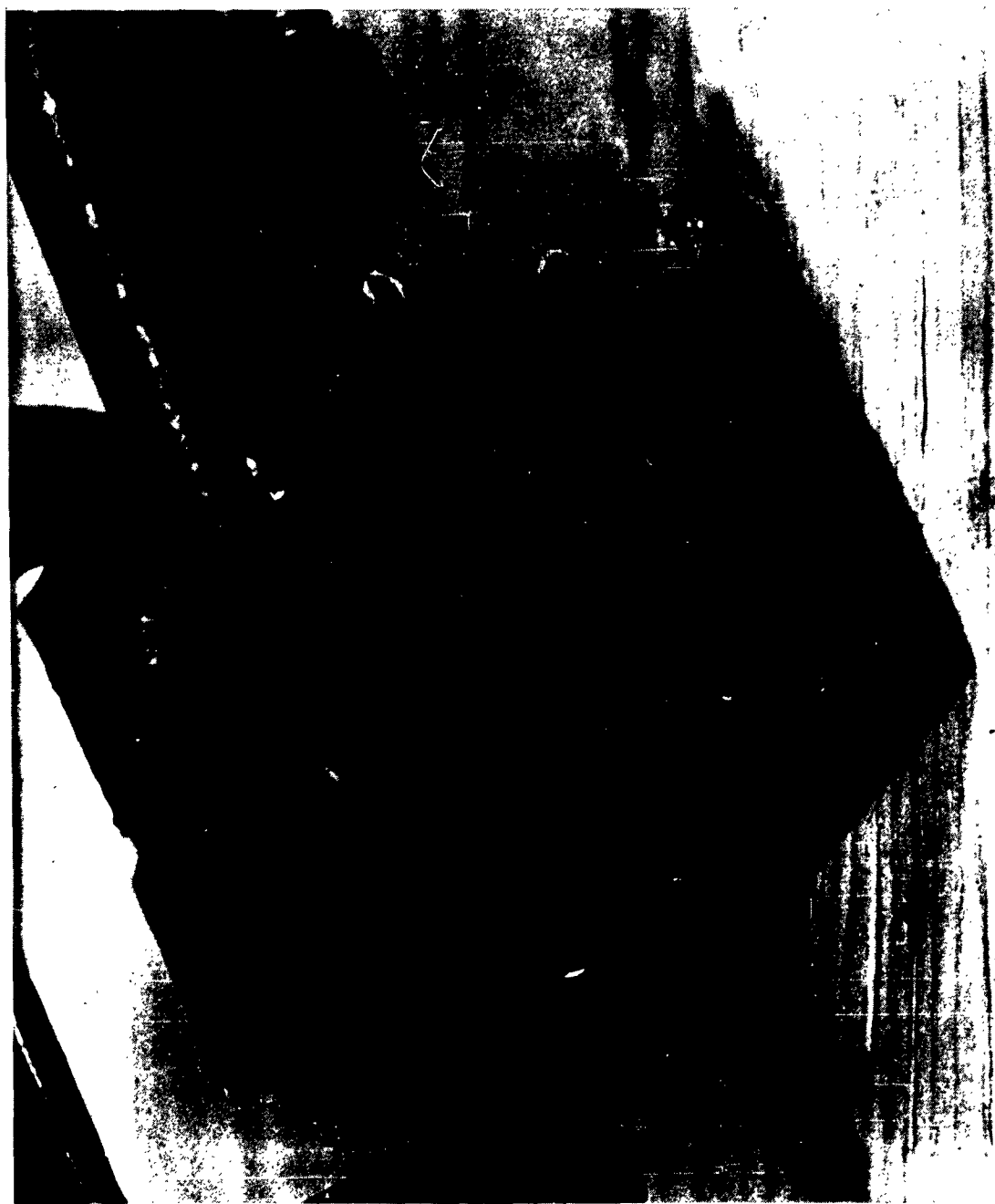


Figure 40

CRATER FORMATION—SEMI-INFINITE TARGETS



CRATER FORMATION—SEMI-INFINITE TARGETS

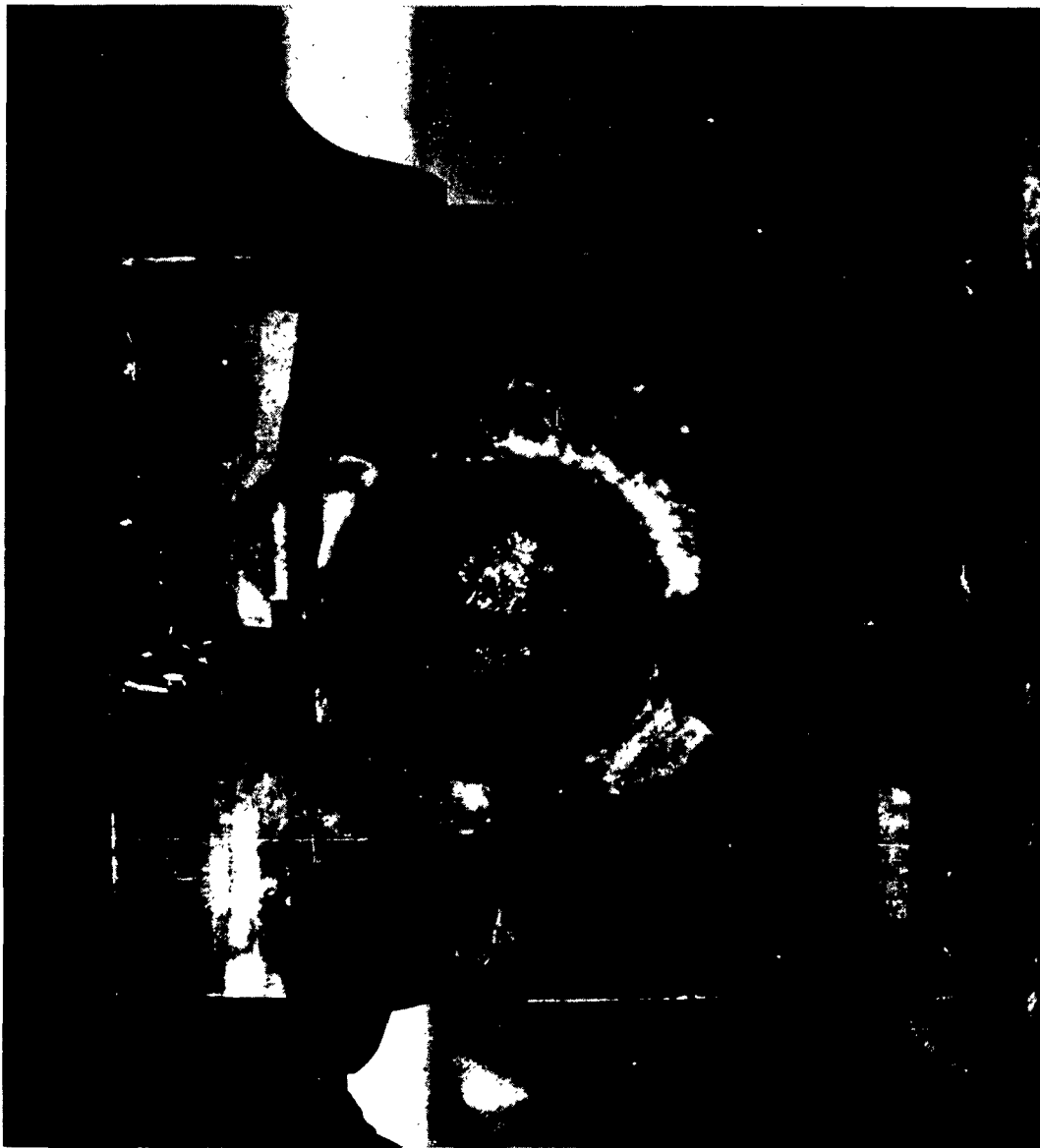


Figure 42

CRATER FORMATION—SEMI-INFINITE TARGETS



Figure 43

CRATER FORMATION — SEMI-INFINITE TARGETS

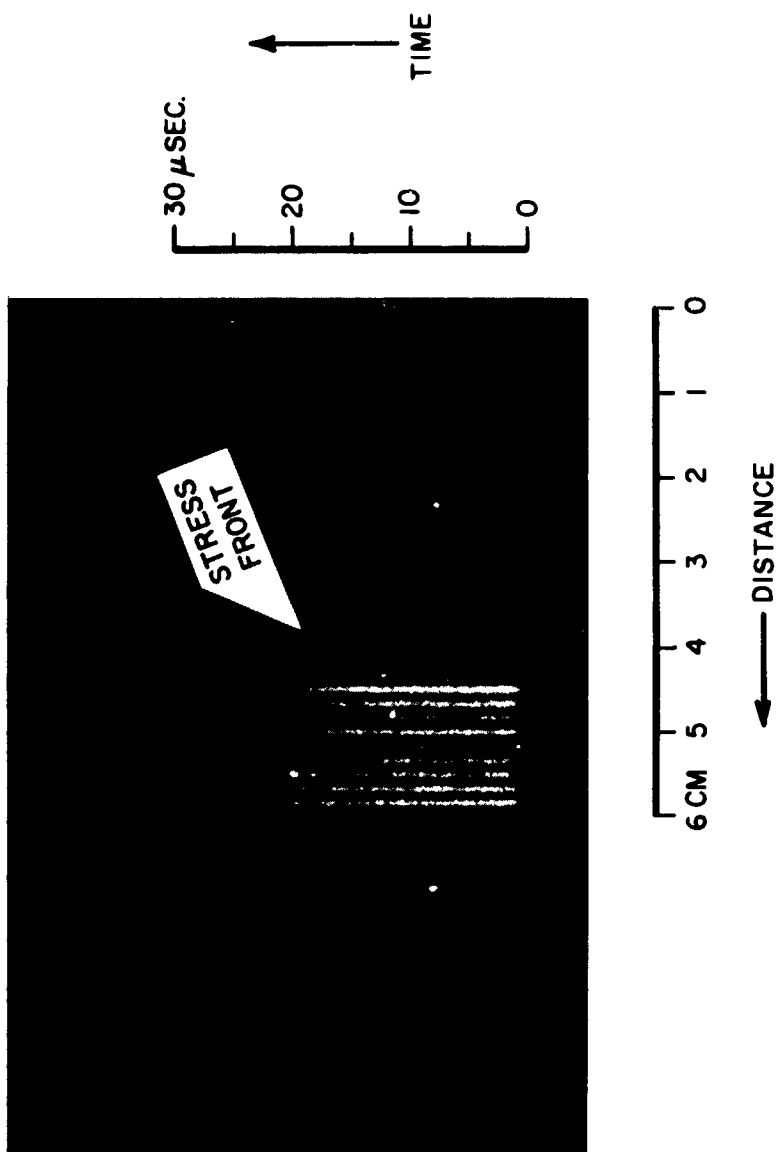


Figure 44

CRATER FORMATION—SEMI-INFINITE TARGETS

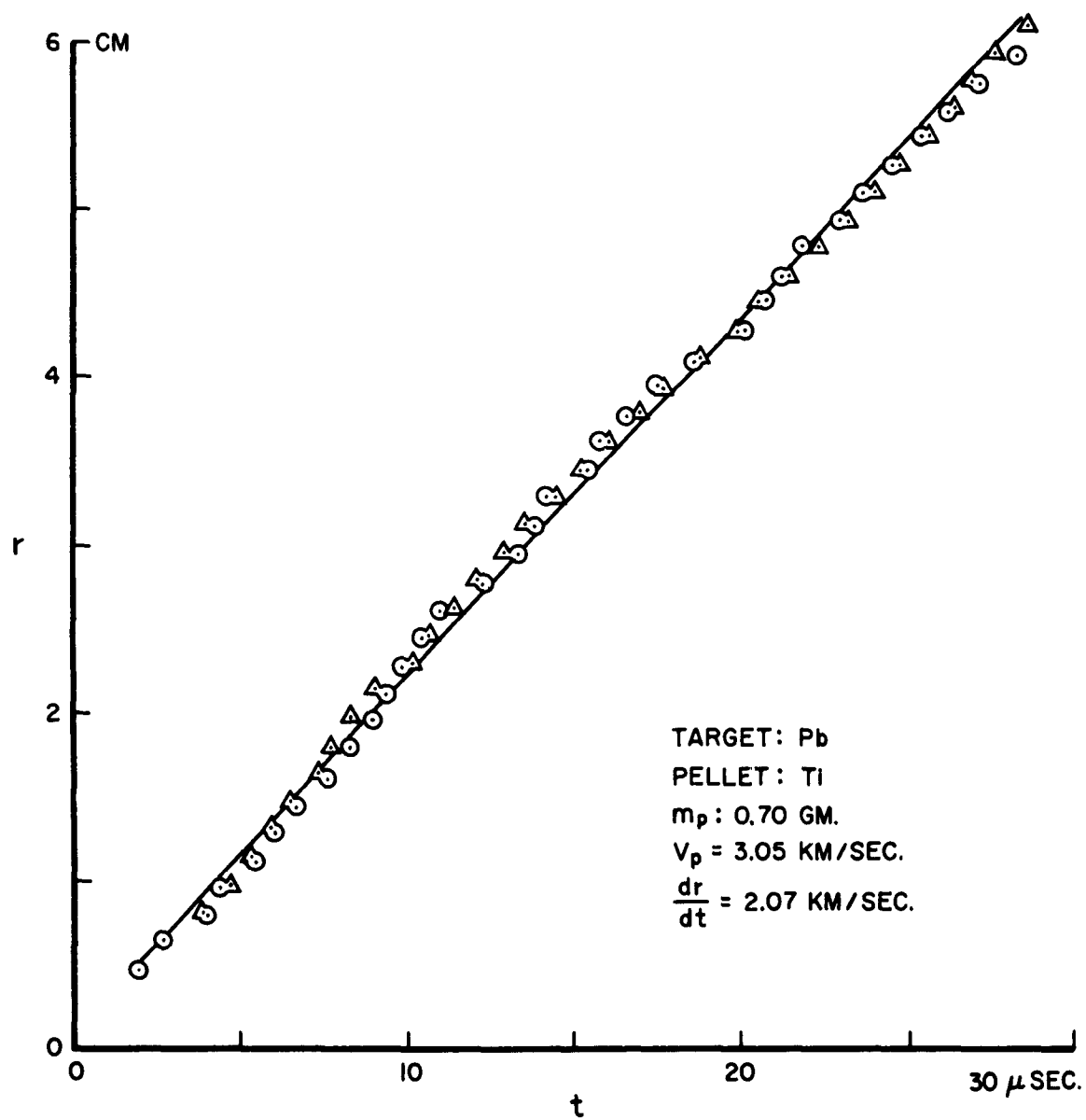


Figure 45

INFLUENCE OF TARGET STRENGTH ON HYPERVELOCITY
CRATER FORMATION IN ALUMINUM

J. H. Kineke, Jr.

L. G. Richards

Ballistic Research Laboratories
Aberdeen Proving Ground, Maryland

INFLUENCE OF TARGET STRENGTH ON HYPERVELOCITY
CRATER FORMATION IN ALUMINUM

J. H. Kineke, Jr.

L. G. Richards

ABSTRACT

Aluminum projectiles with velocity of 9.7 km/sec and beryllium projectiles with velocity of 15.5 km/sec have been used to produce craters in aluminum and aluminum alloy targets. Results indicate that the influence of the mechanical strength of the target in determining final crater dimensions extends unimpaired for impact velocities up to 15.5 km/sec. These data have also been used to verify the linear dependence of crater volume on projectile energy.

TARGET STRENGTH VS. CRATER FORMATION

INTRODUCTION

Earlier Hypervelocity Impact Symposia have seen the presentation of a number of papers dealing with observations of crater dimensions in semi-infinite metallic targets. The linear dependence of crater volume on projectile energy has been fairly well established, for impact velocities up to 6 km/sec. However, consideration of the effect of target strength has been limited and at best oblique. The purpose of the investigation reported in this paper is two-fold: 1. To determine whether or not crater dimensions are significantly influenced by target mechanical properties at impact velocities up to 15.5 km/sec; and 2. To examine the dependence of crater volume on projectile energy at impact velocities up to 9.7 km/sec.

Target Strength

a. Experimental Observations - Previous experimental investigations of the influence of target strength on the cratering process fall into two categories: studies of energy absorbing mechanisms, and empirical correlations of crater dimensions with various mechanical properties. Glass and Pond^(1a) have studied the mechanism of energy distribution in the target after impact in terms of static stress-strain relationships. Empirical correlations have been made of crater data with several mechanical strength properties, including shear strength^(2a), ultimate tensile strength^(2a), Brinell hardness^(1b),

TARGET STRENGTH VS. CRATER FORMATION

and yield strength^(3a). Several groups^(1c,3b) have also made empirical correlations of crater dimensions with ambient target temperature, with the implication that by varying the temperature some pertinent mechanical strength property of the target would also be varied and thus its influence noted. In general, the temperature correlations, as well as the strength correlations, have not pinpointed which strength properties are important, perhaps because the strength-temperature relations were not measured on the particular target materials, over the temperature range used in the impact tests. In most instances, strength parameters are not sufficiently independent to establish a preference, using handbook values. However, the empirical correlations have demonstrated, at least qualitatively,, that final crater dimensions do indeed depend on the mechanical and metallurgical properties of the target, for impact velocities up to 6 km/sec. At sufficiently high impact velocities, and hence high impact pressures, it is generally agreed that only the high pressure properties of materials, the density and the compressibility, are important in determining material behavior early in the crater formation process. Efforts to compute the entire crater formation process by a hydrodynamic approximation^(3c) require neglecting low pressure mechanical properties entirely. The investigation reported in this paper is designed to determine whether: 1. available projectile velocities have achieved a regime where density and compressibility predominate and mechanical strength effects are negligible; or 2. approach to the

TARGET STRENGTH VS. CRATER FORMATION

lower limit of such a regime is indicated.

These questions have been examined by considering the ratio of crater volume in a mechanically strong aluminum alloy, to crater volume in a relatively weak material, commercially pure aluminum. In each case, the high pressure properties, the density and equation of state are identical. If, then, the high pressure properties predominate, the ratio would be expected to be near unity. On the other hand, if the ratio increases with increasing velocity, the role of the mechanical strength can be said to be decreasing.

As a basis for comparison with lower velocity data, 1100 aluminum and 2014 aluminum alloy were chosen as target materials, since, at the Fifth Hypervelocity Symposium, Halperson and Atkins^(3a) of NRL reported crater data for aluminum projectiles into these materials. In order to assure quasi-infinite targets, diameters of 25 cm and thicknesses of 20 cm were used. Impact surfaces were machined in each target, Brinell hardnesses were measured, and ambient target temperatures at the time of firing were recorded, all as controls on the reproducibility of the targets used.

Two sets of experiments were conducted, one with aluminum projectiles at 9.7 ± 0.1 km/sec, and the second with beryllium projectiles at 15.5 ± 0.4 km/sec. In both cases, velocities were determined flash radiographically. The 1100 aluminum projectile was fired from a BRL Inhibited-Jet Charge, which is described in detail by Kronman in another paper at this Symposium^(4a). The projectile is somewhat elongated on shape, having a length-to-diameter ratio between 2.5 and 3, as shown in Figure 1. The

TARGET STRENGTH VS. CRATER FORMATION

beryllium projectile is a BRL Jet-Pellet, similar to that described at the Fifth Hypervelocity Impact Symposium^(3e). Flash radiographs indicate that the pellet is not an integral unit, but rather a cluster of tightly packed particles with a length-to-diameter ratio of five to ten.

A tabulation of crater data appears in Table I, together with a list of target parameters. Typical craters in each of the materials are shown in Figure 1. For a given material there was little difference in appearance of craters at the two impact velocities. At both velocities craters in 1100 aluminum were smooth-walled, with large lips, i.e., in general gave the appearance of typical hypervelocity craters in ductile metals. In contrast, the craters in the 2014 alloy were irregular in shape, with appreciable lip spall, because 2014 alloy is less ductile than 1100 aluminum. Because of this semi-brittle behavior there is more scatter in the depth and diameter data, taken individually, than in the crater volume data, which represents an averaging over the entire crater. For this reason, volume was chosen as the basis for comparison.

An insight into the relative importance of target strength in determining final crater volume can be gained from Figure 2. The ratio of crater volume in the high strength material to that in the low strength material is plotted as a function of the impact velocity. The solid line represents the low velocity NRL results. The plotted ratios indicate no tendency to increase with increasing impact velocity, as would be expected if the effect of target strength on the crater formation process was becoming relatively less important.

b. Conclusions -

1. For impact velocities up to 15.5 km/sec, the mechanical strength of the target is a significant property in determining final

TARGET STRENGTH VS. CRATER FORMATION

crater dimensions.

2. For impact velocities up to 15.5 km/sec, there is no indicated tendency that the influence of mechanical strength of the target on final crater dimensions is decreasing.

ENERGY DEPENDENCE

a. Experimental Observations - In order to examine the energy dependence of crater volume, it is necessary to know not only the projectile velocity, but also the projectile mass. The mass of the 9.7 km/sec aluminum projectile described earlier has been determined to be 3.7 ± 0.3 grams^(4a). The mass of the 15.5 km/sec beryllium projectile is about 0.2 grams, but somewhat uncertain, so beryllium data has not been used. The fact that the beryllium mass has not been satisfactorily determined does not in any way affect the conclusions of the previous section, since only ratios of crater volumes were used. A plot of crater volume per unit projectile mass as a function of the impact velocity is shown in Figure 3, for both 1100 aluminum and 2014 aluminum alloy. Also plotted, as solid lines up to 6 km/sec, with extrapolations to higher velocities, are the NRL results. The recently acquired high velocity data are in agreement with the extrapolated lower velocity curves.

b. Conclusion - The oft-stated conclusion that crater volume is proportional to projectile energy is further supported for impact velocities up to 9.7 km/sec.

TARGET STRENGTH VS. CRATER FORMATION

REFERENCES

1. Fourth Hypervelocity Impact Symposium, Eglin AFB, April 1960.
 - a. Coy M. Glass and Robert B. Pond - "A Metallurgical Approach to the Hypervelocity Problem."
 - b. James B. Feldman, Jr. - "Volume-Energy Relation From Shaped Charge Jet Penetrations."
 - c. F. E. Allison, K. R. Becker, and R. Vitali - "Effects of Target Temperature on Hypervelocity Cratering."
2. Third Hypervelocity Impact Symposium, Chicago, October 1958.
 - a. H. J. James and J. S. Buchanan - "Experimental Studies of Penetration by Shaped Charge Jets."
3. Fifth Hypervelocity Impact Symposium, Denver, October 1961.
 - a. W. Herrmann and A. H. Jones - "Correlation of Hypervelocity Impact Data."
 - b. M. Rockowitz, C. Carey, and J. Dignam - "Hypervelocity Impact of Heated Copper."
 - c. A. E. Olshaker and R. L. Bjork - "Hydrodynamics Applied to Hypervelocity Impact."
 - d. S. M. Halperson and W. W. Atkins - "Experimental Observations of Impact."
 - e. S. Kronman and J. H. Kineke, Jr. - "Explosive Devices for Projecting Hypervelocity Pellets up to 21 Km/sec."
4. Sixth Hypervelocity Impact Symposium, Cleveland, April 1963.
 - a. S. Kronman and A. Merendino - "Inhibited Jet Charge."

TARGET STRENGTH VS. CRATER FORMATION

TABLE I

Target Material	BHN	v_p km/sec	Temp °C	P_c cm	σ_m cm	D_c cm	σ_m cm	V_{c3} cm ³	σ_{m3} cm ³
Al-1100	24-25	9.7	5	5.90	0.17	8.44	0.13	230	18
Al-2014	137	9.7	-4	5.00	0.07	5.60	0.17	92.5	4.0
Al-1100	26-27	15.5	10	4.24	0.31	4.02	0.14	35.6	2.5
Al-2014	146-156	15.5	10	2.97	0.67	3.36	0.37	9.2	0.6

TARGET STRENGTH VS. CRATER FORMATION



AL INHIBITED JET
 V_p : 9.7 KM/SEC.



1100 ALUMINUM
TARGET

0 1 2 3 4 5
CM



2014 ALUMINUM
TARGET

Figure 1

TARGET STRENGTH VS. CRATER FORMATION

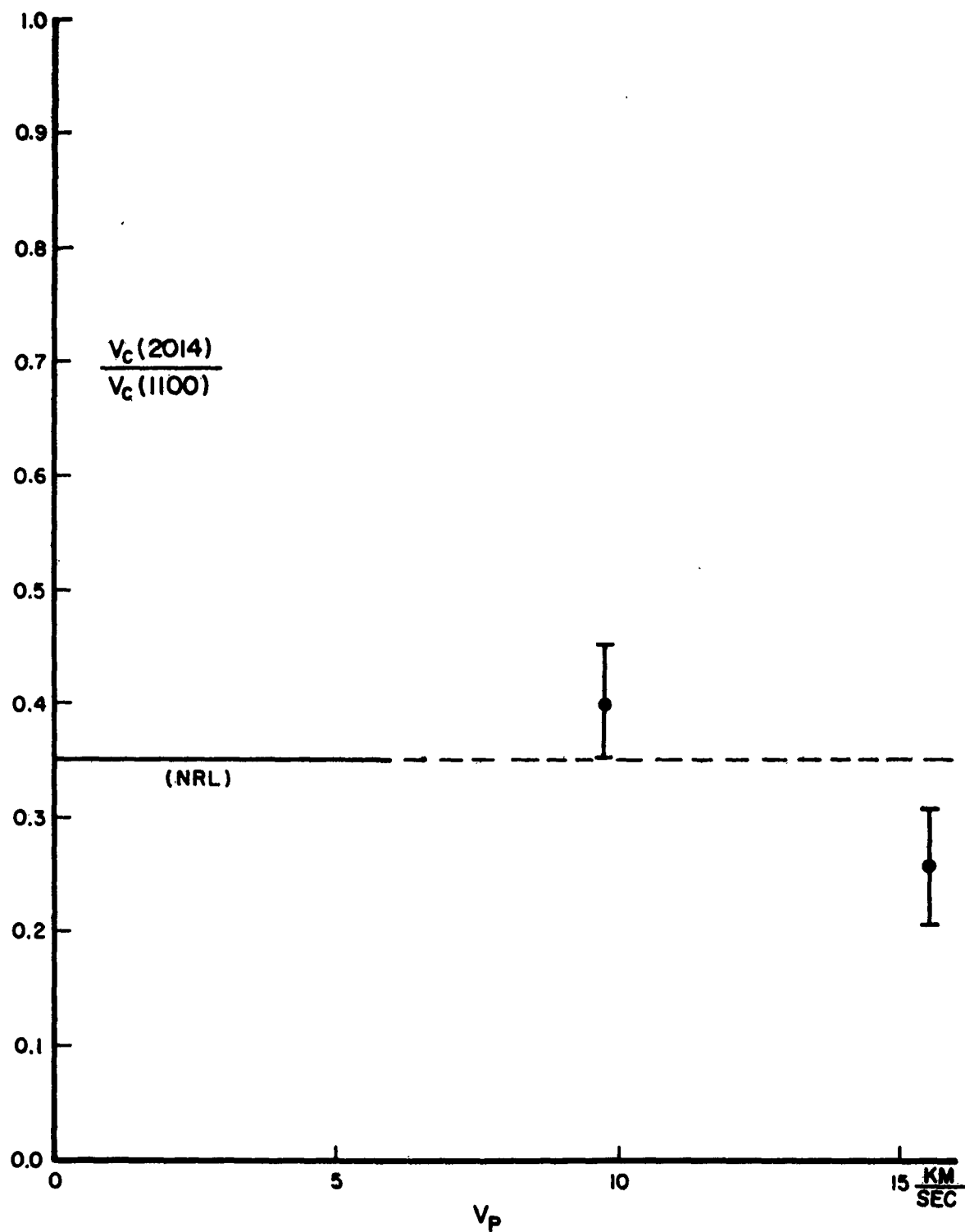


Figure 2

TARGET STRENGTH VS. CRATER FORMATION

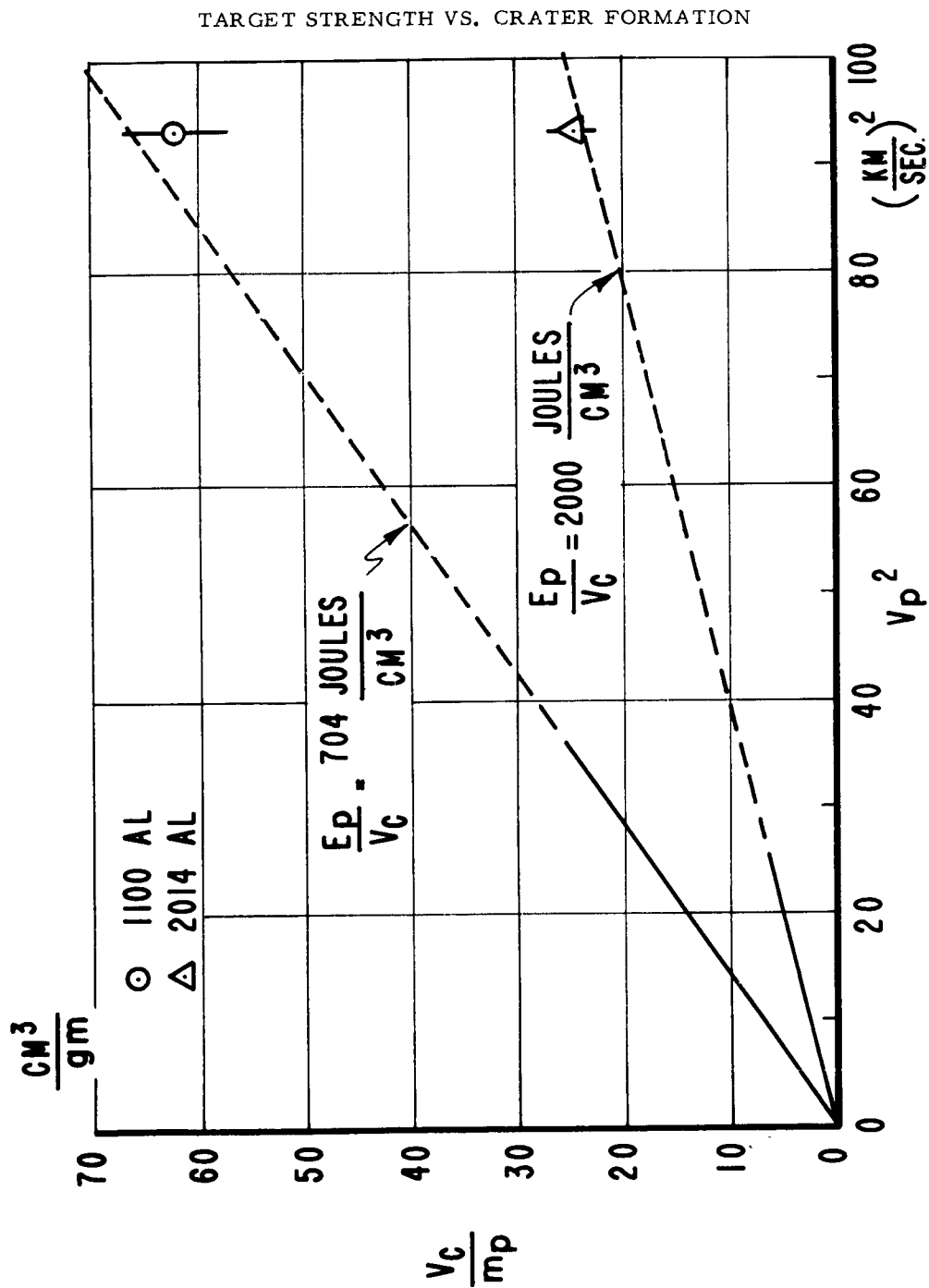


Figure 3

SOME PHENOMENA ASSOCIATED WITH
IMPACTS INTO ALUMINUM

S.M. Halperson

Sponsored by
Office of Naval Research

U.S. Naval Research Laboratory
Washington 25, D.C.

IMPACTS INTO ALUMINUM

ABSTRACT

Impacts of aluminum spheres at velocities up to 7 km/sec have been made into aluminum targets of 1100F and 2014. At the velocities reached target strength still appears to have an effect on penetration. A parametric study of the effect of obliquity on the perforation of finite plates of 2024 aluminum was made. Steel and aluminum projectiles were fired at 5.70 km/sec., and obliquity effects on hole area were noticeable after 25°.

SOME PHENOMENA ASSOCIATED WITH IMPACTS INTO ALUMINUM*

S. M. Halperson
U.S. Naval Research Laboratory

INTRODUCTION

The study of hypervelocity impacts into very thick or "semi-infinite" targets and finite thickness plates is currently a vogue in the fields of experimental and theoretical mechanics. One reason for this is the determination of the extent of the meteoroid threat to satellites and space vehicles. Another reason is the interest in material behavior under high strain-rates and large impulsive loads. The Naval Research Laboratory is interested in both problems, and this paper will present the results of impact tests which are deemed pertinent.

Impacts have been made into thick blocks of 2014 and 1100F aluminum by aluminum (2024) spheres. Damage characteristics such as depth of penetration and crater volume have been correlated with impact parameters to obtain an insight into phenomena which may be associated with impacts at meteoric velocities (11 km/sec - 70 km/sec).

A parametric study has been made of the obliquity effects on hole size for different thicknesses of 2024 aluminum. Steel and aluminum spheres at velocities of 5.70 km/sec impacted four thicknesses of aluminum at four angles of obliquity.

THICK TARGET EXPERIMENTS

There has been a continuation of the previously reported (ref. 1) cratering experiments on two types of aluminum. These are 1100F, commercially pure aluminum, and 2014, a structural grade. The maximum velocity was 6.99 km/sec with a 1.27 grams

* Work supported by the Office of Naval Research

IMPACTS INTO ALUMINUM

aluminum sphere. The majority of the impacts have been into 1100F, however there has been sufficient testing of the 2014 to indicate pertinent trends.

A. Depth of Penetration

Figure 1 shows the depth of penetration beneath the original target surface, P , normalized by the sphere diameter, D_s , plotted as a function of impact velocity. Also shown is the zone postulated by Bjork in his hydrodynamic theory of penetration (ref. 2). A least-squares fit of the data above 4 km/sec has been made. An equation of the form $\frac{P}{D_s} = Av^n$ was chosen, where v is the impact velocity and A and n are determined from the fit. For the 2014 aluminum A is 0.468 and n is 0.751; the 1100F points produced A equals 1.146 and n equals 0.477. An exponent n equal to 1/3 indicates that penetration is dependent on the impact momentum, while n equal to 2/3 indicates an energy dependency. It may be possible that for the velocity extremes examined material strength is more important for the stronger alloy than for the soft, nearly pure aluminum.

Dotted extrapolations of the empirical equations are presented. (These are shown merely to indicate the possible trends and may change with increased data.) Extending the curves beyond the intersection would not be physically meaningful since that would indicate for an equivalent projectile-velocity situation the penetration into the hard aluminum would be greater than into the soft aluminum. These pass through and out of the region defined by Bjork. If extended these curves merge at a velocity of twenty-six kilometers per second.

B. Relationships Between Crater Volume and Impact Energy

One model of hypervelocity impact proposed (ref. 3)

IMPACTS INTO ALUMINUM

states that for hypervelocities the impact energy per unit of crater volume is constant for a given material and is dependent on the target strength. Figure 2 presents the energy/volume curves for 1100F and 2014 aluminum. The data are linear but non-constant. The equations of the lines can be considered to be of the following form

$$\frac{E}{V} = c_1 v + c_2 \quad (1)$$

where c_1 is the slope of the line and c_2 the intercept on the energy/volume axis. Least squares fits of the data give values of $c_1 = 0.1315$, $c_2 = 1.313$ for 2014 aluminum and $c_1 = 0.0637$, $c_2 = 0.4160$ for 1100F aluminum. The energy is calculated in units of 10^3 joules; the volume is measured in cubic centimeters and the velocity is in kilometer/sec. The expression proposed in ref. 3 is written as

$$\frac{E}{V} = c_4 B \quad (2)$$

where c_4 is a constant and B is the Brinell Hardness Number of the target material.

Assuming a crater hemispherical in shape, an expression for penetration can be obtained from equations (1) and (2). Equation (1) leads to

$$\frac{P}{D_s} = \left(\frac{3mv^2}{4\pi(c_1 v + c_2)} \right)^{1/3} \cdot \frac{1}{D_s} \quad (3)$$

where m is projectile mass and the other terms are as previously defined. If $c_1 v$ becomes much greater than c_2 , c_2 can be dropped and this leads to a dependency on penetration to impact momentum. Assuming constant energy/volume it follows that

$$\frac{P}{D_s} = \left(\frac{3mc_4 v^2}{4\pi B} \right)^{1/3} \cdot \frac{1}{D_s} \quad (4)$$

Figures 3 and 4 show the equations plotted for the two aluminums and the available data. There is good agreement

IMPACTS INTO ALUMINUM

between the data and the curves.

The extrapolations shown are indicative of observations obtained for a specific velocity range and are plotted to show trends. Considerably more tests are needed at velocities exceeding 6 km/sec before firm conclusions can be drawn concerning the fundamental mechanism of penetration at meteoroid velocities. This is quite critical in evaluating the hydrodynamic model of penetration which neglects the higher order shear stress and heat conduction terms in the Navier-Stokes equation of hydrodynamics.

A rational model should be based on energy partition and measurements, if possible, should be made of momenta associated with front surface ejecta and thermal effects associated with the impact.

IMPACTS INTO FINITE PLATES OF 2024 ALUMINUM

The analysis of phenomena associated with collisions between thin plates and hypervelocity fragments has been the object of much study. Analysis of the meteoroid threat to satellites and space craft is the main impetus for this work. Emphasis has been on behind-the-target damage and spall studies, not specifically on surface effects.

A program has been instituted to examine the effect of projectile density and obliquity on the hole size of 2024 plates. The holes discussed herein are those which would be seen after projecting light rays perpendicular to the target. A parametric study was made utilizing four thicknesses, four obliquities and two projectiles. Table 1 shows the test conditions and input parameters.

TABLE I

Resume' of Firings Into 2024-T3 Aluminum Plates

Aluminum Projectile:	0.476 cm sphere, 0.158g
Steel Projectile:	0.476 cm sphere, 0.439g
Angles of Obliquity:	90°, 45°, 25° and 10°
Thickness Ratios,	$\frac{t}{d}$: $\frac{1}{3}$, $\frac{2}{3}$, 1, $\frac{8}{3}$ and 4*

* 2024-T4

IMPACTS INTO ALUMINUM

Steel and aluminum spheres of the same diameter, 0.476 cm, were chosen to introduce the effect of density without introducing a size effect. The ability to control velocity of these projectiles is excellent. The average velocity was 5.70 km/sec for all tests.

Figure 5 shows the average hole diameter, D_h , plotted against target thickness, t , at normal incidence. Both items are normalized by the sphere diameter. The convention of dividing by the sphere diameter will be observed for preceding graphs.

For the thinnest targets the intense shock is relieved by the rarefactions from the rear surface so that the hole size approaches the projectile diameter with decreasing thickness. As thickness increases the steel projectile's greater lateral momentum has a longer time to act and the hole is larger than that due to the aluminum projectile. For the range of thicknesses noted the targets struck by aluminum projectiles start to exhibit cratering characteristics at $t/d = 1$ while the targets impacted by steel projectiles exhibit thin target damage for all thicknesses investigated.

Figures 6 and 7 show for the two projectiles the square root of the ratio of the area of the hole to the area of the projectile plotted as a function of impact velocity. The aluminum projectile data show slight change in area with respect to angle above about 25° . Then a marked decrease occurs. At 10° the projectile shatters on the target surface and no remnants of the projectile are found behind the target. On the contrary, the steel projectile data showed an increasing trend and maximum area for t/d ratios of $1/3$, $2/3$, and 1 . Both phenomena can be attributed to the fact that the projectile is in effect "seeing" a progressively thicker target. The aluminum projectile is effectively attacking

IMPACTS INTO ALUMINUM

targets with t/d ratios greater than one. Incidences and thicknesses which were not represented by datum points were not perforated. At ten degrees the steel projectile impacts, shatters and ricochets off the plate surface. Negligible spall fragments are found behind the target, and the hole is primarily caused by the shock wave departing from the impact point.

SUMMARY

Impact data obtained with aluminum spheres at velocities up to 7 km/sec have not resolved the question of material strength effects on perforation. Correlation of existing data with empirical expressions derived from neglecting and introducing strength effects is within the range of experimental scatter.

Obliquity studies of impacts of steel and aluminum projectiles on 2024 aluminum plates show pronounced effects on hole size after the obliquity reaches 25° .

ACKNOWLEDGEMENTS

The author is indebted to J. Condon, P. Boltz, and R. Fuller of NRL for conducting the experimental studies associated with this paper.

IMPACTS INTO ALUMINUM

REFERENCES

1. Halperson, S.M., Atkins, W.W., "Observations of Hypervelocity Impact", Proceedings of Fifth Symposium on Hypervelocity Impact, VOL I - Part 2, April 1962.
2. Olshaker, A.E., Bjork, R.L., "Hydrodynamics Applied to Hypervelocity Impact," Proceedings of Fifth Symposium on Hypervelocity Impact, VOL I - Part 1, April 1962.
3. Eichelberger, R.J., Gerhing, J.W., "Effects of Meteoroid Impacts on Space Vehicles," ARS J. VOL 32, NO.10, October 1962, P. 1583.

List of Figures

- Fig. 1 Penetration of 1100F and 2014 aluminum by aluminum spheres.
- Fig. 2 Energy per Unit Volume as a Function of Velocity for
Impacts into 1100F and 2014 Aluminum.
- Fig. 3 Penetration of 2014 Aluminum by Aluminum Spheres from
Energy/Volume Considerations.
- Fig. 4 Penetration of 1100F Aluminum by Aluminum Spheres from
Energy/Volume Considerations.
- Fig. 5 Hole Dimensions of Specified Thicknesses of 2024
Aluminum Impacted by Steel and Aluminum Spheres at
Normal Incidence.
- Fig. 6 Hole Area of Specified Thicknesses of 2024 Aluminum
Impacted by Steel Spheres at Various Angles of Incidence.
- Fig. 7 Hole Area of Specified Thicknesses of 2024 Aluminum
Impacted by Aluminum Spheres at Various Angles of
Incidence.

IMPACTS INTO ALUMINUM

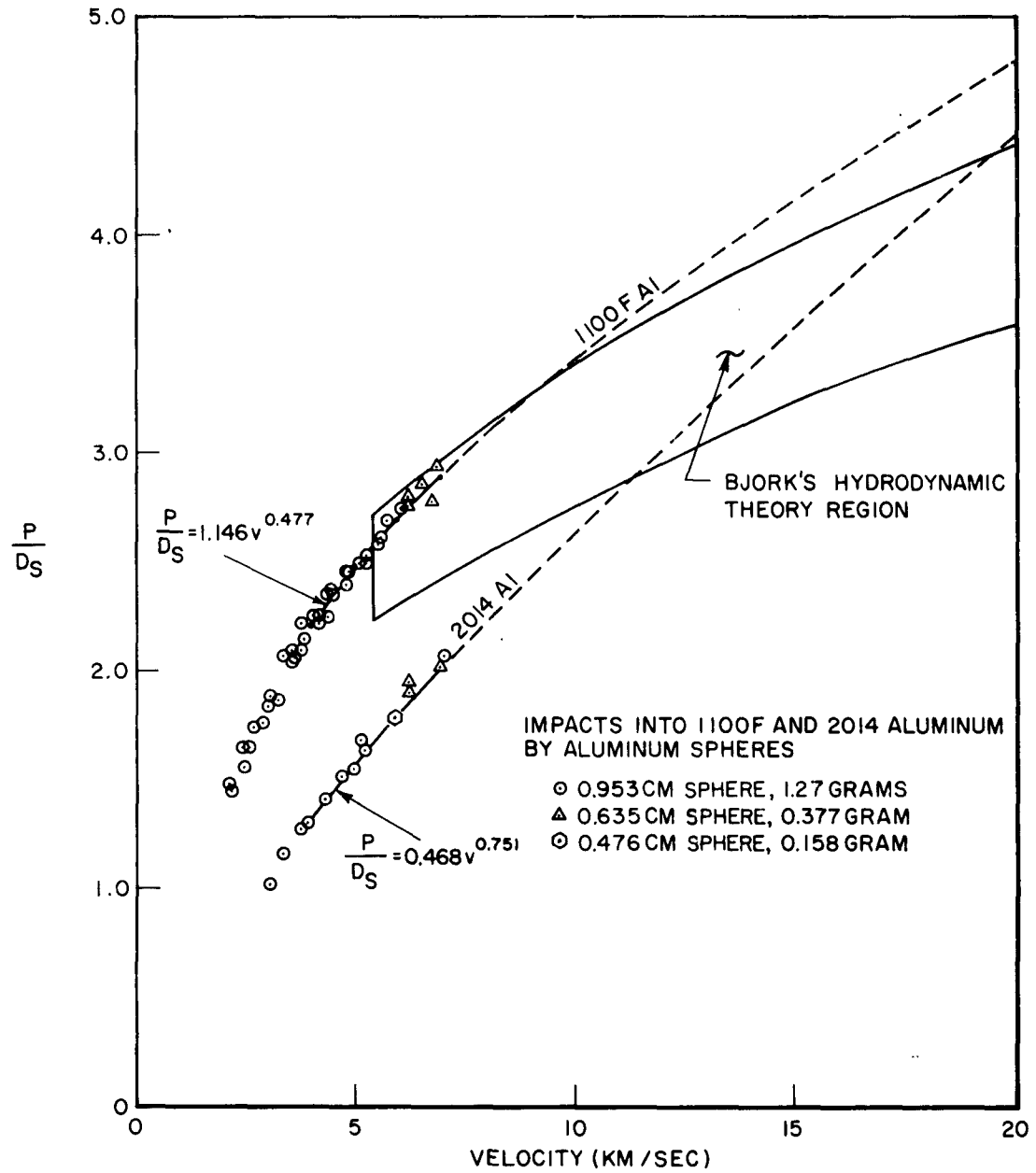


Fig. 1.

IMPACTS INTO ALUMINUM

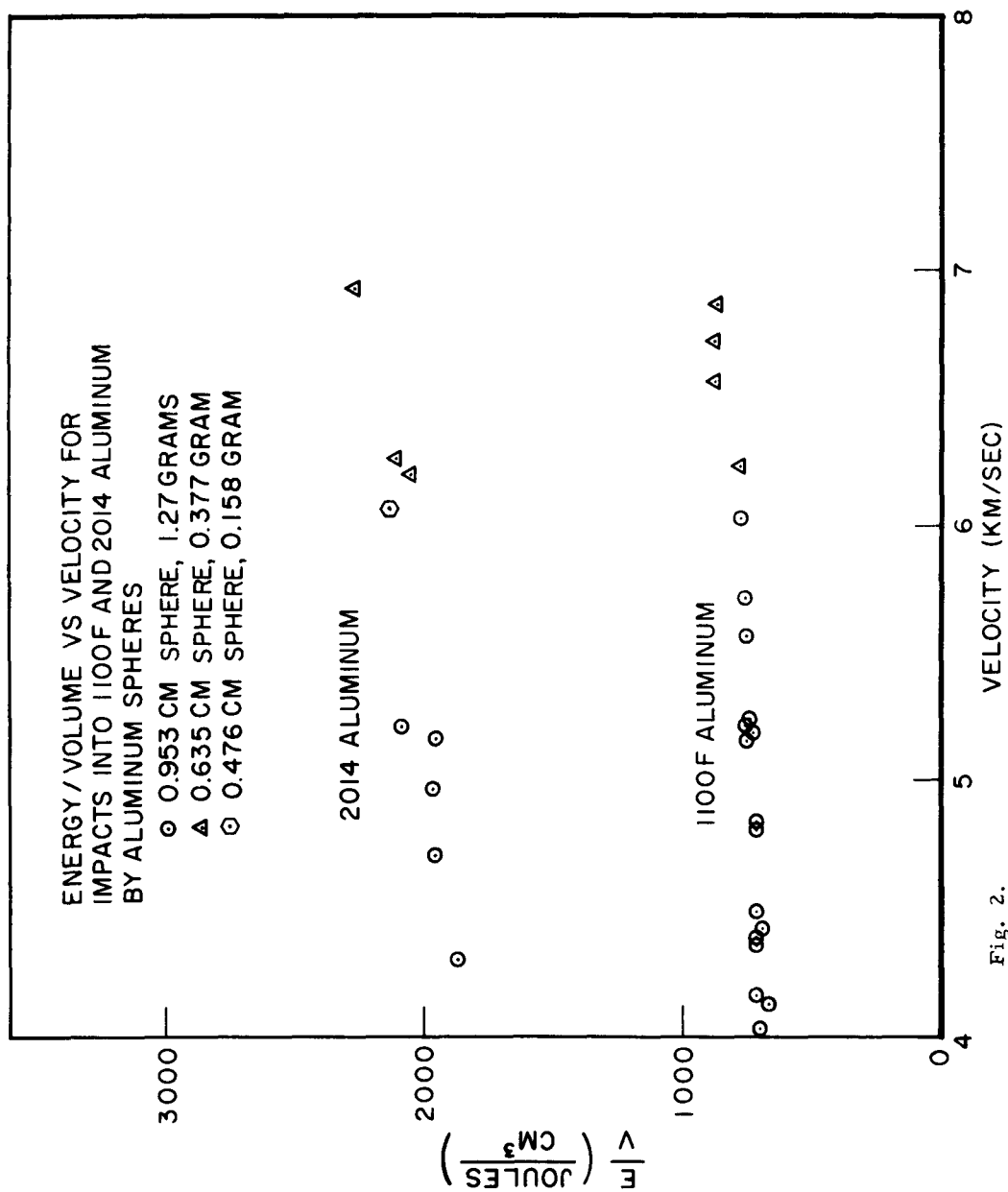


Fig. 2.

IMPACTS INTO ALUMINUM

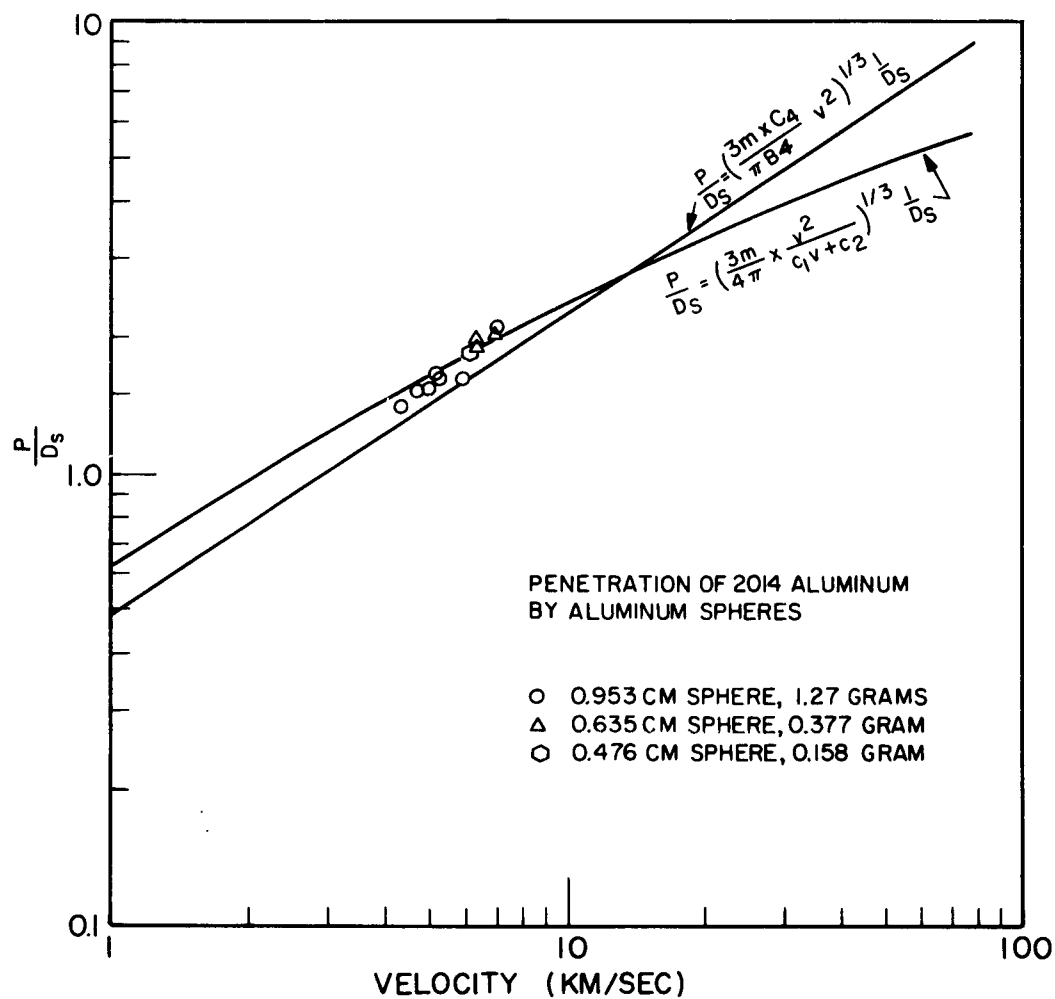


Fig. 3.

IMPACTS INTO ALUMINUM

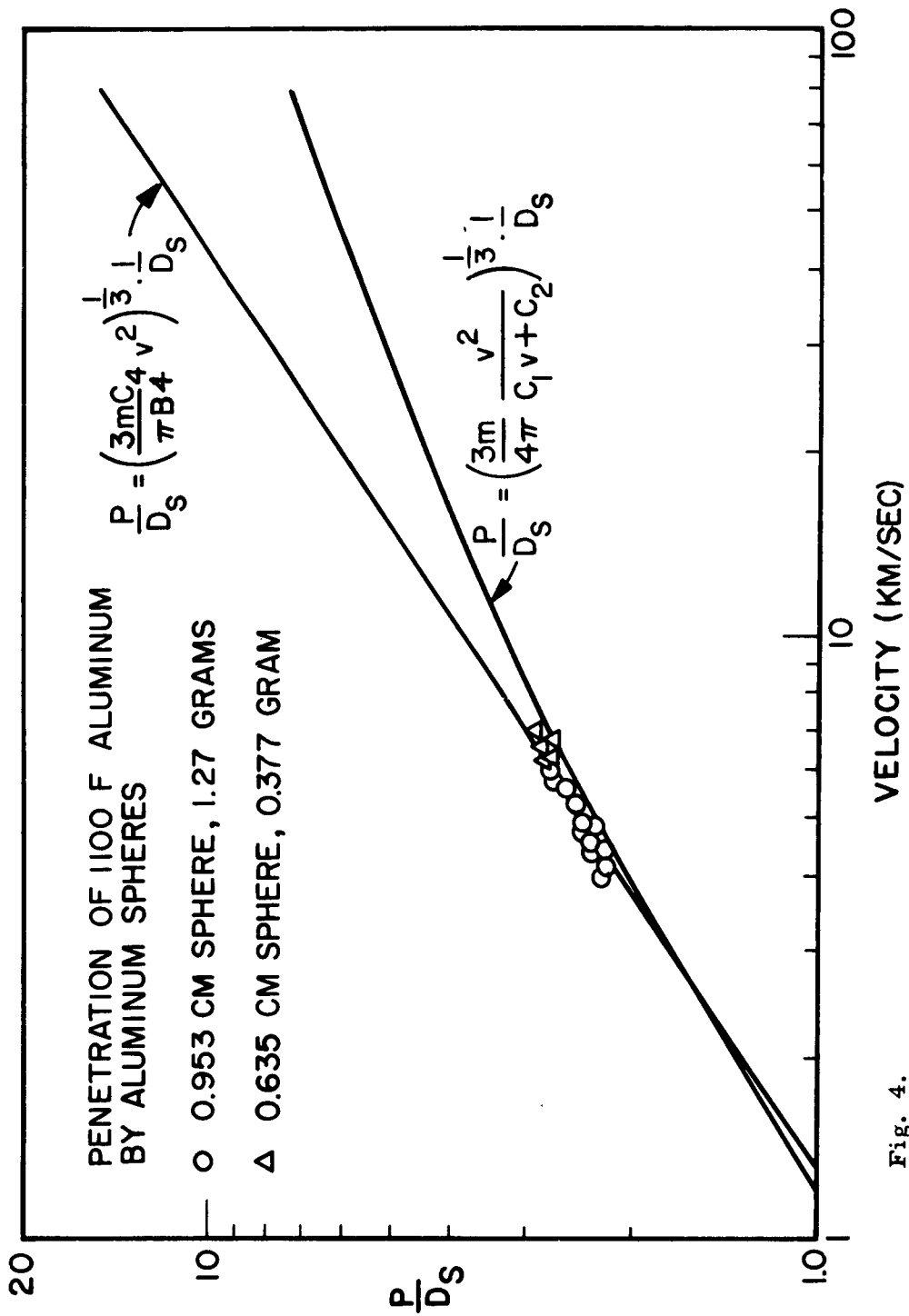


Fig. 4.

IMPACTS INTO ALUMINUM

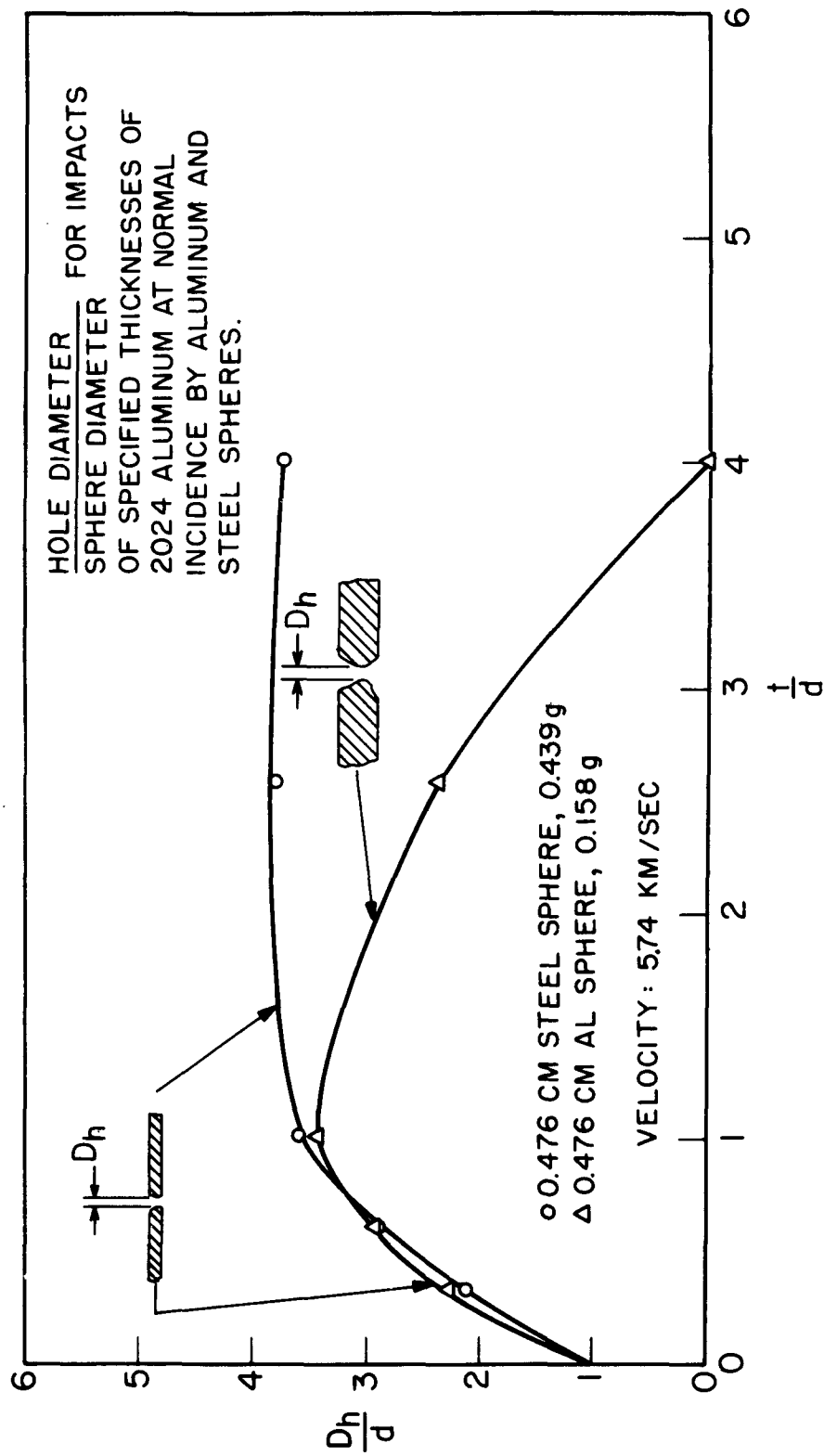


Fig. 5.

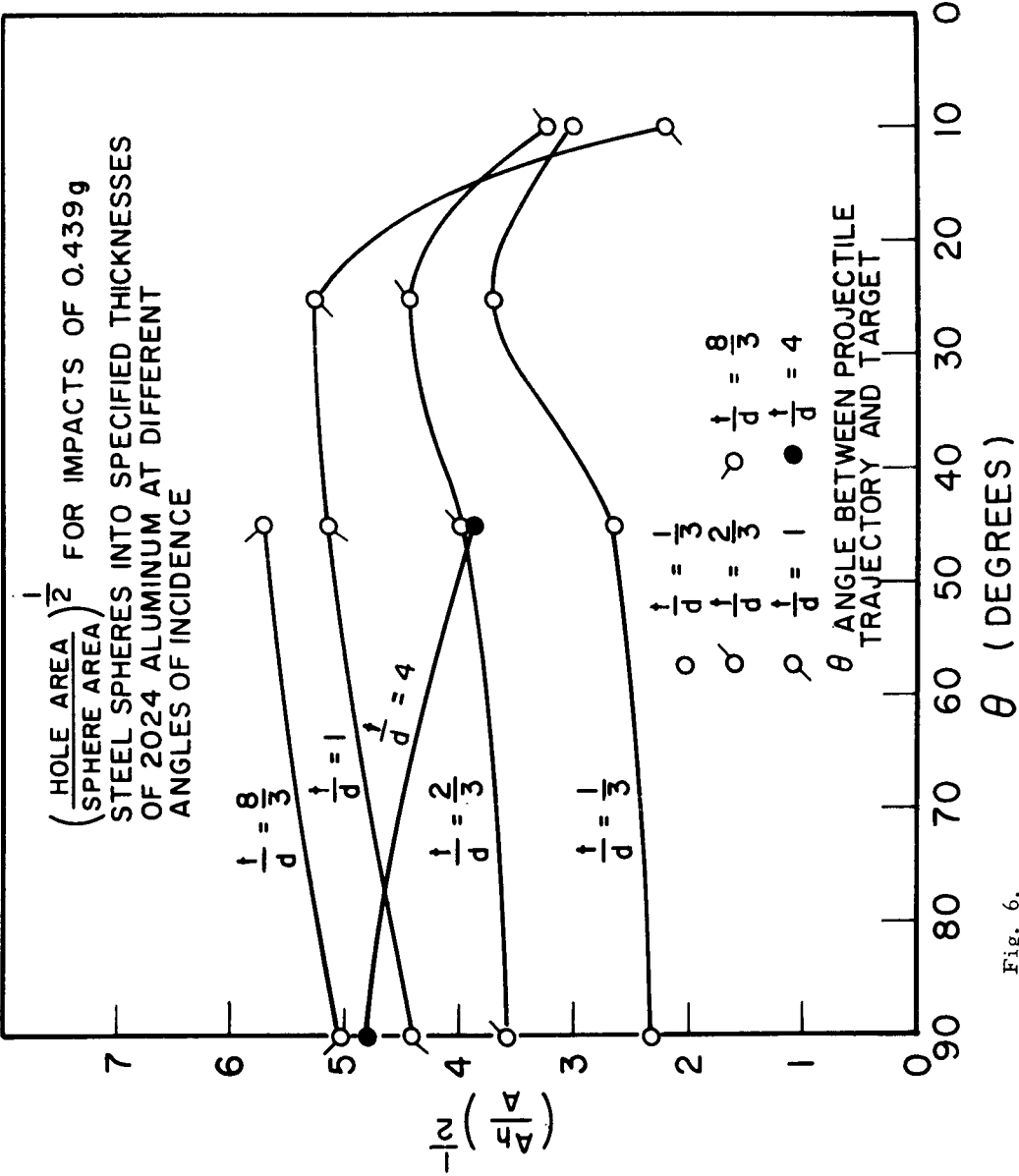


Fig. 6.

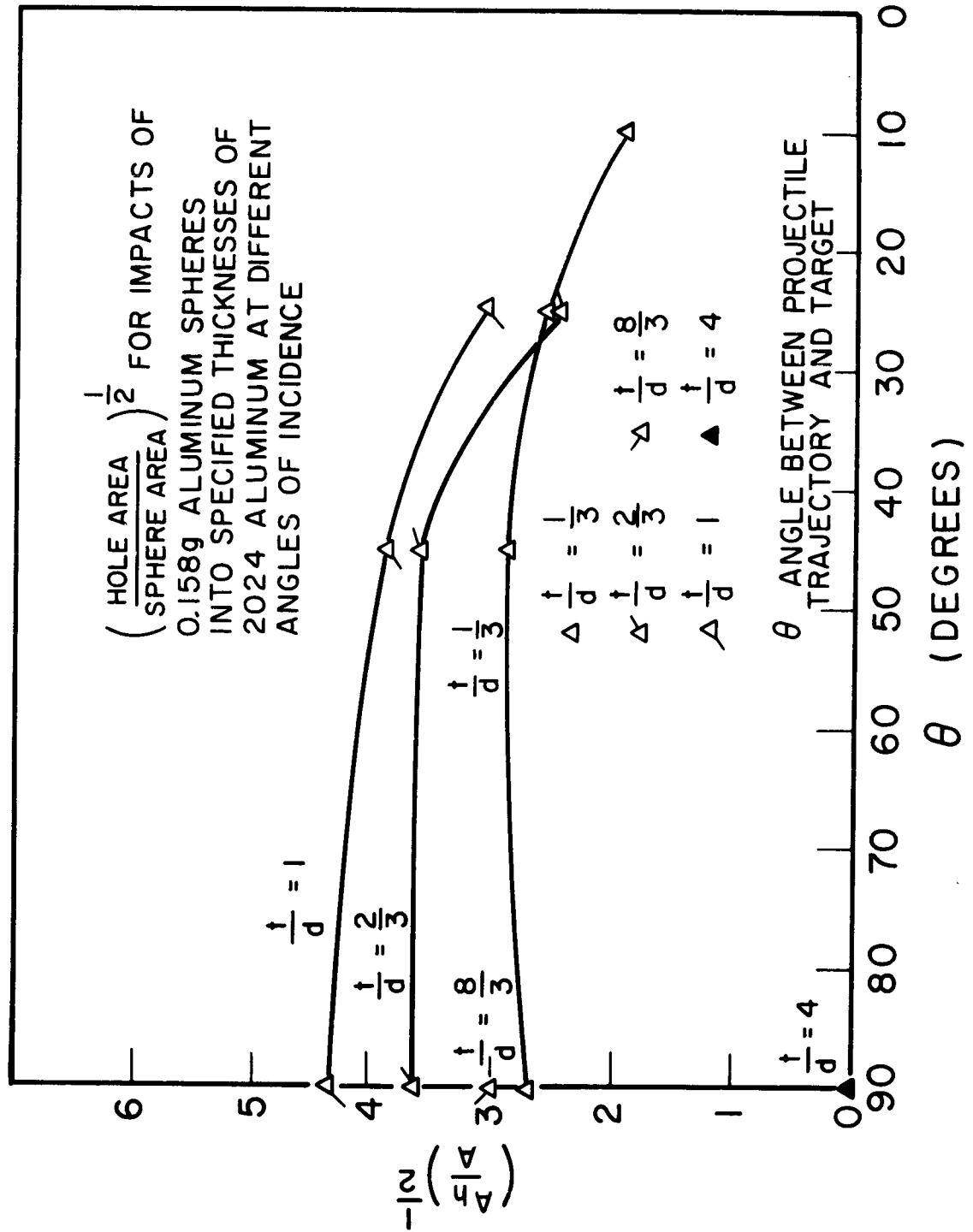


Fig. 7.

PARTICLE-SOLID IMPACT PHENOMENA

By

E. H. Goodman and C. D. Liles
von Kármán Gas Dynamics Facility
ARO, Inc.*

*The research reported in this paper was sponsored by the Arnold Engineering Development Center, Air Force Systems Command, under Contract No. AF 40(600)-1000 with ARO, Inc. Further reproduction is authorized to satisfy needs of the U. S. Government.

PARTICLE-SOLID IMPACT PHENOMENA

ABSTRACT

Hypervelocity impact tests have been performed using projectiles and semi-infinite targets of high purity aluminum, high purity copper, commercial purity aluminum, and projectiles of stainless steel. Data are presented for impact velocities from 0.7 to 8.8 km/sec and are compared with correlating formulas.

PARTICLE-SOLID IMPACT PHENOMENA

CONTENTS

	<u>Page</u>
ABSTRACT	544
SYMBOLS	547
1.0 INTRODUCTION	548
2.0 APPARATUS	
2.1 Launcher and Range	548
2.2 Projectiles and Targets	548
2.3 Instrumentation	550
3.0 PROCEDURE	
3.1 Test Procedure	550
3.2 Data Reduction Procedure	
3.2.1 Velocity Data Reduction	556
3.2.2 Impact Crater Data Reduction	556
3.2.3 Accuracy of Velocity Measurements	560
3.2.4 Accuracy of Crater Measurements	560
4.0 RESULTS AND DISCUSSION	
4.1 Penetration Data	562
4.2 Crater Shape	572
4.3 Crater Volume	572
5.0 CONCLUSIONS	575
REFERENCES	576

TABLES

I. Projectile and Target Combinations	551
II. Physical Properties of Target Materials	552
III. Tabulated Velocity and Crater Data for Projectiles and Targets of H.P. Aluminum and Copper	563
IV. Tabulated Velocity and Crater Data for C.P. Aluminum and SS Projectiles into C.P. Aluminum Targets	567

ILLUSTRATIONS

Figure

1. Typical Hyperballistic Impact Range Layout	549
2. Typical Target Hardness Distribution on Copper Target	553
3. Schematic of Framing Camera and Optical Components	554
4. Photograph of Projectile and Sabot	555
5. Photograph of Sabot Stripper	557
6. X-Ray Shadowgram of Launching Process	558

PARTICLE-SOLID IMPACT PHENOMENA

7.	Four Frames from a Typical Framing Camera Showing Projectile and Target	559
8.	Variation of Maximum Possible Error in Framing Camera Turbine Speed	561
9.	Correlation of Data with Theoretical and Empirical Penetration Prediction Equations	
	a. H.P. Copper Target Material	568
	b. H.P. Aluminum and C.P. Aluminum Target Material .	569
10.	Crater Depth-to-Diameter Ratio for Copper and Aluminum Spheres into Copper and Aluminum Targets . .	573
11.	Correlation of Crater Volume Data with Empirical Volume Prediction Equations	574

PARTICLE-SOLID IMPACT PHENOMENA

SYMBOLS

Al → Cu	Aluminum projectile impacted on a copper target
B	Best number
C.P.	Commercial purity material
c	Sonic velocity in target material, km/sec
D _c	Diameter of crater, mm
d	Diameter of spherical projectile, mm
H	Brinell hardness number of the target, kg/mm ²
H.P.	High purity material
m _p	Mass of projectile, g
P	Penetration, depth of crater, mm
SS	Stainless steel
u _p	Projectile velocity, k/sec
V _c	Crater volume, cc
V _p	Projectile volume, cc
ρ _p	Projectile density, gm/cc
ρ _t	Target density, gm/cc

PARTICLE-SOLID IMPACT PHENOMENA

1.0 INTRODUCTION

Tests here reported were conducted in the von Kármán Gas Dynamics Facility (VKF), Arnold Engineering Development Center (AEDC), Air Force Systems Command (AFSC), USAF, to provide experimental data on hypervelocity impact of solid particles against solids. Part of this program (that which was associated with the high purity (H.P.) aluminum and copper materials) was sponsored by the Aeronautical Systems Division (ASD), AFSC, and coordinated with the Plastics Section, National Bureau of Standards (NBS), where additional analysis of the data will be performed. The rest of the program, which was associated with stainless steel and commercial purity (C.P.) aluminum, was performed concurrently with launcher development at the VKF.

The ASD-NBS tests required impacts of 1.59- (1/16-in.), 3.18- (1/8-in.), and 4.76- (3/16-in.) mm-diam H.P. aluminum and copper spherical projectiles on targets of like and unlike material. Results of these tests were previously published by the authors (Ref. 1) and are here included. Additional data were obtained utilizing 1.59- and 3.18-mm-diam C.P. aluminum and 3.18-mm-diam stainless steel spherical projectiles impacting C.P. aluminum targets. The experimental data obtained were projectile velocity and crater volume, diameter and depth.

2.0 APPARATUS

2.1 LAUNCHER AND RANGE

The hyperballistic impact range in which the tests were conducted consisted of (Fig. 1): (1) a two-stage launcher, (2) an expansion tank to absorb muzzle blast and to provide space for separation of the projectile from the sabot, (3) a connecting tube which had provision for measuring projectile velocity, and (4) a test chamber. A description of the range and launcher is given in Ref. 2.

2.2 PROJECTILES AND TARGETS

The H.P. projectiles and targets were supplied by the National Bureau of Standards. The projectile and target materials were high purity (99.99 percent) aluminum and oxygen-free, high purity (99.96 percent) copper. Both projectiles and targets were annealed to reduce the effects of prior work hardening. Since the projectiles were annealed under the same conditions as the targets, the physical properties of the projectiles were assumed to be the same as those of the targets of like material.

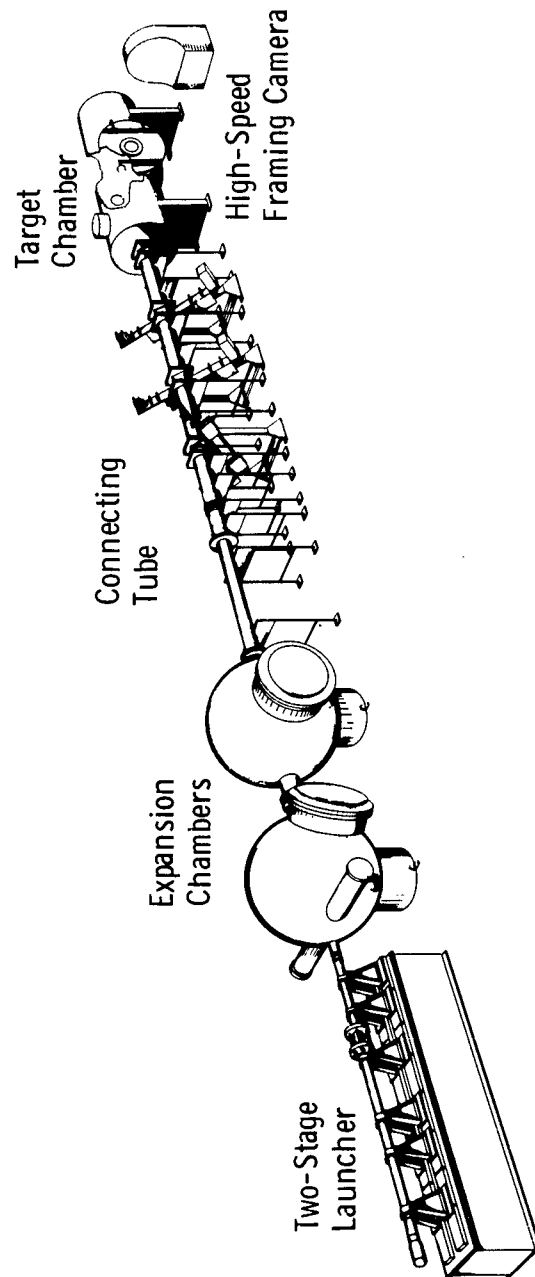


Fig. 1 Typical Hyperballistic Impact Range Layout

PARTICLE-SOLID IMPACT PHENOMENA

The C.P. (nominally 99.0% Al) aluminum target material was used in the half-hard condition. Experimental measurements of hardness of the C.P. aluminum and 302 stainless steel projectile material could not be obtained.

Projectile velocity, diameter, and material, and target thickness ranges and material are listed in Table I. Table II shows the physical properties of the projectile and target materials.

When, as a result of impact, a target exhibited a permanent distortion of the rear face, a thicker target was substituted to maintain semi-infinite target conditions. Figure 2 shows the variation in hardness among typical copper targets; the hardness variation for the aluminum targets was similar. The Brinell hardness variation between targets was 48.9 to 50.9 for the H.P. copper targets, 15.9 to 17.8 for the H.P. aluminum, and 31.2 to 32.8 for the C.P. aluminum.

2.3 INSTRUMENTATION

The velocity measurements were made with the Beckman & Whitley (B&W) Model 192 framing camera. This camera has a maximum framing rate of 1.4×10^6 frames/sec. A sketch of the B&W setup is shown in Fig. 3. The light output from the xenon tube backlights a translucent, plastic screen against which the projectile and target face are silhouetted. The light duration can be adjusted between 30 and 300 μ sec, allowing proper exposure of 82 frames at various framing rates on the B&W film without rewrite or the use of a capping shutter. The 7-in.-diam field of view of the B&W camera allows both impact and pre-impact events to be recorded.

The B&W light source trigger, shown in Fig. 3, is a mechanical switch trigger which consists of two sheets of aluminum film separated by a sheet of Mylar film. The total thickness of the trigger was approximately 0.0127 mm. With a potential across the aluminum-mylar-aluminum sandwich, triggering occurs when the projectile punctures the film and completes the circuit.

3.0 PROCEDURE

3.1 TEST PROCEDURE

The projectile was seated in a sabot (Fig. 4) and then inserted into the launch tube. The sabot carries the projectile through the bore, forms a seal to prevent blow-by, and protects the projectile from loss of material by friction and from contact with the hot propellant.

TABLE I
PROJECTILE AND TARGET COMBINATIONS

PROJECTILES		VELOCITY RANGE		TARGETS
Sphere Diameter, mm	Material	km/sec	Material/thickness, mm	
1.59	H. P. Al	1.75--8.82	H. P. Al/38.10 and 50.8 and H. P. Cu/25.4 and 50.8	
3.18		1.83--8.37		
4.76		2.55--7.31		
1.59	H. P. Cu	0.78--7.58		
3.18		1.28--6.44		
4.76		2.69--5.97		
1.59	C. P. Al	6.17--7.81	C. P. Al/38.10	
3.18		4.03--6.58		
6.35		6.89		
3.18	302 Stainless Steel	6.12--7.45		

TABLE II
PHYSICAL PROPERTIES OF TARGET MATERIALS

Material	Brinell Hardness, kg/mm ²	Approximate Variation in Hardness		Density, gm/cm ³	Sonic Speed in Material*, km/sec	Static Yield Strength**, kg/mm ²	Ultimate Strength**, kg/mm ²	Elonga- tion**, Percent	Reduction of Area**, Percent
		of Each Target, kg/mm ²	of Each Target, kg/mm ²						
H. P. Cooper	48.9-50.9	0.6	0.6	8.77	3.56	9.92	22.03	57.80	83.05
H. P. Aluminum	15.9-17.8	0.6	0.6	2.67	5.10	0.77	5.53	51.65	95.00
C. P. Aluminum	31.2-32.8	1.1	1.1	2.72		11.96	12.67	9.0-20.0	--
302 Stainless Steel	---	---	---	7.97*	--	28.15	63.33	50*	70*

*Handbook values--(Refs. 7 & 8)

**ASTM STANDARD 505 Tensile Test

PARTICLE-SOLID IMPACT PHENOMENA

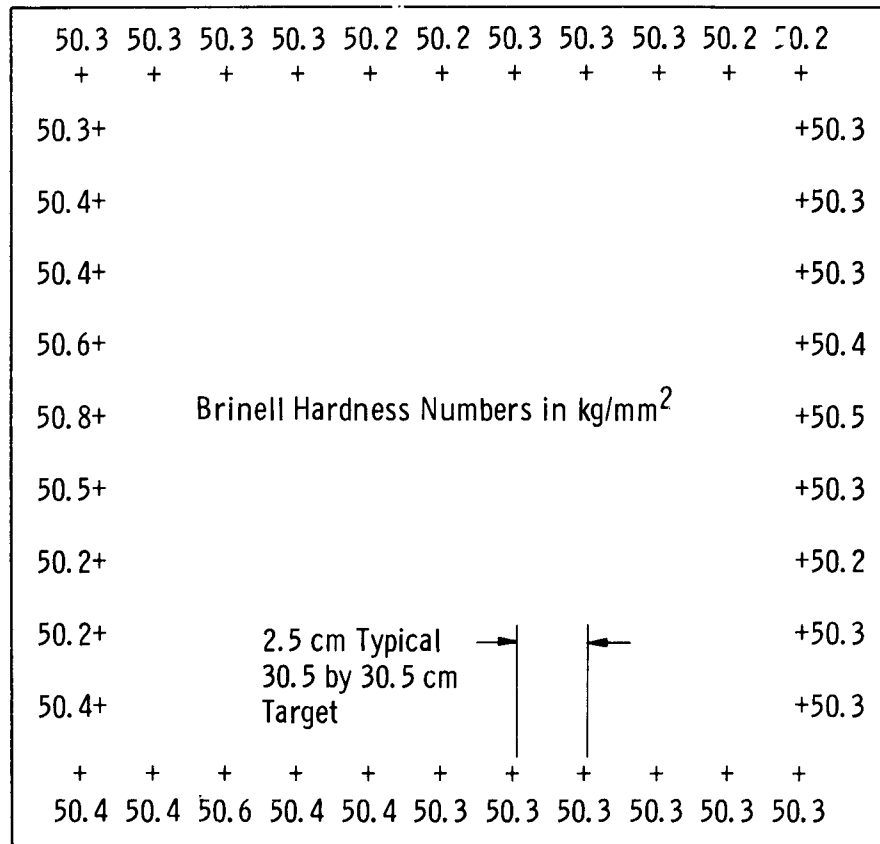


Fig. 2 Typical Target Hardness Distribution on Copper Target

PARTICLE-SOLID IMPACT PHENOMENA

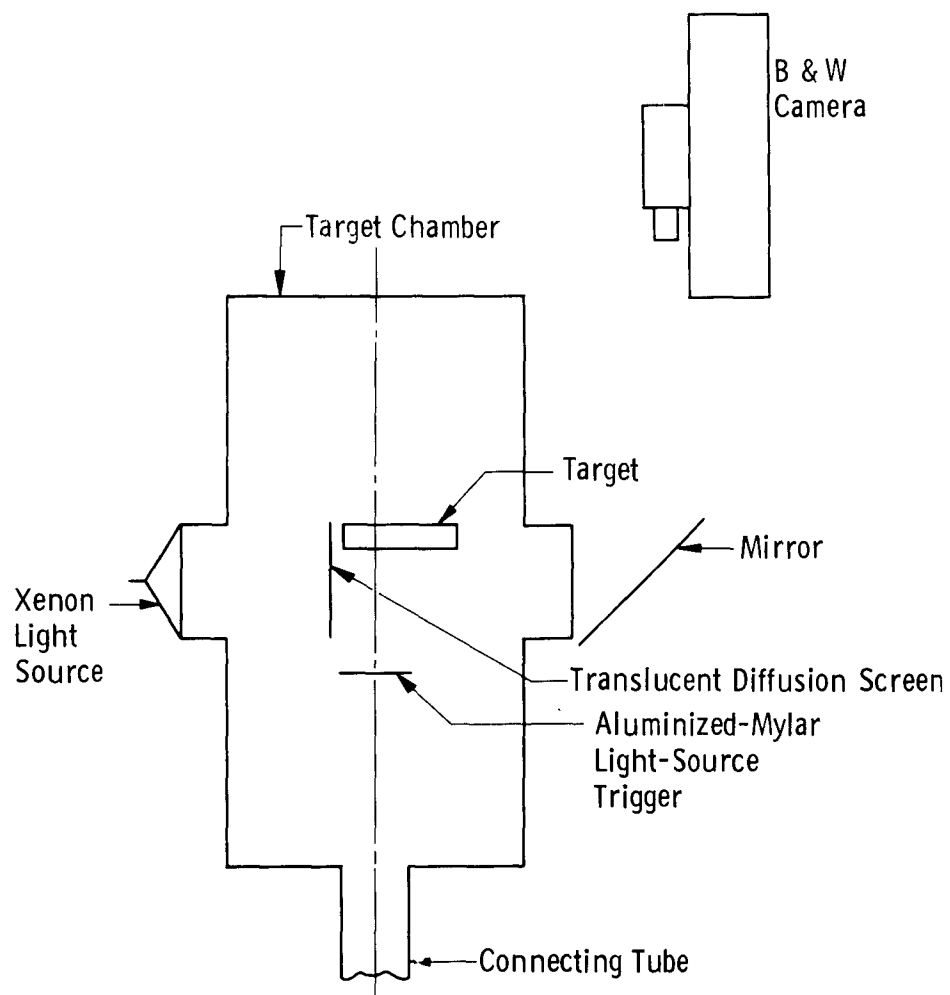


Fig. 3 Schematic of Framing Camera and Optical Components

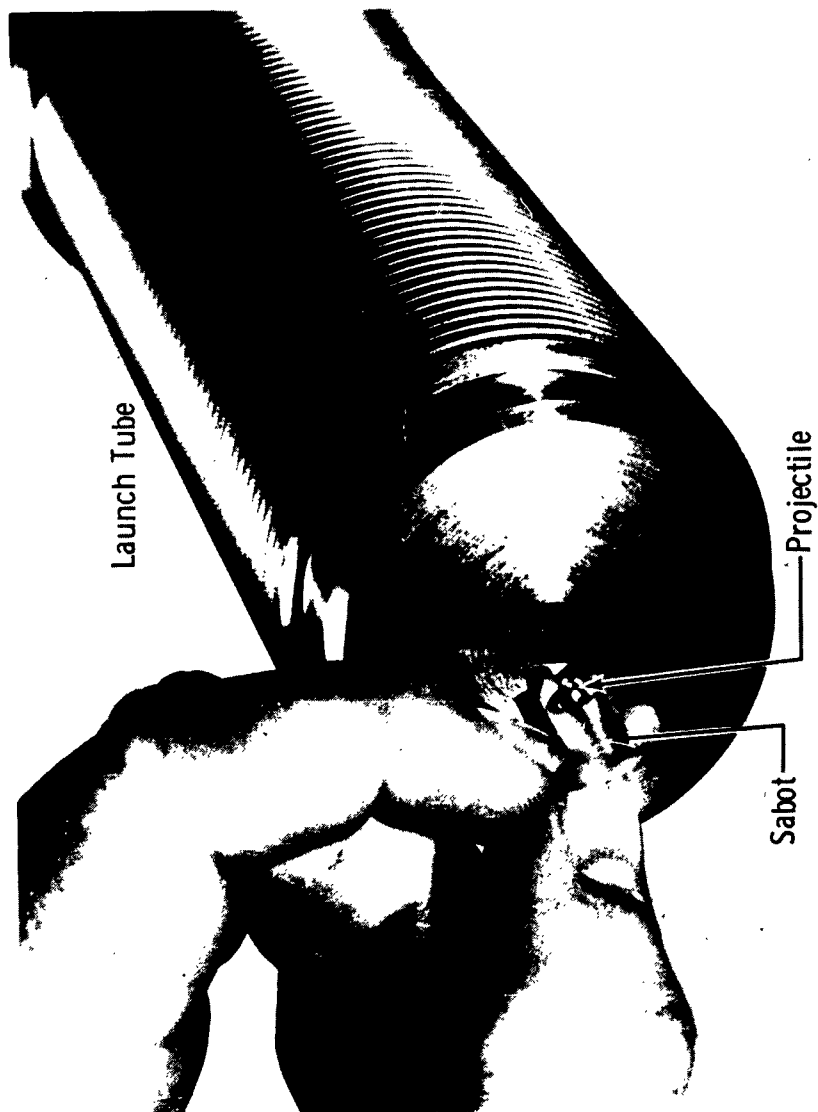


Fig. 4 Photograph of Projectile and Sabot

PARTICLE-SOLID IMPACT PHENOMENA

At the beginning of the test, no attempt was made to prevent the sabot from impacting on the target. Because the projectile craters were too close to the impacts of the sabot, only four good data shots in ten were obtained. A mechanical sabot-stripping device (Fig. 5) was subsequently developed which stripped the sabot from the projectile as it emerged from the muzzle of the launch tube, allowing the projectile to impact at a point far enough from craters formed by the sabot fragments to avoid interference by them. This sabot stripper consisted of four rods or wires that intercepted the sabot at the muzzle, retarding it and causing its course to diverge from the projectile's. Figure 6, a typical X-ray shadowgram, shows the longitudinal separation between the plastic sabot (12.7-mm-diam by 12.7-mm-long right circular cylinder of polycarbonated resin) and the projectile (1.59-mm-diam sphere of stainless steel). Use of this stripper device resulted in approximately seven good data shots in ten.

3.2 DATA REDUCTION PROCEDURE

3.2.1 Velocity Data Reduction

The projectile velocity and integrity just prior to its arrival at the target were recorded on the B&W film. Accurately fiducial lines on the translucent screen, against which the projectile was silhouetted, allowed the projectile's position to be computed and the velocity at impact determined by a least squares fit in a computer program. Figure 7 is typical of a series of frames showing the projectile and target.

3.2.2 Impact Crater Data Reduction

Crater volume, which is defined as the volume below the original target surface, was determined by accurately metering a solution into the crater. To eliminate the error in solution level due to meniscus, a one-percent Alconox-water solution was used. A detailed description of this procedure is given in Ref. 2.

The crater diameter was measured by traversing the vernier table from a point on the crater wall at solution level (as observed with a cathetometer) until the cross-hair of a cathetometer was tangent to the opposite side of the crater at the solution level. Hence, the distance through which the vernier table traveled was the crater diameter at that solution level. The target was then rotated approximately 90 deg, and the measurement was made again. The average of several readings is the reported crater diameter. Crater depth was determined using an optical depth micrometer.

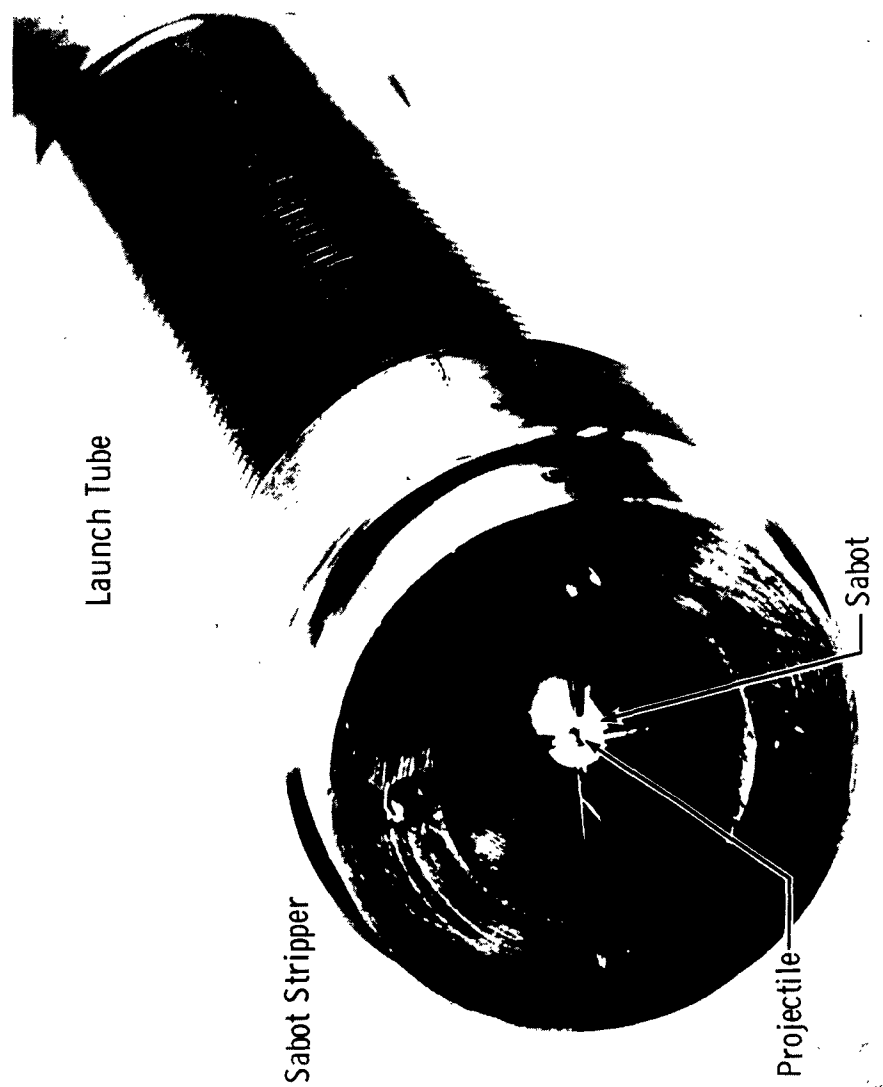


Fig. 5 Photograph of Sabot Stripper

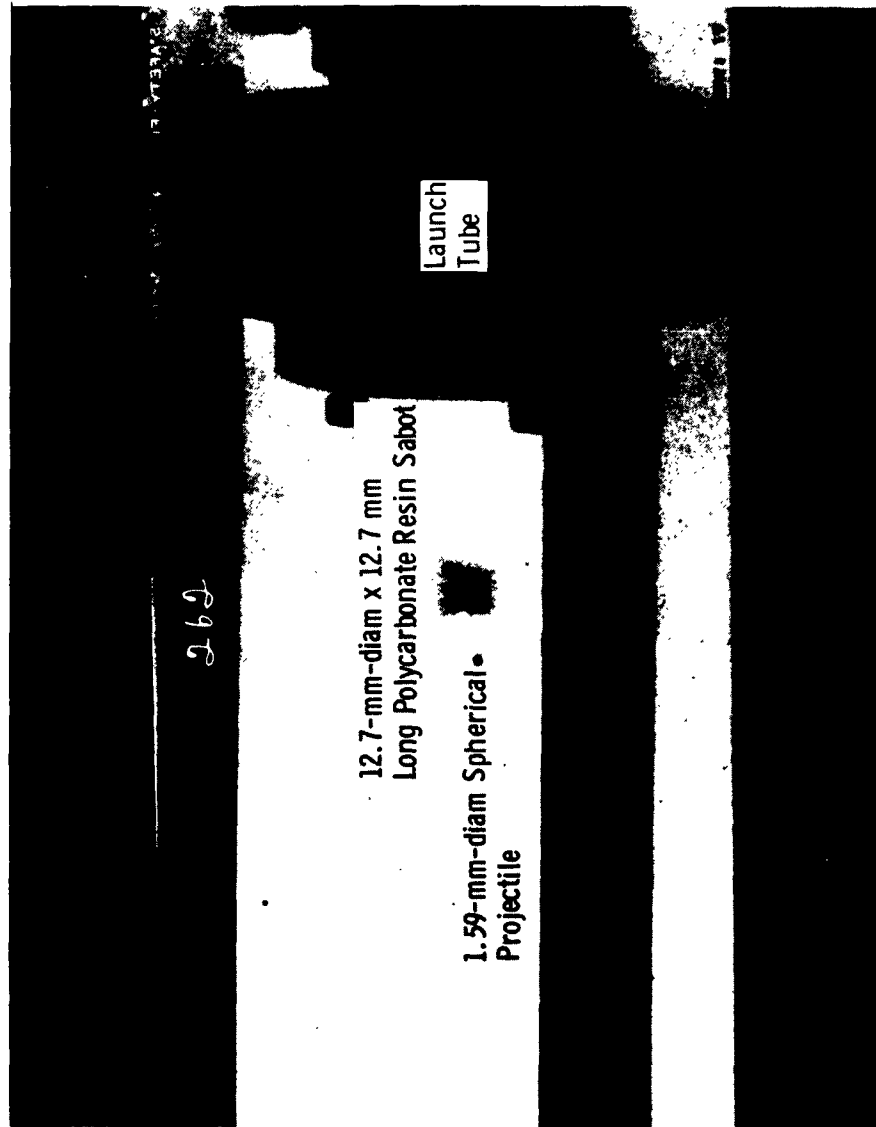
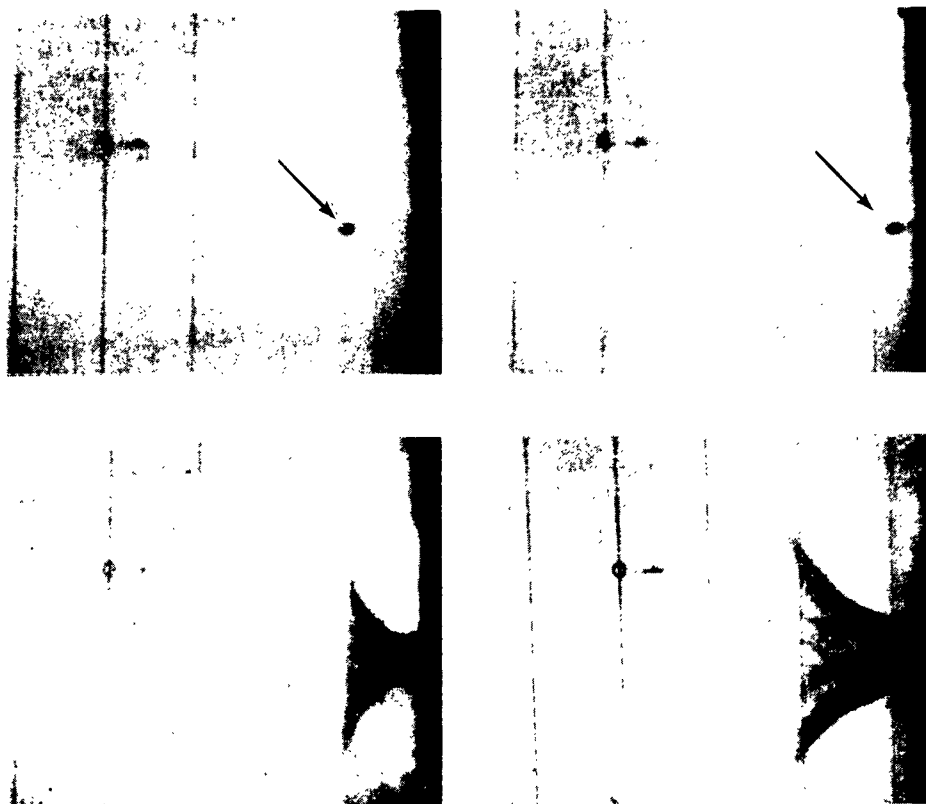


Fig. 6 X-Ray Shadowgram of Sabot and Projectile Emerging at 8.01 km/sec
from Launch Tube

PARTICLE-SOLID IMPACT PHENOMENA



Flight and Impact of a 3.18-mm-diam H. P. Aluminum Sphere
into a H. P. Aluminum Target at a Velocity of 6.523 km/sec

Fig. 7 Four Frames from a Typical Framing Camera Sequence Showing
Projectile, Target, and Spall Formation

PARTICLE-SOLID IMPACT PHENOMENA

3.2.3 Accuracy of Velocity Measurements

The error in distance measurements is due to an inability to judge the exact position of the poorly resolved projectile image on the film. The standard deviation for position, using a Gaussian least squares curve fit, is within 0.25 percent of the base distance. When standard deviation was larger, more points were read from the film.

The error in time stems directly from the error in the camera turbine speed as shown by the equation:

$$\text{camera framing rate (frames/sec)} = 240 \times \frac{\text{turbine speed}}{\text{(rev/sec)}} \quad (1)$$

The error in time can be divided further into two parts:
(1) error due to turbine drift and (2) counter error.

For turbine speeds below 2500 rps there was no appreciable drift in turbine speed; however, as the turbine speed increased above 2500 rps, the drift increased appreciably. An average drift in a 1-sec counting period of ± 10 revolutions at a turbine speed of 5000 rps has been observed for approximately 30 shots. The only significant counter error was a possible ± 1 revolution during each counting period.

Figure 8 shows the maximum error in turbine speed (rps) and, therefore in the time base for the range of turbine speeds and the counting periods used during the test. Fifty-three data shots were made using the 0.1-sec counting period and turbine speeds from 4500 to 5500 rps. All of the other data shots were made using the 1-sec counting period and turbine speeds from 1000 to 5300 rps.

The errors in time and distance allow an absolute velocity determination within one percent.

3.2.4 Accuracy of Crater Measurements

To determine the accuracy of the crater measuring technique, two hemispherical craters were machined in a metal target. The calculated volumes of the craters were compared with the volumes derived by metering an Alconox-water solution and also with the volumes determined by the weight and density of the metered solution. The solution was metered from a hypodermic syringe, pipettes, and burettes. Volumes measured with each of the fluid metering devices were repeatable to ± 0.3 percent. The difference between the calculated volumes and the measured volumes was less than one percent.

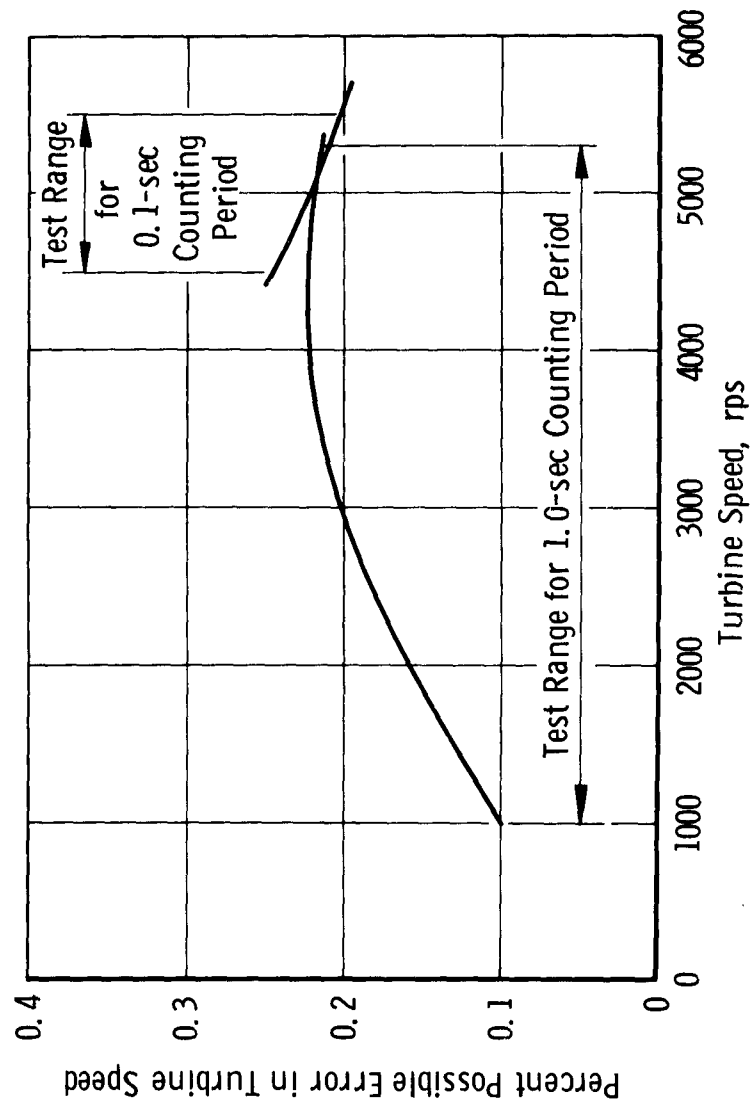


Fig. 8 Variation of Maximum Possible Error in Framing
Camera Turbine Speed

PARTICLE-SOLID IMPACT PHENOMENA

The depth, as determined by the optical depth micrometer, was repeatable to within ± 0.005 mm. The diameter measurement was repeatable to ± 0.127 mm for three measurements.

The evaporation rate of the one-percent Alconox-water solution is one percent per hour as determined from a 2.32-cm^2 surface area of a hemisphere at 25.5°C and 736 mm Hg. Since all of the measurements were made within five minutes, the error attributed to evaporation was considered to be negligible.

4.0 RESULTS AND DISCUSSION

Velocity and crater dimensions for the H.P. targets and H.P. projectiles are given in Table III. The data are grouped by target material, projectile and target combinations and by projectile size. Velocity and crater dimensions for the stainless steel and C.P. aluminum projectiles into C.P. aluminum targets are presented in Table IV.

Several craters, which were formed under similar conditions except for target thickness (a 25.4-mm and a 50.8-mm thick target), were compared to see if the crater dimensions were influenced by a variation in target thickness. The crater dimension data thus compared showed the normal experimental scatter.

4.1 PENETRATION DATA

The raw penetration data, as presented in Fig. 9, have been reduced to the dimensionless form, P/d versus u_p/c , where penetration, P , is the distance from the original target surface to the bottom of the crater. In some cases (H.P. Al \rightarrow H.P. Al, H.P. Al \rightarrow H.P. Cu, and H.P. Cu \rightarrow H.P. Cu) there was a thin layer of projectile material plated on the wall and bottom of the crater. The H.P. Cu \rightarrow H.P. Al series produced different craters. One projectile remained intact after impact but later fell out for the H.P. Cu \rightarrow H.P. Al (0.772 km/sec), but on all other H.P. Cu \rightarrow H.P. Al impacts the copper projectile disintegrated, leaving small, embedded globules in the wall and bottom of the crater. In all cases, measurements were made to the actual bottom surface of the crater.

It was determined experimentally that the aluminized Mylar detector, described in section 2.3, had no effect on the crater formation. This was done by comparing crater data obtained from monitor shots in which a magnetic, instead of the Mylar, detector was used (Ref. 1).

PARTICLE-SOLID IMPACT PHENOMENA

TABLE III

TABULATED VELOCITY AND CRATER DATA
FOR PROJECTILES AND TARGETS OF H.P. ALUMINUM AND COPPER

Proj Material/ Target Material- Proj Diameter, mm	Shot No.	Velocity, m/sec	Crater Depth, mm	Crater Diameter, mm	Crater Volume, ccx10 ⁻²
H.P.Al/H.P.Al- 1.59	W-47	3,200	2.45	5.72	5.3
	W-49	4,076	3.10	5.79	7.4
	W-51	5,322	3.54	7.06	9.1
	W-84	6,654	3.92	8.41	14.2
	W-89	6,793	3.98	8.61	14.2
	W-85	6,924	3.73	8.08	13.3
	W-86	7,292	4.25	8.74	15.5
	W-83	7,507	4.62	8.59	16.8
H.P.Al/H.P.Al- 3.18	W-18	2,048	3.99	9.25	13.4
	W-22	2,254	4.45	9.18	20.1
	W-20	2,263	4.45	9.48	20.7
	W-19	2,317	4.08	9.30	15.5
	W-14	2,348	4.69	8.31	16.0
	W-26	2,548	5.70	11.30	36.5
	W-42	4,549	7.30	14.86	77.5
	W-3	4,820	6.78	14.35	66.1
	W-41	5,148	7.58	15.16	86.9
	W-5	5,289	7.89	13.45	72.9
	W-8	5,612	8.29	16.32	107.4
	W-61	5,694	7.90	15.49	92.9
	W-67	5,751	7.37	15.24	81.9
	W-58	5,881	8.28	15.82	118.0
	W-65	6,920	9.36	18.30	143.0
	T-367	8,367	9.90	20.31	208.1
H.P.Al/H.P.Al- 4.76	W-325	2,548	7.99	15.35	92.9
	W-190	2,977	8.95	17.11	131.3
	W-189	3,024	8.98	17.56	130.8
	W-191	3,049	9.05	17.16	135.2
	W-188	3,107	9.02	17.96	138.7
	W-194	3,131	9.26	17.15	140.6
	W-205	3,146	9.13	17.75	141.0
	W-195	3,447	9.51	18.66	158.3

PARTICLE-SOLID IMPACT PHENOMENA

TABLE III(Continued)

Proj Material/ Target Material- Proj Diameter, mm	Shot No.	Velocity, m/sec	Crater Depth, mm	Crater Diameter, mm	Crater Volume, ccx10 ⁻²
H.P.Al/H.P.Al- 4.76	W-193	4,223	10.88	20.67	227.2
	W-192	4,727	11.94	22.73	286.7
	W-196	5,166	12.98	23.23	347.6
	W-197	5,404	12.96	23.60	358.9
	W-200	6,632	13.37	24.51	451.9
	W-199	6,884	13.63	26.25	467.1
	W-201	6,876	13.34	24.81	413.5
	W-202	6,925	13.92	26.12	478.9
	W-204	7,306	14.29	27.23	520.2
H.P.Al/H.P.Cu- 1.59	W-185	1,748	0.97	3.52	0.7
	W-332	3,134	1.24	4.23	1.5
	W-351	3,603	1.63	4.75	1.7
	W-334	5,106	2.14	5.52	3.4
	W-343	6,020	2.37	5.98	3.4
	W-339	6,106	2.29	5.62	3.9
	W-346	6,539	2.40	5.79	4.4
	W-340	7,205	2.54	6.25	4.6
	T-358	7,574	2.49	6.40	5.9
	T-359	8,819	3.18	6.81	6.9
H.P.Al/H.P.Cu- 3.18	W-186	1,833	1.49	6.69	3.7
	W-187	2,324	1.99	7.28	7.4
	W-275	2,990	2.69	8.39	8.9
	W-263	4,357	3.96	10.19	17.7
	W-264	5,514	4.26	10.71	23.1
	W-266	6,141	4.61	11.54	26.1
	W-271	6,944	5.25	12.75	37.4
	W-274	6,400	4.78	11.94	31.0
H.P.Al/H.P.Cu- 4.76	W-211	2,697	3.74	11.34	25.1
	W-326	2,973	3.84	12.27	29.0
	W-212	3,729	5.03	13.17	41.0
	W-213	3,914	5.28	13.09	43.8
	W-214	4,396	6.41	15.04	69.8
	W-218	4,645	5.74	14.32	57.5

PARTICLE-SOLID IMPACT PHENOMENA

TABLE III(Continued)

Proj Material/ Target Material- Proj Diameter, mm	Shot No.	Velocity, m/sec	Crater Depth, mm	Crater Diameter, mm	Crater Volume ccx10 ⁻²
H.P.Al/H.P.Cu- 4.76 ↓	W-231	4,969	5.91	14.54	65.6
	W-232	5,309	6.62	15.73	80.9
	W-230	5,328	6.35	15.50	75.1
	W-219	5,377	6.09	15.29	68.4
	W-233	6,022	6.93	16.70	95.1
	W-215	6,106	6.82	16.67	88.0
	W-238	6,262	6.13	15.61	71.0
	W-239	6,563	7.22	17.26	103.1
	W-240	6,869	7.66	17.75	101.0
	W-237	6,896	7.84	18.03	121.9
	W-235	6,950	7.55	17.60	114.1
H.P.Cu/H.P.Cu- 1.59 ↓	W-11	806	0.61	2.37	0.6
	W-109	1,146	1.28	3.30	0.9
	W-12	1,289	1.09	2.43	0.8
	W-108	1,798	1.82	3.81	1.8
	W-54	5,038	4.25	7.79	14.3
	W-57	5,716	4.19	8.26	14.6
	W-81	6,775	4.84	8.97	20.8
	T-361	7,574	5.26	10.16	28.0
H.P.Cu/H.P.Cu- 3.18 ↓	W-28	2,448	5.73	10.92	34.4
	W-29	3,287	6.88	12.62	53.7
	W-32	3,518	7.17	13.44	61.1
	W-33	3,582	6.71	13.34	57.2
	W-35	3,833	7.49	13.61	68.8
	W-37	3,978	7.58	13.97	72.3
	W-34	4,088	7.78	14.25	77.2
	W-7	4,908	8.43	15.39	107.4
	W-101	6,146	9.87	16.30	144.0
	W-98	6,305	9.84	17.65	157.0
	W-93	6,440	9.72	17.09	163.0
H.P.Cu/H.P.Cu- 4.76 ↓	W-206	2,926	9.96	17.22	160.8
	W-207	3,520	10.93	19.20	212.4
	W-243	4,038	11.84	21.57	270.1

PARTICLE-SOLID IMPACT PHENOMENA

TABLE III(Concluded)

Proj Material/ Target Material- Proj Diameter, mm	Shot No.	Velocity, m/sec	Crater Depth, mm	Crater Diameter, mm	Crater Volume ccx10 ⁻²
H.P.Cu/H.P.Cu- 4.76	W-242	4,538	12.56	22.02	319.1
↓	W-207	4,605	12.92	22.53	333.0
	W-277	4,736	12.60	22.94	350.1
	W-300	5,270	13.91	23.55	416.1
	W-304	5,586	13.87	24.35	442.2
	W-307	5,967	13.95	25.37	482.2
H.P.Cu/H.P.Al- 1.59	W-178	772	2.29	2.00	1.0
↓	W-179	1,313	3.80	3.38	3.0
	W-182	1,912	5.00	4.92	6.9
	W-183	2,276	5.46	5.45	10.3
	W-354	5,687	8.33	10.40	56.5
↓	W-250	6,090	9.17	11.22	61.0
	W-259	6,436	9.17	11.30	67.9
H.P.Cu/H.P.Al- 3.18	W-169	1,278	8.33	6.92	27.0
↓	W-171	1,678	9.88	9.24	53.1
	W-173	2,133	10.97	11.60	100.3
	W-184	2,240	11.85	11.74	102.3
	W-283	3,604	14.76	16.56	256.0
↓	W-284	4,206	16.31	18.40	340.1
	W-294	5,340	18.97	21.17	485.1
H.P.Cu/H.P.Al- 4.76	W-222	2,690	19.66	19.44	521.2
↓	W-228	3,086	20.47	21.54	636.3
	W-221	3,496	22.58	24.50	814.3
	W-229	3,741	22.76	25.75	904.2

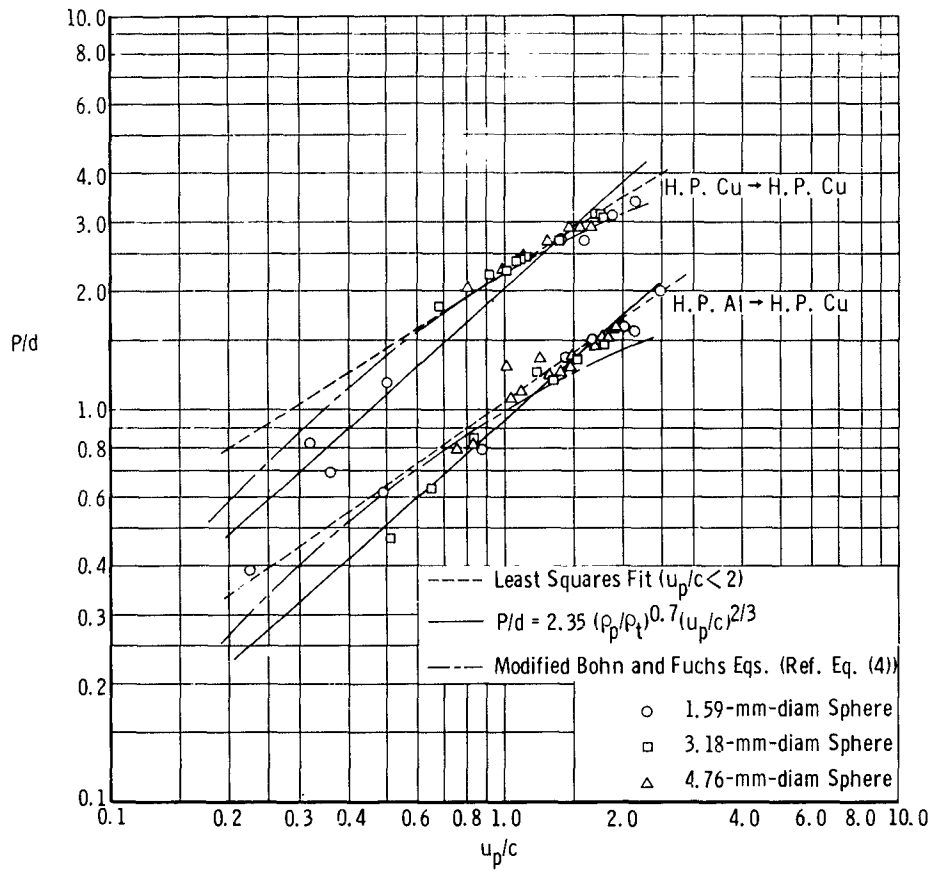
PARTICLE-SOLID IMPACT PHENOMENA

TABLE IV

TABULATED VELOCITY AND CRATER DATA FOR
C.P. ALUMINUM AND SS PROJECTILES INTO C.P. ALUMINUM TARGETS

Proj Material/ Target Material- Proj Diameter, mm	Shot No.	Velocity, m/sec	Crater Depth, mm	Crater Diameter, mm	Crater Volume ccx10 ⁻²
C.P.A1/C.P.A1- 1.59 ↓	W-141	6,173	4.01	8.18	15.4
	W-138	6,429	4.75	8.15	17.7
	W-139	6,633	4.83	8.15	18.2
	W-140	6,684	4.70	8.43	16.7
	W-136	6,786	4.60	8.76	20.6
	W-135	6,837	4.22	8.93	20.1
	W-146	6,939	4.37	8.57	18.7
	T-85	7,449	4.45	8.49	20.0
	T-88	7,806	4.52	7.99	18.5
	T-93	7,806	4.32	8.14	18.1
C.P.A1/C.P.A1- 3.18 ↓	T-44	4,031	6.38	11.97	42.1
	T-55	4,745	7.08	13.15	61.9
	T-73	5,918	7.61	14.70	74.7
	T-72	6,275	8.10	16.00	67.2
	T-75	6,582	8.17	15.86	101.8
SS/C.P.A1- 3.18 ↓	SD-3	6,122	14.91	18.79	337.2
	T-354	6,735	16.15	20.21	388.4
	SD-9	7,449	16.08	19.26	368.2

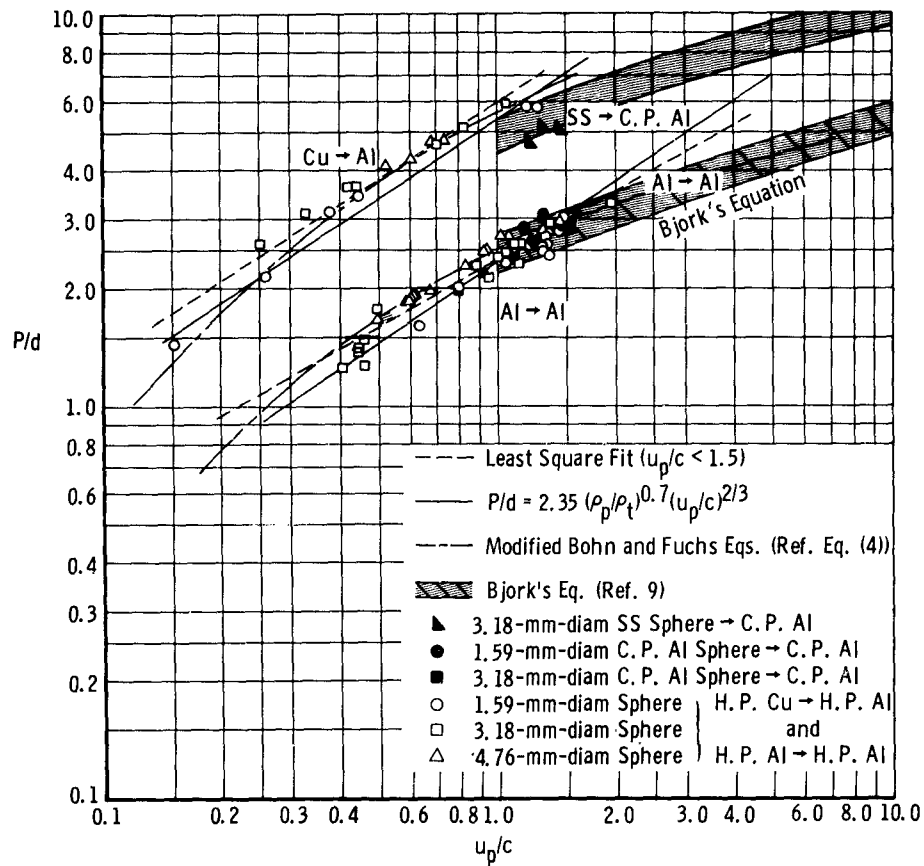
PARTICLE-SOLID IMPACT PHENOMENA



a. H.P. Cu Target

Fig. 9 Correlation of Data with Theoretical and Empirical Penetration Prediction Equations

PARTICLE-SOLID IMPACT PHENOMENA



b. C. P. Al and H. P. Al Targets

Fig. 9 Concluded

PARTICLE-SOLID IMPACT PHENOMENA

The penetration data were correlated with the relationship

$$P/d = K_1 (\rho_p / \rho_t)^n (u/c)^n \quad (2)$$

where d is the diameter of the projectile, and P is the penetration as first used by Charters (Ref. 3) with the values, $n = 0.69$ and $K_1 = 2.28$, and later modified by Summers (Ref. 4) where $n = 2/3$ and $K_1 = 2.28$. By plotting P/d at $u_p/c = 1$ versus ρ_p/ρ_t for the H.P. Al \rightarrow H.P. Al, H.P. Cu \rightarrow H.P. Al, H.P. Cu \rightarrow H.P. Cu, and H.P. Al \rightarrow H.P. Cu projectile-target combinations, the exponent of the density ratio term may be obtained. The constant, K_1 , is then obtained by fitting a straight line to the log of the density ratio times the log of the impact Mach number. The correlation of the H.P. Al \rightarrow H.P. Al, H.P. Cu \rightarrow H.P. Al, H.P. Cu \rightarrow H.P. Cu, and H.P. Al \rightarrow H.P. Cu data results in the relationship

$$P/d = 2.35(\rho_p/\rho_t)^{0.70}(u_p/c)^{2/3} \quad (3)$$

which is shown in Fig. 9. The value of $K_1 = 2.35$ was determined by averaging over the complete body of data, thereby giving data from each projectile-target system equal weight. The K_1 values for each projectile-target system are 2.10, 2.57, 2.32, and 2.41 for the H.P. Cu \rightarrow H.P. Cu, H.P. Cu \rightarrow H.P. Al, H.P. Al \rightarrow H.P. Cu, and H.P. Al \rightarrow H.P. Al, respectively.

A least squares fit whereby both the constant and the velocity exponent were correlated with the experimental values is also shown in Fig. 9, for the H.P. Al \rightarrow H.P. Al, H.P. Cu \rightarrow H.P. Al, H.P. Cu \rightarrow H.P. Cu, and H.P. Al \rightarrow H.P. Cu data. This was computed from

$$\log y = n \log x + \log b \quad \text{or} \quad y = b x^n$$

where $\log(K_1) = \log(P/d) - 0.7 \log(\rho_p/\rho_t) - n \log(u_p/c)$. These values for the target-projectile systems for the K_1 constant and velocity exponent, n , are $K_1 = 2.05$ $n = 0.90$, $K_1 = 2.60$ $n = 0.63$, $K_1 = 2.14$ $n = 0.79$, $K_1 = 2.37$ $n = 0.57$ for the H.P. Cu \rightarrow H.P. Cu, H.P. Cu \rightarrow H.P. Al, H.P. Al \rightarrow H.P. Cu, and H.P. Al \rightarrow H.P. Al, respectively.

Correlation with other empirical expressions involving projectile momentum, target hardness, and velocity of sound of the projectile material were also attempted but were found to

PARTICLE-SOLID IMPACT PHENOMENA

be insufficient for predicting the effects of hypervelocity impact. These expressions are derived and discussed in Ref. 5.

Several theoretical analyses are presently available. In general, they may be divided into four groups: (1) Rigid Projectile, (2) Hydrodynamic, (3) Thermal Penetration, and (4) Explosive Analogy. The experimental data and pertinent theories of each group were compared. Unfortunately, most of the theories apply to thin plates, but several have been extended to cover special cases for thicker targets. Adequate correlations could not be attained with most of these theories. A theoretical formula was derived by Bohn and Fuchs (Ref. 6) based on low velocity penetration considerations but considered by them to be applicable to meteoroid impact. The formula is the following:

$$P/d = \left(\frac{4}{3f} \frac{\rho_p}{\rho_t} \right)^n \left\{ \ln \left[1 + \left(\frac{f}{2} B \right)^{1/2} \right] - \frac{\left(\frac{f}{2} B \right)^{1/2}}{1 + \left(\frac{f}{2} B \right)^{1/2}} \right\} \quad (4)$$

where

$$\text{where } B = \frac{\rho_t u_p^2}{H} \quad (\text{Best No., Ref. 6}) \quad 4, \text{ Best}$$

and

$$f = \text{projectile shape factor (2/3 for spheres)} \\ n = 1$$

It was found that if n is taken as 2/3, a reasonably good fit for all of the aluminum and copper target-projectile combinations is obtained (Fig. 9). Correlation with Bjork's theoretical model (Ref. 9) is also shown.

In the above correlation of penetration data the following shots were not included: H.P. Al \rightarrow H.P. Al Shot No. T-367, H.P. Al \rightarrow H.P. Cu Shots Nos. T-358 and T-359, and H.P. Cu \rightarrow H.P. Cu Shot No. T-361 (Ref. Table 3). It is apparent from Fig. 9 that these data do not alter the correlation. Also the C.P. aluminum data (Table IV) do not vary sufficiently from the H.P. aluminum data to warrant separate correlation. It is also apparent, Fig. 9, that static yield or ultimate strength (Table II) of the projectile and target materials has a secondary effect on penetration. Ultimate strength of the C.P. Al compared to H.P. Al, and SS compared to H.P. Cu varies by factors of 2.3 and 3.2, respectively. Penetration of the C.P. Al is essentially the same as the H.P. Al. Penetration of the SS is approximately 0.8 of the H.P. Cu. If the term $(\rho_p/\rho_t)^{0.7}$ for SS \rightarrow C.P. Al is compared with H.P. Cu \rightarrow H.P. Al, a similar factor of 0.9 is obtained.

PARTICLE-SOLID IMPACT PHENOMENA

4.2 CRATER SHAPE

Several of the empirical expressions and theoretical analyses (Ref. 5) use the simplifying assumption that the crater is hemispherical ($P/D_c = 0.5$). Figure 10 shows the parameter, P/D_c , versus projectile velocity. The craters from all of the projectile-target combinations approach a hemispherical shape as the velocity increases. Within the range of velocities obtained, craters in H.P. aluminum by H.P. copper projectiles and craters in C.P. aluminum by stainless steel projectiles were deeper than hemispherical. H.P. Al \rightarrow H.P. Al and H.P. Cu \rightarrow H.P. Cu craters are essentially hemispherical at the higher velocities. H.P. Al \rightarrow H.P. Cu craters approach a hemispherical shape as the velocity increases, but more data are needed in the higher velocity range to confirm their shape.

4.3 CRATER VOLUME

Crater volume data are shown in Fig. 11 in the dimensionless form, V_c/V_p versus u_p/c . Correlation of the data with the equation

$$V_c/V_p = K_2 (\rho_p/\rho_t)^{3/2} (u_p/c)^2 \quad (5)$$

is also shown. The constant, K_2 , and the density ratio exponent were derived from the H.P. Al \rightarrow H.P. Al, H.P. Cu \rightarrow H.P. Al, H.P. Cu \rightarrow H.P. Cu, and H.P. Al \rightarrow H.P. Cu data, using the same method as described in section 4.2. The crater volume equation (Eq. 5) and the penetration equation (Eq. 3) are not compatible with the assumption of hemispherical craters. A less accurate correlation is obtained by using the equation

$$V_c/V_p = K (\rho_p/\rho_t)^2 (u_p/c)^2 \quad (6)$$

which is compatible with the hemispherical assumption (the cube of Eq. (2) for $n = 2/3$).

The value of $K_2 = 44.1$ is the average value of the projectile-target systems. Values for each system are 35.9, 46.2, 41.0, and 53.4 for H.P. Cu \rightarrow H.P. Cu, H.P. Cu \rightarrow H.P. Al, H.P. Al \rightarrow H.P. Cu, and H.P. Al \rightarrow H.P. Al, respectively.

Figure 11 also shows the best least squares fit. The velocity exponents K_2 and (n) are $K_2 = 35.7$ $n = 1.79$, $K_2 = 46.2$ $n = 2.02$, $K_2 = 45.7$ $n = 1.48$, and $K_2 = 50.6$ $n = 1.68$, for H.P. Cu \rightarrow H.P. Cu, H.P. Cu \rightarrow H.P. Al, H.P. Al \rightarrow H.P. Cu, and H.P. Al \rightarrow H.P. Al, respectively.

It should be noted from Fig. 11 that the crater volume data for the C.P. Al \rightarrow C.P. Al are essentially the same as the H.P. Al \rightarrow H.P. Al.

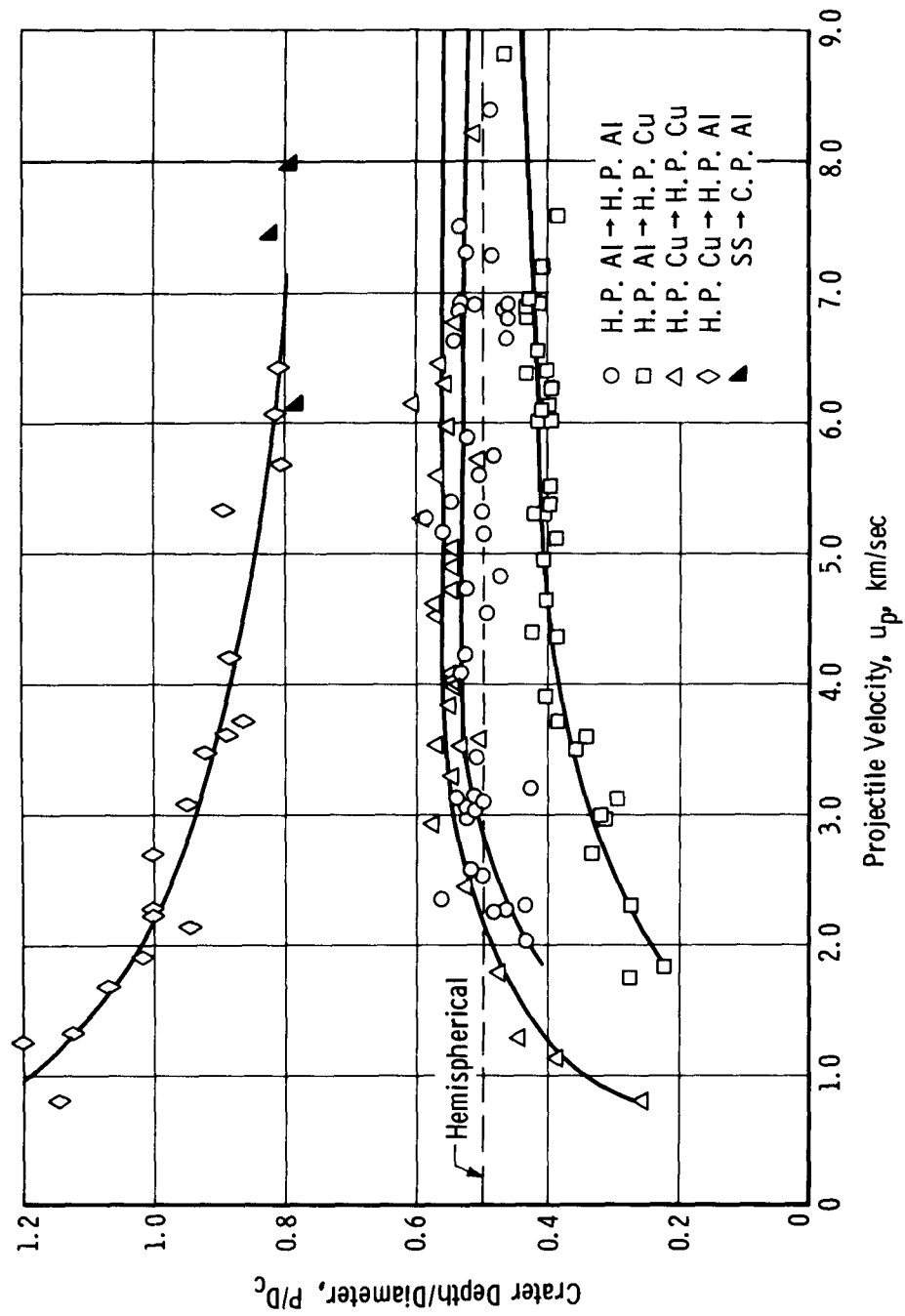


Fig. 10 Crater Depth to Diameter Ratio for Copper and Aluminum Spheres into Copper and Aluminum Targets

PARTICLE-SOLID IMPACT PHENOMENA

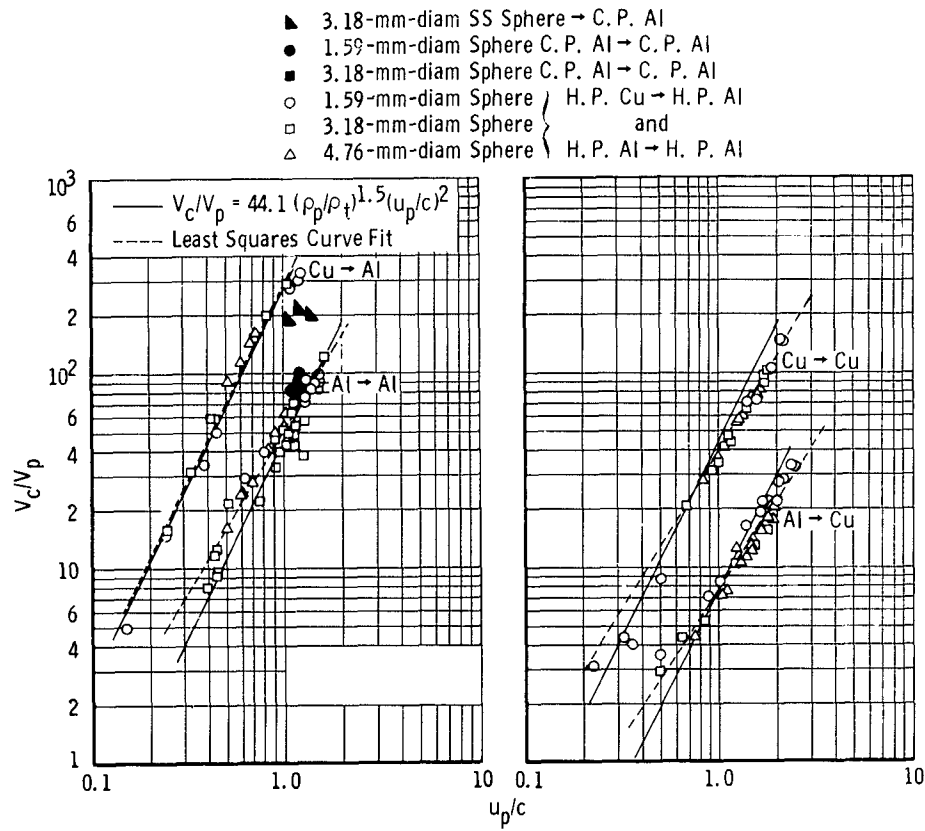


Fig. 11 Correlation of Crater Volume Data with Empirical Volume Prediction Equations

PARTICLE-SOLID IMPACT PHENOMENA

5.0 CONCLUSIONS

When the H.P. aluminum and H.P. copper experimental data are correlated to the kinetic energy of the projectile, the following empirical relations are adequate for engineering purposes:

$$P/d = 2.35(\rho_p/\rho_t)^{0.70}(u_p/c)^{2/3}$$

$$V_c/V_p = 44.10(\rho_p/\rho_t)^{3/2}(u_p/c)^2$$

which is also adequate for the C.P. aluminum projectile-target combination.

Penetration may be adequately described by Bohn and Fuch's theoretical analysis if the density term is modified and by Bjork's theoretical approach. Static strength of the materials has a small effect on the crater dimensions.

The penetration to crater diameter ratios obtained at maximum attainable velocity were: H.P. Al \rightarrow H.P. Cu about 0.45, H.P. Cu \rightarrow H.P. Cu and H.P. Al \rightarrow H.P. Al about 0.55, and H.P. Cu \rightarrow H.P. Al or SS \rightarrow C.P. Al about 0.8, which shows that the majority are nearly hemispherical; however, computations of crater volume which assume hemispherical shape can be significantly in error if a crater shape factor is not employed.

PARTICLE-SOLID IMPACT PHENOMENA

REFERENCES

1. Liles, C. D. and Goodman, E. H., "Particle-Solid Impact Phenomena," AEDC-TDR-62-202 (November 1962).
2. Goodman, E. H., "Description of Terminal Ballistics Ranges," AEDC-TDR-62-104 (May 1962).
3. Charters, A. C. and Locke, G. S., Jr., "A Preliminary Investigation of High Speed Impact: The Penetration of Small Spheres into Thick Copper Targets," NACA RM-A58B26 (May 1958).
4. Summers, J. L., "Investigation of High Speed Impact: Regions of Impact and Impact at Oblique Angles," NASA TN-D-94 (October 1959).
5. Herrman, Walter and Jones, A. H., "Survey of Hypervelocity Impact Information," ASRL Report No. R-99-1, AD-267-290 (October 1961).
6. Bohn, J. L. and Fuchs, O.P., "High Velocity Impact Studies Directed toward the Determination of Spatial Density, Mass, and Velocity of Micrometeorites at High Altitudes," Temple University Scientific Report No. 1 (January 1958).
7. Material Selector, Vol. 56, No. 5, Reinhold Publishing Corporation, New York, New York (October 1962).
8. Handbook of Physics and Chemistry, 39th Edition, Chemical Rubber Company (March 1958).
9. Olshaker, A. E. and Bjork, R. L., "Hydrodynamics Applied to Hypervelocity Impact II. The Role of Melting and Vaporization in Hypervelocity," Proceedings of the Fifth Symposium on Hypervelocity Impact, Vol. 1, Part 1 (April 1962). Also personal communication to E. H. Goodman (March 13, 1963).

INVESTIGATION OF THE IMPACT OF COPPER FILAMENTS
INTO ALUMINUM TARGETS AT VELOCITIES TO
16,000 FEET PER SECOND

By C. Robert Nysmith, James L. Summers, and
B. Pat Denardo

National Aeronautics and Space Administration
Ames Research Center
Moffett Field, Calif.

ABSTRACT

Aluminum targets were impacted by thin copper filaments to determine the effect of filament angle of inclination upon maximum depth of penetration. The effects of small filament curvature, filament diameter, and impact velocity are also discussed. The data are used to evaluate the probability of penetrations greater than any given depth by filaments having random orientation.

INVESTIGATION OF THE IMPACT OF COPPER FILAMENTS
INTO ALUMINUM TARGETS AT VELOCITIES TO
16,000 FEET PER SECOND

By C. Robert Nysmith, James L. Summers, and
B. Pat Denardo

National Aeronautics and Space Administration
Ames Research Center
Moffett Field, Calif.

SUMMARY

One-half-inch-diameter aluminum spheres were fired into thin copper filaments at velocities to 16,000 feet per second, then recovered and sectioned to determine the damage. The principal variable was the filament angle of inclination. Microscopic examination of the sectioned targets and photographs revealed the various crater characteristics and penetration parameters for each shot.

The depth of penetration decreased rapidly as the angle of inclination increased from 0° to 7° and decreased very abruptly in the range from 4° to 5° . The penetration decreased less rapidly in the range from 7° to 15° and quite slowly in the range from 15° to 90° . The characteristic features of the craters also changed in these inclination ranges.

A 66-percent increase in filament diameter caused an 85-percent increase in penetration for one specific diameter ratio. This result is very preliminary and may not be applicable to conditions other than those of this test. Incidental observations showed that small curvature of the filament may have a large effect on depth of penetration for end-on impacts but has essentially no effect for impacts of inclined filaments. The data are used to evaluate the probability of penetration greater than a selected depth for randomly oriented filaments.

INTRODUCTION

Investigations concerning the impact of thick metal targets by low-fineness-ratio projectiles, such as spheres and cylinders, have yielded a considerable amount of data relating the various impact parameters. This information has made it possible to predict, with fair confidence, the penetration of a target by a given projectile at velocities to about 30,000 ft/sec. Extrapolation of this information to higher impact velocities depends upon the assumption made as to the physical law that governs cratering at these higher velocities.

IMPACT OF COPPER FILAMENTS

On the other hand, information concerning the impact of targets by high-fineness-ratio projectiles is rather limited and has been obtained at relatively low-impact velocities with few variables considered. Even so, the information indicates that high-fineness-ratio projectiles are more efficient in penetrating targets than corresponding blunt projectiles of the same mass (see ref. 1). Thus, it is felt that more information pertaining to the impact of high-fineness-ratio projectiles should be obtained so that the penetration efficiency of these bodies can be evaluated.

With this in mind a program of research directed toward determining the damage produced by the impact of high-fineness-ratio projectiles upon space vehicle structures is being conducted at the NASA Ames Research Center. The filament-impact results described here concern only the depth of penetration of a very high-fineness-ratio projectile. Specific applications of this information will not be discussed here.

TEST PROCEDURE

The launching of a projectile involves accelerating the projectile from zero to some finite velocity in a fairly short time. As the launch velocity is increased, the acceleration loads on the projectile also increase and the model is subjected to high-compression loads along the line of the model trajectory.

Low-fineness-ratio projectiles, such as spheres and cylinders, can tolerate compressive loads as high as the compressive strength of the projectile material and thus can be launched to fairly high velocities. High-fineness-ratio projectiles, on the other hand, have essentially no compressive strength along their longitudinal axis, since they fail as columns, and it is virtually impossible to launch them to any reasonable velocity.

Thus, the experimental technique used in this impact program was unusual because the target was launched into a stationary projectile. The "target" in this case was an aluminum sphere. The "projectiles" were fine copper filaments placed directly in the path of the sphere.

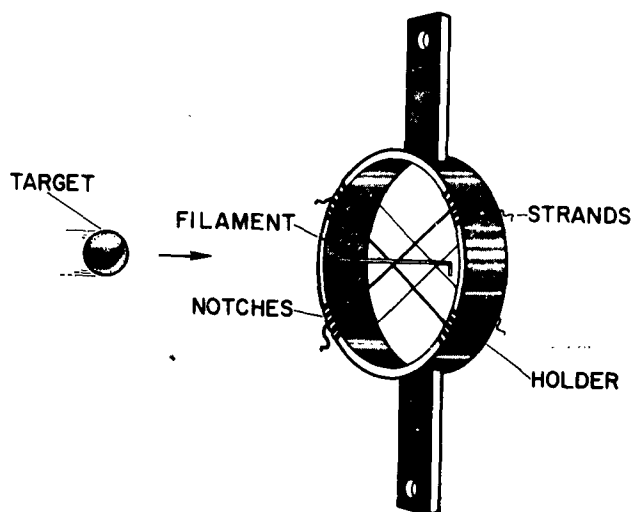
The targets used in this experiment were 1/2-inch-diameter 2017-T4 aluminum spheres launched from a 20-millimeter light-gas gun in nylon sabots. Upon leaving the launch tube, the targets entered the first section of the flight-test range which contained air at a pressure of 4-mm Hg. This pressure was sufficient to insure the target's separation from the sabot, so that impact with the filament would not be complicated by sabot effects, but was low enough that deceleration of the target in this section was negligible. This section of the range was 25 feet

IMPACT OF COPPER FILAMENTS

long, had three velocity measuring stations, and was separated from the second section by a 1-mil mylar diaphragm. The second section of flight-test range, approximately 200 feet long, contained air at one atmosphere and had four velocity measuring stations. A model catcher made of polystyrene foam and cotton waste was located at the end of the second section. The target decelerated in this section to a velocity at impact of about 3500 feet per second. As the result of this particular recovery technique damage to the target was very slight and always appeared as ablation rather than severe damage.

The wire filaments were supported on the range center line by 1/4-mil nylon strands just uprange of the diaphragm at the end of the first section of the flight-test range. Angles of inclination could be varied by placing the supporting nylon strands in various notches in the holder as shown by sketch (a). Holder tolerances were such that angles of inclination were

FILAMENT SET-UP



Sketch (a)

held within an accuracy of 20 minutes of arc. A 90° bend was made in the rear of the filament to insure its remaining in place during range evacuation and to give a clearer representation of the filament-target orientation at impact. Two filament diameters were used in this series of tests, 0.0025 inch and 0.0015 inch. The length of the straight sections was always 3/4 inch, and the length of the tails, as a result of the 90° bend mentioned above, was 1/8 inch. Filament fineness ratios then were 300 and 500, respectively. All filaments were straightened

before they were mounted in the holder. This was done by heating the wires electrically and simultaneously applying a tensile load. This process annealed the copper filaments and reduced the filament curvature to what was felt to be a practical minimum. In some cases several filaments were placed in the holder (by adding additional sets of nylon supporting strands) and several noninterfering impacts were obtained from a single shot.

The velocity at impact was determined from the time-distance history obtained by the seven spark-shadowgraph stations located along the flight

IMPACT OF COPPER FILAMENTS

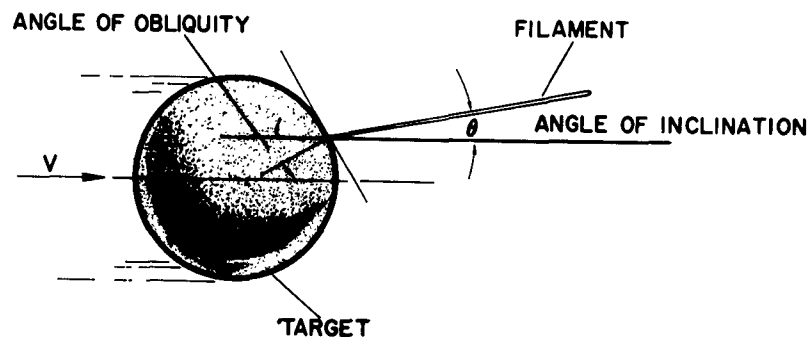
path. The accepted method of plotting the reciprocal of the model velocity versus time (ref. 2) was used.

After recovery, the targets were sectioned parallel to the crater plane on a milling machine and the penetration was measured microscopically. Figure 1(a) is a photograph of a target just after recovery and prior to sectioning. One can see the impression made by the 90° bend and the ablation due to flight through the second section of the flight-test range. Figure 1(b) is a photograph of the same target after sectioning. The crater is clearly visible. The loss of material due to ablation was estimated in determining the various penetration parameters.

DISCUSSION OF RESULTS

Tests were conducted to determine the effect of filament inclination upon maximum depth of penetration. The inclination is defined here as the angle between the filament longitudinal axis and the flight trajectory. It is not a function of the obliquity which is defined as the angle between the trajectory and the line normal to the plane tangent to the sphere at the point of impact (a definition consistent with the usual definition of obliquity for impact work). Sketch (b) below illustrates these two definitions. The maximum depth of penetration is measured from the target surface parallel to the trajectory and thus is not dependent upon target obliquity.

FILAMENT-TARGET ORIENTATION



Sketch (b)

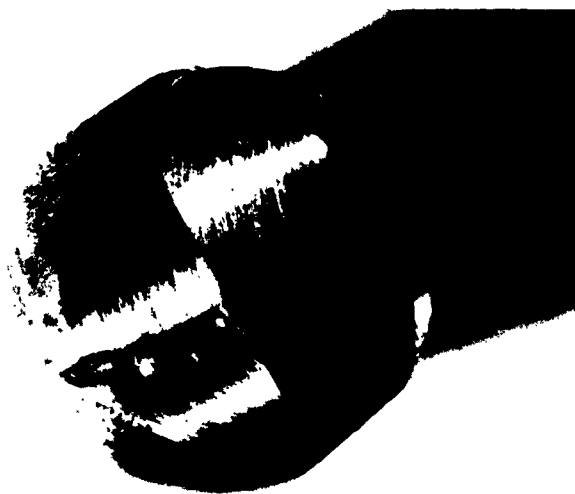
Plotted in figure 2 is the maximum depth of penetration in inches versus filament inclination in degrees for 0.0025-inch-diameter filaments of fineness ratio 300. Each square symbol shown in figure 2 represents

IMPACT OF COPPER FILAMENTS



AR-1583-23

(a) Photograph of model after recovery
and prior to sectioning.



AR-1583-54

(b) Photograph of model after sectioning.

Figure 1.- Model before and after sectioning.

IMPACT OF COPPER FILAMENTS

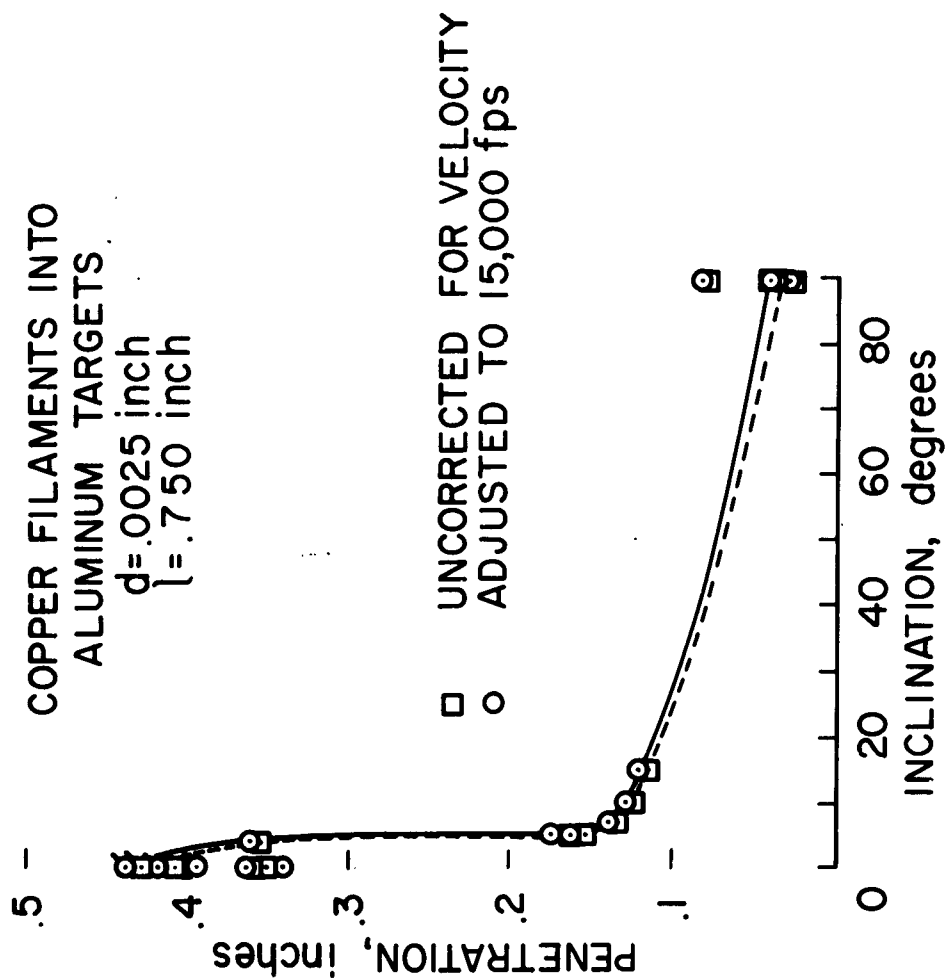


Figure 2.- Variation of penetration with angle of inclination.

IMPACT OF COPPER FILAMENTS

one experimental point determined from target examination and measurement. Flagged symbols indicate that the sphere was completely penetrated by the filament. However, it may be noted that the penetration in these cases was always less than 1/2 inch, the target diameter. This simply indicates that the filaments impacted the spheres slightly off center.

It should be noted that target velocities from the 20-mm shock-heated light-gas gun used in this series of tests are not necessarily repeatable from round to round. Thus, square symbols in figure 2 represent data in which the impact velocities varied from 13,500 to 15,700 ft/sec. It is felt that one can adjust the data to any particular velocity so long as the adjusted data are in the same impact regime in which the original data were acquired. (See ref. 2.) For the case described here, it is desired to adjust the data to 15,000 ft/sec. If it is assumed that the volume of material removed is proportional to the kinetic energy of the projectile, then the penetration will be proportional to the $2/3$ power of the velocity. Thus, it will be assumed that

$$p \approx v^{2/3}$$

as in reference 3.

The original data of figure 2 adjusted to a velocity of 15,000 ft/sec are replotted as round symbols and the solid curve of figure 2. The two curves of figure 2 differ slightly because of the variation in original impact velocities. For normal impacts (0° angle of inclination) and broadside impacts (90° angle of inclination) there appears to be considerable scatter in the data. This is not surprising, however, since for normal impacts, it is felt that any curvature of the filament will greatly influence the depth of penetration; for broadside impacts, ablation loss was of the order of the depth of penetration and deduced penetration depths were accordingly very sensitive to ablation-loss measurements.

It is interesting to note that there appears to be essentially no scatter in the data throughout the inclination range from 4° to 15° . This indicates that small filament curvature does not influence inclined impacts.

The data of figure 2 show that impacts occurring at 0° angle of inclination produce relatively deep craters. As the inclination is increased to 4° the penetration decreases rapidly. Craters from impacts within this inclination range, however, are similar in appearance in that they have small diameters (about 10 filament diameters) and are relatively deep. Figures 3(a) and 3(b) are photographs of sectioned targets impacted at 0° and 4° , respectively. The similarity between these two craters is evident.

As the inclination is increased from 4° to 5° , the penetration decreases abruptly. In figure 2 the penetration resulting from impact

IMPACT OF COPPER FILAMENTS

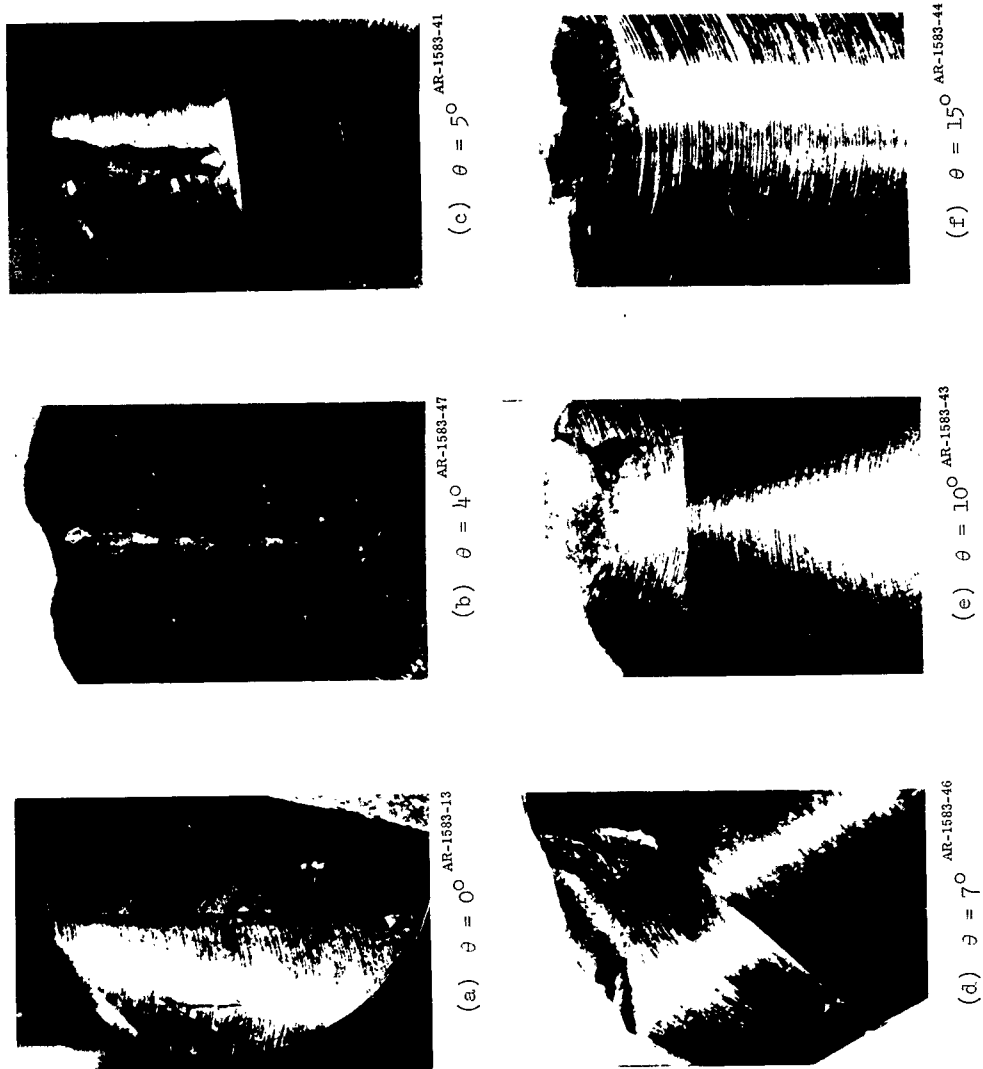


Figure 3.- Photographs of sectioned filament craters at various angles of inclination.

IMPACT OF COPPER FILAMENTS

at 5° is roughly half that from impact at 4° . One would suspect that the cratering process must undergo some drastic change to account for this phenomenon. Figure 3(c) is a photograph of a sectioned crater from impact at 5° inclination. Comparison of this figure with figure 3(b) (impact at 4°) shows that these craters are very dissimilar. The 5° inclination impact crater appears to be fairly shallow and relatively broad in the plane of the filament while the other is narrow and deep. It appears that the nature of the cratering process has suddenly undergone a transition within this small inclination range.

Increasing the inclination from 5° to 15° reduces the penetration to some extent but the reduction is not nearly so abrupt as the change from 4° to 5° mentioned above. Figures 3(d), 3(e), and 3(f) are photographs of sectioned models after impact at inclination angles of 7° , 10° , and 15° , respectively. These craters all exhibit much the same characteristics that were observed for impact at 5° . As the inclination is increased from 5° to 15° , the penetration decreases systematically and the craters become broader, in the filament plane, according to the projected filament length in the direction of the target trajectory.

At angles of inclination from 15° to 90° the penetration decreases a small amount and it is clear that damage within this inclination range is similar to broadside impacts.

In addition to the inclination tests described above, a number of firings were made with a 0.0015-inch-diameter filament with fineness ratio 500 at 0° and 90° inclination. It was observed that for these inclination extremes, a 66-percent increase in filament diameter resulted in an 85-percent increase in penetration. It should be pointed out that this result is very preliminary in nature and should be used with caution. Future tests will enable the effects of this variable to be evaluated more completely.

The information presented in the previous sections may be used to estimate the probability that a particular impact of one of these filaments will produce a crater of greater than a given depth in an aluminum structure. First, it is assumed that the vehicle being considered will be struck by the given filament. Second, it is assumed that impacts will occur at a velocity of 15,000 ft/sec. The probability to be calculated is nothing more than the probability that the impact will occur at an inclination, θ , less than that which yields the chosen penetration. If the distribution of filament inclinations is assumed to be random, the probability that impact will occur at $\theta < \theta_c$ is

$$\eta = 1 - \cos \theta_c$$

where $\theta = 0^\circ$ for end-on impact and 90° for broadside impact.

IMPACT OF COPPER FILAMENTS

As shown in figure 4, for the assumed conditions, all impacts yield penetrations greater than 0.039 inch; thus, the probability is 1.0. The probability of twice this penetration is 0.32, and the probability of four times this penetration is 0.0045. This illustrates the extreme insensitivity to inclination in the range from 15° to 90° .

Extrapolation of these data to other materials, projectile fineness ratios, and impact velocities is not possible because these parameters have not been varied sufficiently. It is interesting, however, to compare the penetrating ability of the inclined filaments with that of spheres as functions of their respective masses: First, a sphere with a mass 130 times that of a filament is required to penetrate to the same depth as the filament striking end-on. Second, a filament at a 39° inclination penetrates to the same depth as a sphere of the same mass. These observations clearly show the penetrating superiority of aligned filaments over spheres on a mass to mass basis.

IMPACT OF COPPER FILAMENTS

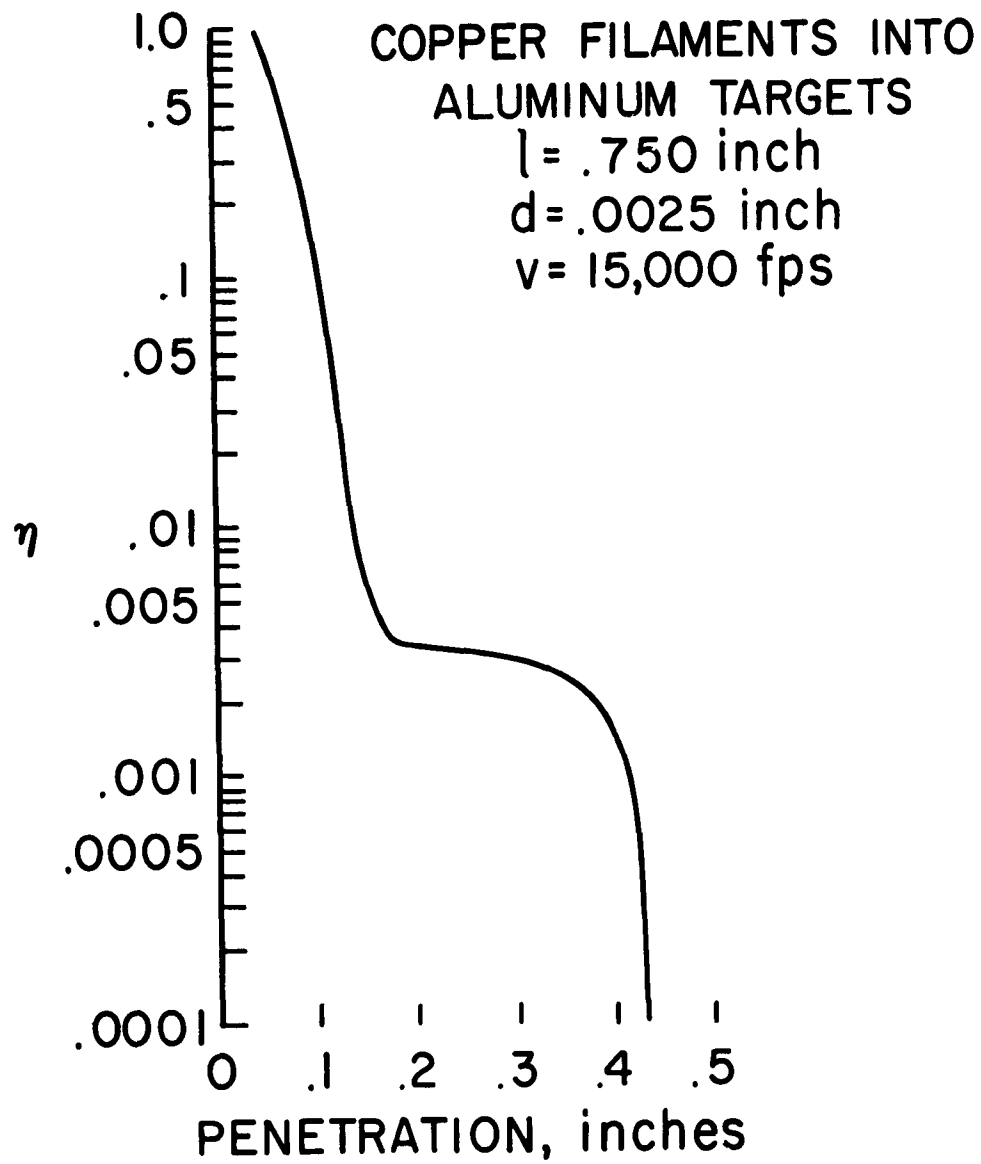


Figure 4.-

Probability of penetration greater than a selected depth for randomly oriented filaments.

IMPACT OF COPPER FILAMENTS

REFERENCES

1. Summers, James L., and Niehaus, William R., "A Preliminary Investigation of the Penetration of Slender Metal Rods in Thick Metal Targets," NASA TN D-137, 1959.
2. Yee, Layton, Bailey, Harry E., and Woodward, Henry T., "Ballistic Range Measurements of Stagnation-Point Heat Transfer in Air and in Carbon Dioxide at Velocities up to 18,000 Feet Per Second," NASA TN D-777, 1961.
3. Summers, James L., "Investigation of High-Speed Impact: Regions of Impact and Impact at Oblique Angles," NASA TN D-94, 1959.

"IONIZATION ASSOCIATED WITH HYPERVELOCITY IMPACT"

by

J. F. Friichtenicht and J. C. Slattery

**PHYSICAL ELECTRONICS LABORATORY
Physical Research Division**

**Space Technology Laboratories, Inc.
a Subsidiary of Thompson Ramo Wooldridge, Inc.
One Space Park, Redondo Beach, California**

IONIZATION ASSOCIATED WITH HYPERVELOCITY IMPACT

ABSTRACT

Interest in the development of micrometeoroid detection systems has led to a program of research at Space Technology Laboratories, Inc., where efforts have been concentrated on phenomena associated with hypervelocity impact which have properties applicable to such systems. It has been found that electrically charged particles are emitted from the site of a hypervelocity impact. Presumably, the large energy release associated with the impact is sufficient to produce ionization and the ions or electrons can be extracted by means of electrical collector systems. The quantity of charge emitted from semi-infinite targets as a function of target material, projectile material, and particle velocity and mass was measured. The experiments were conducted with micron-sized iron and carbon black (graphite) particles from the STL electrostatic hypervelocity accelerator. Data were collected for velocities up to 16 km/sec. All of the data fits the empirical relationship $Q_c = K E_p \frac{v}{A}$, where Q_c is the charge collected, K a constant, E_p the particle energy, A the atomic weight of the particle material, and v the particle velocity. The quantity K contains target material parameters and has not been evaluated, as yet. Qualitative observations of ionization produced from thin foil impacts have also been made.

IONIZATION ASSOCIATED WITH IMPACT

I. INTRODUCTION

An increasingly large effort has been devoted towards the direct measurement of small bodies in space in recent years. The properties of meteoroids and cosmic dust particles are interesting from both the engineering and scientific points of view, and it appears that experiments pertaining to these particles will be continued for some time to come. The experimental techniques for determining the quantity and properties of particles in interplanetary space by means of instruments aboard satellites and rocket probes and the results of some of the measurements are discussed briefly in a recent paper¹. Although all of the data are in reasonably good agreement, it is evident that additional, more refined experiments, are required. One of the difficulties encountered in this type of experiment is the development of sensitive, reliable particle sensors.

Generally speaking, the encounter between an earth satellite and a meteoroid in space takes the form of a hypervelocity impact with the meteoroid serving as the projectile and the sensor as the target. The impact velocity may range from nearly zero up to 85 km/sec depending upon the relative orbits of the satellite and the meteoroid. The size range of the particles is also extremely large, although the frequency of occurrence increases with decreasing size. The smallest of them may be only a micron or so in size. Thus, the problem of assessing the characteristics of interplanetary dust can be described as the remote analysis of a hypervelocity impact of a projectile of unknown mass, velocity, composition, and direction, and whose velocity may be such that the impact

¹W. M. Alexander, C. W. McCracken, L. Secretan, and O. E. Berg, "Review of Direct Measurements on Interplanetary Dust from Satellites and Probes", oral paper presented to the COSPAR Meeting, May, 1962.

IONIZATION ASSOCIATED WITH IMPACT

mechanism is not adequately understood. Considering these complexities, the good agreement of the existing data is all the more remarkable.

Most of the experiments have utilized a crystal transducer type sensor. The assumption is made that the magnitude of the electrical signal resulting from meteoritic impact is proportional to the momentum of the meteoroid. If an average velocity is assumed, the mass distribution of particles can be obtained from this instrument. It is clear from the nature of these assumptions that the development of more sophisticated sensor elements would be desirable. Consequently, Space Technology Laboratories, Inc., has been involved in a research program on those properties of hypervelocity impact which might serve as a basis for meteoroid detection systems. The program has been sponsored by the NASA, under Contract Nos. NASw-269 and NASw-561. One of the properties under study has been the emission of charged particles associated with hypervelocity impact.

We have concluded that some of the atoms near the impact site of a high speed particle are ionized by the large energy release associated with the impact. The emitted charge (either positive or negative) can be collected by means of electrically biased collectors and the resulting signal may be used in various types of meteoroid detectors. The quantity of charge emitted depends upon particle velocity and mass, and upon characteristics of the materials in question. An experimental study of this effect was undertaken and results of these experiments are described below.

II. GENERAL EXPERIMENTAL TECHNIQUES

The STL electrostatic hypervelocity projector was used as a source of high speed particles for all of the work described in the following paragraphs. The operation and properties of this accelerator have been described in the

IONIZATION ASSOCIATED WITH IMPACT

literature² and need not be discussed here.

The electrostatic method of accelerating particles is generally restricted to particles with dimensions the order of microns or smaller. Carbonyl iron and carbon black (graphite) particles were used in these experiments. The iron particles were quite spherical while the carbon particles were somewhat more irregular in shape. The average size of the iron particles was about 1.5 microns diameter while the average carbon black particle had a corresponding dimension of about 0.6 micron. Particle velocities ranged from 1.5 to 16 km/sec depending upon particle material and size. The upper part of the velocity spectrum was obtained with the carbon particles while the iron particles were restricted to velocities of 10 km/sec and less. The velocity and mass of each particle were measured prior to impact by techniques described elsewhere.³ The size of the particles was then computed from the known mass and density. For the iron particles, the radius can be computed exactly. For the slightly irregular carbon particles we defined an effective radius, r , as the cube root of the quantity $\frac{3m}{4\pi\rho}$, where m is the mass and ρ the density.

For the experiments where the resulting signal was electrical in nature, the signal was displayed on one trace of a Tektronix Model 551 dual-beam oscilloscope while the signal from the particle velocity detector was displayed on the other trace. The signals were photographed with a Polaroid camera for later analysis. Time-of-flight techniques were used to correlate the observed event with the particle producing the event in order to eliminate spurious measurements.

²J. F. Friichtenicht, "Two-Million-Volt Electrostatic Accelerator for Hypervelocity Research", Rev. of Sci. Inst., Vol. 33, 209 (1962).

³H. Shelton, C. D. Hendricks, Jr. and R. F. Wuerker, "Electrostatic Acceleration of Microparticles to Hypervelocities", J. Appl. Phys., Vol. 31, 1243 (1960).

IONIZATION ASSOCIATED WITH IMPACT

III. IMPACT IONIZATION FROM THICK TARGETS

A. Experimental Procedures

The geometrical configuration of the detector and collector system used in examining charge emission from thick targets is illustrated in Figure 1. Particles from the accelerator pass along the axis of a velocity-charge detector, pass through a grid structure, and impact upon the surface of the target sample at normal incidence. For all of the measurements discussed here, the target was biased 300 volts negative with respect to the grounded grid. With this bias, negative charge produced at the target surface is repelled from the collector while positive charge is retained. The quantity of charge retained by the target is determined from the relationship $q_c = C V$, where C is the electrical capacitance of the collector and V is the amplitude of the induced voltage signal. The RC time constant of the collector system was made long compared to the signal duration so that the signal is proportional to charge as opposed to current flow. We had previously determined that the quantity of collected charge was nearly independent of the polarity and magnitude of the bias voltage for biases exceeding a few tens of volts. For this work, the choice of bias voltage and polarity was made arbitrarily and it is assumed that corresponding results would be obtained with different choices.

Figure 2 is a tracing of a typical photographic record of an event. In this case, a copper target sample was used. The particle detector signal is displayed on the lower trace while the collected charge signal appears on the upper trace. Since the impacting particle is charged, a voltage signal is induced on the collector independently of that produced by subsequent charge emission. This effect accounts for the structure on the upper trace. The particle charge produces the first step in the signal while the charge emission effect accounts for

IONIZATION ASSOCIATED WITH IMPACT

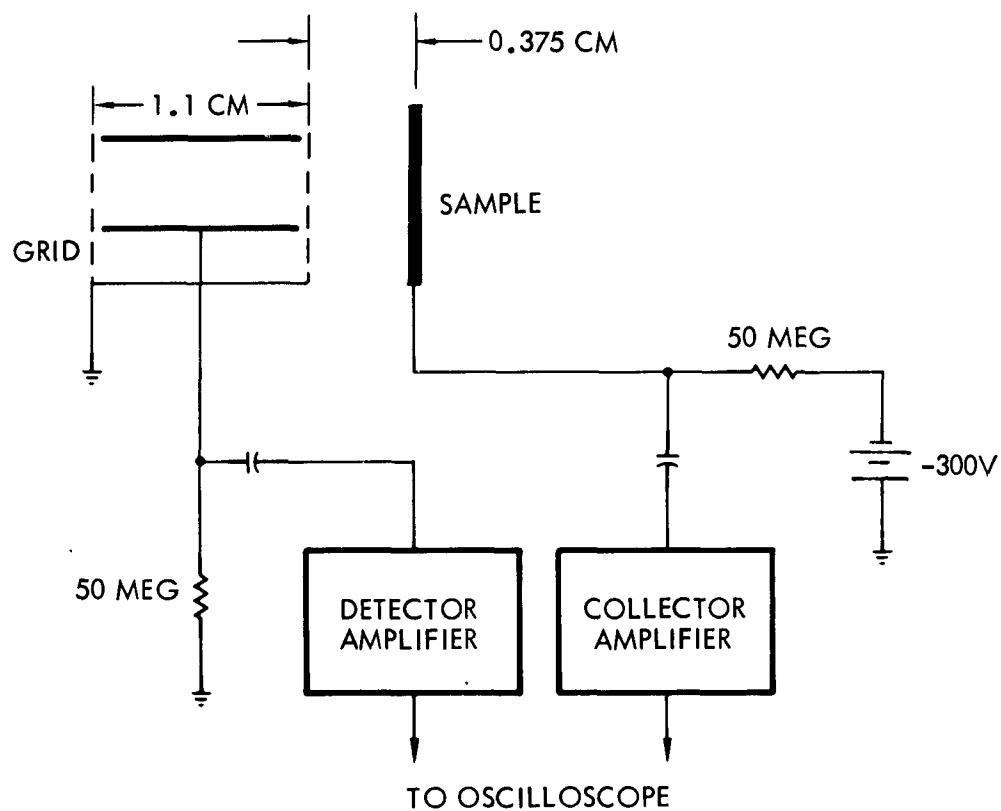


Figure 1. Experimental arrangement for the measurement of impact ionization from thick target impacts.

IONIZATION ASSOCIATED WITH IMPACT

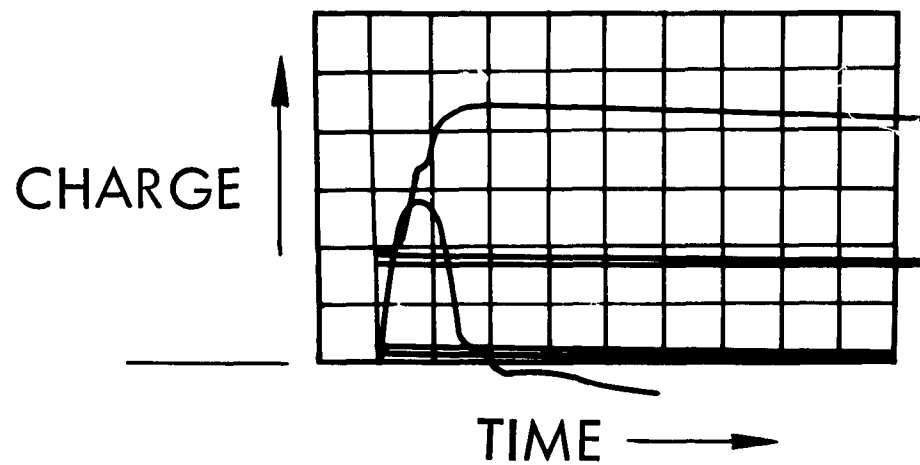


Figure 2. Tracing of an oscillograph obtained from the thick target measurements.

IONIZATION ASSOCIATED WITH IMPACT

the remainder. The total charge emitted is obtained by subtracting the particle charge from the total signal. In cases where the signal from the particle charge was small compared to the total, the particle charge was determined from the particle detector.

B. Velocity Dependence of Impact Charge Emission

Since few theoretical guidelines were available to assist us in interpretation of the experiments, the data were compared on a more or less empirical basis*.

For purposes of discussion, assume that the amount of charge liberated upon impact is proportional to the kinetic energy of the particle. Further, assume that the energy term is modified by a velocity dependent function which takes into account threshold effects and variations of cratering mechanisms with velocity, i.e., $Q_c \propto E_p f(v)$. This is equivalent to

$$\frac{Q_c}{m} = K_1 v^2 f(v) \quad (1)$$

where m is the particle mass and K_1 is a constant of proportionality.

To evaluate $f(v)$, the quantity, Q_c/r^3 , (which is equivalent to $\frac{Q_c}{m}$ for a given particle material) was plotted as a function of particle velocity for all of the particle-target combinations used. Figures 3 and 4 show these plots for iron particles impinging on targets of tantalum and indium respectively, while Figure 5 shows data for carbon particles on a tungsten target. Generally speaking, these data exhibit

*The format of the succeeding sections is primarily chronological in nature. The data are presented in this way to illustrate the evolution of the final result.

IONIZATION ASSOCIATED WITH IMPACT

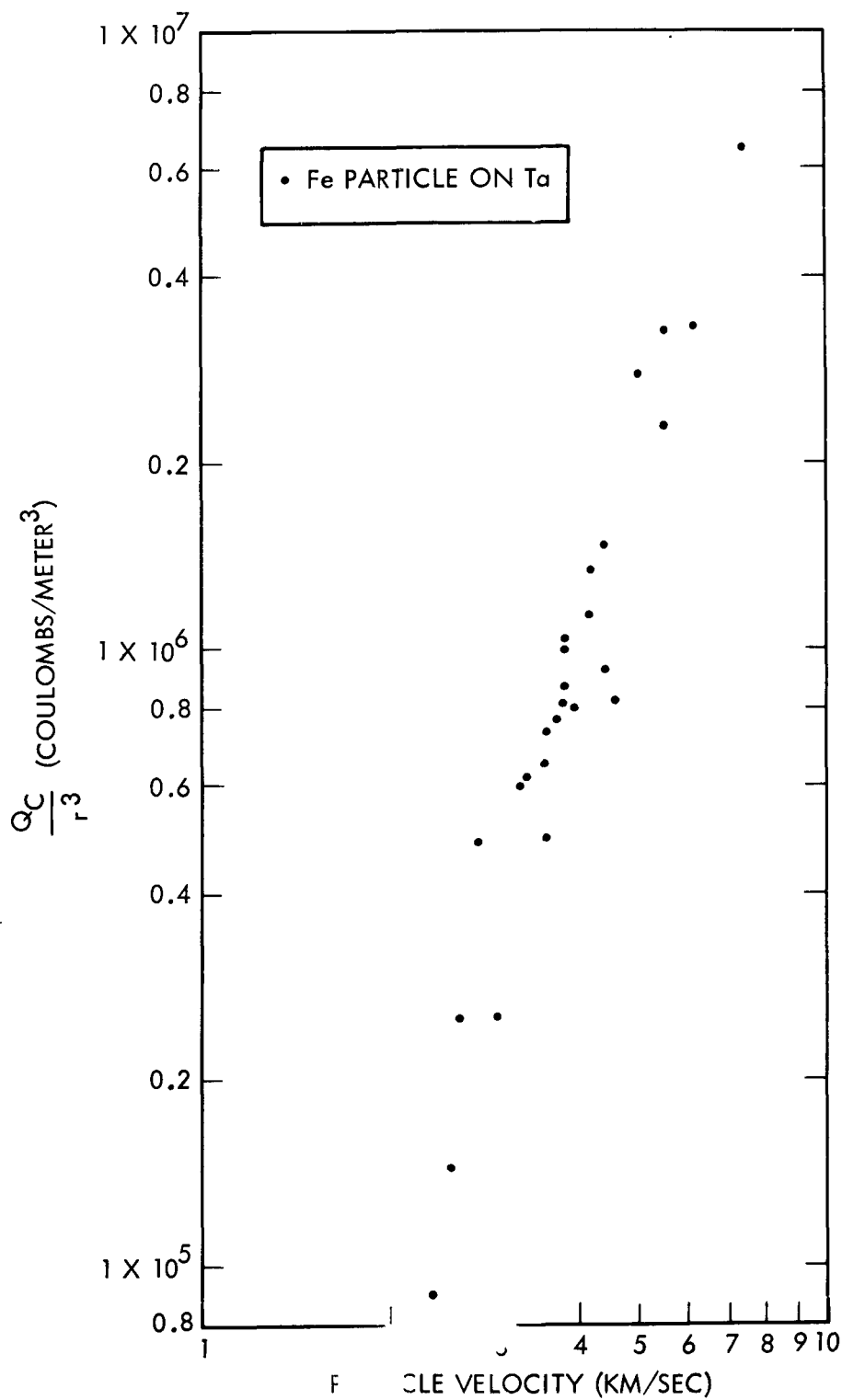


Figure 3. Charge collected normalized to r^3 plotted as a function of particle velocity for iron particle impacts on a thick tantalum target.

IONIZATION ASSOCIATED WITH IMPACT

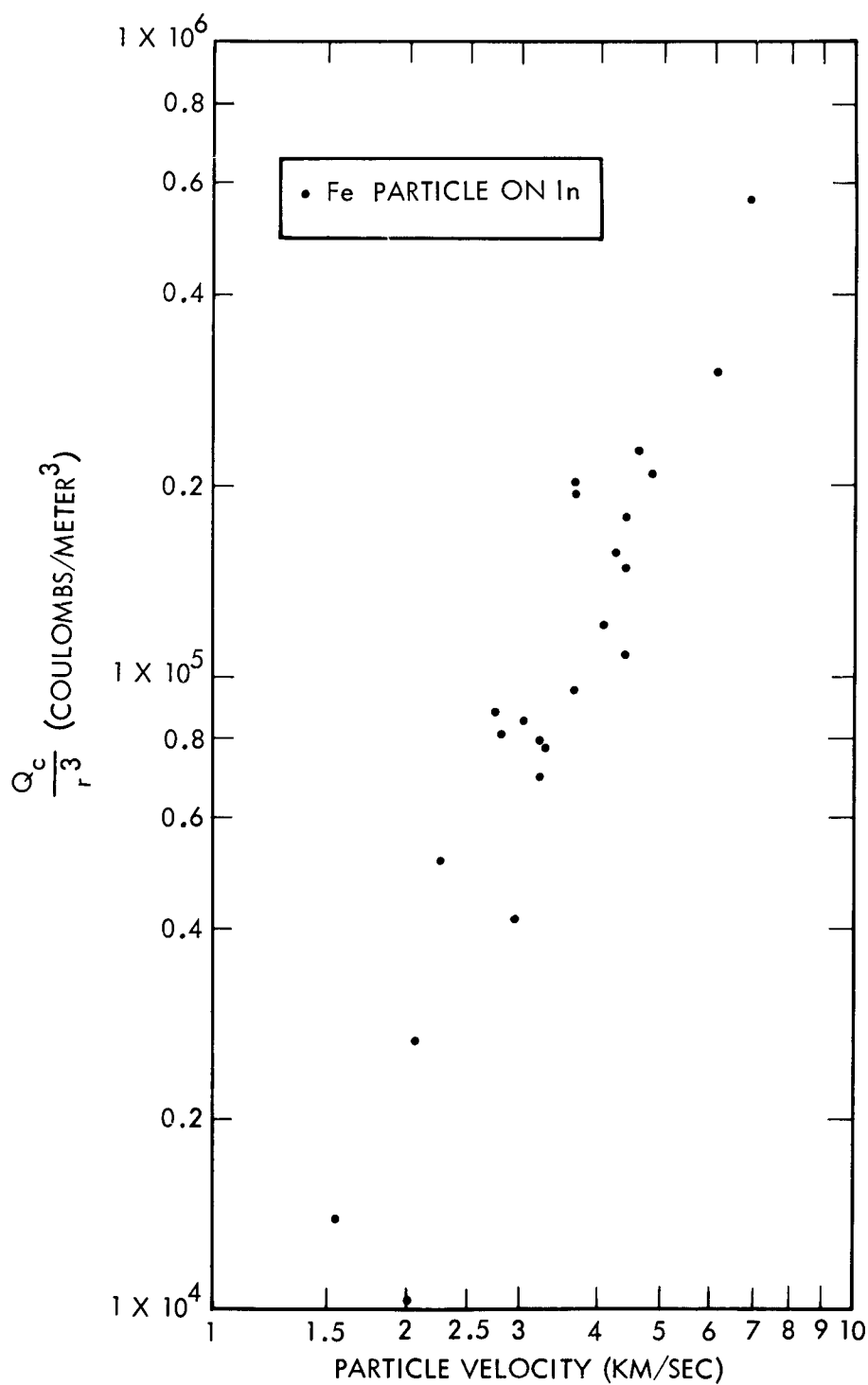


Figure 4. Charge collected normalized to r^3 plotted as a function of particle velocity for iron particle impacts on a thick indium target.

IONIZATION ASSOCIATED WITH IMPACT

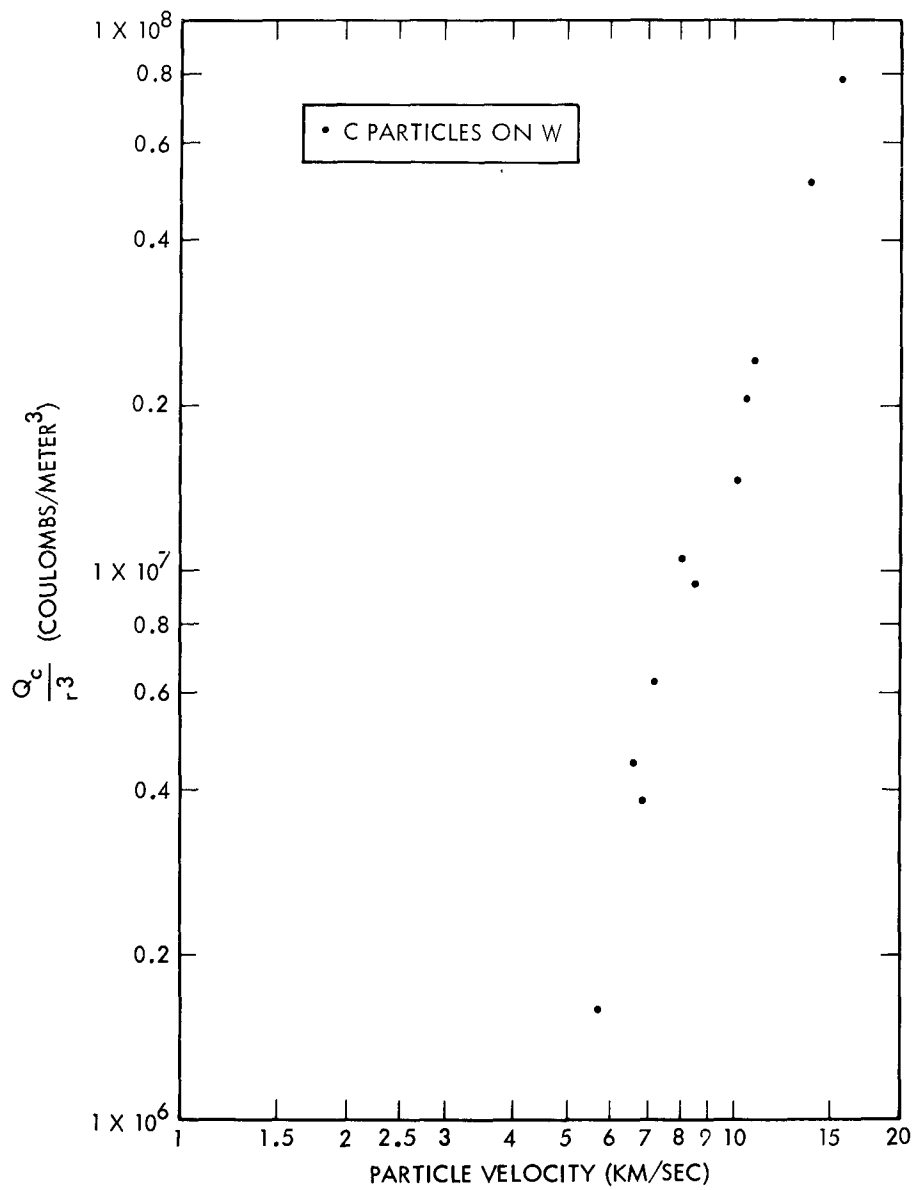


Figure 5. Charge collected normalized to r^3 plotted as a function of particle velocity for carbon particle impacts on a thick tungsten target

IONIZATION ASSOCIATED WITH IMPACT

little scatter and the data points tend to lie along straight lines on the logarithmic presentation. The slope of the lines, drawn by eye through the data points, is about three for all of the material and particle combinations used. This implies that $f(v) \approx v$. Consequently, we can write

$$Q_c = K_1 m v^3 . \quad (2)$$

It should be emphasized that this is an empirical relationship and is valid only for the conditions described above. It can readily be seen, for example, that the expression is invalid for massive particles at very low velocities since charge emission does not occur under those circumstances. Yet, Equation (2) predicts a charge emission proportional to m .

C. Target Material Dependence

For a given particle mass and impact velocity, the quantity of charge emitted is dependent upon the target material. This is illustrated in Figure 6 where smoothed curves are plotted for each of the target materials. These data were obtained with iron particles. It can be seen that the materials examined fall into two distinct categories. More charge is emitted from the Ta, W, and Pt targets than from targets of Cu, Be-Cu, In, and Pb. With the possible exception of lead, all of the targets exhibit identical results.

It is almost certain that the quantity of charge emitted is a function of more than one characteristic of the target material. Because of the complexity of the problem, no attempt has been made to explain the material dependence. However, certain characteristics of the materials exhibit a similar grouping. For example, Ta, W, and Pt all have higher melting and vaporization temperatures than the others. Also these same materials are classified as good thermionic

IONIZATION ASSOCIATED WITH IMPACT

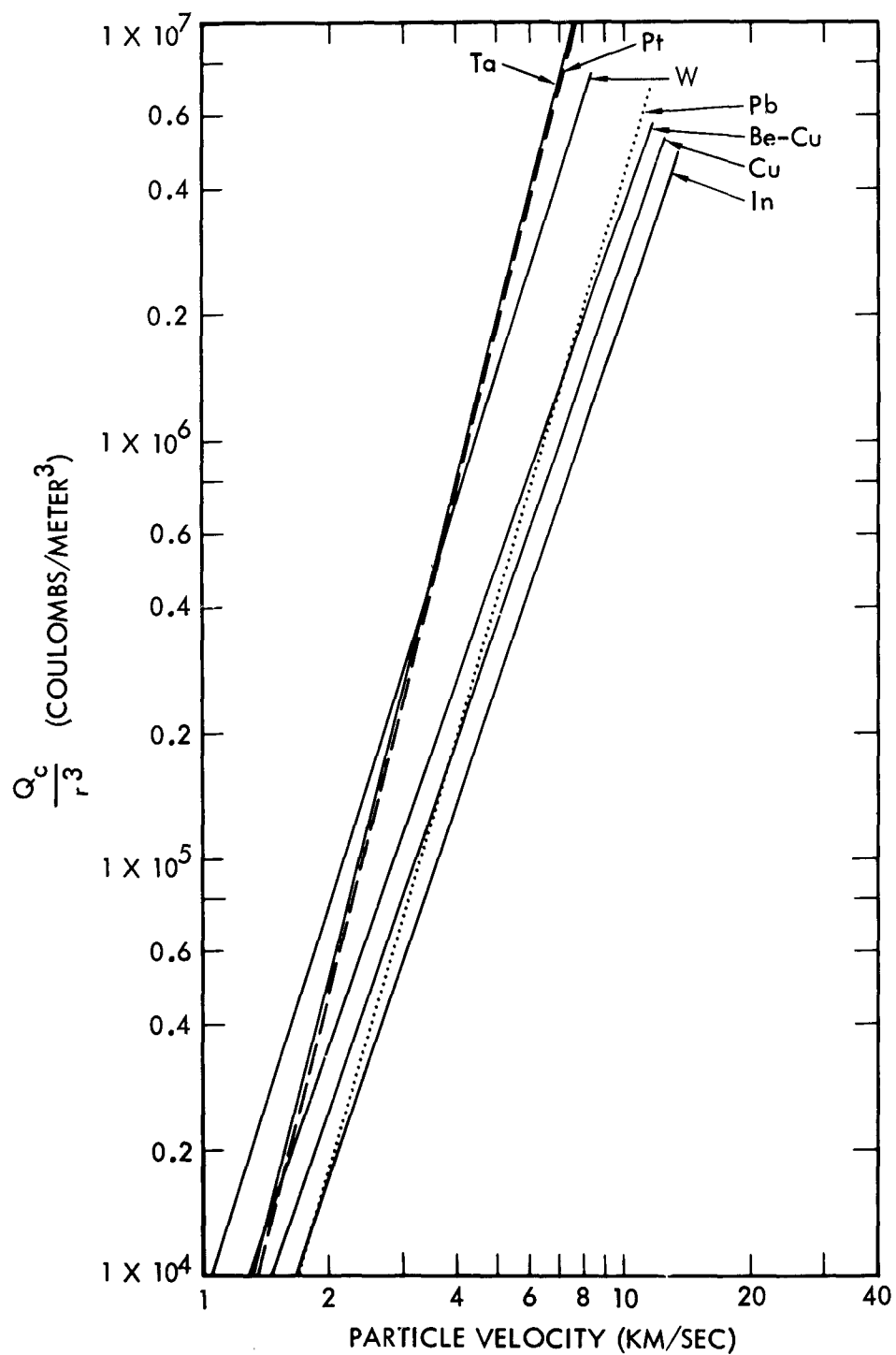


Figure 6. Q/r^3 vs. v for iron particle impacts on several target materials.

IONIZATION ASSOCIATED WITH IMPACT

emitters while the others are not. Perhaps the most significant property of all (based on the discussion of the next section) is that of resistance to hypervelocity penetration. The craters produced in Pb, In, Cu, and Be-Cu, are generally larger than those in Ta, Pt, and W.

D. Particle Material Dependence

As mentioned earlier, both iron and carbon particles were used in these experiments. The relationship given by Equation (2) appears to fit the experimental results for both kinds of particles separately, but does not yield consistent results for both kinds of particles impacting on identical targets. When normalized to particle mass, the amount of charge produced by carbon particles was greater than that produced by iron particles at a given impact velocity. In order to explain this difference, one must invoke a mechanism for the charge production process. Initially, the assumption was made that the charge produced at the impact site was strongly dependent upon the energy per unit mass imparted to the target material. The quantity of charge collected would depend upon the extraction mechanism. For example, the charge could be dependent upon either the surface area or the volume of the emitting material. Application of several combinations of hypervelocity penetration formulae and assumed extraction mechanisms failed to provide the desired agreement. All of these hypotheses assume that the bulk of charge results from ionization of atoms of the target material. Failure to achieve correlation in this manner led to the development of the model discussed below.

Let us assume that most of the charge results from ionization of atoms of the impacting particle. The number of atoms ionized depends upon the number available, the energy required for ionization, and the energy available for ionization. The kinetic energy of the particle is dissipated in

IONIZATION ASSOCIATED WITH IMPACT

several ways and the relative amount available for ionization is impossible to predict on the basis of existing knowledge on hypervelocity impact. Therefore, let us again adopt the empirical approach. Rather than normalizing the charge to the particle mass, let us normalize it to the number of atoms in the particle. This quantity, Q_c/N , is plotted as a function of velocity for iron and carbon particle impacts on a tungsten target in Figure 7 and for a lead target in Figure 8. Since N is proportional to m , the same v^3 dependence is obtained. However, the agreement between the results of using iron and carbon particles is much better in this case. Normalization to the number of atoms is equivalent to the following expression:

$$Q_c = K_2 \left(\frac{N_o}{A} \right) m v^3 \quad (3)$$

where N_o is Avogadro's number, A the molecular weight of the particle atoms, and K_2 a constant of proportionality. Equation (3) can be rewritten in the form

$$Q_c = K E_p \frac{v}{A} \quad (4)$$

From this we see that Q_c depends upon the kinetic energy of the particle and upon a quantity which can be interpreted as a factor which determines the fractional part of the energy which is available for ionization. The role of the target in this interpretation is simply that of resisting penetration by the particle. The higher the resistance, the larger is the fraction of energy which goes into ionization.

The problem resulting from empirical data analysis is that one has difficulty in attaching physical significance to the results. The choice of $\frac{v}{A}$ as a multiplying factor is

IONIZATION ASSOCIATED WITH IMPACT

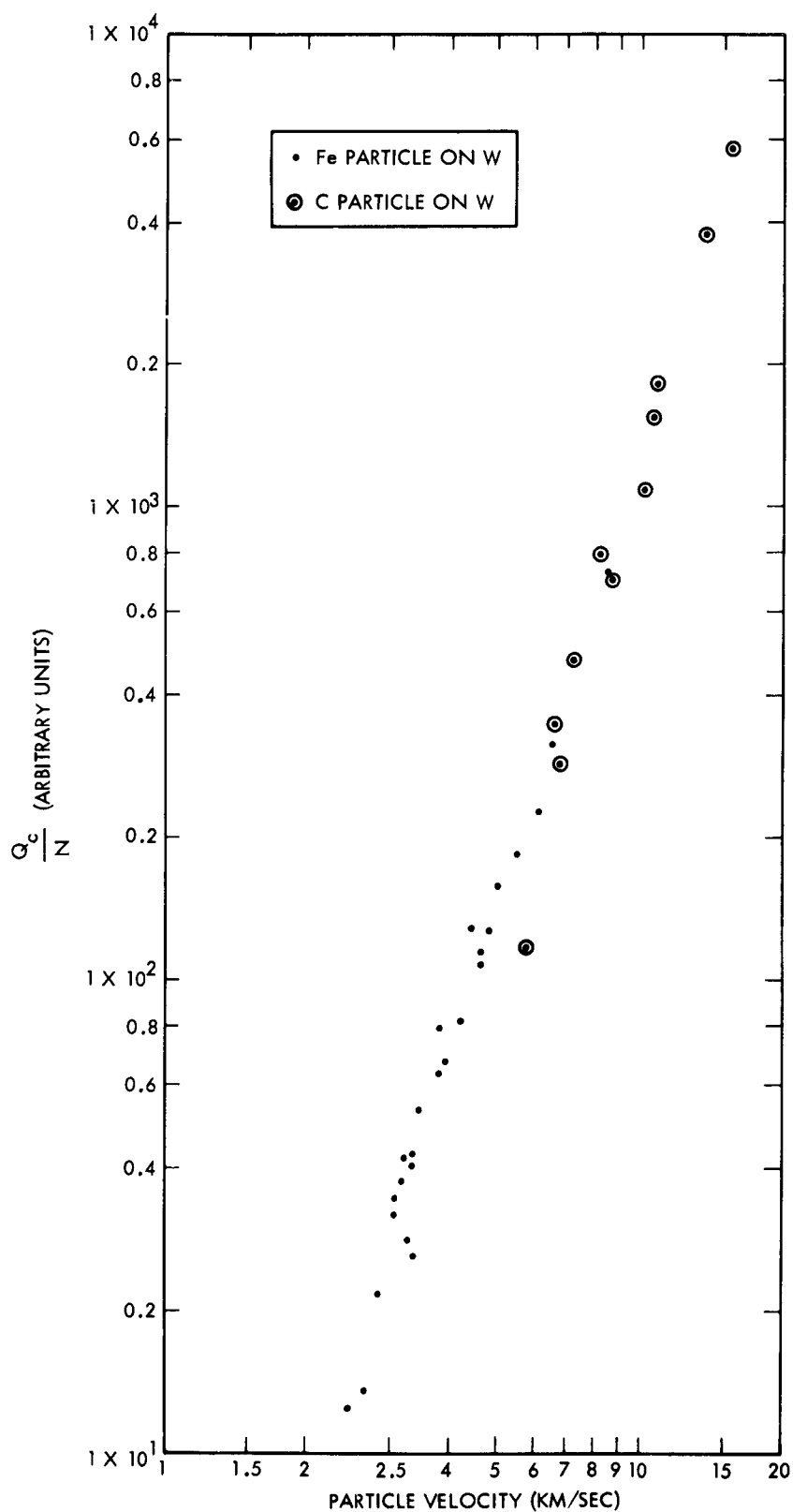


Figure 7. Charge collected normalized to the number of atoms in the particle as a function of velocity for carbon and iron particle impacts on a tungsten target.

IONIZATION ASSOCIATED WITH IMPACT

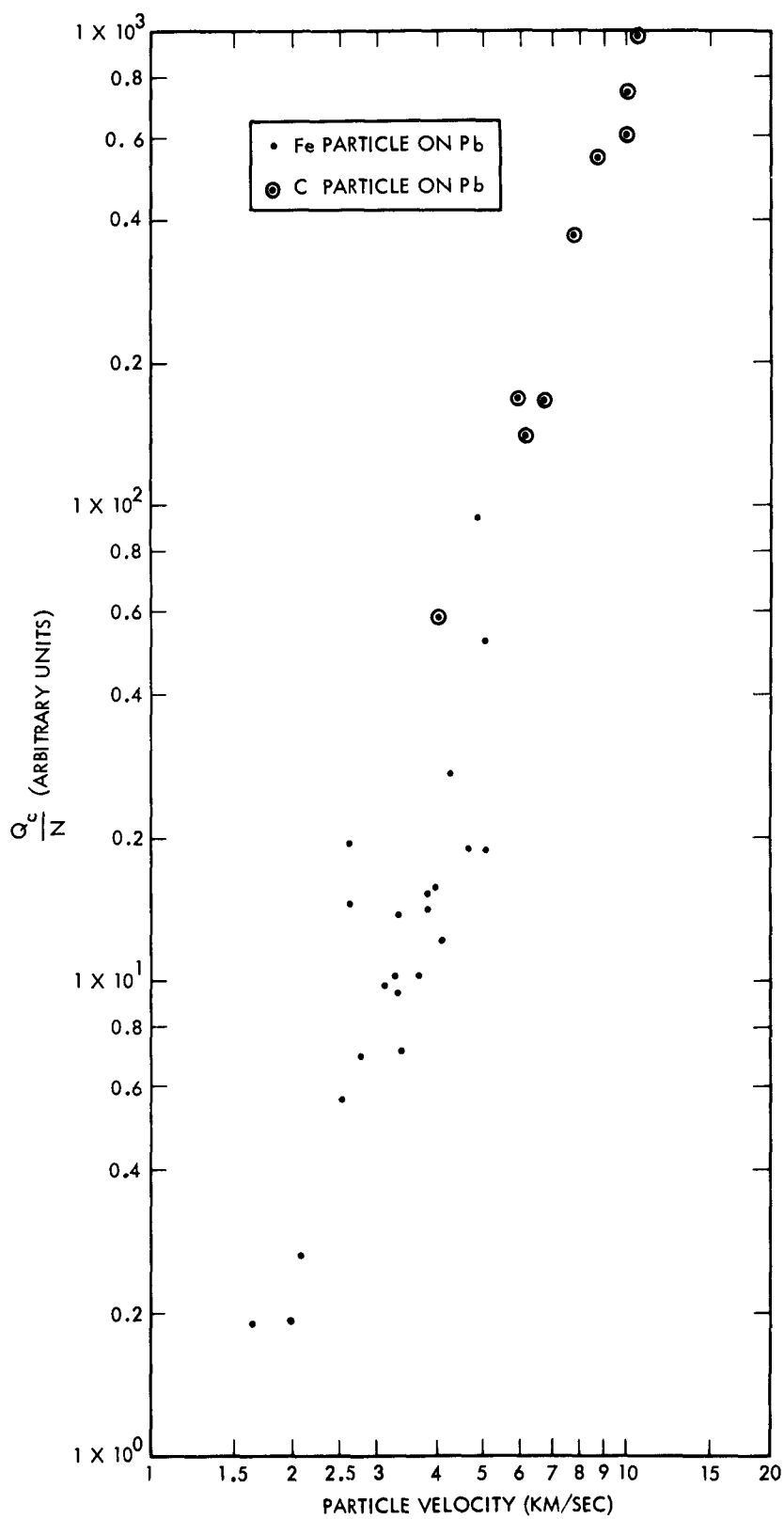


Figure 8. Charge collected normalized to the number of atoms in the particle as a function of velocity for carbon and iron particle impacts on a lead target.

IONIZATION ASSOCIATED WITH IMPACT

strictly empirical and we cannot justify it from a physical point of view. Despite these drawbacks, one must have a framework within which to work and the approach used in the preceding section provides such a framework. Additional experiments should be helpful in developing physical concepts to describe the charge emission phenomenon.

IV. IMPACT IONIZATION FROM THIN TARGETS

Ionization produced by particle impacts on thin foils has also been the subject of experimental investigation. The observations have been more qualitative in nature than thick target measurements because of the increased complexity. A brief discussion of the more interesting observations is given in the following paragraphs.

We have found that electrical charge is produced by a high speed particle impact on a thin foil. The charge can be collected by means of various types of electrically biased collectors placed on the "downstream" side of the foil. Generally, we find that the charge collected is greater in magnitude than would be predicted on the basis of thick target measurements. One possible explanation of the results (suggested by O. E. Berg from NASA) is that "spray" particles from the foil interact with the surface of collectors. Each spray particle would produce charge upon impact in a manner analogous to that described in Section III.

Since the velocity and size distribution of spray particles is dependent upon the nature of the impact, qualitative analysis is difficult. The nature of the impact depends upon particle velocity and the thickness of the foil relative to the size of the particle. We have observed at least three types of impacts, namely: (1) those where the energy loss is small and the particle passes through the foil intact; (2) those where particle break-up occurs; and (3) those where

IONIZATION ASSOCIATED WITH IMPACT

the particle appears to be completely vaporized. A recently developed technique has enabled us to photograph these events. The foil is placed in the high pressure region (pressure the order of a few mm Hg) of a differential pumping system. Debris from a high speed impact interacts with the gas leaving trails which can be photographed with the aid of a sensitive image intensifier tube. Typical photographs are shown in Figure 9. Figure 9-a shows a particle which passes through the foil with only a slight brightening of its trail. The fragmentation of a particle is illustrated in Figure 9-b. In this case, large discrete trails are left by the fragments. Complete vaporization of a particle is shown in Figure 9-c. These are unretouched photographs and the consistent pattern on the photographs is the result of a low-level image intensifier background which is repetitive from photograph to photograph.

V. SUMMARY

Preliminary experiments on the impact ionization effect have been described along with an empirical analysis of the results. Clearly, more definitive measurements are required to adequately assess the impact ionization effect. A continuing program of research may answer some of the questions raised by the results of experiments described above. The authors wish to express their appreciation to Mr. N. L. Roy for his invaluable assistance in the acquisition of the data described in this report.

IONIZATION ASSOCIATED WITH IMPACT



a



b



c

Figure 9. Photographs of particle impacts on an 800 Å thick gold foil in a low pressure oxygen atmosphere.

IONIZATION ASSOCIATED WITH IMPACT

LIST OF FIGURES

	Page
Figure 1. Experimental arrangement for the measurement of impact ionization from thick target impacts.	5
Figure 2. Tracing of an oscillograph obtained from the thick target measurements.	6
Figure 3. Charge collected normalized to r^3 plotted as a function of particle velocity for iron particle impacts on a thick tantalum target. .	8
Figure 4. Charge collected normalized to r^3 plotted as a function of particle velocity for iron particle impacts on a thick indium target. . .	9
Figure 5. Charge collected normalized to r^3 plotted as a function of particle velocity for carbon particle impacts on a thick tungsten target. .	10
Figure 6. Q/r^3 vs. v for iron particle impacts on several target materials	12
Figure 7. Charge collected normalized to the number of atoms in the particle as a function of velocity for carbon and iron particle impacts on a tungsten target	15
Figure 8. Charge collected normalized to the number of atoms in the particle as a function of velocity for carbon and iron particle impacts on a lead target	16
Figure 9. Photographs of particle impacts on an 800 Å thick gold foil in a low pressure oxygen atmosphere	19

INVESTIGATION OF IMPACT FLASH

AT LOW AMBIENT PRESSURES

By Robert W. MacCormack

National Aeronautics and Space Administration
Ames Research Center
Moffett Field, Calif.

ABSTRACT

The luminosity produced by aluminum projectiles impacting aluminum targets at a velocity of 2.5 kilometers per second has been measured in a small test chamber at ambient air pressures from 4×10^{-4} to 2×10^{-1} millimeters of mercury. The luminosity after impact is found to vary directly with pressure to a power less than 1. Spectral lines characteristic of the target and projectile material have been identified in impacts of aluminum projectiles into the following targets: (a) aluminum, (b) aluminum coated with sodium silicate, and (c) solid rock.

INVESTIGATION OF IMPACT FLASH

AT LOW AMBIENT PRESSURES

By Robert W. MacCormack

National Aeronautics and Space Administration
Ames Research Center
Moffett Field, Calif.

INTRODUCTION

This investigation of impact flash was begun to determine the feasibility of a proposal by Dr. John O'Keefe of the National Aeronautics and Space Administration's Goddard Space Flight Center. O'Keefe proposes to drop a mass on the dark side of the moon, observe the spectrum of the flash produced on impact, and so determine the chemical constitution of the lunar surface. The success of the proposal depends upon the production of sufficient radiation containing spectral line and band structure, as opposed to grey-body continua, to permit qualitative analysis of the materials present in the absence of an atmosphere. The atmospheric pressure at the surface of the moon is thought to be less than 10^{-12} earth atmospheres (ref. 1).

Early work in this field has been conducted at the University of Utah by Clark, Kadisch, and Grow (ref. 2). They found that atomic copper lines are the predominant feature of the flash obtained from impacting copper spheres into copper targets at a velocity of 2.2 km/sec in an atmosphere of argon at a pressure of 60 torr, or 60 mm of Hg. In an atmosphere of hydrogen at a pressure of 635 torr, however, the line structure is not detectable, and the flash is dimmer by at least two orders of magnitude. They concluded that impact flash results primarily from the collisions between spray particles ejected from the crater and the surrounding atmosphere, and thus presented a qualitative theoretical explanation for this difference (see Theoretical Considerations). On the other hand, Gehring and Sieck (ref. 3) studied the flash from the impact of nylon spheres with sand targets at velocities of 2.1, 2.6, and 3.1 km/sec, and found, in tests with air at pressures from 4×10^{-2} to 80 torr and with helium at pressures of 4 and 76 torr, no apparent significant effect of the composition or the pressure of the gas surrounding the area of impact on the magnitude of the impact flash.

The present paper deals with the onset and spectrum of radiation due to impact of aluminum projectiles into aluminum and basalt rock targets. The onset of radiation has been reported here because the effects of confining the test in a small volume may change the peak intensity and total radiated energy. The onset, on the other hand, should not be affected because the volume from which the radiation emanates lies well short of the walls.

IMPACT FLASH AT LOW PRESSURES

THEORETICAL CONSIDERATIONS

The spectrum of a self-luminous event is expected to consist of line emission by atoms, band emission by molecules, and a continuum by the hot surfaces of solids and liquids. In an impact event, all three are expected to be present. Because grey-body radiation carries little information about the chemical constitution of the emitter, the present analysis is restricted to line and band spectra only.

If, during cratering, there is a mechanism by which the atoms and molecules of the target and projectile material can be vaporized and excited, the radiation so produced would be independent of the atmosphere surrounding the target. Radiation produced from the interaction of ejecta and atmospheric particles would be, however, dependent upon the atmosphere. Ejecta traveling at velocities as much as triple the impact speed have been observed; this high-speed matter may be expected to radiate in the same manner as meteors if a gas is present.

Atoms and molecules can be excited by absorbing incident radiation or by a transfer of kinetic energy from other atoms or molecules. Energy producing excited electronic states can be accepted by the atom or molecule only in discrete quantities or quanta. The excited atom or molecule can then decay to a lower state by the emission of a photon. The primary process of excitation of atoms and molecules is by collision with other particles. Let us consider an interaction, scattering, between two particles of mass m_1 and m_2 , from which a photon, of energy $h\nu$, may be emitted. Let particle 2 be initially at rest and particle 1 have the velocity V . The equations for the conservation of energy and momentum are

$$\begin{aligned} 1/2m_1V^2 &= 1/2m_1v_1^2 + 1/2m_2v_2^2 + h\nu \\ m_1\bar{V} &= m_1\bar{v}_1 + m_2\bar{v}_2 + (h\nu/c)\bar{k} \end{aligned}$$

where v_1 and v_2 are the respective particle velocities after scattering, h is Planck's constant, ν the frequency of the emitted radiation, and c the velocity of light. The bars in the momentum equation indicate vectors and \bar{k} is a unit vector in the direction of propagation of the photon. Solving these for a minimum V , for a photon of frequency ν to be emitted, we arrive at a threshold equation for the relative velocity between the two particles.

$$V_{\min} = \sqrt{\frac{2(m_1 + m_2)h\nu + (h\nu/c)^2}{m_1m_2}}$$

IMPACT FLASH AT LOW PRESSURES

Table I contains values of V_{min} computed from this equation. For each value, particle 1 is an aluminum atom and ν is the frequency of radiation emitted by an aluminum atom when an electron jumps from its first excited state to the ground state.

TABLE I

$\nu = 7.57 \times 10^{14} \text{sec}^{-1}$ (3962 A.U.)
Particle 1: aluminum atom

Particle 2	V_{min} , km/sec
Lead atom	5.0
Aluminum atom	6.7
Nitrogen molecule	6.6
Argon atom	6.1
Helium atom	13.2
Hydrogen molecule	17.9

Radiation produced solely by interaction of projectile and target is expected to depend upon the projectile mass, shape, and velocity and the materials involved. All other factors remaining equal, table I shows that higher atomic or molecular weights of the target material lead to lower threshold velocities, and therefore to an increased probability of satisfying the threshold condition for excited states. Also the specific energy in the impact zone, temperature and pressure, is generally greater for higher target atomic or molecular weights. This effect should also increase the amount of radiation for targets of high atomic or molecular weights.

The same considerations show that radiation produced by ejecta interacting with the atmosphere should depend on atmospheric composition. If all variables except ambient pressure are held constant, higher pressure and therefore higher atmospheric density should result in a compressed time scale and hence a higher rate of increase of luminosity.

DESCRIPTION OF APPARATUS

The apparatus (fig. 1) consisted of the gun, the range, and the instrumentation. A commercial 220 Swift sporting rifle was used to fire sabot-mounted, 1/8-inch-diameter aluminum spheres at a velocity of 2.5 km/sec. This velocity is approximately equal to lunar escape velocity, the proposed impact velocity of the Ranger rocket on the moon. The sabot-mounted model was fired into a blast tank containing gas at pressures of about 400 torr, where the sabot and powder gases were stopped. The range consisted of an impact chamber, 11x11 cm in cross section, and a 10-foot length of stainless steel pipe connecting the chamber to the blast tank.

IMPACT FLASH AT LOW PRESSURES

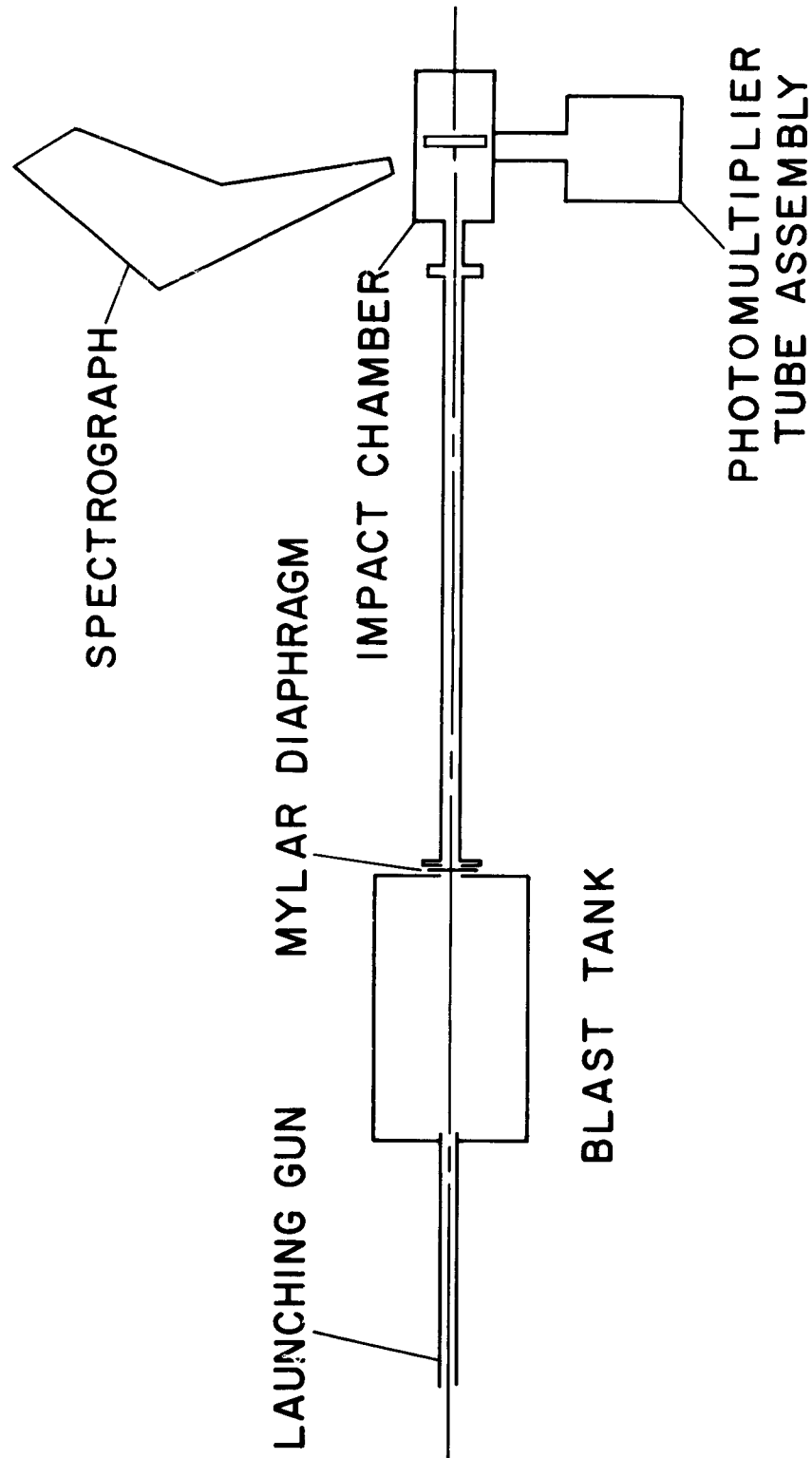


Figure 1.- Gun, range, and instrumentation.

IMPACT FLASH AT LOW PRESSURES

A 1/2-mil mylar diaphragm between the blast tank and steel pipe separated the range from the blast tank. The diaphragm was sufficient to maintain the pressure difference of 400 torr and yet not fracture the penetrating model. The 10-foot length of pipe prevented the blast-tank gases from reaching the test chamber until after the luminosity measurements had been made. The range could be evacuated to 10^{-4} torr with a 4-inch oil diffusion pump. Range pressure was measured with a McLeod type gage. The inside of the impact chamber was blackened to reduce reflected light. The time variation of luminous intensity of the flash was measured with a DuMont 6292 photomultiplier tube. This tube is sensitive to radiation between the wavelengths 3500 and 5500 A.U., or approximately half the visible spectrum. The absolute spectral response of the entire optical train was measured using a ribbon filament lamp, calibrated by the National Bureau of Standards, and a grating monochrometer. The photomultiplier tube, together with a calibrated neutral density filter, was arranged as a "pinhole camera" (fig. 2) with the optical axis in the plane of the target surface. The volume in the test chamber viewed by the system contained all points within approximately 4 centimeters of, and uprange of, the optical axis. The phototube output was recorded on two oscilloscopes which provided time axes. One oscilloscope was triggered by breaking a thread of silver painted on the mylar diaphragm. This oscilloscope recorded peak luminosity and an accurate measurement of the time between rupture of the diaphragm and impact, from which projectile velocity was calculated. The second oscilloscope, triggered internally by the flash and sweeping at a much faster rate, measured the variation of luminosity with time. On several rounds a Huet CI spectrograph, with a camera lens aperture of $f/0.7$ and a dispersion of 150 A.U. per mm at 4350 A.U. and 500 A.U. per mm at 5500 A.U., was used to record spectra.

RESULTS AND DISCUSSION

Luminosity Studies

Figure 3 shows two oscilloscope traces of luminosity produced by 1/8-inch aluminum spheres impacting aluminum targets in air at ambient pressures of 1.6×10^{-3} torr, and 8×10^{-2} torr. The impact flash at 1.6×10^{-3} torr is double peaked. The second peak occurs shortly after the fastest particles of ejecta strike the impact chamber walls. At 8×10^{-2} torr the luminosity from secondary impacts is nearly masked by the primary impact flash. At the highest test pressure the secondary impact radiation appears to be suppressed. It should be stated again that the luminosity measurements refer to radiation between the wavelengths 3500 and 5500 A.U. from a small volume about the impact point. Figure 4 is a log-log plot of the initial rate of increase of luminosity in watts per 4π steradians per microsecond versus ambient pressure. The reason for selection of this parameter is discussed in the Introduction. This plot, which covers a range of pressures from 4×10^{-4} to 2×10^{-1} torr, shows

IMPACT FLASH AT LOW PRESSURES

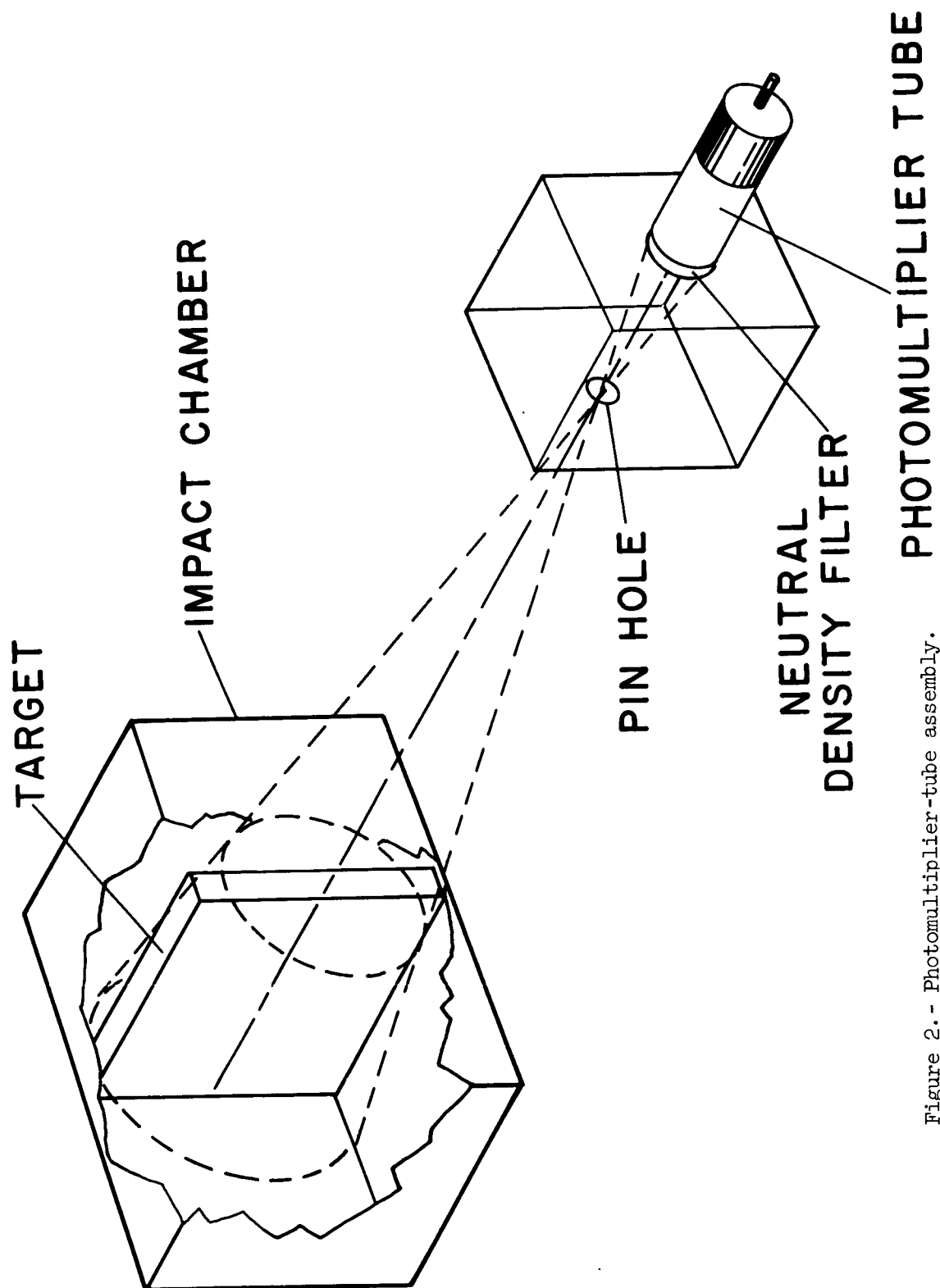


Figure 2.- Photomultiplier-tube assembly.

IMPACT FLASH AT LOW PRESSURES

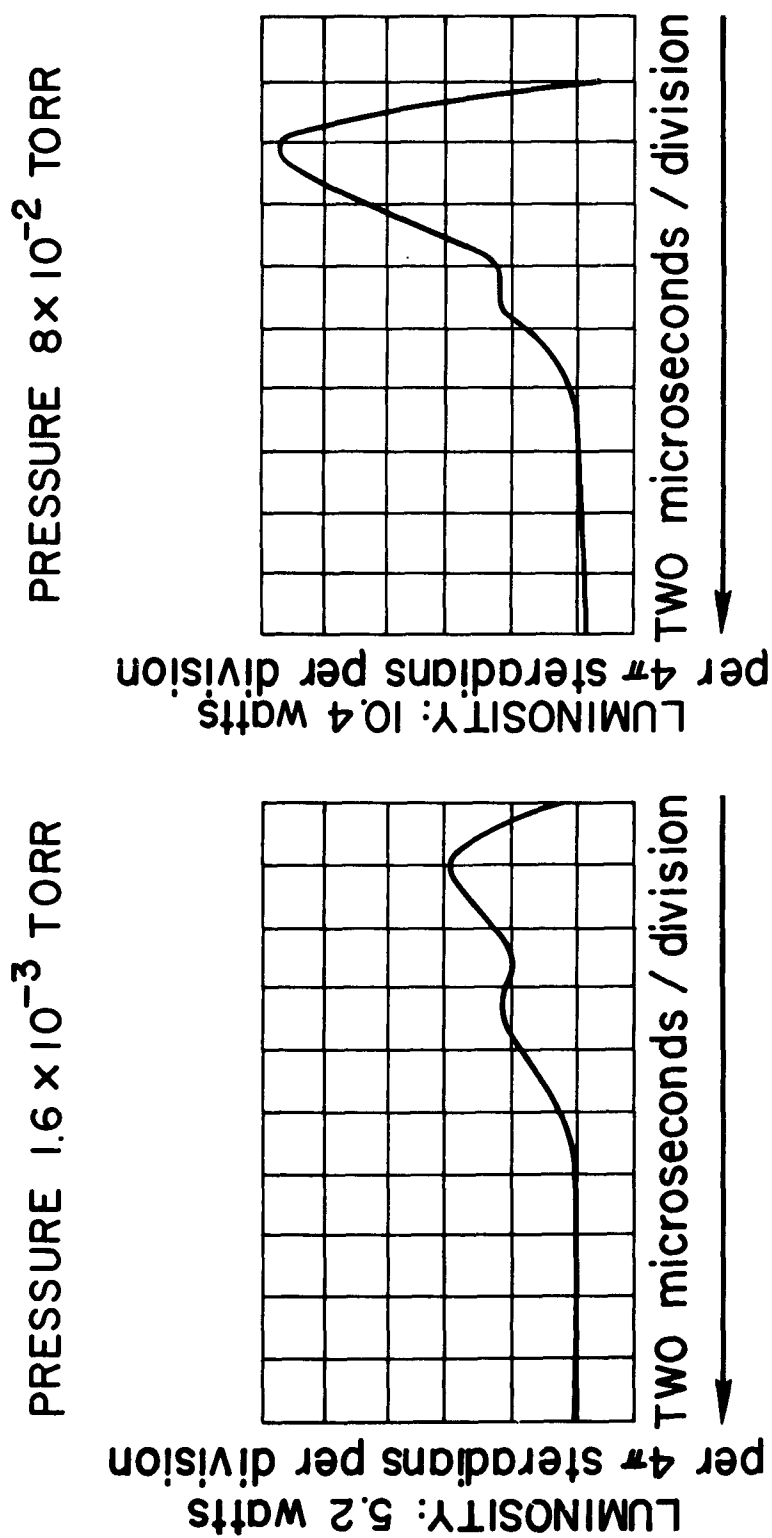


Figure 3.- Photomultiplier-tube-oscilloscope traces.

IMPACT FLASH AT LOW PRESSURES

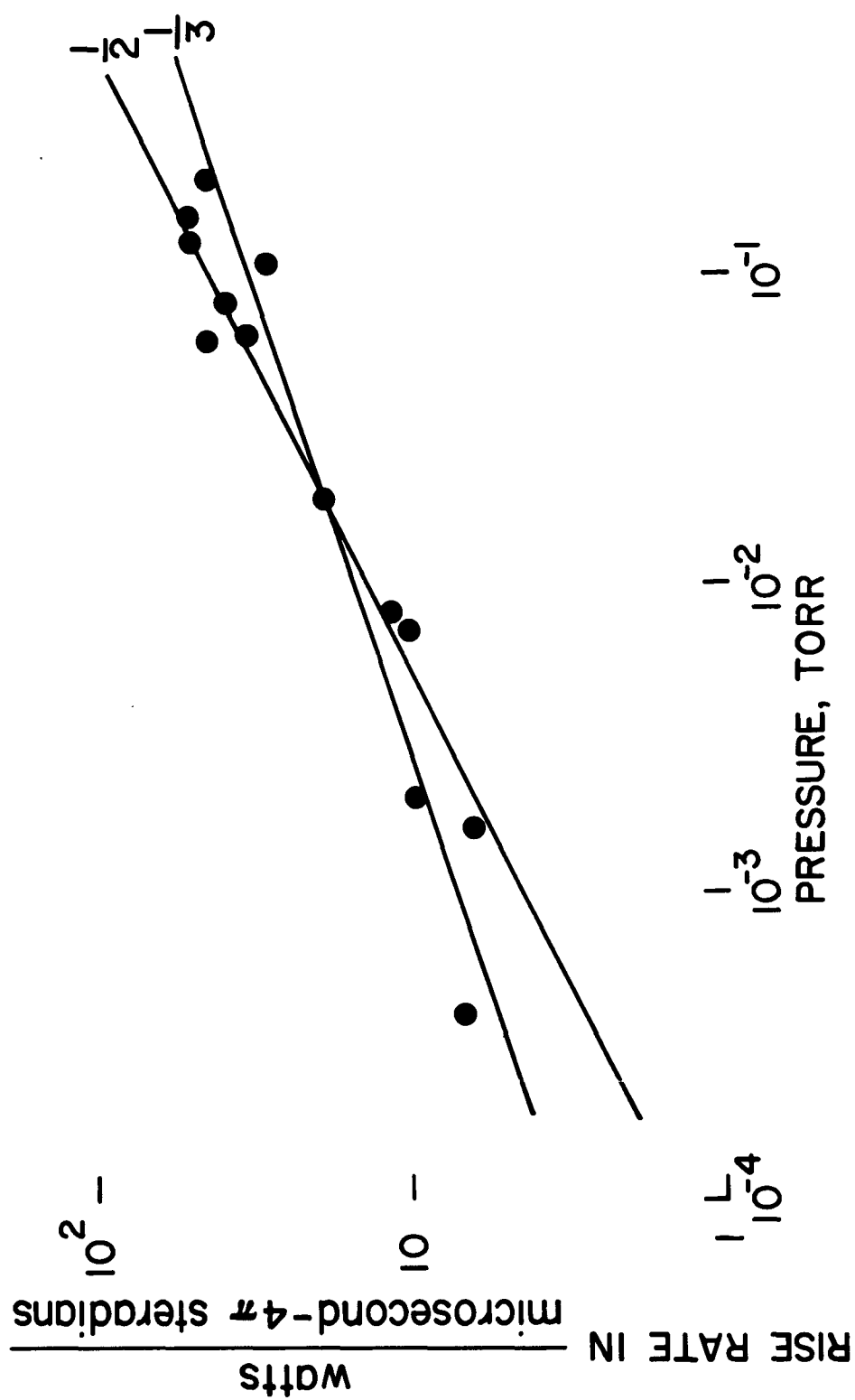


Figure 4.- Rise rate of luminosity versus pressure.

IMPACT FLASH AT LOW PRESSURES

that the onset rate of luminosity varies approximately as the cube root of the ambient pressure, which is qualitatively consistent with Clark, et al. The duration of flash, the time from initiation to the decay to one-half peak value, is approximately 4 to 5 microseconds for pressures below 10^{-1} torr, but this may be influenced by the test-chamber size. The energy of radiation calculated from the area beneath the luminosity-time curve on the oscilloscope traces is of the order of 10^3 ergs at 10^{-2} torr, or about 10^{-4} percent of the projectile kinetic energy.

Spectrographic Studies

Since the ultimate application of the present test results rests on analysis of spectra, several tests were recorded with a conventional visible-light spectrograph.

Figure 5 shows three densitometer traces of spectra obtained from impact flash. The top trace is for an aluminum target coated with sodium silicate and an ambient air pressure of 8×10^{-4} torr. The predominant feature is the atomic sodium D doublet at about 5890 A.U. Two lines are also detectable at about 3950 A.U., the approximate wavelength for radiation from excited aluminum atoms. The presence of these latter lines indicates a fairly large number of collisions at velocities greater than the threshold of 6.6 km/sec (roughly 2.6 times the impact velocity). For the middle trace the target was aluminum without sodium silicate and the ambient pressure was 1.2×10^{-3} torr. The predominant features are the same two lines of aluminum at 3944 and 3962 A.U. Manganese line structure is seen at 4034 A.U. along with the unavoidable sodium. Bands consistent with those expected for AlO are also present. Manganese is found by chemical analysis to be present in the aluminum alloys of both the target and projectile and also, it should be added, in the steel of the impact chamber; sodium is found on everything. Sodium D line radiation was found on all spectra. Basalt rock was the target for the bottom trace and the ambient pressure was 2×10^{-1} torr. The lines of sodium, calcium at 4227 A.U., and aluminum and the bands of aluminum oxide are detectable. Sodium, aluminum, and calcium, also an exceptional radiator, are found in basalt as oxides. Aluminum in the projectile may mask the effect of aluminum in the rock.

CONCLUDING REMARKS

The rate of onset of luminosity from high-speed impact depends upon the atmosphere surrounding the target. This result is consistent with those of Clark and appears to disagree with those reported by Gehring

IMPACT FLASH AT LOW PRESSURES

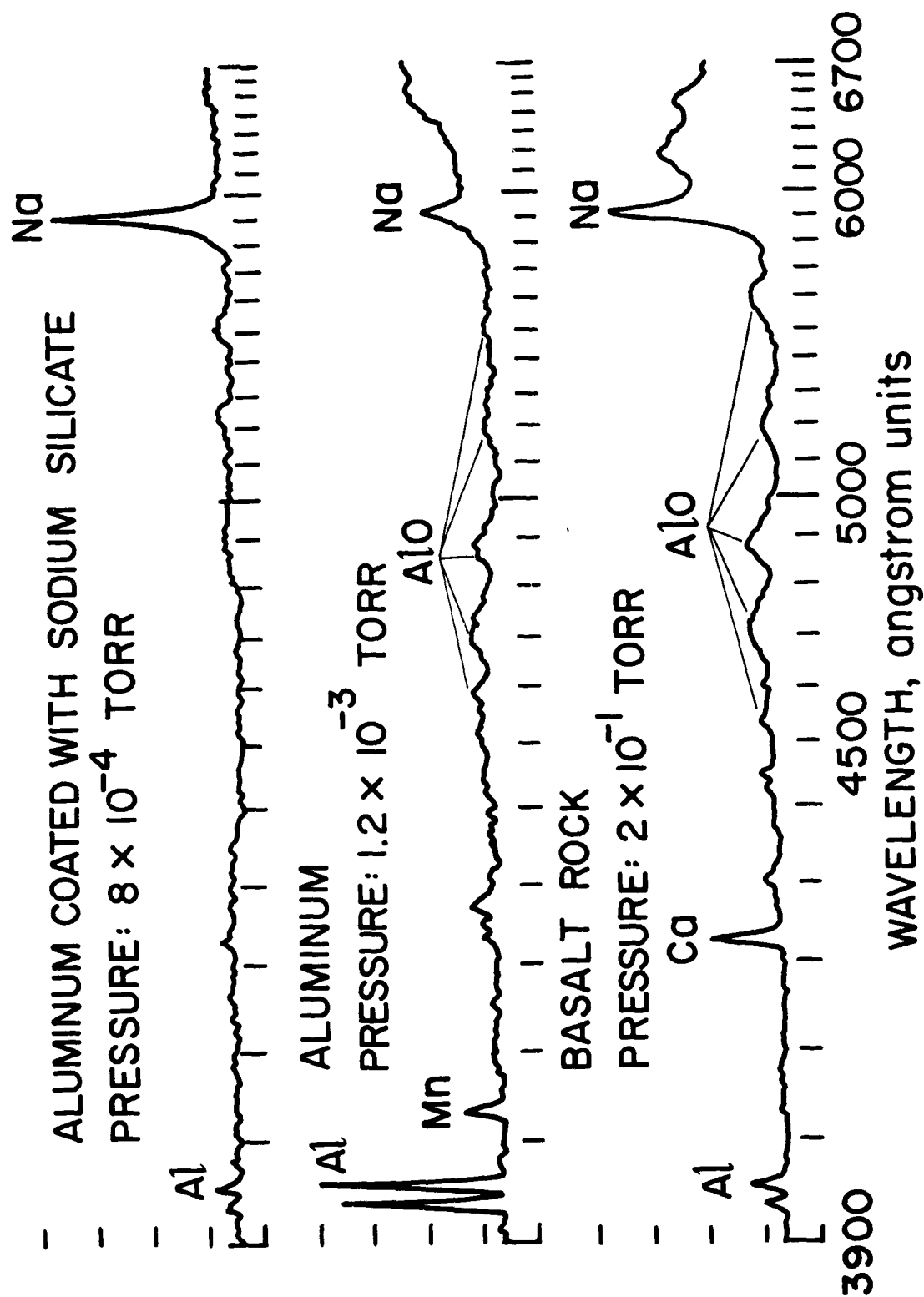


Figure 5.- Densitometer traces.

IMPACT FLASH AT LOW PRESSURES

and Sieck. A possible explanation for this disagreement centers on the fact that the luminosity measurements of Clark, as well as those of this paper, were made of a metal impacting a solid and Gehring and Sieck's were made on a plastic impacting a granular material. In the shocked impact region, the pressure, which is responsible for the acceleration of ejecta, is expected to be greater for a metal impacting a solid than for a plastic impacting a granular target. The luminosity, produced by ejecta interacting with the atmosphere, may not constitute a significant quantity of radiation in Gehring and Sieck's tests. The principal part of their luminosity measurements may be radiation produced entirely by the mechanics of cratering.

At the low ambient pressures of the present tests the observed spectra contain line and band features consistent with the elements known to be present.

IMPACT FLASH AT LOW PRESSURES

REFERENCES

1. Elsmore, B., "Radio Observations of the Lunar Atmosphere," Philos. Mag., 2, (20), 1040 (1957).
2. Clark, W. H., Kadisch, R. R., and Grow, R. W., "Spectral Analysis of the Impact of Ultra Velocity Copper Spheres into Copper Targets," Technical Report OSR-16 of the University of Utah, Sept. 1, 1959.
3. Gehring, J. W., and Sieck, D. W., "A Study of the Phenomena of Impact Flash and its Relation to the Reaction of the Lunar Surface in the Impact of a Lunar Probe," American Rocket Society, Lunar Missions Meeting, Cleveland, Ohio, Print 2476-62, July 1962.

**AN INVESTIGATION OF THE
PHENOMENA OF IMPACT FLASH
AND ITS POTENTIAL USE AS A HIT DETECTION
AND TARGET DISCRIMINATION TECHNIQUE**

by

J. W. Gehring and R. L. Warnica

**General Motors Corporation
GM Defense Research Laboratories
Aerospace Operations Department
Santa Barbara, California**

AN INVESTIGATION OF THE
PHENOMENA OF IMPACT FLASH
AND ITS POTENTIAL USE AS A HIT DETECTION
AND TARGET DISCRIMINATION TECHNIQUE*

by
J. W. Gehring and R. L. Warnica

General Motors Corporation
GM Defense Research Laboratories
Aerospace Operations Department
Santa Barbara, California

*This work was performed for the Jet Propulsion Laboratory,
California Institute of Technology, under Contract No. 950299,
sponsored by the National Aeronautics and Space Administration
under Contract No. NAS7-100, and for the United States Air Force
under Contract No. Eglin AFB/AF-8(635)-2783.

IMPACT FLASH

ILLUSTRATIONS

Figure		Page
1	Summary of Launcher Performance	637
2	Horizontal Impact Range	638
3	Vertical Impact Range	639
4	Schematic of Ballistics Range Velocity Station	640
5	Typical Shadowgraph Showing Separation of Model and Sabot	641
6	Typical Impact Flash in Sand	645
7	Typical Impact Craters Formed in Sand and Granite	646
8	Effects of Velocity and Pressure on Peak Luminosity for the Impact of 0.22 - in. Diam. Nylon Spheres on Sand Targets	648
9	Variation of Peak Luminosity for Nylon Spheres Impacting Sand and Aluminum at Various Pressures of Air and Helium at 8,000 fps	649
10	Peak Luminosity for Glass and Aluminum Projectiles Impacting Sand	651
11	Peak Luminosity of 1/8-in. Diam. Aluminum Spheres Impacting Sand and Granite Targets	652
12	Effects of Velocity on Peak Luminosity for the Impact of 0.220-in. Diam. Nylon Sphere on Aluminum Targets	653
13	Peak Luminosity of Various Sizes of Steel Spheres Impacting Sand Targets	654

IMPACT FLASH
ILLUSTRATIONS (cont.)

Figure		Page
14	Reduced Data – Variation of Peak Luminosity for Three Projectile Materials Impacting Sand and Aluminum at 8,000 fps	656
15	Reduced Data – Variation of Peak Luminosity for Eight Projectile Masses (Diam. = Constant = 1/8 Inch) Impacting Aluminum at 8,000 fps	658
16	Typical Photomultiplier Scope Traces for Impacts of Various Projectile/Target Combinations	661
17	Sequential Beckman-Whitley Photographs of a 1/8-in. Glass Sphere Impacting an Aluminum Target at 23,000 fps	664
18	Spectrogram of Impact Flash Generated by Nylon Cylinder Impacting an Aluminum Target at 24,600 fps	666
19	Spectrogram of Impact Flash Generated by Nylon Spheres Impacting Sand Targets at Approximately 10,000 fps – 10 Rounds Superimposed	667

IMPACT FLASH

ABSTRACT

This paper presents the results of an experimental research program on the impact radiation associated with hypervelocity collision. Specifically, the phenomena of impact flash and its potential use in two areas is analyzed as follows: (1) estimation of the flash from impact of a lunar probe with the moon, and correlation of impact flash measurements made of an actual impact with a surface of the same physical characteristics as the lunar surface; (2) selection of hypervelocity impact flash phenomena which could provide significant information for determining that a collision had occurred, what damage was inflicted upon the target (satellite, ICBM, decoy, etc.), and composition of the target material.

The program consisted of a parametric study of the variables associated with impacting a projectile against various targets, some of which simulate the lunar surface. The tests consisted of firing projectiles of varied mass, material, diameter, and velocity into targets under various ambient conditions. Observations were made and quantitative data obtained for the magnitude of the luminosity of the impact flash, the total radiated power, the duration of the flash, and the spectrum of emitted light.

IMPACT FLASH

INTRODUCTION

This research program was directed toward the possibility of identifying the impact of a projectile or probe against a target and developing techniques for identifying the target material. The program, therefore, was carried out with the specific goal of learning what observations and techniques at a remote position will answer the important questions related to the impact phenomena.

When a high-velocity projectile strikes the moon, it will (1) generate an intense flash of light, and (2) form an impact crater.⁽¹⁾ If either or both of these reactions are of sufficient magnitude, they can be observed here on earth. Whether or not a lunar probe (or meteor) can cause an impact flash of sufficient magnitude will be estimated on the basis of the results to be reported in this paper. In contrast to the findings of Russian observers,⁽²⁾ astronomers have succeeded in drawing no significant conclusions about the impact of meteors on the moon⁽³⁻⁷⁾. Experimental researchers have also attempted to look at the phenomena of impact flash^(8, 9) and cratering in rocks,^(10, 11) but under conditions which may be inapplicable to the investigation of lunar impact flash or spacecraft hit-detection and discrimination. Consequently, GM Defense Research Laboratories, General Motors Corporation, undertook a program to determine the

IMPACT FLASH

specific features of an impact flash and to measure the reaction of a target to a high-velocity projectile. Results of this program may make it possible to identify both impact and the composition of the impacted surface. Whether or not the impact of a projectile will provide this information depends upon the peak intensity of the flash, the duration of the flash, and the spectral distribution of light in the flash. If these aspects of the phenomena are known, it will be possible to design instruments for recording the flash and to estimate whether or not data from these instruments will provide a record of the conditions of the impact. It may also be possible, through the choice of materials from which the projectile is made, to augment the chances of success in the test by increasing the luminosity of the flash. Therefore, the experiments were designed to permit observations and to describe quantitatively the phenomena of impact flash (peak luminosity, time duration, and the spectrum of light emitted).

The first environmental condition to be considered is the effect of the gas density at the target's surface. Since most experiments on high-speed impact have been made with gas at appreciable pressure, that is, many orders of magnitude greater than pressure near the lunar surface or at extreme altitudes, it is essential to learn the effect of pressure on impact flash if results of laboratory experiments to predict the phenomena of impact flash on the moon are to be used. Early work at the University of Utah⁽⁹⁾

IMPACT FLASH

indicated that the gas surrounding the target played an important part in producing the impact flash. This conclusion was based on the observation, in metal-to-metal impact, of a line spectrum attributed to the reaction of the surrounding gas with high-velocity spray thrown out of the crater during the crater's formation. Therefore, it might be concluded that impact on an atmosphere-free moon would not cause a flash. These conclusions will be shown to be inapplicable here for both the early experiments by the NASA-Ames Labs⁽¹⁾ and the tests to be described show that impact flash occurs under reduced ambient gas pressures.

The second condition to be considered is that of materials. Satellites, ICBM's, decoys, etc. are fabricated from standard structural materials such as, aluminum, magnesium, and steel. The composition of the lunar surface, however, is unknown, and investigators are confused by contradictions found in hundreds of papers published on the subject. Suffice to say, the majority of references agree that the rough and cratered lunar surface was caused by the impact of meteors occurring over the eons following the solidification of the entire lunar mass. According to currently accepted views, the moon's surface is a rocky rubble covered with a thin layer of dust,⁽¹²⁾ its composition and character undoubtedly varying from place to place and including, perhaps, steep slopes of bare rock in the mountainous regions.

IMPACT FLASH

The other conditions to be considered are those related to the projectile or the lunar probe. The probe will have a given size, be made of a certain material, and strike at a specified velocity. The Ranger vehicles will impact the moon at a velocity close to 10,000 ft/sec – a speed easily attainable in the laboratory – and will be made of metals and plastics (these also can be duplicated in the laboratory). On the other hand, the vehicle will weigh more than 700 pounds, and projectiles of this weight are beyond the capability of the tests in this program. Accordingly, part of the investigation will be concerned with projectiles of different sizes to determine scaling laws for extrapolating the results of the laboratory to the conditions of full-scale flight.

Velocity will also be a factor in evaluating conditions of satellite impact; therefore, velocities up to 25,000 ft/sec will be used to evaluate scaling effects.

RANGE AND MONITORING INSTRUMENTATION

The tests were conducted in the Ballistics Range (described in GM DRL Report No. ER62-201 and Ref. 12). The basic equipment consists of a gun, a flight range and an impact chamber. The projectile is launched by either of two guns – a 0.22-in. accelerated-reservoir, light-gas gun (AR-LGG), or a 0.22-in. SuperSwift

IMPACT FLASH

smoothbore rifle. The choice of guns depends on the desired projectile mass and velocity (Fig. 1). The 0.22-in. AR-LGG (Fig. 2) may be fired horizontally at velocities up to 28,000 ft/sec, while the SuperSwift is used horizontally or vertically when the velocity requirement does not exceed 10,000 ft/sec (Fig. 3). The vertical firing capability of the SuperSwift is especially useful when non-solid targets such as sand or crushed stone are used. In these cases no alien binders are required to maintain the target shape.

During the course of flight, the model's position and time of flight are recorded at both of two spark shadowgraph stations in an instrumented velocity chamber (Figs. 3, 4). Figure 4 is a schematic of the instrumentation associated with each station. When the model interrupts the photobeam, electronic counters are started and a short-duration spark exposes a film plate. Figure 5 is a shadowgraph which shows a spherical model separated from its sabot at a velocity of 21,000 ft/sec. These measurements of time and distance of the projectile between stations serve to determine velocity along the trajectory and, in particular, at the target. The accuracy of the impact velocity determined in this manner is within 1.0 percent.

IMPACT FLASH

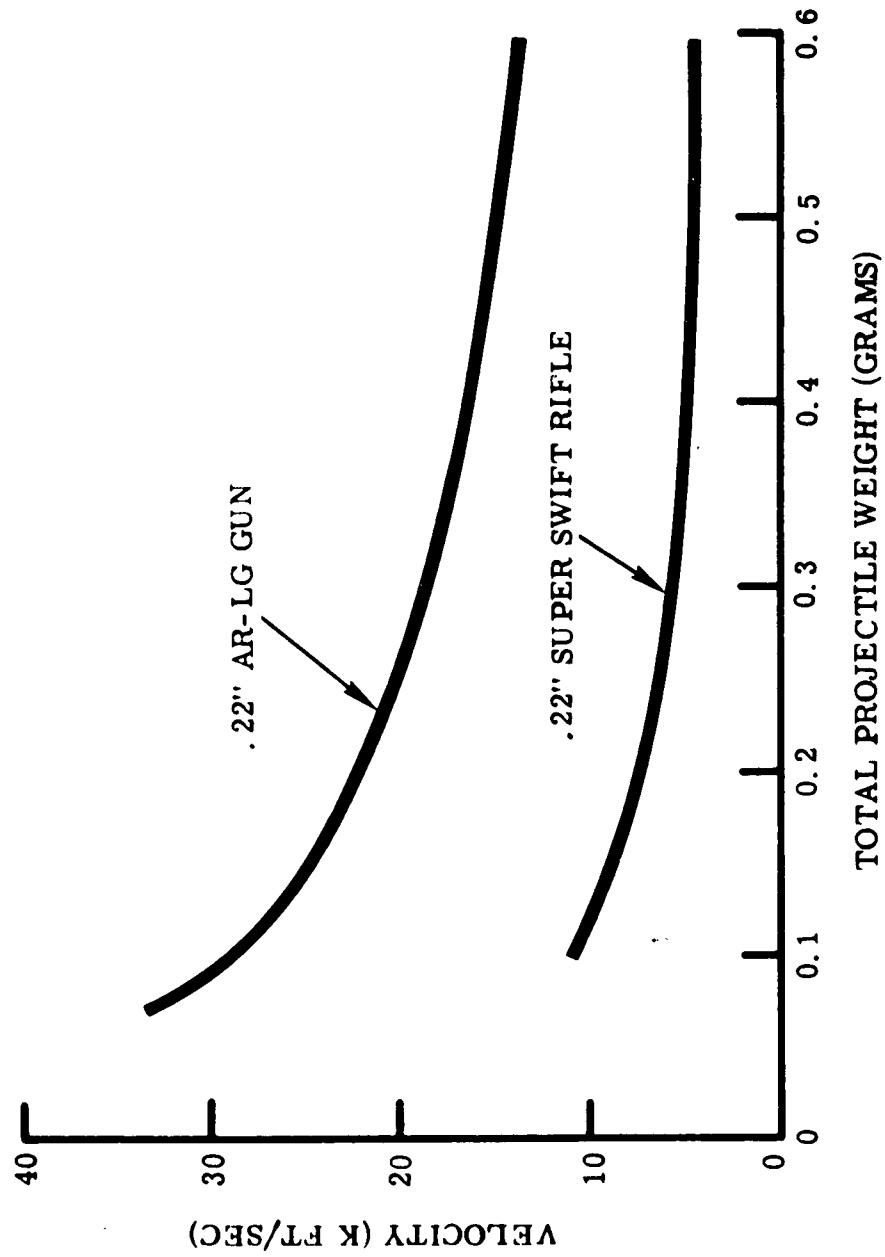


Fig. 1. Summary of Launcher Performance.

IMPACT FLASH

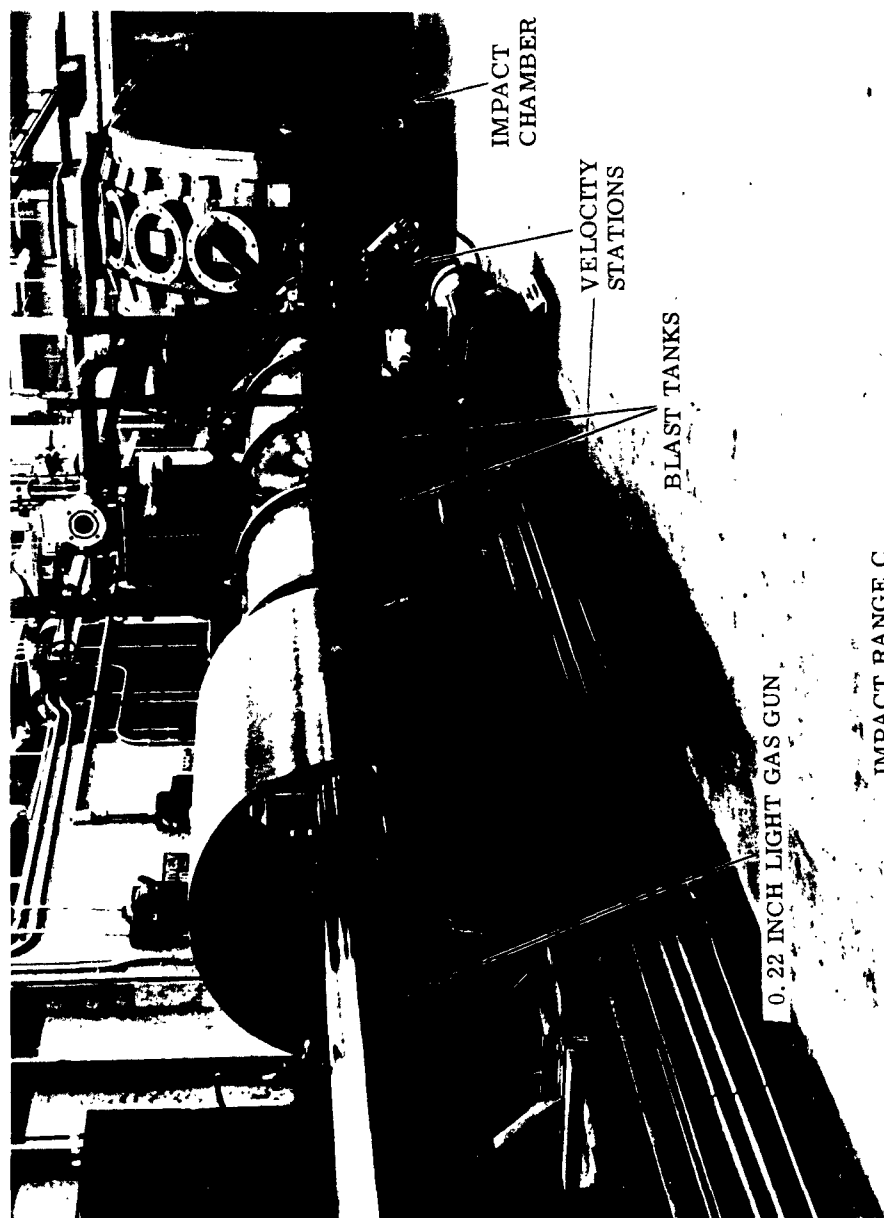


Fig. 2. Horizontal Impact Range.

IMPACT FLASH

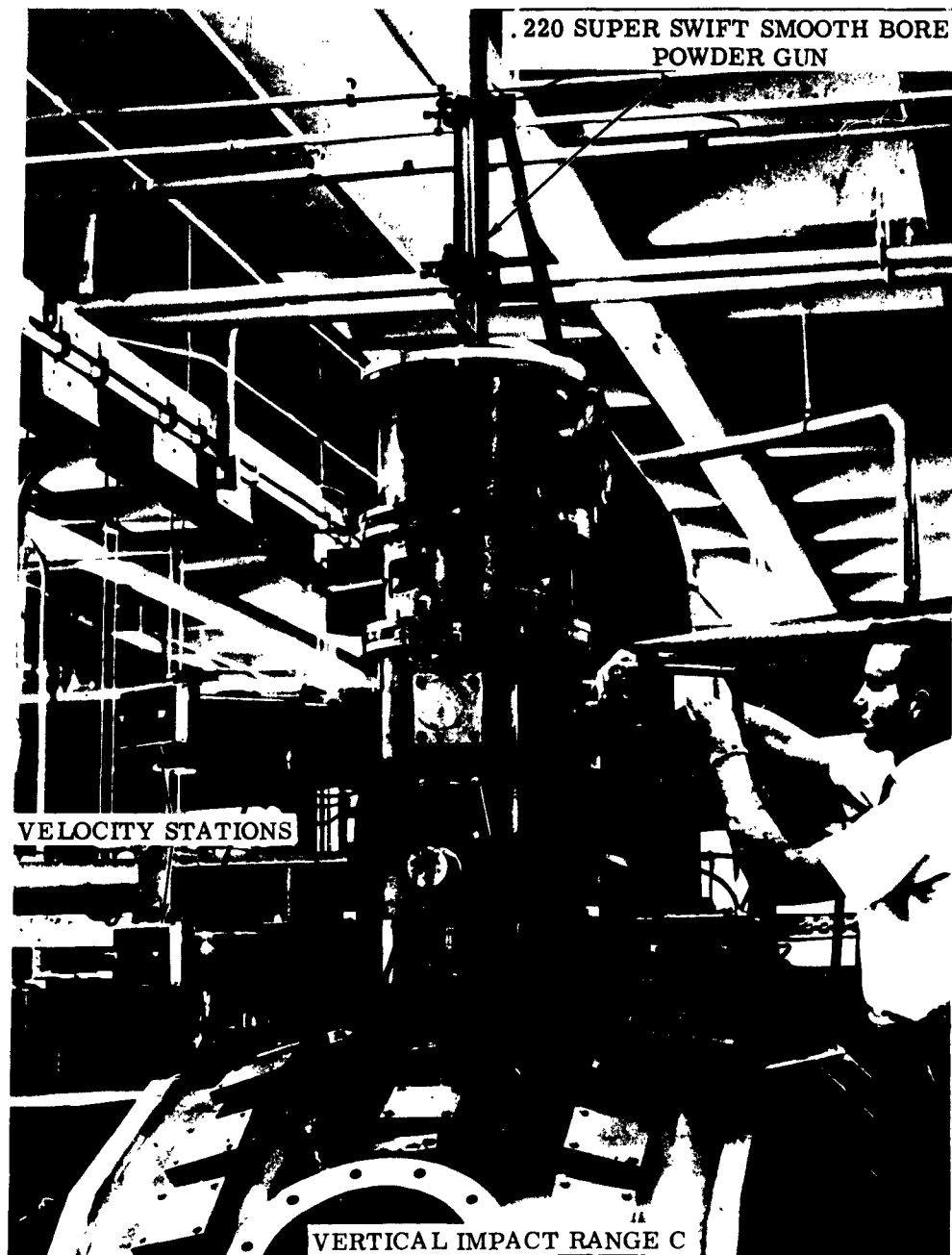
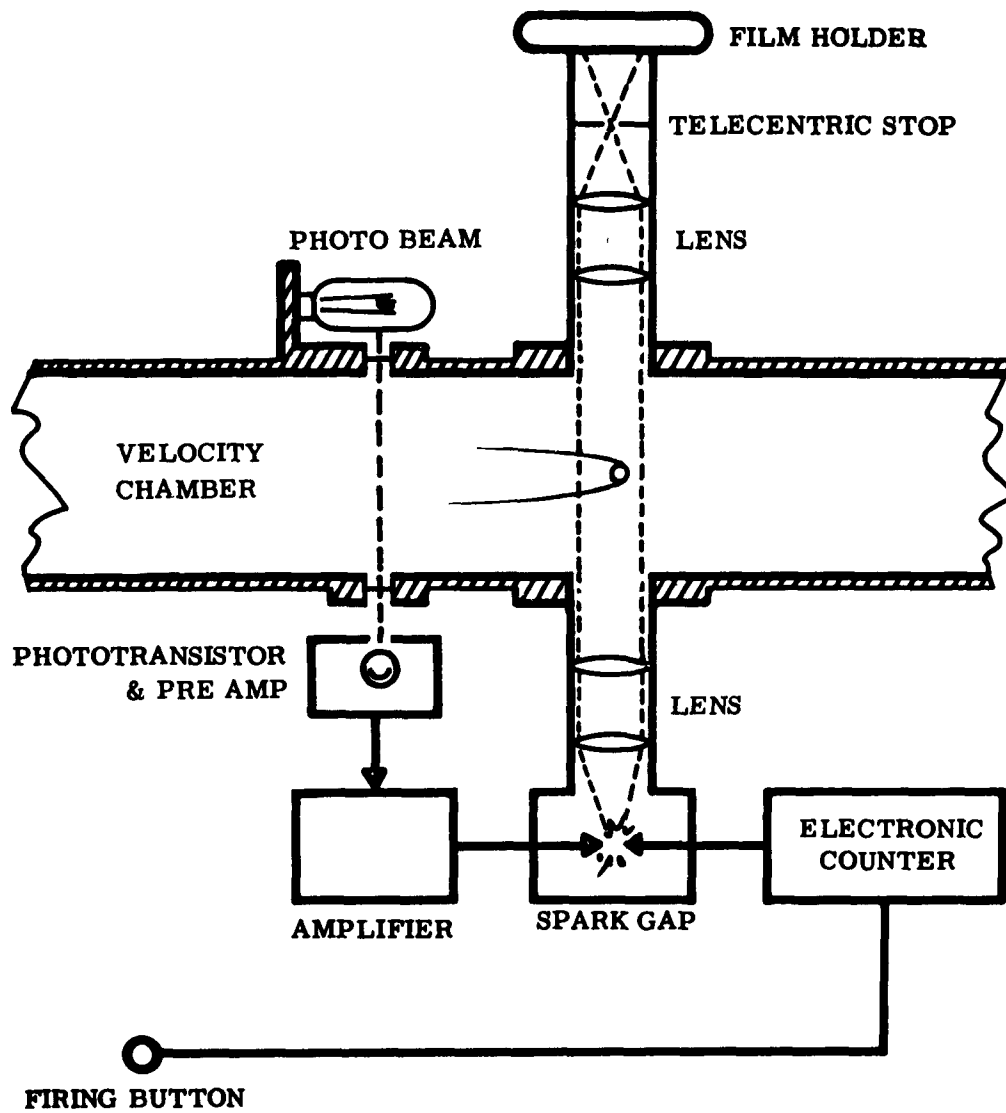


Fig. 3. Vertical Impact Range.

IMPACT FLASH



A 0169

Fig. 4. Schematic of Ballistics Range Velocity Station.

IMPACT FLASH

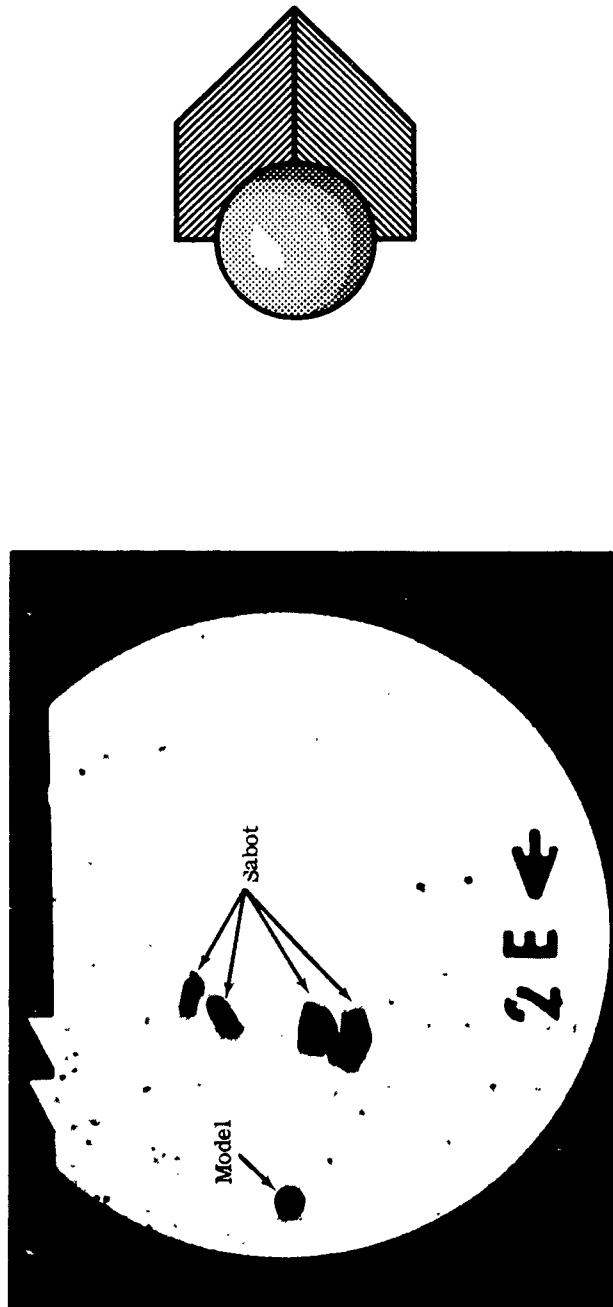


Fig. 5. Typical Shadowgraph Showing Separation of Model and Sabot.

IMPACT FLASH

The model flight terminates in an impact chamber (Fig. 2) which has numerous viewing ports. The rear wall of the chamber, a full-size door, allows easy insertion and removal of the targets. The targets are held by a mount attached to the floor of the chamber. The impact and velocity chambers are vacuum sealed and can be pumped down to less than one micron of mercury. Air or any desired gas mixture can be introduced into the chamber as a test medium. An alphasatron vacuum gauge and mercury manometers provide accurate and reliable pressure measurement.

Photographic and photoelectric equipment, and open-shutter cameras with black and white or color film have been used to monitor the impact flash. Because initial records showed that radiation from the impact flash lay in the visible and near infrared, quantitative optical monitoring devices were chosen for their response to these wavelengths. Three photomultiplier tubes were used to record peak luminosity and total time duration of emitted light – a PM tube (Dumont Type 6911) sensitive (with filter) to infrared radiation from 5,940 Å to 10,000 Å, a tube (Dumont Type 6292) sensitive to the visible spectrum from 3,500 Å to 5,500 Å, and a PM tube (Dumont 7664) sensitive to the region from 1,800 Å to 5,500 Å. The PM tubes were calibrated to measure radiance in watts per unit-solid-angle as a function of both impact velocity and ambient gas pressure in the impact chamber.

IMPACT FLASH

To study the emitted spectra from a point 20 degrees off normal, a spectrograph was placed on the impact chamber. The system had a typically nonlinear dispersion of from 100 A/mm to 300 A/mm (total dispersion 30 mm) and a resolving power of less than 20 A. The spectrograph was calibrated with a point-source mercury lamp which also served to locate the position of the impact on the vertical axis of the film.

In addition to the quantitative analysis of the light emitted during the impact flash, the phenomena were observed with the Beckman & Whitley Model 192 framing camera. This camera, capable of framing rates as high as 1.4 million frames per second, can be used to record precisely the (1) incoming projectile velocity, (2) the phenomena of impact flash, and (3) the motion, velocity, and, approximate quantity of minute particles being ejected from the crater. This camera also makes it possible to observe, in a plane across the surface of the target, the growth of the crater in time.

RESULTS AND ANALYSIS

The experiments thus far have been conducted with projectiles of nylon, aluminum, glass, steel, magnesium, brass (hollow and solid), and silver (hollow and solid) ranging in diameter from 1/32-inch to 3/16-inch, and launched at velocities from 6,800 to 24,000 ft/sec.

IMPACT FLASH

A portion of the tests used sand or granite targets. The sand, commercially known as "Nevada 135", was a fine-grade silica sorted through a 100-mesh screen and retained on a 200-mesh screen. The granite is commercially known as "Georgia Grey". In order to establish the effects of certain projectile parameters, many rounds were fired into titanium and aluminum targets. The projectiles and targets tested were systematically varied to cover the observables of interest. The results of the experiments are reported below.

Within the range of the experiments, impact flash was observed under all conditions. A typical impact flash observed by an open-shutter camera is shown in Fig. 6. A study of some 600 records of impact flashes shows that the intense luminosity in the center of the impact is associated with both the projectile and the area of the target under the projectile, while the striated luminosity surrounding the point of impact is associated with the debris ejected from the crater. These conclusions are in agreement with the flash pictures obtained at the Ames Research Laboratories ⁽¹⁾. Open-shutter flash pictures (Refs. 1, 9) depict a dark spot surrounded by an intense flash in the center of the impact. The dark spot is believed to be the opaque copper projectile used in those tests. In the pictures shown in Fig. 6, however, taken of a translucent (nylon) projectile, the dark spot does not appear. Typical craters formed in both sand and granite targets are shown in Fig. 7.

IMPACT FLASH



V = 10, 360 ft/sec
P = 1mm Hg - AIR

Fig. 6. Typical Impact Flash in Sand.

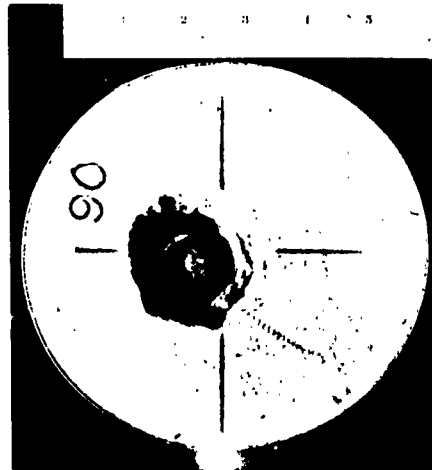
IMPACT FLASH

V = 10,360 ft/sec
P = 76mm Hg - AIR



GRANITE TARGET

V = 8440 ft/sec
P = 1 mm Hg - AIR



SAND TARGET

Fig. 7. Typical Impact Craters Formed in Sand and Granite.

IMPACT FLASH

EFFECT OF AMBIENT GAS AND PRESSURE

Since the impact of a lunar probe will occur in the absence of any atmosphere, it was necessary to test the effect of various ambient gases and gas pressures on the magnitude of the impact flash. In pilot experiments, nylon spheres were fired into sand targets under conditions of varying velocity and ambient air pressures (Figs. 8, 9). The ordinate in this figure is the peak luminosity of the flash I_{np} (in watts per steradian) which is equal to the measured value normal to the target surface. In Fig. 8, the peak luminosity I_{np} is then plotted as a function of both impact velocity and ambient range pressure. In Fig. 8a, three selected impact velocities were chosen and the values of I_{np} corrected to a best-fit slope of the data. These three velocities were then made the dependent variable and the data points replotted as a function of ambient pressure. One important result of the research program is demonstrated by Fig. 8b. At ambient pressures of 10 mm of Hg and down to 0.042 mm of Hg (nearly three orders of magnitude change in pressure), the magnitude of the peak luminosity of the impact flash did not vary significantly. Extrapolation of these data to lower pressures would indicate that the flash is independent of the surrounding pressure.

To further demonstrate this important conclusion, the tests were extended to include a test of the magnitude of the impact flash over a wider range of pressures in air and to test the impact flash in an inert

IMPACT FLASH

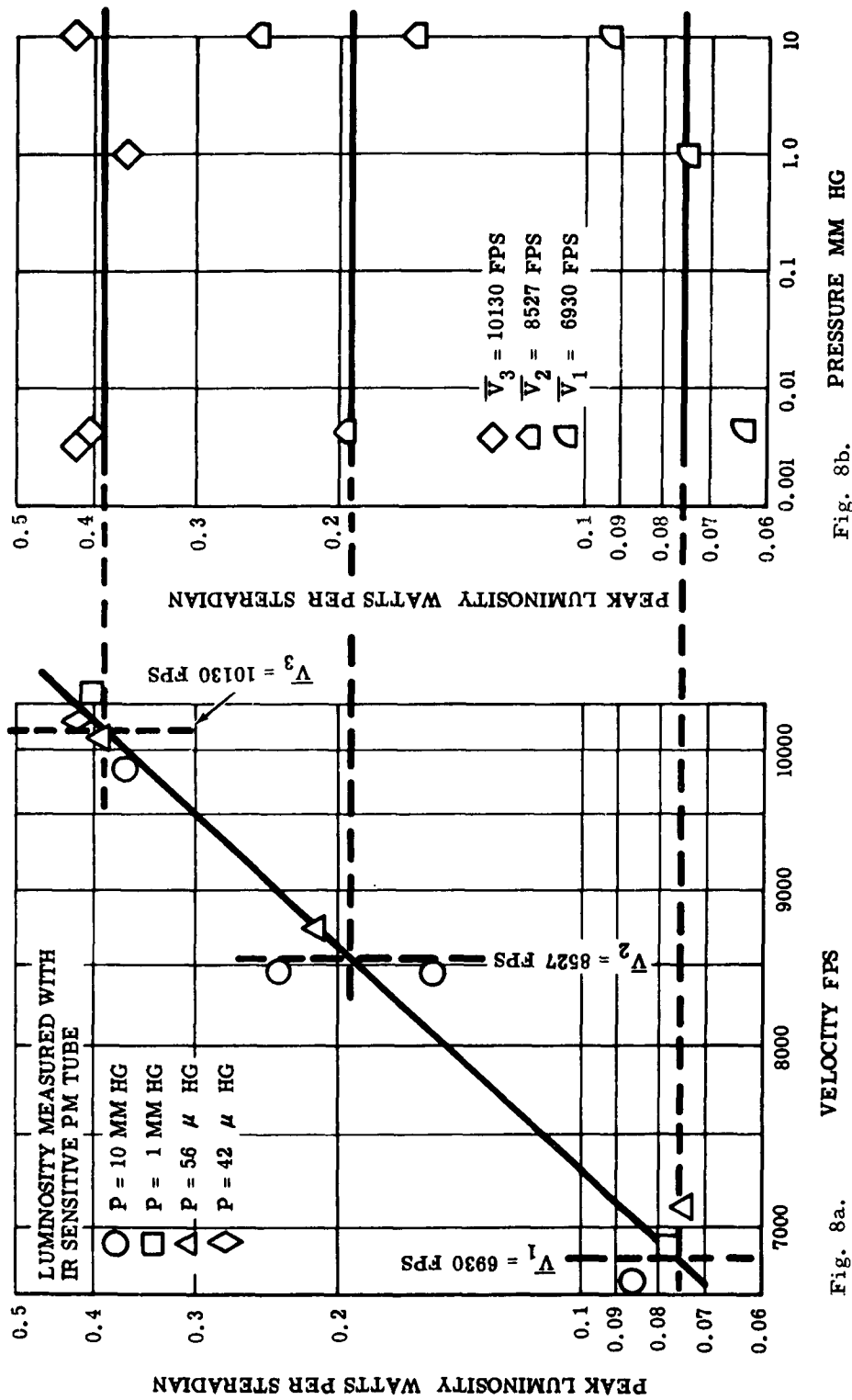


Fig. 8. Effects of Velocity and Pressure on Peak Luminosity for the Impact of 0.22 - in. Diam. Nylon Spheres on Sand Targets.

IMPACT FLASH

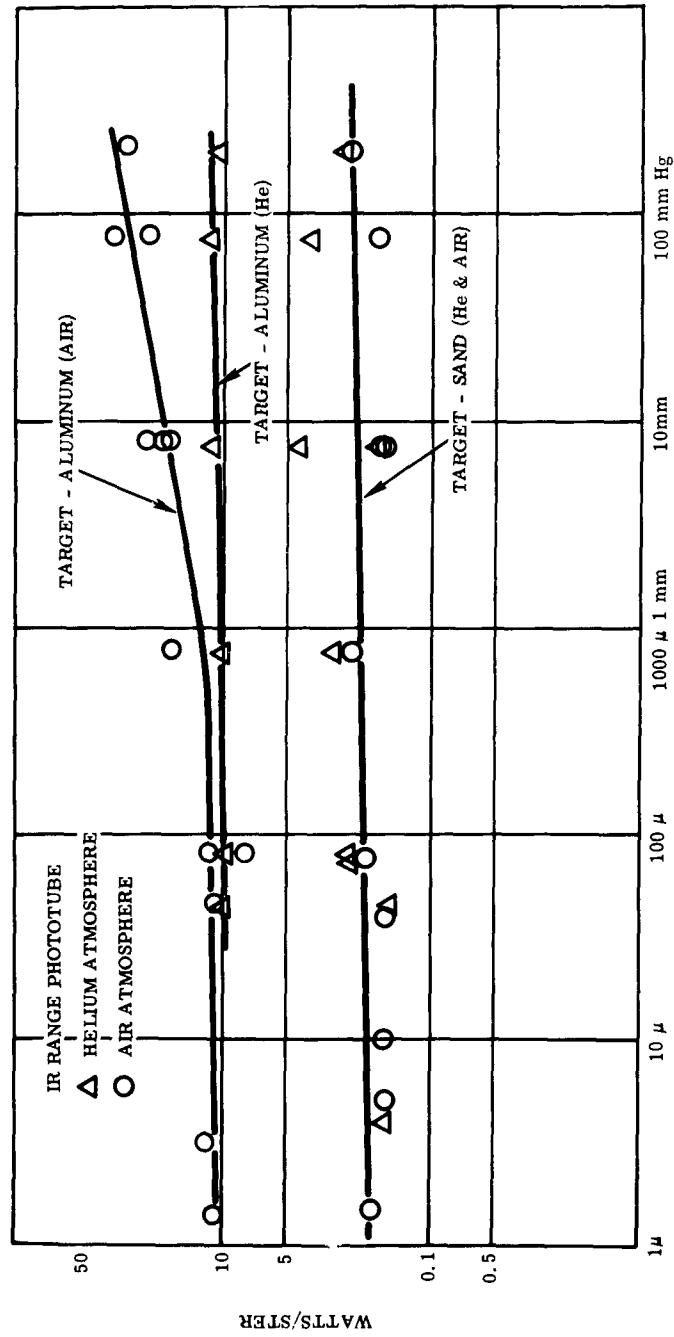


Fig. 9. Variations of Peak Luminosity for Nylon Spheres Impacting Sand and Aluminum at Various Pressures of Air and Helium at 8,000 fps.

IMPACT FLASH

atmosphere. To do this, nylon projectiles were fired against both aluminum and sand targets at pressures ranging from one micron of Hg pressure to one atmosphere pressure in environments of both air and helium. The resulting data demonstrate that there is little measurable effect of the surrounding gas or the ambient gas pressure on the peak intensity of the impact flash. In fact, only in the case of aluminum targets at air pressures over 10 mm of Hg was any significant effect of a surrounding gas observed.

EFFECTS OF VARIED PROJECTILE PARAMETERS AND TARGET MATERIAL

In order to determine the relationship of the impact flash to the many possible projectile parameters, experiments were conducted in which the size, material, and velocity of the projectile varied. The targets used in these tests consisted of either sand, granite, or aluminum. Some of the results of these tests have already been observed in Fig. 8a, which shows that the intensity of impact flash increases with projectile velocity. Within the scope of the data obtained thus far, the intensity appears to increase as some power of the impact velocity (v^n).

With nylon projectiles against sand targets, the data of Fig. 8b show that I_{np} varies approximately as $v^{4.0}$. This relationship of I_{np} to impact velocity is further tested by the data shown in Figs. 10 – 13a: Using aluminum and glass projectiles to impact sand (Fig. 10) and aluminum projectiles against granite (Fig. 11), I_{np} can be seen to vary

IMPACT FLASH

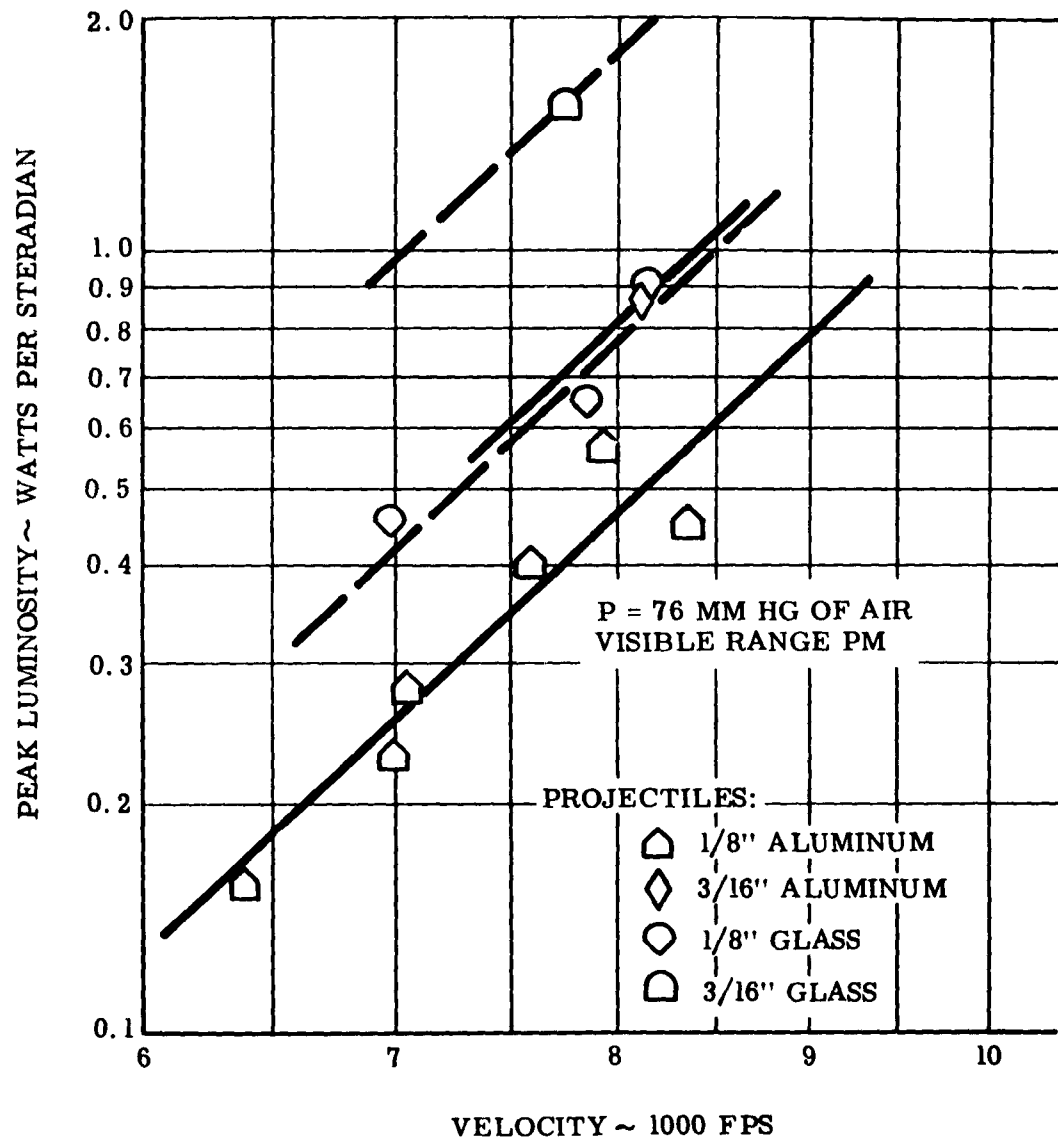


Fig. 10. Peak Luminosity for Glass and Aluminum Projectiles Impacting Sand.

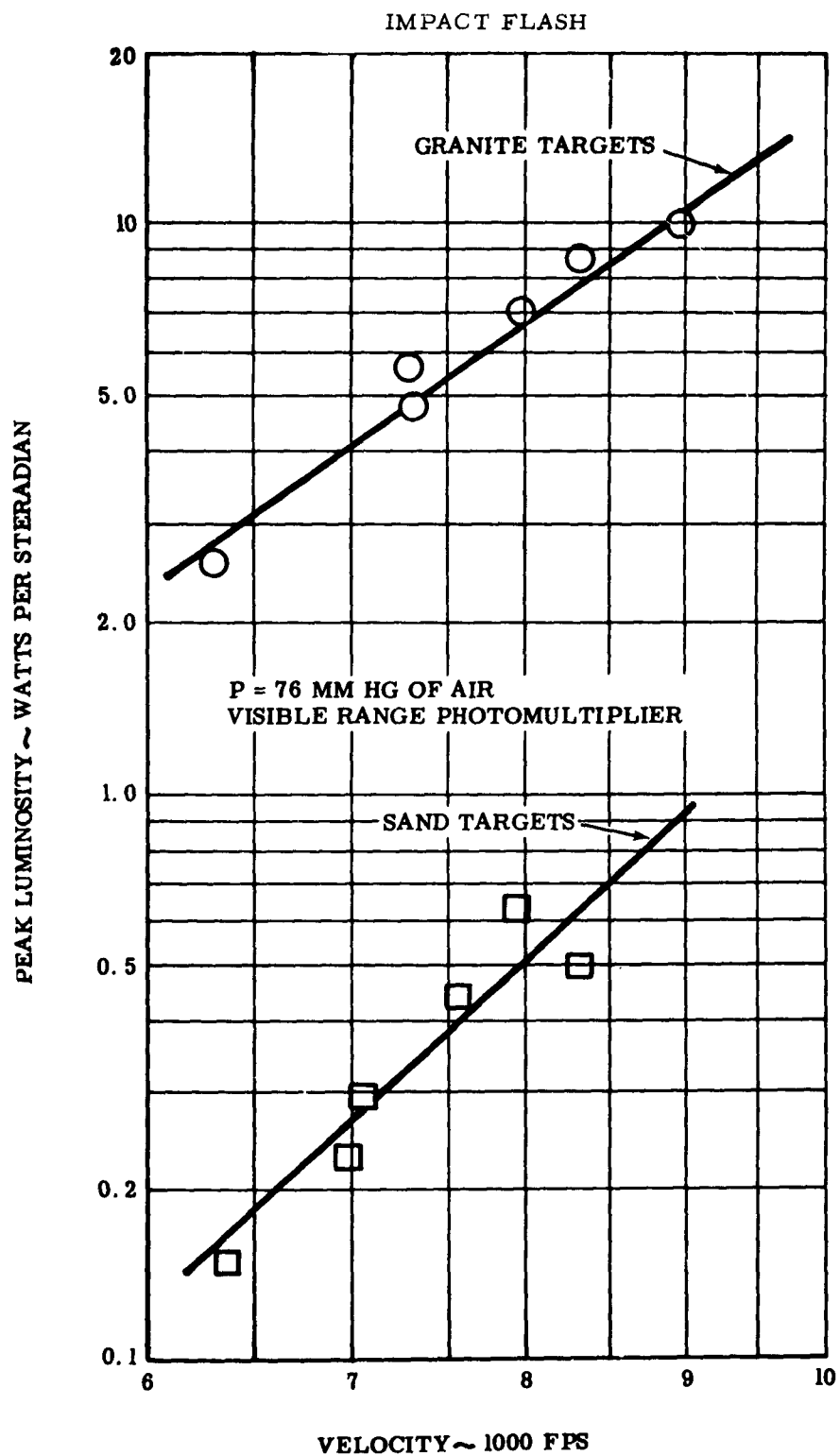


Fig. 11. Peak Luminosity of 1/8-in. Diam. Aluminum Spheres Impacting Sand and Granite Targets.

IMPACT FLASH

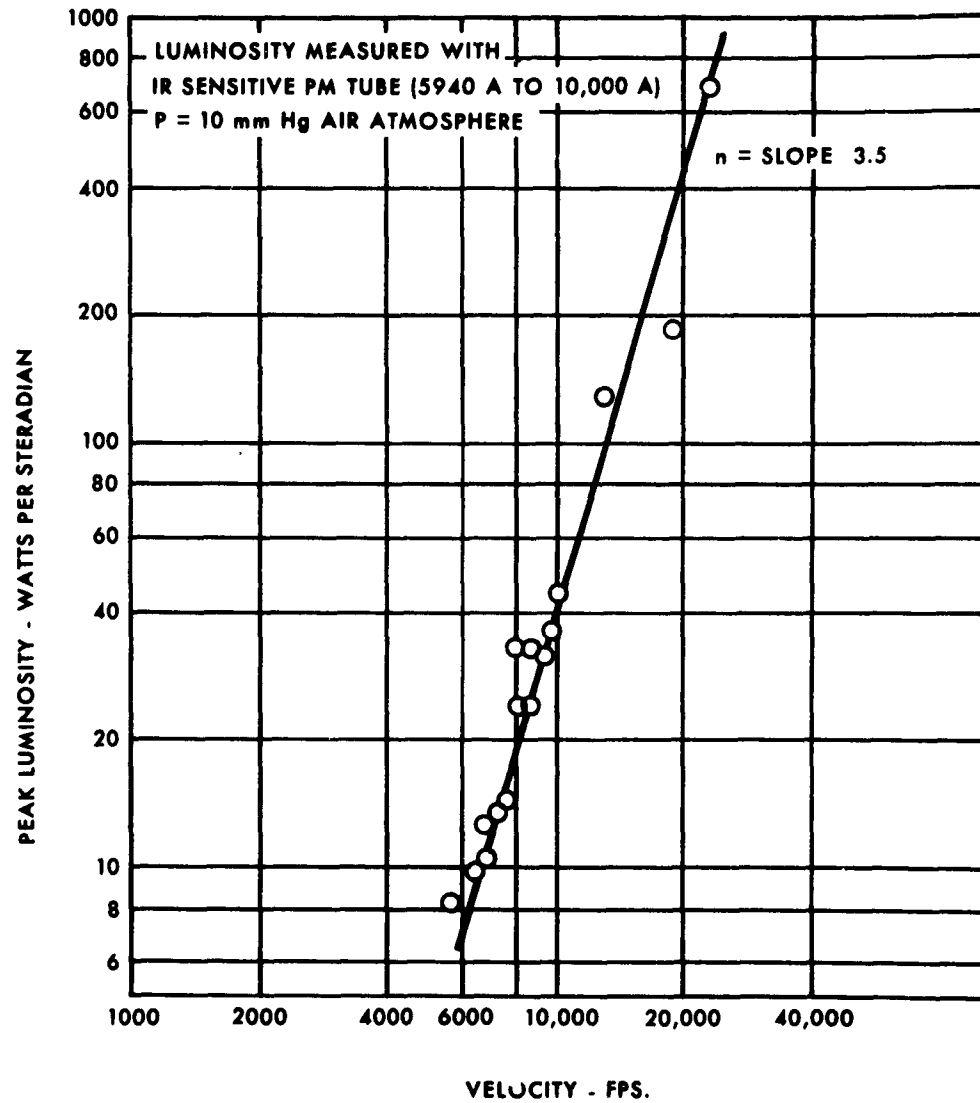


Fig. 12. Effects of Velocity on Peak Luminosity for the Impact of 0.220-in. Diam. Nylon Sphere on Aluminum Targets.

IMPACT FLASH

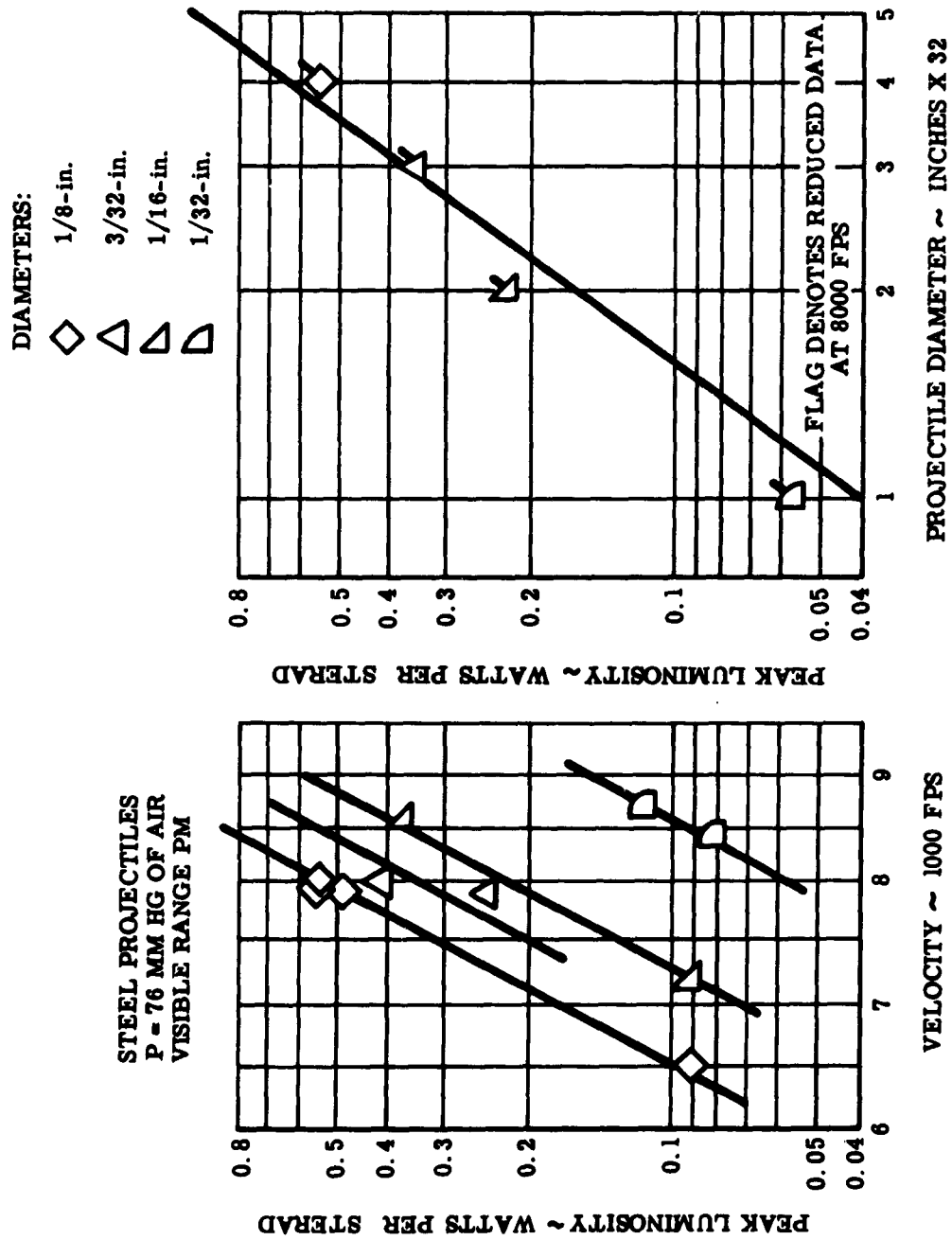


Fig. 13. Peak Luminosity of Various Sizes of Steel Spheres Impacting Sand Targets.

IMPACT FLASH

as $v^{3.88}$ and $v^{4.96}$, respectively. In Fig. 12, for nylon projectiles vs. aluminum targets, I_{np} is seen to vary as the 3.5 power of velocity. In Fig. 13a, the data obtained from steel projectiles against sand targets indicate that I_{np} varies as $v^{8.30}$. Although the exact power relationships cannot yet be determined, it is anticipated that the exponent of velocity will lie between 3 and 9 for a variety of projectile sizes and materials against either sand, rock, or aluminum targets.

In addition to the velocity scaling effects, a third important conclusion is demonstrated in Figs. 13a and 13b. Values of I_{np} were taken from the plot for the case of four sizes of steel projectiles impacting sand targets at a constant velocity of 8,000 ft/sec. These four values of I_{np} were replotted as a function of projectile diameter as shown in Fig. 13b. A method of least square fit was then applied to these data points, with the result that the best fit of the data showed I_{np} to vary as the square of the projectile diameter (D_p). This technique was also applied to the data for two sizes of both glass and aluminum projectiles; again, I_{np} can be shown to vary as D_p^2 are given in Fig. 14.

It can be concluded (Fig. 14) that projectiles of the same surface area and material produce the same impact flash if fired under identical conditions, and, from this, that the impact flash is a phenomenon associated with the surface area of the projectile rather than with its

IMPACT FLASH

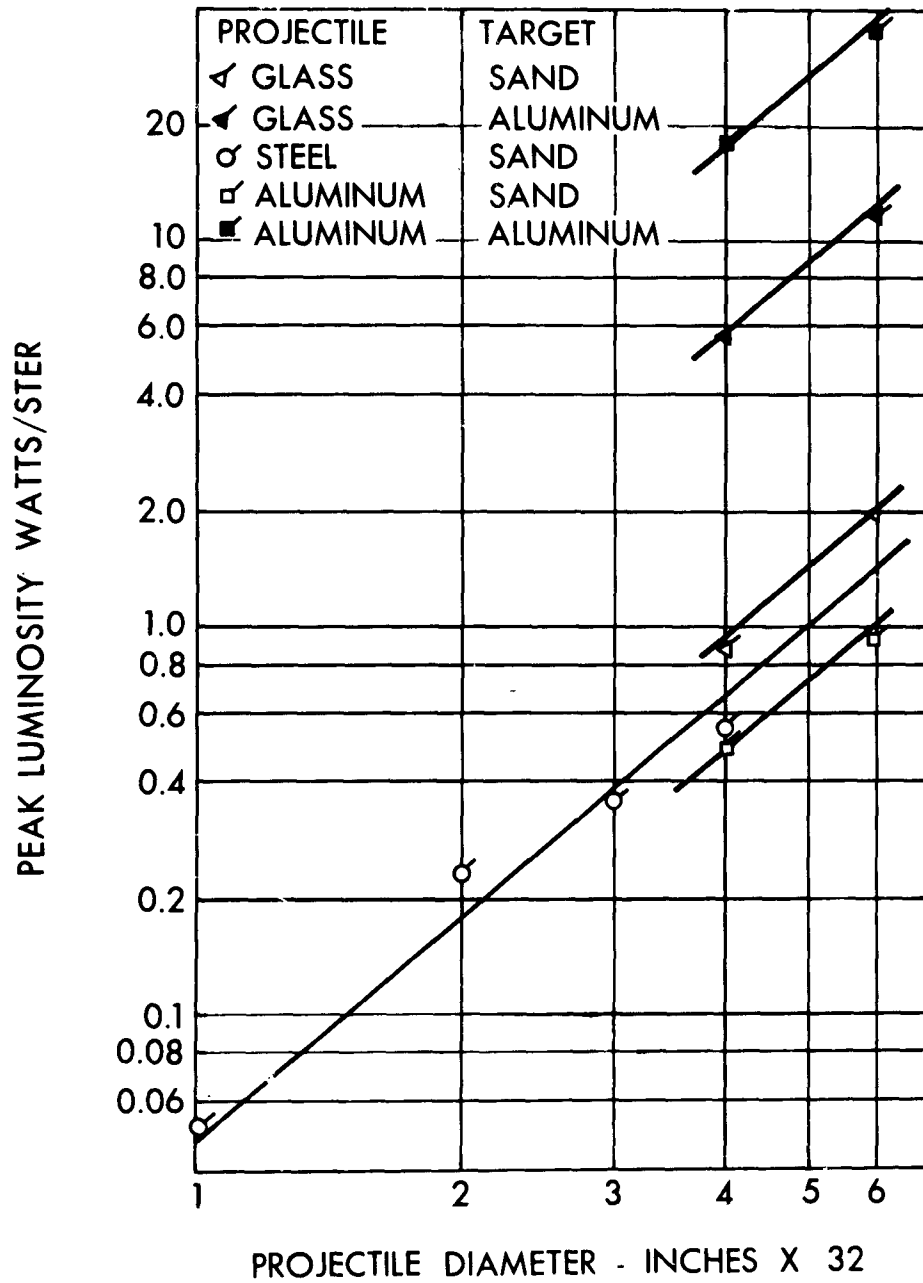


Fig. 14. Reduced Data - Variation of Peak Luminosity for Three Projectile Materials Impacting Sand and Aluminum at 8,000 fps.

IMPACT FLASH

mass. To test the effect of projectile mass, projectiles of a variety of materials were fired under identical conditions and all yielded the same impact flash (Fig. 15). The only exception to this was that of the glass projectiles which yielded a flash of lower intensity. Allowing this single exception, the impact flash is not seen to change with increasing projectile mass. To investigate the mass effect further, hollow and solid brass spheres and hollow and solid silver spheres of the same diameter ($1/8$ in.) were fired at the same velocity against aluminum targets (data in Fig. 15). The surface areas of the two spheres were identical, of course, but the difference in mass between the two was 40 percent. Result: the peak luminosities of impact flashes were identical, and time-durations of the two flashes were almost equal.

Figures 11 and 12 show that for a given projectile a change of target material produces a variation in impact flash; for example, the peak luminosity of the impact flash in granite is more than ten times that in sand. Also, over the range of velocities of interest here, the data are represented by a variation of peak luminosity, with approximately the fourth power of the velocity for granite and aluminum targets, and the fifth for sand targets.

At this point, an empirical relationship to describe the results thus far can be written as:

IMPACT FLASH

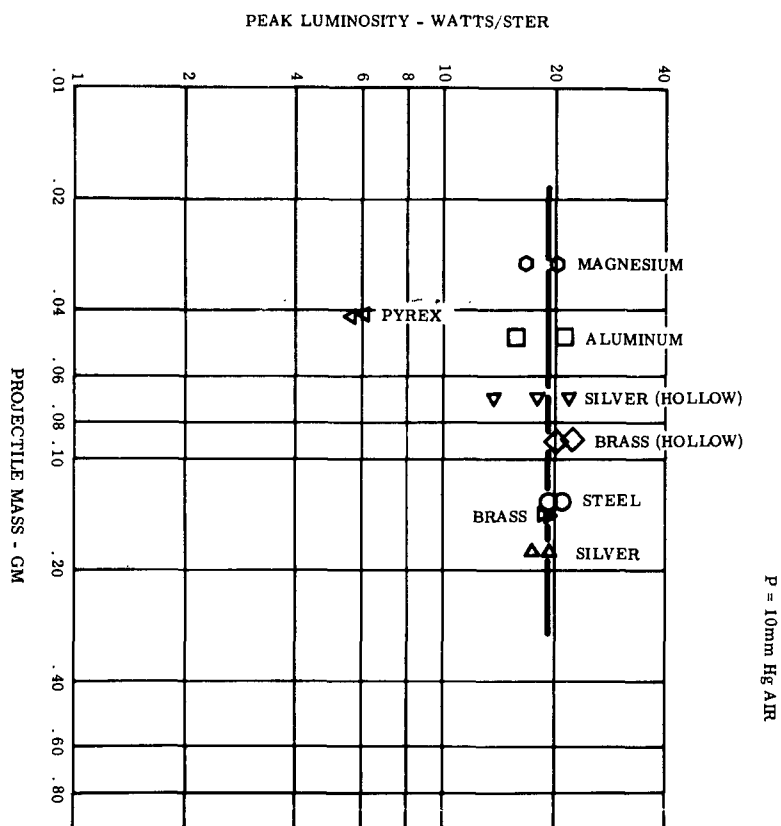


Fig. 15. Reduced Data - Variation of Peak Luminosity for Eight Projectile Masses (Diam. = Constant = 1/8 Inch) Impacting Aluminum at 8,000 fps.

IMPACT FLASH

$$I_{np} = CA v^n \quad (1)$$

where I_{np} = peak luminosity (visible)

A = area of projectile on target surface

v = velocity of impacting projectile

n = velocity exponent $3 \leq v \leq 9$

C = a constant (a primary function of the target and a secondary function of the projectile)

Within the scope of the experiments conducted so far, measured values for the coefficient C are listed in Table I for a variety of projectile-target combinations.

TABLE I
Values of Terms in Equation 1

Projectile	Target	C	watts per sterad		Photo-multiplier
			ft ²	(fps) ⁿ	
Aluminum	Granite	0.059 x 10 ⁻⁹		3.88	Visible
Aluminum	Sand	0.025 x 10 ⁻¹⁴		4.96	Visible
Steel	Sand	0.030 x 10 ⁻²⁷		8.30	Visible
Glass	Sand	0.048 x 10 ⁻¹⁴		4.96	Visible
Nylon	Sand	0.035 x 10 ⁻¹¹		4.02	Infrared

DURATION OF IMPACT FLASH

In previous discussion, only the peak luminosity associated with impact flash and not the integrated total luminosity over the time of

IMPACT FLASH

of emission was considered. However, it is of interest to determine the time of occurrence of the flash with respect to moment of impact, and to relate the duration of the flash to the elapsed time of projectile penetration and crater formation. Available references (for instance, Refs. 1, 10, 14) show that behavior of the projectile and the mechanism of the crater's formation vary, depending upon such factors as the velocity of impact and the relative strength of the specific projectile-target combination. It was suspected, therefore, that the initial peak luminosity was associated with the penetration of the more-or-less-intact projectile and the trailing off of the flash with the deformation of the projectile and the expansion of the crater. This hypothesis is consistent with the greatly increased duration of the flash with a granite target as compared to the shorter duration of the flash with a sand target; the instrumentation which is available has permitted a critical test of this hypothesis by displaying the photomultiplier outputs on oscilloscopes and photographing the results. Several of these will be examined.

The variation of luminosity with time is shown for three typical impact conditions in Fig. 16. The case of a hard projectile striking a soft target is illustrated by the top trace, a steel sphere impacting a sand target. There are two distinct phases in the generation of the impact flash. A sharp peak appears first, lasting in this case less

IMPACT FLASH

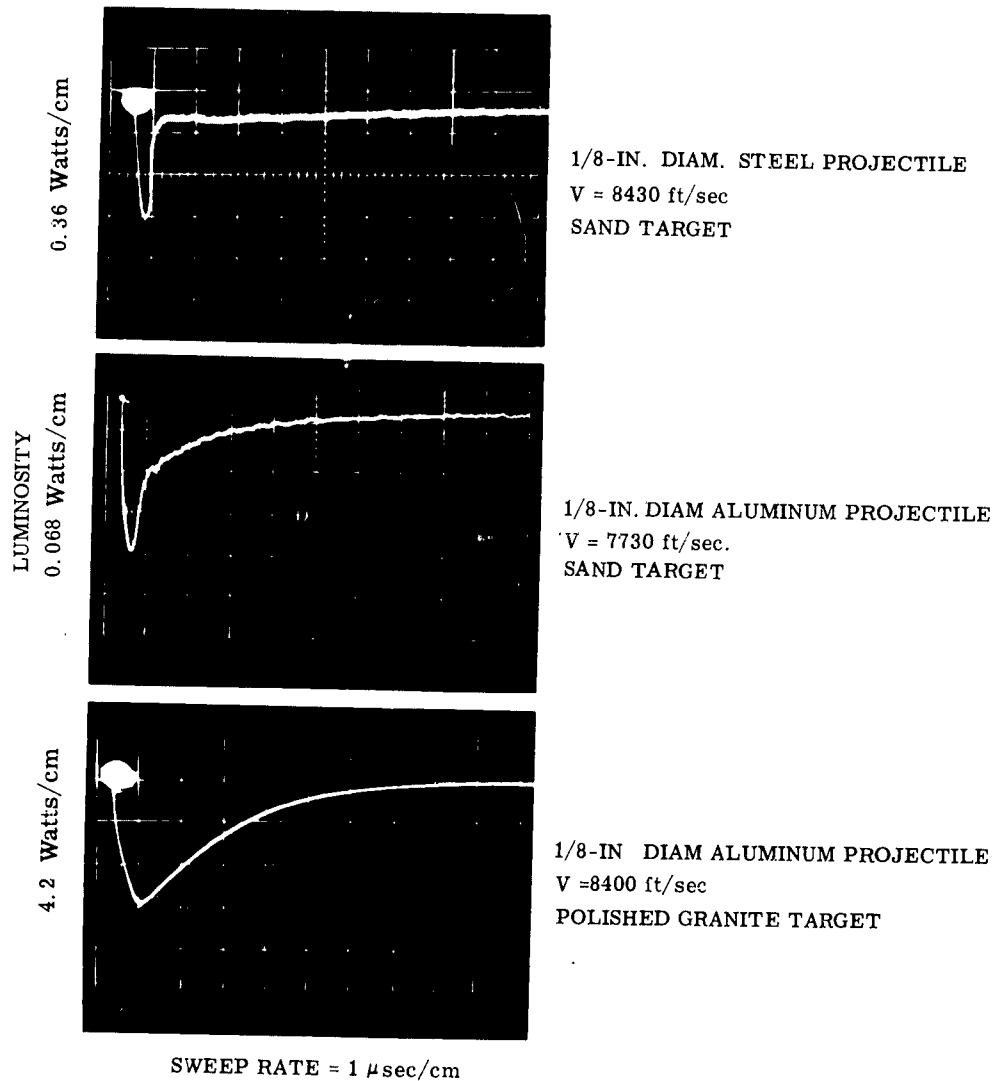


Fig. 16 Typical Photomultiplier Traces from Impacts of Various Projectile-Target Combinations

IMPACT FLASH

than a microsecond, followed by a long, low-intensity tail lasting many microseconds. Records with a high-speed framing camera show that the impact flash begins almost as soon as the projectile contacts the target; the peak is thus associated with the initial phase of penetration and cratering. For the case in question, the peak lasts less than the time it takes the projectile to penetrate the target to a depth equal to its own diameter.

The case of an aluminum projectile striking a sand target is shown by the center trace. The first part of the peak lasts about the same time as that from the steel projectile. This initial peak is followed by a region in which the light decays from 0.5 to 0.1 of peak value in approximately 3 microseconds, perhaps because of the increased deformation of the aluminum projectile as compared to that of the steel projectile.

This point is borne out by the variation of luminosity with time for the impact of an aluminum projectile into a granite target as shown in the bottom trace. The entire peak region of the flash is now seen to be broadened. The time from the initial rise through the decay to 0.1 of peak value lasts nearly 5 microseconds. The case of aluminum into granite at 8,400 ft/sec begins to approach the fluid impact region; a crater is formed in the initial instance of impact, and material is jetted from the periphery of this initial crater at very high velocity.

IMPACT FLASH

Consequently, a surface of highly-shocked material is exposed during the initial phase of cratering. The intensity of the shock is greatest at the beginning of impact, diminishing as the shock phenomena decrease with the increasing volume of material affected by the growing crater and expanding wave phenomena. The combination of these two effects produces the elongated shape of the light pulse seen in the case of aluminum into granite. In contrast to this, the case of steel into sand is probably close to the region of unbroken projectile impact, and the short light pulse might indicate that highly shocked material is generated only during the moment of initial penetration. The case of aluminum into sand is probably an intermediate case somewhere between the unbroken projectile and the fluid impact cases.

Two additional experiments substantiate the fact that the luminosity occurs at the instant of impact and persists for only a very brief period. In the first experiment, the Beckman & Whitley high-speed framing camera was used to observe several projectile-target collisions. A typical framing sequence (Fig. 17) shows the projectile to have moved approximately 0.5 inch to impact the target, then the flash occurs in a single frame and is extinguished in a total time of less than 2.4 microseconds.

IMPACT FLASH

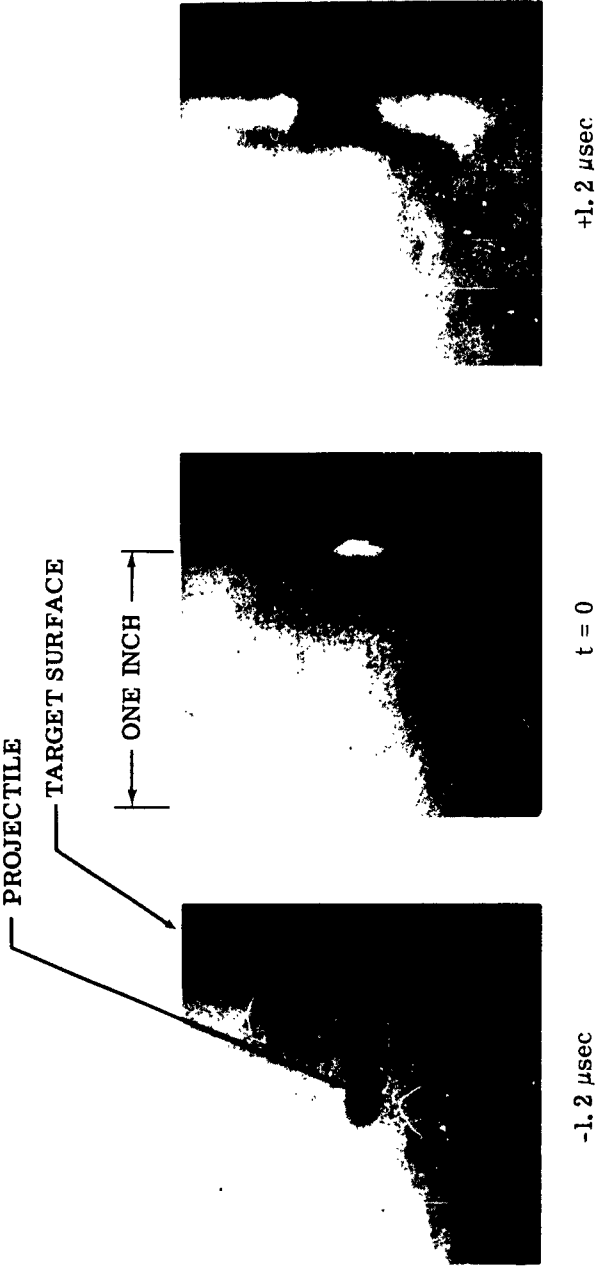


Fig. 17 Sequential Beckman-Whitley Photographs of a 1/8-In. Glass Sphere Impacting an Aluminum Target at 23,000 ft/sec

IMPACT FLASH

In the second experiment which was aimed at demonstrating the short duration of the flash, 3/16-in. aluminum projectiles were fired at an average velocity of 17,600 ft/sec against varying thicknesses of titanium sheets. Three sheet thicknesses were tested — 0.012 in., 0.020 in., and 0.040 in. — and the measured peak luminosities were 523, 505, and 543 watts/steradian, respectively. These data show that the peak luminosity is unaffected by the thickness of the target and that the impact flash is produced on, or very near, the surfaces of the projectile and the target (collision interface).

SPECTRUM OF AN IMPACT FLASH

To permit a more complete description of the phenomena of the impact flash, it was necessary to observe the spectrum of the emitted radiation. From an analysis of the spectra obtained under varying conditions of impact, it is anticipated that the composition of an unknown target might be determined.

Only a few spectra have been observed to date, but the results are most interesting. Two typical spectrograms, obtained from the impact of a nylon cylinder against both an aluminum and a sand target, are shown in Figs. 18 and 19. Figure 18 is the result of the fairly intense flash generated by a nylon cylinder impacting an aluminum target at 24,600 ft/sec. The aluminum doublet at 3,950 Å appears in

IMPACT FLASH

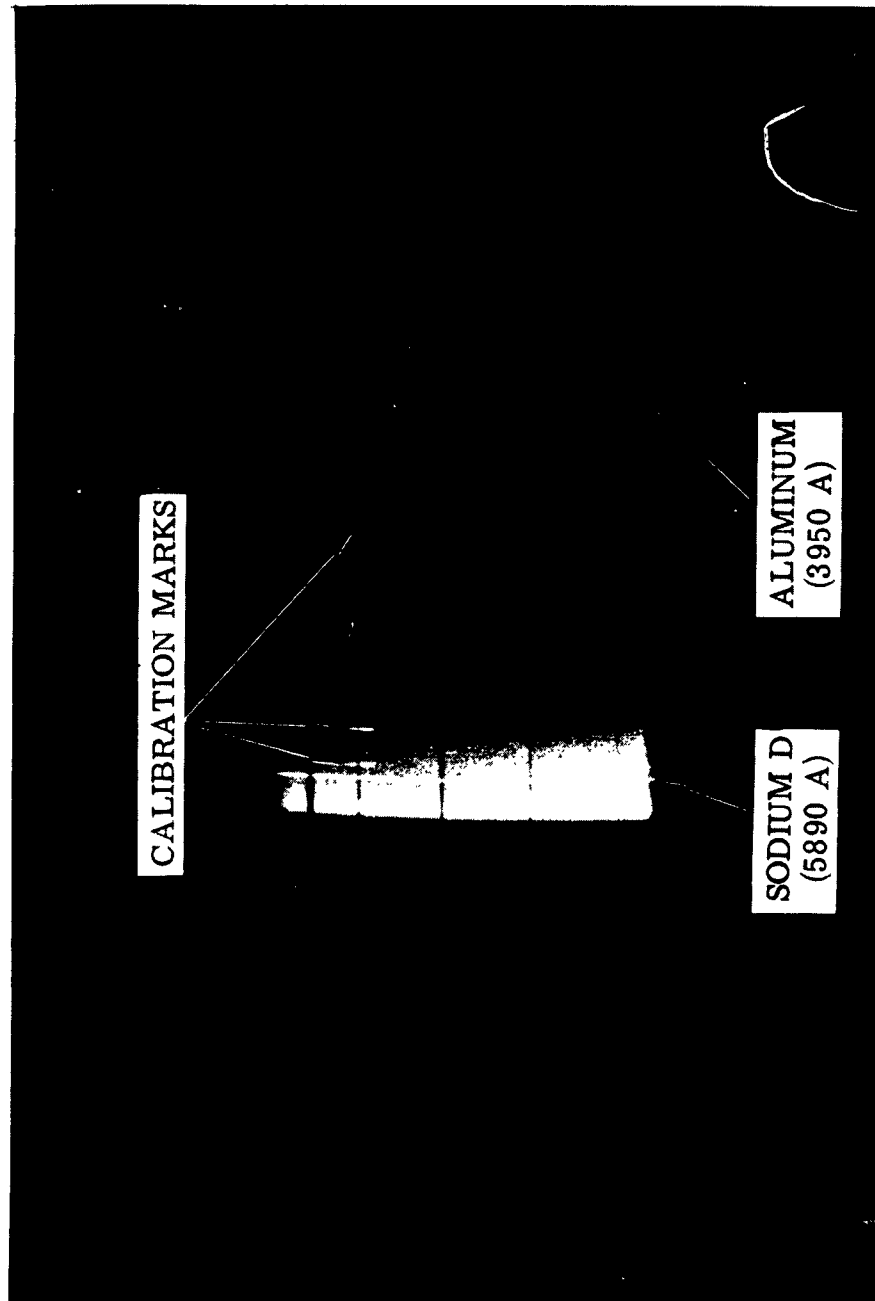


Fig. 18. Spectrogram of Impact Flash Generated by Nylon Cylinder Impacting an Aluminum Target at 24,600 fps.

IMPACT FLASH

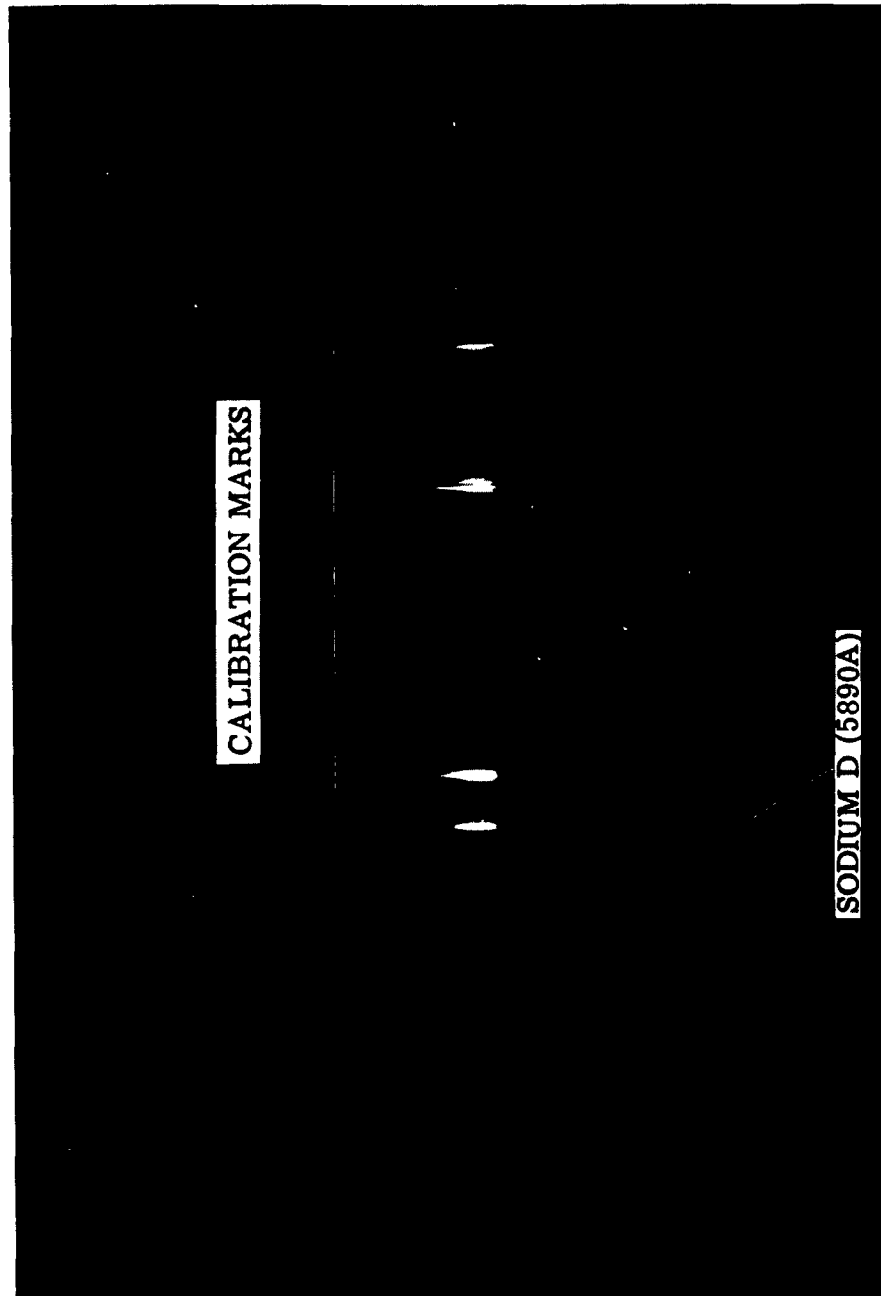


Fig. 19. Spectrogram of Impact Flash Generated by Nylon Spheres Impacting Sand Targets at Approximately 10,000 fps - 10 Rounds Superimposed.

IMPACT FLASH

the near ultraviolet on the right side of the figure, and the aluminum oxide bands appear between the blue and the green. There is a continuum extending from the near infrared to the green, and the sodium D line appears strongly. (The short line segments are, of course, the image of a point-source mercury calibration which serves also to locate the point of impact along the vertical axis of the film.) The appearance of the aluminum oxide bands in the spectrum shown in Fig. 18 suggests an apparent anomaly when compared with the data of Figs. 8 and 9 which show the impact flash to be independent of the ambient gas and the surrounding gas pressure. It is believed, however, that the oxide bands appear as a result of surface oxidation on the unpolished surfaces of both projectile and target.

The second typical spectrograph (Fig. 19) is the result of the relatively weak flash generated by a nylon cylinder impacting a sand target at approximately 10,000 ft/sec. The intensity of the flash, so far below the demands of the spectrograph, made it necessary to superimpose the flash of ten successive rounds in order to obtain a legible record. Although the photographic quality of the resulting spectrograph leaves much to be desired, it seems clear that no line spectrum is generated -- rather, there is a continuum in the near infrared. On the basis of Fig. 19, it would be difficult to determine the atomic and molecular composition of a sand target, as the line and

IMPACT FLASH

band spectra may be present but too weak to be discernible. Further measurements with a more sensitive instrument are needed to investigate this possibility.

DISCUSSION OF EXPERIMENTAL RESULTS

Referring to the data given in Fig. 15, the luminosity-vs. -time plots of Fig. 16, and the empirical relationship given in Eq. (1), the observed phenomena can now be defined.

The appearance of an intense flash of light upon impact is a result of the conversion of mechanical energy to light. Most certainly, the energy of the projectile is expended in a number of possible reactions: heat is generated, radiation is emitted (possibly over the spectrum from gamma rays to microwaves), and mechanical work is done in forming the impact crater. These experiments, however, were concerned with monitoring only that portion of the projectile energy which appears as visible light. It is reasonable to assume that the magnitude of radiated visible light will be a function of the energy of the impacting projectile.

Since the target reacts to the impact in a manner dictated by the magnitude of the pressure pulse, it may also be reasonable to relate the intensity of impact flash to the properties of the materials after being shocked by collision. Since a process by which luminosity is derived from the rapid application of pressure is unknown, a causal

IMPACT FLASH

relationship between impact-generated pressure and luminous radiation cannot be established by these experiments. More complex, and much more difficult to define, are the excitation energy of atoms under compression and the multiple-electron problem which is a result of the many possible ways in which electrons of different binding energies may react. Therefore, the present analysis is restricted to the establishment of an empirical relationship (Eq. (1)) to describe the phenomena and to estimate the intensity of impact flash.

OBSERVATIONS OF LUNAR IMPACT

In applying the results of laboratory tests to observations of lunar impact by instruments on the earth, two cases will be considered: (1) the crash landing of a Ranger lunar probe at lunar escape velocity, and (2) the impact of a marble-sized meteoroid. The question is whether or not a discernible record of the impacts of these objects can be obtained from the accompanying flash of light.

The answer to this question is critically dependent upon the design and sensitivity of the recording instrument. A full treatment of the subject is beyond the scope of this paper, and the discussion will be restricted to a limited study of two examples. The intent here is to present a method of analysis and to give a rough indication of possible answers.

IMPACT FLASH

Any earth-placed instrument will see the flash of the impact against the background intensity of the lunar surface. This background intensity represents noise on the record, and ability to "see" the flash will depend on whether or not the flash is distinct from the background noise. The first step in the analysis is to obtain an estimate of the lunar background intensity.

In computing the lunar background intensity, only the positions of conjunction (moon and sun in the same direction from the earth - dark of the moon) and opposition (moon and sun in opposite directions from the earth - full moon) will be analyzed. In opposition, the moon is illuminated by light from the sun with an irradiance of 140 watts/sq ft.⁽¹⁵⁾

Considering a small, flat, diffuse area of lunar surface, it is seen that the intensity of reflected light along a normal to the surface is

$$I_N = \frac{\bar{a} I_R}{2 \pi} \quad (2)$$

where \bar{a} is a normal albedo which may be taken as approximately 0.1. Substitution into this equation establishes the luminous intensity of the moon to be 2.2 watts/sterad sq ft when the surface is in full sunlight (opposition). By a similar analysis, it can be established that when the moon is illuminated only by light reflected from the earth (conjunction), the solar irradiance is decreased to about 0.002 watts/sq ft,

IMPACT FLASH

giving a reflected intensity of 3.0×10^{-5} watts/sterad-sq ft. Thus, part of problem is to establish the feasibility of observing a given impact flash against this background radiation.

The next step in the analysis is to estimate the intensity of the impact flash. The Ranger lunar probe is taken to be a vehicle of aluminum with a projected area of 19.6 sq ft, an effective length of 2 ft, and an impact velocity of 8,000 ft/sec. The lunar surface may be either sand or granite. The intensity of the flash is calculated from Eq. (1) using Table 1.

The effective duration of the flash \bar{t} is estimated to be the time it takes the probe to travel one-half its length; \bar{t} is used to compute the total light from the relation,

$$\int I_n dt = I_{np} \cdot \bar{t} \quad (3)$$

The results of these estimates are summarized in Table II.

TABLE II
Predicted Impact Flash for Ranger Lunar Probe

Surface	I_{np} w/sterad	\bar{t} sec	$\int I_n dt$ w sec/sterad
Sand	1.1×10^5	1.3×10^{-4}	14
Granite	1.6×10^6	1.3×10^{-4}	200

IMPACT FLASH

The meteoroid may be either stone or iron and will be approximated by glass (for stone) and steel (for iron). Since the experimental data have been derived from a sand target for glass and steel projectiles, estimates of the impact flash can be made only for a lunar surface of sand. The meteoroid is taken to be a sphere 1/2 in. in diameter striking at 78,000 ft/sec.

TABLE III
Predicted Impact Flash for 1/2-Inch Meteoroid

Type	Surface	I_{np} w/sterad	τ sec	$\int I_n dt$ w sec/sterad
Stone	Sand	1.2×10^6	0.3×10^{-6}	0.33
Iron	Sand	1.7×10^9	0.3×10^{-6}	450

The next step requires specification of the observing instrument. The two examples considered here are telescopes equipped with (1) a movie camera, and (2) a photocell that measures the intensity of light. In example (1), continuous observation can be made by using two cameras, one recording while the other changes film.

The performance of either instrument will depend on its sensitivity and on the signal-to-noise ratio. The question of sensitivity involves a consideration of the instrument's design that is beyond the scope of this discussion. The signal-to-noise ratio also depends on the design of the instrument, but it is possible to treat this subject

IMPACT FLASH

broadly for the classes of instruments which depend upon the physical quantity measured. Leaving the question of sensitivity to be answered separately, certain conclusions concerning the possibility of observing the impact can be drawn.

For the example of the telescope equipped with a movie camera, the impact flash will be recorded by a darkening of the film caused by the increase in light at the point of impact. The question, then, is whether or not the "dark" spot can be distinguished from the background. The contrast between the spot and the background on the negative will depend on the ratio of the lumens produced by the flash to the lumens falling on a corresponding area of the background during the exposure time Δt of the camera. The signal-to-noise ratio is determined by the ratio,

$$\frac{\text{signal}}{\text{noise}} = \frac{\int I_{np} dt}{I_N \sigma A \Delta t} \quad (4)$$

where I_N is the intensity of light from the lunar surface, and A is the area of the moon's surface that corresponds to the area of the impact flash. If the flash area is smaller than the minimum resolvable area of the instrument – considered to be the case here – the correct area to take is believed to be this minimum resolvable area,

$$\sigma A = \frac{\pi}{4} \left(\frac{5}{4} \frac{\lambda}{d} R \right)^2 \quad (5)$$

IMPACT FLASH

where λ = wavelength of the light
 d = aperture of the telescope
 R = distance from the earth to the moon

Considering a telescope with an aperture of 12 inches and taking green light as representative, $\lambda = 2 \times 10^{-5}$ inches. Under these conditions, $A = 5 \times 10^6 \text{ ft}^2$.

Considering also that the exposure time of the movie camera attached to the telescope is 0.1 second,

$$\Delta t = 0.1 \text{ sec}$$

Now the signal-to-noise ratio for various conditions of impact being investigated can be determined. This ratio is given in Table IV.

TABLE IV
 Observation of Lunar Impact with Telescope

Lunar Surface	Object	<u>Signal</u> <u>Noise</u>	
		Full Moon	Dark Moon
Sand	Ranger probe	0.00002	1.3
Granite	Ranger probe	0.00026	19.1
Sand	Stone meteoroid	0.00043×10^{-3}	31.4×10^{-3}
Sand	Iron meteoroid	0.00058	42.8

Table IV shows that on the basis of signal-to-noise ratio, a 12-in. telescope with a 0.1-sec exposure camera will not produce a discernible record of the flash from the impact of either the Ranger

IMPACT FLASH

probe or a 1/2-in. meteoroid on the bright side of the moon (at full moon). On the other hand, there is the distinct possibility that a record could be made of the impact of either probe or meteoroid on the dark side of the moon (at opposition). Whether or not a photographic record could actually be made will depend upon questions of sensitivity and other factors which include frequency of occurrence in the case of meteoroids. This is a subject for future investigation.

For the example of the telescope equipped with a photocell for continuous monitoring of the total light received by the telescope, the peak intensity of the impact flash will increase the background signal produced by the light received from the lunar surface. This background signal will depend on the angle of view of the telescope as determined by the area of the moon's surface to be observed, A_o . The signal-to-noise ratio is thus given by

$$\frac{\text{signal}}{\text{noise}} = \frac{I_{np}}{I_N A_o} \quad (6)$$

For this example, the angle of view will be arbitrarily selected as 2 minutes of arc, which corresponds to a circular surface on the moon with a diameter of 135 miles and an area of 3.9×10^{11} sq ft. The signal-to-noise ratios for the various conditions of impact are listed in Table V.

IMPACT FLASH

TABLE V
Observation of Lunar Impact with Photocell

Lunar Surface	Object	<u>Signal</u> <u>Noise</u>	
		Full Moon	Dark Moon
Sand	Ranger probe	1.3×10^{-7}	1.0×10^{-2}
Granite	Ranger probe	1.9×10^{-6}	1.4×10^{-1}
Sand	Stone meteoroid	1.4×10^{-6}	1.1×10^{-1}
Sand	Iron meteoroid	2.0×10^{-3}	1.4×10^2

Table V gives much the same information as Table IV. Impacts on the bright surface of a full moon could not be distinguished from the background. On the other hand, the impact of a meteoroid on the dark side could readily be recorded. In contrast to the previous example, however, the 2-minute telescope could not "see" the impact of a Ranger probe even on the dark moon.

There is one obvious improvement in technique which should be mentioned, since it may have a bearing on the conclusions drawn from these estimates of the performance of the 2-minute telescope with continuous photocell monitor. The duration of the flash is very short, lasting only about 0.1 millisecond in the case of the Ranger probe. This suggests that the photocell circuit should be provided with a filter passing only high-frequency signals (above 1,000 cycles per second). The background signal should be greatly reduced by this technique, and

IMPACT FLASH

the signal-to-noise ratio improved accordingly. Again, the improvement realized in this manner is a subject for future investigation.

CONCLUSIONS

Although there is only limited data on the phenomena of impact flash and, more important, no definitive theory to relate the generation of a flash to the mechanics of impact, certain conclusions may be drawn concerning the feasibility of observing impacts of meteoroids and space probes on the lunar surface.

(1) In the experimental program described, in all cases of impact above velocities of about 5,000 ft/sec, an impact flash was observed regardless of projectile or target material.

(2) Although tests were conducted only with air at pressures ranging from 0.002 to 200 mm Hg, and with helium at pressures of 0.060 and 200 mm Hg, there appears to be no significant effect of the composition or the pressure of the gas surrounding the impact area on the magnitude of the impact flash. This being the case, it is highly probable that a flash will occur in the case of a lunar impact at a velocity greater than 6,000 ft/sec.

(3) An empirical fit of the luminosity data indicates that the peak luminosity varies with the projected area of the projectile and

IMPACT FLASH

with a power of the velocity that ranges between 3 and 9. The constant of proportionality between the peak luminosity and the product of the projectile area with a power of the impact velocity depends primarily on the materials of the target.

(4) Examination of high-framing-rate camera records and photo-cell records shows that the flash starts at the first contact of the projectile with the target and rises to peak value during the first part of the impact process. The flash appears to be closely associated with the surface of the material that is highly shocked in the initial phase of the impact. The time duration of the flash varies markedly with changes in materials of projectile and target, particularly the latter.

(5) The spectrograms indicate that only a continuum, rather than a distinct atomic line spectra, is obtained under conditions of impact on sand targets below 10,000 ft/sec.

(6) To record the impact of a space probe or a meteoroid on the surface of the moon by observations made from the earth, a very limited study indicates the possibility of doing so if the impact takes place on a "dark" moon (illuminated by earthshine only). But if the impact occurs on the bright surface of a full moon, recording the impact would appear to be a most difficult task unless the monitoring photocell is equipped with a high-frequency bandpass filter or other signal-processing circuitry to reduce the background noise.

IMPACT FLASH

REFERENCES

- 1 A. C. Charters, "High Speed Impact", Sci. American, Oct 1960
- 2 Royal Aircraft Establishment, On Phenomena Observed at the Instant of Impact of the Second Soviet Cosmic Rocket on the Moon, by O. B. Dluzhnevskaya, ASTIA No. 243914, Feb 1961
- 3 P. S. Epstein, "What is the Moon Made Of?", Phys. Rev., Vol. 33, 1929, p. 269
- 4 A. J. Wesselink, "Heat Conductivity and Nature of the Lunar Surface Material", Bull. Astron. Inst., Neth., Vol. 10, 1948, pp. 350 - 363
- 5 J. C. Jaeger and A. F. A. Harper, "Nature and Surface of the Moon", Nature, Vol. 166, 16 Dec 1950, p. 1026
- 6 T. Gold, "The Lunar Surface", J. Roy. Astron. Soc., Vol. 115, No. 6, 1955
- 7 Aviation Week, Vol. 76, No. 10, 5 Mar 1962, p. 70
- 8 W. W. Atkins, "Flash Associated with High Velocity Impact on Aluminum", J. Appl. Phys. Vol. 26, 1955
- 9 W. H. Clark, R. R. Kadisch, and R. W. Grow, "Spectral Analysis of the Impact of Ultra Velocity Copper Spheres into Copper Targets", Tech. Report OSR-16, University of Utah, 1 Sep 1959
- 10 W. C. Maurer and J. S. Rinehart, "Impact Crater Formation in Rock", Proc. 4th Symposium on Hypervelocity Impact, APGC-TR-60-39, Eglin AFB, Florida, Sep 1960
- 11 H. J. Moore, R. V. Tugu and D. E. Gault, "The Geology of Hypervelocity Impact Craters", (paper presented at 5th Symposium on Hypervelocity Impact, Denver, Nov 1961). B. Pat Denardo, "Measurements of Momentum Transfer from Plastic Projectiles to Massive Aluminum Targets at Speeds up to 25,600 ft/sec", NASA Tech. Note d-1210, Mar 1962. D. E. Gault, "Changes in Lunar Characteristics by Micrometeoroids and the Shape and Size of Particles", and E. M. Shoemaker, "Size Frequency

IMPACT FLASH

Distribution of Small Primary and Secondary Impact Craters", Proc. Lunar Surface Materials Conf., Boston, Massachusetts, May 1963. See also R. W. MacCormack, "Investigation of Impact Flash at Low Ambient Pressures" (paper presented at Sixth Symposium on Hypervelocity Impact, Cleveland, Ohio, 1 May 1963)

- 12 R. B. Baldwin, The Face of the Moon, The University of Chicago Press, Chicago, Illinois, 1949
- 13 A. C. Charters, "The Free Flight Range: A Tool for Research in the Physics of High Speed Flight", ARS Preprint 1986-61 (paper presented at the International Hypersonics Conference, MIT, Aug 16 - 18, 1961)
- 14 J. W. Gehring, "Observations of the Phenomena of Hypervelocity Impact", Proceedings of the 4th Symposium on Hypervelocity Impact, APGC-TR-60-39, Vol. II, Eglin Air Force Base, Florida, Apr 1960. Also R. J. Eichelberger and J. W. Gehring, "Effects of Meteoroid Impact on Space Vehicles", ARS J., Vol. 32, No. 10, Oct 1962
- 15 See for instance, Fielder, Gilbert, Structure of the Moon's Surface, Pergamon Press, New York, 1961; also, Satellite Environment Handbook, Stanford University Press, 1961; and E. J. Opik, "The Density of the Lunar Atmosphere", Irish Astron. J., Vol. 3, 1955, pp. 137 - 143

SUMMARY: THEORETICAL AND EXPERIMENTAL STUDIES
OF CRATER FORMATION

By Robert J. Eichelberger

Ballistic Research Laboratories
Aberdeen Proving Ground, Maryland

INTRODUCTION

The purpose of the present paper is not so much to summarize the contributed papers presented during the 6th Hypervelocity Impact Symposium as to compare them with one another and with earlier publications and to supplement them with information derived from discussions during the symposium. This appears to be a particularly important function with regard to the fundamental treatment of crater formation since the 6th Symposium, far from resolving the points of controversy that have arisen during previous years, have brought them even more sharply into focus.

The papers presented at the 6th Symposium seemed to the author to represent a high point in the fundamental treatment of the problem of hypervelocity impact. The number of papers representing different approaches to the theory is encouraging and the quality of the papers is particularly gratifying. The papers describing experimental work are encouraging insofar as they demonstrate a diversification of effort and closer attention to the testing of theory, as opposed to the earlier widespread devotion to almost random tests, superficial observations, and empirical formulations. The rate of progress in exploitation of refined experimental techniques has been somewhat discouraging, however. Only one paper was presented in which the particularly important observations of transient phenomena during crater formation are treated. While that single paper demonstrates a substantial advance in the state of the art, the dearth of similar contributions indicates a decrease in apparent effort in an important facet of the research problem.

The papers to be discussed in this summary fall into four general categories, (1) theory, (2) quasi-theory, (3) experiment pertaining to crater formation, and (4) impact ionization and flash. The classification of the specific papers is as follows:

I. Theory

a. Hydrodynamic Computations

(Walsh and Tillotson; Riney; Wilkins and Giroux)

SUMMARY: STUDIES OF CRATER FORMATION

- b. Similarity Method
(Rae and Kirchner; Davids, Calvit and Johnson)
- c. "Traditional"
(Luttrell)

II. Quasi-Theory

(Heyda; Kinslow; Engel; Moore, MacCormack and Gault)

III. Experiment

- a. Crater Dimensions
(Halperson; Goodman and Liles; Kineke and Richards; Nysmith, Summers and Denardo)
- b. Energy Partition
(Pond, Mobley and Glass; Gault and Heitowit)
- c. Transient Observations
(Kineke and Vitali)

IV. Impact Ionization and Flash

(MacCormack; Friichtenicht and Slattery; Gehring and Warnica)

We shall consider first, as a group, the papers in the first three categories, all of which are devoted to the mechanics of crater formation. The papers on ionization and flash will be considered separately.

Before proceeding to a detailed comparison of results and conclusions derived by the various authors, a few general comments are appropriate. First, the papers presented at the 6th Symposium were notable for the consistency of interpretation of the physical model of crater formation. This applies to the theoretical papers as well as the experimental. It also includes those discussions of impact on brittle targets as well as on plastic targets. It appears that the viewpoint of nearly all contributors to the field is converging on the model constructed earlier from transient observations and described in the literature.^{1/} It is difficult to determine whether this convergence of opinion is spontaneous or whether it has been influenced by exposure to the descriptions of the phenomenological model, and the results of Bjork's earlier computations.^{2/}

The model of crater formation that is emerging visualizes a phenomenon consisting of two major stages. Immediately after impact, pressures of the order of 1 to 100 megabars arise in the neighborhood of the contact surface

SUMMARY: STUDIES OF CRATER FORMATION

between projectile and target. This stage persists for only a very short time, however, being relieved by reflected tension waves from free boundaries and the resultant flow of the projectile and the target material. Thus, the extremely high pressure attenuates quite rapidly, before the crater has attained very large dimensions. After a few microseconds the pressure pulse has degenerated into an essentially elastic wave. But the crater continues to expand for a much longer time, under low pressure conditions. The duration of the cavitation process depends substantially upon the physical characteristics of the target material. In very plastic target materials, the expansion of the crater continues for extremely long times; in more brittle materials, the crater expansion terminates at relatively early times and is followed by profuse crushing and fracture of the target material.

While essentially all of the papers presented agree upon the qualitative aspects of this physical model, there is still little agreement as to the quantitative relationships between the crater formation parameters and the impact parameters. It may seem strange that after the amount of effort, both theoretical and experimental, that has been expended upon this problem there should still be no definitive correlations available. We shall attempt to point out the reasons for this failure during the ensuing discussion. In general, the disagreements arise from lack of sufficient precision and difficulty of interpretation, in both the theory and the experiments. Specifically, the current treatments of theory lack: (1) proper equations of state for the lower pressure regime; (2) precision in the finite differencing methods; and (3) certainty as to the influence of the mechanics of the program coding in the machine computations. The experiments lack: (1) perspicacity in the design of the experiments; (2) capability of projection at sufficiently high velocities; (3) sufficient precision and assured accuracy for detailed analysis of transient conditions.

In addition to the failings within the separate realms there has been entirely too little coordination between theoretical and experimental work. It is imperative, in order to test the validity of the theories, that computations be carried out representing conditions that can be achieved experimentally and under which detailed experimental observations of transient as well as final conditions can be or have been made.

I. THEORY PAPERS

a. Hydrodynamic Computations

All the papers in this category follow the same general approach as that used in earlier crater formation studies by Bjork - that is, they use some variation of the "point-in-cell" code. This method has been

SUMMARY: STUDIES OF CRATER FORMATION

considered by some (particularly those with no personal experience in such computer techniques) as being infallible. Perhaps the most important result of the 6th Symposium has been a demonstration that, as a result of differences in computational techniques and/or interpretation of the results, different workers can arrive at substantially different conclusions while using nominally the same mathematical methods and the same input data.

1. Walsh and Tillotson

The work described in the paper by Walsh and Tillotson follows the earlier calculations of Bjork in treating the problem of crater formation as a purely hydrodynamic process and in discussing only impacts of like materials. Ostensibly, the only significant difference between the procedures of Walsh and Tillotson and those of Bjork lie in the fact that the former have carried their computations only to the point where the maximum pressure in the system has fallen to approximately one megabar. Thus, they have treated only those portions of the problem which can be considered as truly hydrodynamic. They have then been forced to use their "equivalence" principle to make deductions concerning later stages of the crater formation phenomenon. In contrast, Bjork has carried his computations through the entire process, assuming that the purely hydrodynamic equations used remain valid throughout the lower pressure phases of crater formation until the expansion of the crater ceases. He has used a rather arbitrary but plausible criterion for terminating the crater expansion.

The equivalence principle used by Walsh and Tillotson states that if, at any time during the formation of craters resulting from two different impacts, the pressure pulses (in identical or in appropriately scaled coordinate systems) are identical, then the subsequent reaction of the target to the action of the pressure pulses will also be identical (in scaled coordinates). By application of this principle to problems involving impacts by particles varying in mass but having equal kinetic energies, the authors arrive at the conclusion that the depths of the craters resulting from the impacts will vary as the impact velocity to the exponent 0.62. This is to be contrasted with Bjork's conclusion that crater depth will vary as $V^{1/3}$. The Walsh and Tillotson conclusion corresponds very closely to that espoused by many experimentalists, according to which crater volume is proportional to the kinetic energy of the projectile, whereas Bjork's corresponds to a crater volume proportional to the momentum of the particle.

SUMMARY: STUDIES OF CRATER FORMATION

The equivalence principle, as stated by Walsh and Tillotson cannot be seriously questioned. If two (scaled) pressure waves are truly identical at any stage, then their subsequent effects (also scaled) on the target must also be identical. On the other hand, it seems quite clear that pressure pulses resulting from different impact conditions cannot be exactly identical at any stage, no matter how similar they may appear according to the computations. In fact, Walsh and Tillotson do not claim that the conditions in their computations are identical. They do claim close similarity. Questions immediately arise, then, concerning two aspects of their approach: first, the accuracy of the computations leading up to the similar states discussed and, second, the sensitivity of the subsequent cavitation of the crater to small residual differences in the pressure pulses.

Corresponding questions can of course, be raised concerning Bjork's computations. The same questions exist concerning the accuracy of the computations during the initial, high pressure (truly hydrodynamic) stage of the phenomenon. Secondly, it is clear that the use of hydrodynamic principles during the later, low pressure stages of the phenomenon must be an approximation, and it is uncertain how close an approximation it may be.

Thus, it would appear that there is no means at present to decide upon a preference for one approach or the other. In view of the importance of this theoretical approach to the solution of the hypervelocity impact problem, it is imperative that some means be found to decide which result, if either, provides an accurate description of the phenomenon. The following procedures are suggested for consideration:

- (1) a specific problem should be selected for treatment by both parties; computations should be run concerning the early, high pressure phases of the crater formation process and the results compared carefully and in detail. If significant differences appear in the descriptions derived, the source of these differences should be identified. Since identical input data will have been used (including the hydrodynamic equations of state), any discrepancies at this stage can only arise from variations in the computational techniques and it should be possible to decide which technique, if they differ, is preferable.
- (2) If significant differences are found in the results of the computations described above, both parties should conduct calculations on an identical selection of problems

SUMMARY: STUDIES OF CRATER FORMATION

in which projectile kinetic energy is held constant but the mass varied. If no significant differences are found in the first computations, only one party need carry out the further computations. In this phase, the computations should be carried through to the late, low pressure stages of the crater formation process, in accordance with Bjork's approach. Several stages should be selected however, in accordance with the Walsh and Tillotson procedure, at which the degree of similarity between the several problems can be tested. In their initial work, Walsh and Tillotson have been extremely conservative in stopping their computations while pressures of the order of 1 megabar still remained. The computations could undoubtedly be carried down to pressures of the order of 200 kilobars before serious objections to the use of hydrodynamic principles would be raised. Thus, it should be possible to ascertain whether the degree of similarity tends to increase or decrease during the intermediate stages of crater formation, but preceding the drop in pressure to very low values. If the small variations in the distribution of the significant parameters (pressure, particle velocity) tend to diminish as the process continues, then the equivalence principle applied by Walsh and Tillotson would be validated.

(3) While the procedures outlined in (1) and (2) will assuredly uncover the sources of the differences between the two sets of computations, there remains a substantial probability that a clear-cut preference, based on sound physical or mathematical grounds, will still escape. Both approaches may contain, at their present stage of development, features of uncertain validity. The ultimate means of judging of course, is comparison with experimental observations. Consequently, a vigorous attempt must be made to obtain experimental observations under conditions identical to those used in the computations (the accessibility to experimental observation should be a primary criterion in choosing the impact conditions used in the computations).

Insofar as possible, observations on the transient phenomena taking place during the early, high pressure stages should be made and compared with the results of computations carried out under (1) above. It seems unlikely however, that differences between the two parallel computations for this stage of the process will be large

SUMMARY: STUDIES OF CRATER FORMATION

enough that experimental observations will provide a choice. It is more likely that experiments involving detailed observations of transient conditions during the later stages of the crater formation process will provide decisive comparisons. This approach would, of course, comprise mainly a test of the later stages of Bjork's calculations, since Walsh and Tillotson use their equivalence principle, together with an empirical determination of crater dimensions for a single impact condition, to predict variations in crater dimensions for other conditions.

(4) The most obvious means of deciding between the two methods of computation would be to determine experimentally whether crater depth actually varies with either the 0.62 power or the $1/3$ power of the impact velocity. This approach seems to hold little promise, however, for the near future since the available experimental data do not permit a definitive choice. Bjork has attempted to use certain selected experimental data to support his calculations; more will be said in this regard in discussing the experimental papers. Suffice it to say, at this point, that the author does not agree with Bjork's use of the experimental data and that his interpretation of the experimental data does not agree with that of the authors who have provided the data.

The Walsh-Tillotson paper contains no comments upon the influence of projectile intensive properties. However, during his oral presentation, Walsh commented that from more recent computations he has concluded that projectile density and wave propagation velocities have no significant influence upon the final crater dimensions. This, again, is in distinct contrast with the conclusions of Bjork.^{2/3/} There is not sufficient information available concerning the Walsh and Tillotson computations on this point to warrant discussion; it should, however, be noted that Bjork's conclusion is not based upon actual computations treating impacts of various materials upon a common target - he has treated only impacts involving like materials. It is, rather, based upon an implicit assumption that differences in the initial pressure resulting from impact will persist through the later stages, and that the density and compressibility of the projectile material can thus manifest their influence upon the final crater dimensions. This difference of opinion is closely

SUMMARY: STUDIES OF CRATER FORMATION

related to the one involving variations in velocity, and similarly, cannot be resolved by available experimental data.

While the controversial points in the Walsh-Tillotson paper are perhaps the most interesting, currently, because of the controversy, there were several other points brought out in the paper which are equally important from a longer range point of view. One of these is the correlation of equations of state for various materials and the application of this correlation to "scaling" of the effects of impact involving various materials. In this manner, the results of a single machine computation can be extended, with very little uncertainty, to a wide variety of impact conditions. In view of the time and cost involved in carrying out each computation of the crater formation problem, this procedure is an extremely useful one.

The momentum distributions provided by Walsh and Tillotson are of considerable interest, also. The distributions of axial momentum provide a detailed explanation of the momentum "amplification" that has been often discussed and experimentally observed. The details of the variation in radial momentum are interesting to those who have followed earlier theoretical work, particularly the work of Opik. It will be recalled that an essential assumption in Opik's treatment concerned the time independence of radial momentum. This was an assumption used by Opik to provide the additional relation needed to solve the equations representing his penetration model. The results of Walsh and Tillotson indicate that the radial momentum varies drastically during the early stages of the penetration process. This should serve to make one extremely cautious about ad hoc assumptions used in conjunction with arbitrary physical models.

2. Riney

The paper presented by Riney offers more for the future than for the immediate present. It provides a detailed description of means for including either visco-elastic equations or elastic-plastic equations, or both together, to augment the hydrodynamic equations of state currently in use. No results of computations using the supplemented equations of state were offered, however.

3. Wilkins and Giroux

The paper of Wilkins and Giroux is particularly interesting as a sequel to Riney's. While the authors have not addressed themselves specifically to the problem of crater formation resulting

SUMMARY: STUDIES OF CRATER FORMATION

from hypervelocity impact, they have shown a variety of examples of phenomena involving "moderate" pressures and have delineated the influence of strength properties of materials. The results described essentially provide a preview of the results that might be expected from computations using Riney's procedures and treating the hypervelocity impact problem.

Wilkins and Giroux have demonstrated the effects of an elastic-plastic property of materials upon a number of aspects of high pressure phenomena, including the form of the stress wave propagated, the mechanical deformation due to detonation of an explosive charge in contact with a metal surface, the expansion of a spherical cavity due to detonation of high explosives internally, and a low velocity impact concerning unlike materials.

The results are, of course, pertinent only to the later stages of hypervelocity crater formation in view of the relatively low pressures treated. At the extremely high pressures existing during the initial stages of a hypervelocity impact, the relatively low forces involved in the elastic-plastic relation assumed would be completely overwhelmed by the hydrodynamic effects. Thus, the results of the paper are more significant insofar as they forecast possibilities for future theoretical treatment of hypervelocity impact than in their impact upon the current situation. They show the means by which material properties can be taken into account during later stages of crater formation and illustrate some of the specific effects that may be anticipated. It remains to carry out calculations of hypervelocity impact problems, using similar techniques, to determine whether the elastic-plastic properties of the material have a substantial influence upon the outcome of a truly hypervelocity problem.

b. Similarity Method

1. Rae and Kirchner

This paper must be considered one of the outstanding contributions to the symposium. While it does not provide results of completed calculations that can be compared with experiments, it does offer a particularly critical and thorough analysis of one theoretical approach to the hypervelocity impact problem. But the paper not only discloses the essential characteristics of the similarity approach and its shortcomings; it also offers a generalization or extension that should enable this method to make more substantial contributions to the impact field in the future.

SUMMARY: STUDIES OF CRATER FORMATION

Among the more specific conclusions drawn by the authors were the following:

- (i) The late stages of the crater formation process will not proceed in accordance with the similarity principle. This results necessarily when real equations of state are used since these relations do not behave in accordance with the similarity method at moderate pressures.
- (ii) During the initial stages of the crater formation process, the energy of the projectile is much more important in determining the nature of the event than the momentum. In this respect, the similarity method is in agreement with the results of hydrodynamic computations. It should be noted that Rae and Kirchner do not extend this conclusion to state that energy is more important than momentum in determining ultimate crater dimensions. They conservatively refrain from any comments concerning the later stages due to the non-similar nature.
- (iii) Initial results of the "quasi-similar" approach yield very good agreement with mixed computed results from Bjork and experimental results from BRL and NRL concerning wave propagation resulting from hypervelocity impact.
- (iv) The authors conclude that strength effects in the target must be considered at least for terminating the crater formation process, although their significance in determining final crater dimensions cannot be predicted without detailed calculations using the quasi-similar method.

While it appears to the author that the hydrodynamic code approach to the crater formation problem is the more powerful, the work of Rae and Kirchner has advanced the similarity method to such an extent that it becomes a very useful and even powerful supplementary tool. In view of the present circumstances surrounding the hydrodynamic method, it is particularly desirable that an alternative approach be followed; such alternative may finally become an arbitrator in deciding which of the two or more competitive hydrodynamic treatments is more accurate.

SUMMARY: STUDIES OF CRATER FORMATION

2. David, Calvit and Johnson

This paper represents a straightforward application of the similarity method, using a polytropic equation of state. The results should be considered in the light of the analysis provided by Rae and Kirchner; however, since the authors limited their treatment of the expansion of a spherical cavity due to detonation of an explosive to only the early stages of wave propagation, there is no essential disagreement between their conclusions and those of Rae and Kirchner.

Several significant quantitative points are made by the authors. In the first place, they compute that the pressure at the wave front drops from approximately 400 kilobars to only 100 kilobars during a time of only 1.6 microseconds after the beginning of the cavity expansion. The shock wave ceases to be ideal after only 0.7 microseconds. They have concluded that the two-fifth power law for the rate of shock wave attenuation, which has been a typical characteristic of the similarity approach, fails after only about 1.6 microseconds. By comparison of the results of the computations with experimental observation of crater dimensions and wave propagation times, the authors conclude that the expansion of the cavity continues for extremely long times compared with the time required for the shock wave to attenuate to essentially an elastic level.

While the results of the treatment have yielded some very satisfying agreement with experimental observations on early conditions in the cavity expansion, they lend little to resolution of the major points of uncertainty or controversy in the hypervelocity impact problem. By some means they must be extended and subjected to more detailed experimental tests, aside from the refinement and modification of the basic mathematical procedures suggested by Rae and Kirchner. It seems possible that a combination of similarity treatment of early conditions in crater formation with the equivalence principle used by Walsh and Tillotson might be profitable. The similarity approach has the virtue of providing very detailed and precise calculations, as compared with point-in-cell method, although its accuracy is subject to considerably more question. The success of both Rae and Kirchner and the authors of this paper in demonstrating satisfactory agreement between prediction and experimental observation for early stages of the event, however, would seem to warrant an attempt to exploit the method to a greater degree.

SUMMARY: STUDIES OF CRATER FORMATION

c. Traditional

Luttrell

The term "traditional" is used in the present context to designate theory based upon more or less arbitrary physical models that are chosen, at least in part, for their amenability to simple mathematical treatment. An inevitable consequence of such an approach is the use of numerous simplifying assumptions. Such theory must always be treated with skepticism and the essential assumptions, either explicit or implicit, examined for plausibility. Such is the case with the paper presented by Mr. Luttrell. The paper starts by applying a hydrostatic principle to a high speed, non-steady hydrodynamic process; the use of an additional apparent mass added to the real mass of the penetrator is valid only for steady state, low velocity processes. This assumption plays a major role throughout the subsequent mathematical analysis. Further, in computing the forces involved in penetration, a mixture of vector and scalar quantities is used without apology or justification.

The author feels that this paper should be treated with extreme caution and tested thoroughly against experimental observation before it is used for any predictions. It is particularly disturbing to note that this theory has been used in a systems feasibility study (Lane, in this symposium).

II. QUASI-THEORETICAL PAPERS

1. Heyda

This paper presents what amounts to a fitting of experimental data pertaining to propagation of shock waves in water subsequent to impact by metal projectile at fairly high velocities. The results should not be generalized beyond the specific application nor extrapolated beyond the conditions from which the data were obtained. The only significant general result derived from the paper lies in the fact that Heyda is in agreement with Rae and Kirchner and with Davids et al concerning the fact that the late stage wave propagation does not obey the predictions of a simple similarity calculation; that is, the attenuation of the wave is not in accord with the two-fifth power law. Other than this point, several minor objections can be raised to generalization of the statements made in the paper. The major one pertains to the discussion of a maximum shock propagation rate occurring at some time significantly later than the actual impact - specifically at a time when the radius of the shock wave is equal to $4k^2$ (see paper for definitions). It must be emphasized that this result arises

SUMMARY: STUDIES OF CRATER FORMATION

solely from the form of the equation chosen for the data-fitting process. Since the form of the equation was entirely arbitrary, no physical significance should be attributed to peculiarities in the results arising from the form of the equation. In particular, it should be noted that the predicted time or distance at which the maximum shock propagation rate occurs corresponds to times previous to or only shortly after the first experimental observation obtained. In no case do the experimental data themselves actually show any such maximum propagation rate at times after the initial impact.

2. Kinslow

This paper is similar to Heyda's in that it utilizes experimental observations on the propagation of low pressure waves; the similarity ends there, however. Kinslow attempts to make use of the observations to deduce conditions existing at earlier stages of the event in considerable detail and proceeds to test the conclusions by recourse to specific experimental observations.

Two major assumptions are involved in the theoretical analysis: (1) it is assumed that the ultimate radius of the crater formed is equal to the radius of the stress wave at the instant the pressure level in the stress wave falls to the elastic limit; (2) a specific mathematical form is assumed for the "forcing function" - that is, the pressure pulse profile - with only nominal justification for the particular form chosen. Using these two assumptions and the experimental observations, the author proceeds to compute details of the pressure pulse shape at both early and late times. The test of accuracy of the results depends upon comparison of predicted and observed spallation resulting from reflection of the pressure pulses from free boundaries.

Several objections can be raised to the general approach. There is of course, the arbitrary character of the choice of forcing function, as well as the unvalidated assumption relating the intensity of the pressure pulse at one time to the dimensions of the crater at a very considerably later time. The general approach has a distinct disadvantage in that it uses observations obtained during an essentially elastic phenomenon to deduce conditions existing during earlier stages when pressures are extremely great. This is at best a risky procedure, since one is depending upon rather small manifestations of parameters that originally were very large. In at least partial compensation for this disadvantage, the experimental observations that can be made under the later, elastic propagation conditions are much more precise than those that can be made under the early, high pressure conditions. The choice of an experimental test is also subject to question. The use of a spallation phenomenon implicitly entails additional assumptions. Furthermore, it is likely to be quite insensitive to the significant parameters in the wave propagation or crater formation phenomena and is likely to be very seriously affected by properties of the specimens which are not important in the phenomena under investigation.

SUMMARY: STUDIES OF CRATER FORMATION

In the author's viewpoint, this paper should be considered as a forerunner of future work. The procedure used appears to hold some promise, but should be considered with skepticism until it has been validated by detailed and precise experimental observations. It is suggested that the spallation experiment be replaced by one more sensitive to parameters that are important to the basic problem; in the pressure range under consideration, sensing devices are available that would permit accurate determination of actual pressure profiles, thus eliminating the indirect experimental test involved at present. Momentum measurements are also entirely feasible and would make a useful adjunct to pressure profile observations.

3. Engel

The intent of the author of this paper is to estimate the extent of fusion occurring during hypervelocity impact. The approach used, however, involves the analysis of an essentially intuitive model of crater formation which is in disagreement with conclusions reached by other workers. The results are applied to a set of experimental data and the conclusion reached that the amount of material fused during the crater formation process bears a constant relationship to the volume of the crater formed. In this writer's opinion the only conclusion that is really justified is that there is a constant relationship between the volume of the crater and the initial kinetic energy of the projectile. The analysis of the constant of proportionality and identification of its components with various properties of the materials, particularly with the heat of fusion, is not substantiated by the paper, and is in distinct contradiction to conclusions based upon more fundamental reasoning by Bjork.^{2/} The conclusions reached by the author are not really substantiated in the paper and they are in distinct disagreement with conclusions reached by Pond and Glass and by Gault and Heitowit on the basis of actual experimental observation of energy partitioning.

The argument connecting hypervelocity impact in metals with impact by liquid drops upon liquid targets is hardly convincing. It is based upon the empirical observation that

$$p \propto V^n$$

(p = depth of crater, V = impact velocity) for three situations studied:

- (i) Undeformed metal projectiles striking water;
- (ii) Liquid drops striking water;
- (iii) Metal projectiles striking metal targets at hypervelocity;

and that n for case (iii), being 2/3, lies between those for case (i), n = 1, and for case (ii), n = 1/2.

SUMMARY: STUDIES OF CRATER FORMATION

4. Moore, MacCormack and Gault

This paper comprises a semi-quantitative discussion, together with comparisons with available experimental data, of material properties that may be important in hypervelocity crater formation. The most significant conclusion reached in the paper is that even for fluid targets the resistance of the target material to flow is an important parameter in the crater formation process. A corollary conclusion is that the velocity of sound is not a fundamental parameter. The authors propose a new measure of resistance to deformation - namely, the compressive strength of the target material under the appropriate confining pressure. Following this concept, the resistance to flow will depend upon the pressure at the instant under consideration; it would vary from a minimum value corresponding to the compressive strength of the target material under very low confining pressure to a maximum value equal to the product of the density and the latent heat of fusion of the target material.

Unfortunately, appropriate values of the compressive strength are not available for high confining pressures. The correlations developed by the authors are quite convincing, however, especially insofar as they demonstrate that experimental observations with water drops impinging on water targets and plastic projectiles striking wax targets correlate quite well with hypervelocity impact data for metal projectiles striking metal, provided the appropriate strength parameters are used. Consequently, the paper provides significant data relevant to the fundamental subject of controversy - that is, whether under truly hypervelocity impact conditions the strength of the target material plays a significant role.

As an interesting side-light to this paper, one should note the considerable discrepancy between the treatment by the authors and that by Dr. Engel of the same experimental observations concerning water drops impinging on water targets.

III. EXPERIMENT

a. Crater Dimensions

1. Halperson

The experimental results presented by Halperson assume an extraordinary importance because of their use by Bjork in attempting to validate his theoretical computations. Thus, although they are merely an extension to higher velocities of data presented previously, they require particular attention.

SUMMARY: STUDIES OF CRATER FORMATION

It should first be noted that the data obtained by Halperson are among the most consistent and most reliable, in a statistical sense, that are available today. Second, it should be especially noted that the author's own analysis of his experimental results differs markedly from that of Bjork. In fact, Halperson quite clearly demonstrates that his own data are not suitable to determine whether crater volume is proportional to kinetic energy or to momentum of the impacting projectile. One cannot fail to take into account this presentation of the data in considering the relative merits of the Walsh-Tillotson and the Bjork theoretical results.

Two objections to Halperson's treatment of his data must be raised. In the first place, the use of a linear least squares treatment of the data over a velocity range that is known to include changes in the basic mechanism seems entirely inappropriate. A more sophisticated statistical analysis of the data is called for. In part, the over-simplified treatment of the data is less obviously objectionable than it might be because only impacts involving like materials for projectile and target are considered. The second objection pertains to the statements following Equation 3 in Halperson's paper. In considering the implications of Equation 3, which is a purely empirical relation of arbitrary form. Halperson conjectures concerning the importance of an extreme case in which $c_1 V$ becomes much greater than c_2 in his formula. He does not point out, however, that $c_1 V$ becomes equal to c_2 only when the impact velocity is nearly 10 kilometers per second. Consequently, the inference that the depth of penetration depends upon momentum rather than energy could become valid only after the impact velocity exceeds 100 kilometers per second. This obviously is too great an extrapolation from the actual experimental observations at less than 7 kilometers per second, using a purely empirical formula. The statement should therefore be discounted. The subsequent analysis of the data is far more pertinent to the question of relative importance of momentum and kinetic energy in the crater formation process.

The decision to treat impact into aluminum only is an unfortunate one; as a result of this exclusive attention to a material having very high shock propagation velocities, the author is able to observe impacts only in the lower region of the truly hypervelocity regime.

2. Goodman and Liles

Little can be said about this paper, except that it represents a regression to the approach followed by many experimentalists during the formative years of the hypervelocity impact problem.

SUMMARY: STUDIES OF CRATER FORMATION

It raises again, controversies that were ostensibly settled during earlier symposia. It cannot be considered profitable to raise them again on the basis of the data provided by Goodman and Liles. While the experiments reported have ostensibly been carried out under very carefully controlled conditions, there is nevertheless an unduly large amount of scatter in the data. The quality of the data also represents a regression and they are bound to be indecisive. The inclusion of data obtained at very low velocities in statistical analyses distorts the overall effect; such points have an exorbitantly large moment in determining empirical formulae. The use of log-log plots is also objectionable. On the whole, one strongly prefers the data presented by Halperson, as well as his approach to analysis of data.

3. Kineke and Richards

The authors of this paper have addressed themselves to two of the most important controversies presently haunting the hypervelocity crater formation problem. They have concentrated on an exploitation of their special capability to produce massive projectiles traveling at very high velocities. The two points under consideration are the influence of target strength at very high velocities and the relationship between crater volume and impact velocity. In both instances, while the data are not as precise as one would like, the results appear to be conclusive. At velocities up to 15 kilometers per second the influence of target strength is no less than at much lower velocities. The crater volume is apparently proportional to kinetic energy at least to 9.7 kilometers per second. It is unfortunate that the masses of the faster projectiles is not known precisely enough to permit extension of the latter test.

This is perhaps a suitable point at which to note the importance of a few observations at very high velocities. A glance at the plots provided by Kineke and Richards points up dramatically the relative significance of moment and of precision of datum points in establishing the relationship between dependent and independent variables. Despite the rather large variability of the authors' data, the high velocity enables them to provide a far more conclusive result than could be obtained from much more precise data at lower velocity. It should perhaps also be pointed out that, while the data presented by Kineke and Richards are less precise than those obtained by some experimenters using light gas guns, they are no worse than those presented by others. Furthermore, there is no attempt to diminish the variability of the data by using log-log plots instead of cartesian coordinates.

SUMMARY: STUDIES OF CRATER FORMATION

The present writer considers the results presented by Kineke and Richards to be the most significant experimental results presented at this symposium. Until more precise data are obtained at comparable velocities, these must be excepted as the definitive data concerning energy-volume relationships and strength effects at very high impact velocities.

4. Nysmith, Summers and Denardo

The experimental observations of penetration by rod-shaped projectiles presented by the authors should be very useful not only to theorists but also to those concerned with application of hypervelocity impact. The experiments have been carried out with exceptional care and the results appear to be very reliable.

Since no theoretical analysis was attempted in the paper, it is particularly interesting to note that the experimental results presented are in essential agreement with shaped charge experiments and with theoretical treatments of the penetration by a "skewed"

jet.^{4/} The critical parameters determining the influence of rod inclination upon its penetration characteristics are the rate and extent of expansion of the crater and the angle of inclination. Essentially, if the crater produced by impact of front portions of the rod opens quickly enough and to a large enough diameter that the later parts of the rod can enter the crater without interference, the inclination of the rod will result in very little reduction in penetration; the crater will be very nearly as deep as that produced by a perfectly aligned rod but will itself be somewhat inclined. On the other hand, if the rod is skewed so much that the following parts impact the walls of the early portion of the crater, an elongated scar will be produced and the depth of penetration will be very substantially decreased. The theoretical treatment provided by Allison should be useful for generalization of the data provided by the authors of this paper.

b. Energy Partition

1. Pond, Mobley and Glass

The subject of this paper, the partitioning of energy resulting from a hypervelocity impact, is an extremely important but exceptionally difficult one. A proper understanding of crater formation cannot be achieved without knowing quantitatively how much of the kinetic energy of the projectile is absorbed by each of the several mechanisms active in the process.

SUMMARY: STUDIES OF CRATER FORMATION

The technique used by the authors is certainly a novel one. It may be sufficiently novel for its plausibility to be questioned. The reported results, however, should go a long way in validating the approach. It should perhaps be noted that the very essence of the method used is at variance with the principles of hydrodynamics. The authors propose to use the measure of the strain energy stored in the target material to determine the partitioning of energy, whereas a purely hydrodynamic approach allows for no such means of energy absorption. All energy in an ideal hydrodynamic system must eventually return to the form of kinetic energy. With this in mind, the results presented in this paper, indicating that approximately 60% of the initial kinetic energy is transformed into strain energy in the target in aluminum and 80% in copper are extraordinary, especially when one contrasts them with the implications of Bjork's approach in which ideal hydrodynamic conditions are assumed to be valid even through the late, low pressure stages of crater expansion.

One must also note the very strong disagreement between the hypothesis and conclusions of this paper and the conclusions reached by Engel. The disagreement is particularly significant since the materials and the impact velocities were very similar in the two studies.

One lack in this paper should be noted: the authors have treated the energy partition as an energy dependent phenomenon alone. It would seem better to treat it as a velocity dependent phenomenon, accepting the simple scaling laws, and to attempt to discover systematic trends in the partitioning of energy with variations in the impact velocity. Such an effort would be extremely useful in resolving the present controversies over strength effects and the relationship between crater volume and impact velocity.

2. Gault and Heitowit

This paper was not available to the author at the time of writing.

c. Transient Observations

1. Kineke and Vitali

In view of the importance of observations of the transient phenomena occurring during crater formation, it is regrettable that this is the only paper in the 6th Symposium describing such observations. The paper of Kineke and Vitali may contain within it, however, a partial explanation. It is clear that a tremendous effort, involving extremely sophisticated instrumentation and analysis together with a high degree of ingenuity, is required in order to obtain satisfactory data concerning transient phenomena.

SUMMARY: STUDIES OF CRATER FORMATION

The paper contains data pertaining to two aspects of crater formation, but deals only with impact upon lead targets. The first portion of the paper treats the expansion of the crater. The data obtained do not include the very early stages of crater formation nor the very late, but they do provide a comprehensive treatment of the intermediate period during which a large portion of crater is formed. They yield not only specific data for a few experimental conditions but provide a complete treatment of scaling effects and of the velocity dependence of the crater expansion. With the normalizing procedures developed, a single relationship is derived for velocities from 2 kilometers per second to 5 kilometers per second. It is clear from the results that the first stage of crater formation takes place with great rapidity but that thereafter the expansion of the crater proceeds at velocities of the order of few hundred meters per second.

One can only anticipate with impatience the development of comparable data for higher impact velocities and for materials other than lead.

The measurements of stress wave propagation resulting from impact in lead, while very few at the time of the symposium, are also of extraordinary importance. The data currently available show only that the stress wave resulting from an impact at rather modest velocity on lead is not distinguishable, insofar as velocity of propagation is concerned, from an elastic wave at radii greater than 0.4 centimeters. The qualitative agreement of this experimental observation with the theoretical deductions of Davids et al and of Walsh and Tillotson should be noted. Of perhaps more specific importance, however, is the essential disagreement between the observations and the assumption used by Kinslow and others in their analyses. Although crater dimensions for the specific impact observed were not given by the authors, it is easily determined that the final crater radius for the impact would have been between 1.5 centimeters and 2.0 centimeters - that is, about 4 to 5 times the maximum radius at which the stress wave has attenuated and become essentially an elastic wave. While this result cannot be generalized without further evidence, it is clear that the assumption used by Kinslow and others, to the effect that the final crater radius is approximately equal to the radius of the stress wave at the instant it becomes an elastic wave, cannot be generally valid either. Insofar as the assumption is critical to any theoretical analysis, then, that analysis must be regarded with a high degree of skepticism.

SUMMARY: STUDIES OF CRATER FORMATION

IV. IMPACT IONIZATION AND FLASH

The three papers presented at the 6th Symposium pertaining to this general research area will be treated as a group. The papers by MacCormack, Gehring and Warnica, and Friichtenicht and Slattery present data obtained under a great variety of experimental conditions and treat a diversity of parameters. Consequently, they are not easily compared. There are ostensible differences, especially between MacCormack on the one hand and Gehring and Warnica, on the other, but the variations in approach are sufficiently great that the differences cannot be resolved at present and may ultimately be found to not represent essential disagreement.

Since studies of ionization and flash represent a relatively new departure in the hypervelocity impact problem, it is reasonable to expect that the variations in experimental method and analysis will be resolved in the future and that the rather large amount of experimental information already obtained will be rationalized and explained by theory.

CONCLUSION

In summary, it appears to the author that the high points of the 6th Symposium insofar as fundamental investigations of crater formation are concerned were the following papers:

1. Walsh and Tillotson
2. Riney
3. Wilkins and Giroux
4. Rae and Kirchner
5. Pond
6. Kineke and Richards
7. Kineke and Vitali

The contents of these seven papers represent the chief prospects for future progress in solution of the crater formation problem. Fortunately, they comprise an essentially complete study also, except for the aspects of the phenomenon treated in the relatively new efforts on ionization and flash. It seems reasonable that a vigorous continuation of the studies conducted by these authors would result in a conclusion of the basic research on crater formation in the relatively near future, that is, perhaps two to three years.

It is also noteworthy, however, that the major progress in hypervelocity impact study is represented by a relatively small fraction of the papers presented at the 6th Symposium. There are still far too many pedestrian research projects in existence and too few really new approaches to the problem. There are still too many experimenters, and theoreticians as well, who are re-plowing old ground and ignoring the guidelines that are available

SUMMARY: STUDIES OF CRATER FORMATION

in the literature. It is hoped that in the future the effort on hypervelocity impact will be concentrated in fewer research laboratories and along only those lines that have proven profitable. Closer coordination of the theoretical and experimental work in the near future is critical; only by very close coordination of the two efforts will a really satisfactory resolution of the current controversies be attained.

Briefly, the 6th Symposium has certainly not resolved any of the major questions on the fundamental aspects of crater formation. It has, however, brought into clearer focus the nature of the disagreements and it has shown that the means of resolving the remaining questions are in hand. The chief need now for final solution of the basic problems is an intelligent and vigorous application of the available theoretical and experimental techniques.

SUMMARY: STUDIES OF CRATER FORMATION

REFERENCES

1. R. J. Eichelberger and J. W. Gehring, "Effects of Meteoroid Impacts on Space Vehicles," ARJ Jour. 32, 1583-1591, October 1962.
2. A. E. Olshaker and R. L. Bjork, "Hydrodynamics Applied to Hypervelocity Impact," Proceedings of the Fifth Symposium on Hypervelocity Impact, 185-240, April 1962.
3. R. L. Bjork, "Numerical Solutions of the Axially Symmetric Hypervelocity Impact Process Involving Iron," Proceedings of the Third Symposium on Hypervelocity Impact, Vol. II, February 1959.
4. F. E. Allison, Ballistic Research Laboratories, unpublished.

AUTHORS

Atkins, W. W.	Vol. 4, p. 385
Baer, Paul G.	Vol. 1, p. 41
Baker, J. R.	Vol. 1, p. 175
Barbarek, Louis A. C.	Vol. 4, p. 395
Becker, K. R.	Vol. 3, p. 207
Bjork, R. L.	Vol. 2, p. 1
Brown, J. M.	Vol. 4, p. 1
Calvit, H. H.	Vol. 2, p. 229
Carey, Charles A.	Vol. 4, p. 271
Chandler, R. L.	Vol. 4, p. 37
Chapman, R. L.	Vol. 1, p. 317
Charters, A. C.	Vol. 1, p. 1
Christman, D. R.	Vol. 4, p. 101
Coley, R. B.	Vol. 4, p. 345
Condon, J. J.	Vol. 1, p. 175
Cox, C. M.	Vol. 4, p. 193
D'Anna, Philip J.	Vol. 3, p. 281
Dailey, James J.	Vol. 4, p. 329
Dauids, N.	Vol. 2, p. 229
Davis, Dale M.	Vol. 4, p. 151
.	Vol. 3, p. 387
Denardo, B. Pat	Vol. 2, p. 577
Dittrich, W. H.	Vol. 4, p. 101
Donaldson, Coleman duP.	Vol. 4, p. 305
Eckerman, J.	Vol. 1, p. 247
Eichelberger, R. J.	Vol. 2, p. 683
Emmons, R. H.	Vol. 3, p. 249
Engel, Olive G.	Vol. 2, p. 337
Ferguson, J. E.	Vol. 1, p. 349
.	Vol. 3, p. 157
Friichtenicht, J. F.	Vol. 2, p. 591
Gates, D. F.	Vol. 1, p. 155
Gault, D. E.	Vol. 2, p. 367
.	Vol. 2, p. 419
Gaydos, George M.	Vol. 4, p. 167
Gehring, J. W.	Vol. 2, p. 627
.	Vol. 4, p. 101
Gibson, F. C.	Vol. 3, p. 207
Giroux, Richard	Vol. 2, p. 141
Glass, C. M.	Vol. 2, p. 401
Goodman, E. H.	Vol. 2, p. 543
Halperson, S. M.	Vol. 2, p. 525
Harms, D. E.	Vol. 1, p. 317
Harrity, Edmund M.	Vol. 4, p. 167

Heitowit, Ezra D.	Vol. 2, p. 419
Heyda, James F.	Vol. 2, p. 321
Howell, William G.	Vol. 1, p. 305
Ipson, Thomas W.	Vol. 1, p. 305
Johnson, O. T.	Vol. 2, p. 229
Joyce, J. P.	Vol. 1, p. 349
.	Vol. 3, p. 157
Kineke, John H., Jr.	Vol. 2, p. 457
.	Vol. 2, p. 513
Kinslow, Ray.	Vol. 2, p. 273
Kirchner, Henry P.	Vol. 2, p. 163
Kraus, H.	Vol. 3, p. 13
Kreyenhagen, K. N.	Vol. 1, p. 349
.	Vol. 3, p. 157
.	Vol. 4, p. 101
Kronman, S.	Vol. 1, p. 331
.	Vol. 4, p. 21
Lane, D. C.	Vol. 4, p. 373
Lemcke, Bo	Vol. 1, p. 107
Liles, C. D.	Vol. 2, p. 543
Long, Loren L.	Vol. 3, p. 357
Luttrell, J. L.	Vol. 2, p. 157
MacCormack, R. W.	Vol. 2, p. 367
.	Vol. 2, p. 613
Maiden, C. J.	Vol. 3, p. 69
Margolis, P. K.	Vol. 4, p. 1
McKay, W. L.	Vol. 1, p. 247
McMillan, A. R.	Vol. e, p. 309
Merendino, A.	Vol. 1, p. 331
Mobley, C.	Vol. 2, p. 401
Moore, H. J.	Vol. 2, p. 367
Mortensen, R. B.	Vol. 3, p. 157
.	Vol. 4, p. 101
.	Vol. 4, p. 345
Nysmith, C. Robert	Vol. 2, p. 577
Persechino, Mario A.	Vol. 4, p. 235
Piacesi, R.	Vol. 1, p. 155
Pond, R. B.	Vol. 2, p. 401
Porter, C. D.	Vol. 1, p. 175
Rae, William J.	Vol. 2, p. 163
Randall, R. R.	Vol. 1, p. 349
Recht, Rodney F.	Vol. 1, p. 305
Reynolds, B. W.	Vol. 3, p. 249
Richards, L. G.	Vol. 2, p. 513

Riney, T. D.	Vol. 2, p. 105
Rhea, W. A.	Vol. 4, p. 345
Rockowitz, Murray	Vol. 4, p. 271
Sandorff, P. E.	Vol. 3, p. 41
Seigel, A. E.	Vol. 1, p. 155
Slattey, J. C.	Vol. 2, p. 591
Smith, Horace C.	Vol. 1, p. 41
Sorenson, G. P.	Vol. 1, p. 317
Stein, Samuel D.	Vol. 4, p. 167
Sterbentz, William H.	Vol. 3, p. 357
Summers, James L.	Vol. 2, p. 577
Swift, H. F.	Vol. 1, p. 175
.	Vol. 1, p. 375
Thorn, E. S.	Vol. 4, p. 193
Tillotson, J. H.	Vol. 2, p. 59
Vitali, Richard	Vol. 2, p. 457
Walsh, J. M.	Vol. 2, p. 59
Warnica, R. L.	Vol. 2, p. 627
Watmough, T.	Vol. 4, p. 37
Watson, R. W.	Vol. 3, p. 207
Wilkins, Mark L.	Vol. 2, p. 141
Zernow, L.	Vol. 3, p. 1
Zimmerman, F. J.	Vol. 4, p. 37
Zimney, H. S.	Vol. 4, p. 345